1996

The rules for the exchange and analysis of dynamic information in structural vibration

Paulo Sergio Varoto
Iowa State University

INFORMATION TO USERS

This manuscript has been reproduced from the microfilm master. UMI films the text directly from the original or copy submitted. Thus, some thesis and dissertation copies are in typewriter face, while others may be from any type of computer printer.

The quality of this reproduction is dependent upon the quality of the copy submitted. Broken or indistinct print, colored or poor quality illustrations and photographs, print bleedthrough, substandard margins, and improper alignment can adversely affect reproduction.

In the unlikely event that the author did not send UMI a complete manuscript and there are missing pages, these will be noted. Also, if unauthorized copyright material had to be removed, a note will indicate the deletion.

Oversize materials (e.g., maps, drawings, charts) are reproduced by sectioning the original, beginning at the upper left-hand corner and continuing from left to right in equal sections with small overlaps. Each original is also photographed in one exposure and is included in reduced form at the back of the book.

Photographs included in the original manuscript have been reproduced xerographically in this copy. Higher quality 6" x 9" black and white photographic prints are available for any photographs or illustrations appearing in this copy for an additional charge. Contact UMI directly to order.

UMI

A Bell & Howell Information Company
300 North Zeeb Road, Ann Arbor, MI 48106-1346 USA
313/761-4700 800/521-0600

The rules for the exchange and analysis of dynamic information in structural vibration

by

Paulo Sergio Varoto

A dissertation submitted to the graduate faculty

in partial fulfillment of the requirements for the degree of

DOCTOR OF PHILOSOPHY

Department: Aerospace Engineering and Engineering Mechanics

Major: Engineering Mechanics

Major Professor: Kenneth G. McConnell

Iowa State University

Ames, Iowa

1996

Graduate College
Iowa State University

This is to certify that the doctoral dissertation of

Paulo Sergio Varoto

has met the dissertation requirements of Iowa State University

Signature was redacted for privacy.

Major Professor

Signature was redacted for privacy.

For the Major Department

Signature was redacted for privacy.

For the Graduate College

DEDICATION

This dissertation is dedicated to

Vania, Júlia, and ?

for their constant love and unconditional support

during these exciting years at Iowa State

There is never the last try
There is always the first of a new series

by the author

TABLE OF CONTENTS

LIST OF TABLES

LIST OF FIGURES

ACKNOWLEDGEMENTS

I would like to thank the "Conselho Nacional de Desenvolvimento Científico e Tecnológico - **CNPq**", a sponsoring agency of the Brazilian federal government for funding my PhD studies at Iowa State University of Science and Technology, and the "Departamento de Engenharia Mecânica da Escola de Engenharia de São Carlos, da Universidade de São Paulo, São Paulo, Brasil" for allowing me to pursue graduate studies abroad.

I would like to thank the Department of Aerospace Engineering and Engineering Mechanics at ISU for accepting me as a graduate student and for providing me with the required facilities so that I could develop my Ph.D..

I feel elated facing the opportunity to formally state in print my gratitude and sincere regard for my major professor at ISU, Dr. Kenneth G. McConnell. This work would be incomplete without his valuable suggestions and guidance. I gratefully acknowldege all the opportunities that he gave me to share some of his experience and knowledge regarding academic and non academic matters.

I would like to thank Profs. A. Flatau, J. A. Mann, L. Zachary, J. Bernard, and L. Peters for being part of my committe and for all sugestions received.

I would like to express my gratitude, love, and respect for my family in Ames and in Brazil for the continuous support during these years of graduate school: My loving wife, Vania and my dear daughter Júlia were always there when I needed them, being a sweet source of inspiration and relaxation to me; my parents, Luzia and Paulo for giving me continuous love and support during all stages of my life, and for believing that one day I would have this dream fulfilled, Here I am !; my parents in law, Cidinha and Alceu

("Chiquinho") and my brothers in law, Valdir, Valmir, Cris, and Vanessa, as well as to Caio and my dear niece Cristininha, for the support and encouragment.

Many thanks to Gayle, Sally, Tammy, and Tom Elliot from AEEM-ISU for the kind attention and support received during the course of my POS.

A special thanks goes to Mrs. Deborah Vance, from the Office of the International Students and Scholars for her continuous, efficient, and tireless support with important matters regarding our lives in the USA.

I would like to thank Mr. Elias B. Teodoro (now Dr. Teodoro), a former ISU-AEEM graduate student from Brazil, for the great deal of help during our first days in Ames, and for the continuous friendship and encouragment in the past four years.

Last, but most important, I thank the Lord for giving me the intelligence and strength to achieve this historic moment of my life.

Ames, IA, June of 1996

1 INTRODUCTION

Vibrating systems are usually composed of several structural components that are connected together to form a combined system with unique dynamic characteristics. When this system is subjected to a set of inputs, each structural component contributes to its dynamic response. Two different approaches can be used to evaluate this dynamic response. They differ in terms of *how the structure under test is defined* and they can be described as follows

- *The system formed by the connection of different components constitutes the structure under investigation.* This approach applies to the situation where two or more components are attached and the resulting system is expected to have vibration response characteristics that fall within desired limits. Knowledge of the dynamic characteristics of each substructure is required in order to obtain the system's vibration response

- *A particular component that is part of the system constitutes the structure under investigation.* In this case, the interaction of this component and the remaining parts of the system is of major importance. Knowledge of interface and external forces applied to the structure under test as well as its frequency response function characteristics are required in order to predict the structure's dynamic response

Examples of the first procedure are usually found in the automotive industry. The design of brakes must meet certain requirements so that the Judder effect [1] (brake induced vibrations that are transmitted to the driver's hands through the steering wheel)

can be minimized. Similarly, the design of the seats that will be placed into the automobile interior must meet certain requirements so that vehicle vibrations are reduced to acceptable levels [1]. Both examples reflect the same situation, i.e, two structures being coupled (brakes and chassis, seats and automobile's floor) so that the resulting assembly will have an expected dynamic response.

A major problem detected in the automotive environment [2] is that the groups who are responsible for the design and evaluation of the many different parts tend to be isolated from one another. The major question is, "how does one establish effective communication between these various groups ? Which dynamic characteristics need to be transmitted from one group to another in order to decrease the time required in achieving an effective design" ?

The second type of analysis described above is often encountered in the aerospace and electronics industries. In this case, the vibrations exhibited by a given component that is part of a collection of substructures is of major concern. Usual examples of this situation concern electronic equipment being transported by flight hardware [33]. A satellite is to be sent into orbit by a launch vehicle. In this case, the satellite must survive the dynamic strains during launch in order to operate correctly when placed in orbit. These dynamic strains are usually caused by interface loads that occur at the attachment points between the satellite and the launching vehicle as well as by acoustic loads applied at other locations on both structures.

Before discussing some preliminary aspects that are involved in obtaining a structure's vibration response, it is appropriate to define some terminology that will be used throughout this dissertation. Three structures (test item, vehicle, and vibration exciter) are constantly referred to, and are defined as

[1] Personal communication from Dr. Mark French, Lear Seating Corporation, Detroit, MI, Feb. 1996

[2] Personal communication from Mr. Gary R. Penn, Manager, Noise and Vibration Center, General Motors Proving Ground (USA), Feb. 1996

- **The test item** represents the structure under investigation (e.g, the satellite). It is treated as a single component that is attached to the vehicle at one or more connection points.

- **The vehicle** is the structure that is used to transport the test item (e.g., the launch vehicle).

- **The vibration exciter** is the structure that is used to generate inputs that are applied to the test item in order to simulate its dynamic environment.

Similarly, three dynamic environments will be considered as shown in Figure 1.1. The **field** represents the actual dynamic environment experienced by the test item. In the field environment the test item is attached to the vehicle to form the combined structure. The **laboratory** is the dynamic environment where the test item is attached to the vibration exciter in order to simulate the field vibration environment. The **finite element model** of the test item is an environment where appropriate computational tools are used in the design of a new product. It can be employed to evaluate the test item's dynamic response when exposed to the field environment.

Figure 1.1 shows three different communication paths between the field, laboratory, and finite element environments where structural dynamic characteristics and data must be exchanged. For example, certain field data may be useful for both laboratory tests as well as finite element simulations that are used to design a given test item. On the other hand, laboratory test results may be used to either verify a finite element model or determine that the test item will function in a satisfactory manner when in the field. The crucial question is "What information should be transmitted in order to achieve the best results at minimum cost ?"

Two major field cases often occur. In the first, the test item is not present so that the only information available consists of vibration responses at the interface points when the vehicle is in service. How does this bare vehicle response compare to that which will

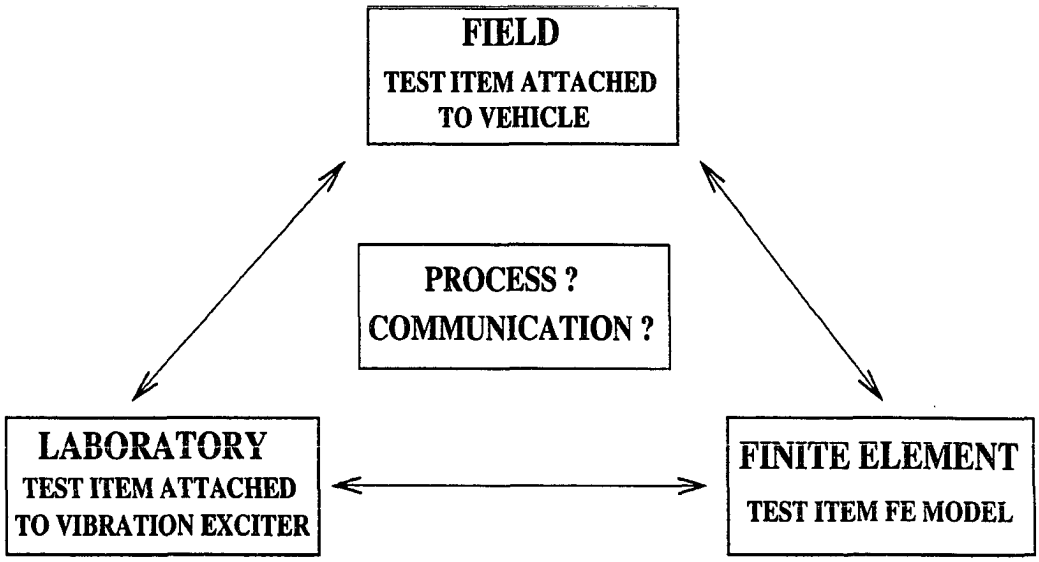

Figure 1.1 Dynamic environments involved in the design and evaluation processes

occur when the test item is attached ? Should this bare vehicle field data be modified before it is used in either the laboratory or finite element environment ? If it should be modified, then how can this modification be done in a rational manner ? In the second field case, the actual test item is attached to the vehicle at one or more points when the vibration data is measured. The ability to measure interface forces and accelerations is usually dependent on the complexity of the attachment hardware.

Laboratory data is obtained by attaching the test item to the vibration exciter and defining suitable test item inputs. The key question in laboratory simulations is: Can the test item field behavior be predicted in the laboratory prior to attaching the test item to the vehicle in the field ? The process of simulating the test item dynamic behavior in the laboratory environment is part of the technology of **Vibration Testing** and it requires that tailored inputs be applied to the test item such that the field environment can be properly simulated. Vibration Testing can be defined as (pp. 10 of [25])

"... the art and science of measuring and understanding a structure's response while exposed to a specific environment; and if necessary, simulating this environment in a satisfactory manner to ensure that the structure will either survive or function properly when exposed to this dynamic environment under field conditions"

Clearly, the above definition consists of two parts. The first part is concerned with measuring the dynamic response when the structure is in operation in its field environment. The second part of the definition is concerned with simulating the structure's dynamic behavior in the laboratory environment such that field vibration data can be reproduced and/or predicted. Some important reasons for conducting vibration tests are [25]: (1) Verify a theoretical model of a structure; (2) Determine the structure's modes of failure; (3) Develop adequate quality assurance test methods; (4) Qualify a structure to meet a set of specifications; (5) Develop dynamic inputs from field data for use in either laboratory or finite element simulations or other analysis methods.

The subject of this work is concerned with laboratory simulations of field vibration environments. Before outlining the objectives of this dissertation, it is appropriate to review the most recent developments in the area of vibration test tailoring.

Literature Review

When attached to a vehicle in the field environment, a given test item is subjected to a variety of loads that can be classified as [25]: (a) internal loads; (b) external loads; (c) boundary (interface or connector) loads. Test item field motions are due to these three types of excitation sources. Knowledge of the forces that act on a test item while in the field environment is one of the most important issues in vibration testing since these forces are needed in order to achieve realistic laboratory simulations.

A commonly employed laboratory simulation procedure consists in attaching the test item to a single vibration exciter through a test fixture [8, 36, 37]. Choice of

appropriate test fixtures is of major importance in obtaining realistic simulation of a field environment. MIL - STD810D [8] recommends that: (*i*) The test item be attached to the exciter through a *rigid* test fixture; (*ii*) When available, *Field data* should be used to define the test item inputs in the laboratory environment. In this case, enveloping techniques are frequently used with the field data in order to define the input that will be applied in the laboratory.

The choice of tailored laboratory inputs to a test item such that field measurements are reasonably simulated constitutes an important issue in laboratory testing where field interface forces (and possibly motions) [26] are natural candidates as test item inputs. However, interface force measurements are usually difficult [41] since they require force transducers to be placed in the force paths at the interface between the test item and vehicle, a requirement that may not be possible due to design or space limitations.

Early vibration testing techniques [28, 29] used blocked force measurements in the definition of vibration tests specifications. The blocked force is a concept that originates from the application of Norton's theorem [45] from the theory of electric circuits, that deals with equivalent systems. This theorem can be used to describe a system in terms of the forces and motions that occur at the boundaries of the system. The blocked force is defined as the boundary force required to produce a constrained boundary that has zero motion. When used to define test item laboratory inputs, this theorem requires the measurement of this blocked force between the test item and the foundation so that the true input interface force is applied to the test item by the vibration exciter. Due to the difficulties in achieving satisfactory blocked force measurements, test item inputs from blocked force measurements are not frequently used.

Smallwood [42] proposed to use the unloaded vehicle interface motion measurements as test item inputs in laboratory simulations as opposed to inputs derived from the blocked force technique. His work is based on another theorem from the theory of equivalent electric circuits, called Thevenin's theorem [45]. This theorem states that the

motion at the interface between the test item and the vehicle is composed of the sum of two motions: the vehicle's interface motion when the test item is absent and the test item's interface motion that is due to the interface force that results when the structures are combined. The unloaded or *bare* vehicle interface motions correspond to the motions measured at the vehicle's interface points, i.e, the attachment points between test item and vehicle when the test item is absent from the field environment. These motions result from the field inputs that act on the vehicle alone.

In a recent publication, McConnell [25] investigated the issues involved in taking field data and defining suitable laboratory inputs. An analytical and experimental study was performed on a test configuration where the test item is attached to the vehicle through a single interface connector. Three different field measurements are used to define the test item's laboratory inputs: the bare vehicle interface acceleration, the combined interface force and the combined interface acceleration. The conclusions of this work indicate that: (*i*) When the test item is subjected to no external forces in both the field and laboratory environments, the field interface force and motion constituted suitable test item inputs in laboratory simulations; (*ii*) when using the bare vehicle interface motion as the test item input, incorrect motions are obtained in the laboratory; (*iii*) correct interface forces and motions can be obtained from bare vehicle motions when modified by driving point accelerances.

When laboratory inputs are defined by enveloping techniques, the bare vehicle interface motions are selected most often for, and as Smallwood [41] points out, they are larger than those that occur when the test item is attached to the vehicle. When a single vibration exciter is employed, the vibration standards [8] usually recommend that the interface acceleration be enveloped by a flat (constant magnitude) acceleration that is slightly higher than the highest resonant peak.

An improved vibration testing technique has been recently proposed [34] in order to reduce the over-testing that occurs due to test fixture characteristics and enveloping

of the bare vehicle interface motions. This technique is called frequency shift method and consists in notching the test item input acceleration at the test item's resonant frequencies since little input force is required to drive the test item at those frequencies. This notching of the test item input acceleration causes a reduction of the force delivered by the exciter to the test item through the fixture, thus reducing the amount of over-testing.

The application of tailored inputs to a test item in the laboratory environment requires that the vibration exciter be controlled over the test frequency range. The control strategy chosen for a particular test can be defined in terms of controlling the input acceleration or input force applied to the test item. Acceleration controlled tests using the bare vehicle interface motions tend to be very conservative, as discussed in the previous paragraphs. Force controlled tests require the placement of transducers between the fixture and test item so that the laboratory interface force can be measured. The control system uses these force signals to perform signal compensation that is based on a reference drive signal. It is desired that the reference signal be defined in terms of measured field data. In this case, knowledge of the field interface variables is required either by direct measurement of interface forces or indirect force identification from acceleration measurements.

Dual control [27, 41] is usually employed in laboratory simulations using a single exciter. This technique consists in controlling the input force applied to the test item so that a given acceleration limit is not exceeded. This is equivalent to controlling the acceleration when a specified force limit is exceeded. Successful test results have been reported when using dual control in single vibration exciter applications [33, 36, 38].

The vibration testing procedures outlined so far correspond to the situation where a single vibration exciter is used to predict what vibration levels will be experienced by the test item when in the field environment. This procedure is particularly useful in situations where the test item is attached to the vehicle in the field by a single interface

connector and the interface force that is applied to the test item represents the major cause of test item motions.

However, in many field environments several interface points exist between the test item and the vehicle. In these cases, the use of a single vibration exciter with rigid test fixture as recommended by standard procedures [8] represents a major problem since in the field all test item interface points experience different forces and motions. In the laboratory, all test item interface points experience essentially the same motion due to the rigidity of the fixture. This situation becomes even more critical when the number of interface points are different in the field and laboratory environments [3]. Another difficulty is: Which motion or force should be used to define the control strategy ? Should one of the field interface motions be used ? In this case, which one ? Or should a combination of all interface motions be used to define the reference signal ?

Little research has been reported in the field of vibration test tailoring with multiple excitation. Smallwood [39, 40] outlines a procedure to test a single test item with multiple random inputs where it is shown that cross coupling effects between excitation channels must be accounted for in the control process. No practical results of this procedure have been reported since its publication. More recently, a vibration testing procedure has been proposed [12] for applications in automobile simulations. This procedure attempts to improve the numerical stability of the deconvolution process that is used to obtain reference input force signals from motion measurements.

Similarly, in addition to the interface forces that occur in single or multiple connector field configurations, the test item may be subjected to field external loads that can be caused by interactions between the test item and the environment. In some situations, as it is the case of aerodynamic and acoustic [32] loading, the experimenter might not be aware of the occurrence of these loads and the resulting test item field motions will be affected by these external loads. When performing the laboratory simulations, these

[3]Personal communication from D. Smallwood, XIII IMAC, Nashville, TN, Feb. 1995

external force effects need to be accounted for [32, 46] in addition to interface force effects. Otherwise, incorrect simulation results in terms of vibration levels are obtained. From this discussion, it is clearly evident that, even in the case of a single interface point, additional exciters may be required in order to simulate these external force effects.

Knowledge of a test item external forces is required when attempting to account for their effects in laboratory simulations. Since in most field environments a direct measurement of these external forces is difficult, an indirect solution for the unknown forces in terms of the measured field motions and the test item frequency response function (FRF) characteristics is usually employed. The identification of unknown input forces from measured motions represents an inverse problem [2], which tends to be numerically unstable since it represents a deconvolution problem. Among the techniques available for the indirect prediction of input forces, the **S. W. A. T.** (**S**um of the **W**eighted **A**ccelerations **T**echnique) [15] and the **Pseudo-Inverse** techniques are most often employed.

The **S. W. A. T.** method is a force prediction technique that is based on the principle of motion of the mass center that is commonly employed in texts on rigid body dynamics. This technique can be used to obtain an estimate of the *total resulting force* acting on a structure from knowledge of the structure's mass characteristics and the structure's measured accelerations.

The **Pseudo-Inverse** technique [18, 9] is used to calculate a set of pseudo forces from knowledge of the test item FRF characteristics and the measured motions. This set of pseudo forces may or may not resemble the true test item input forces since the pseudo-inversion of the test item's FRF matrix is required for all frequencies in the test frequency range. This pseudo-inversion process is usually ill conditioned [18, 19] since the FRF matrix to be inverted tends to be rank deficient at the test item's natural frequencies. The nature of this rank deficiency has been the subject of investigations for deterministic [10, 11, 43] as well as random [18, 49] excitation and response sig-

nals. Fabunmi [10, 11] performed an analytical study of the pseudo-inverse method for deterministic signals and concluded that the rank deficiency problems that occur at some frequencies is due to an insufficient number of mode shapes participating on the structure's response at those frequencies.

Hillary and Ewins [18, 19] investigated the force identification problem for deterministic (periodic and transient) as well as random forces. In the case of deterministic signals, they found that by employing strain gages in the structure's response measurements an improvement is obtained in the conditioning of the inversion process at the low frequencies. In the case of random forces, they assumed that the forces are statistically uncorrelated [18]. In their numerically simulated results, the predicted random forces are not in good agreement with the measured forces. Zhang [49] made the same assumption that the forces are uncorrelated when trying to identify random loads from sea waves.

Objectives and Dissertation Organization

This dissertation presents a theoretical model that describes the pertinent variables and physical processes that control the vibration data that needs to be measured as well as how this data is to be handled in generating suitable inputs to either a laboratory experiment or a finite element model of a given test structure.

This theoretical model is referred to as **READI** (**R**ules for the **E**xchange and **A**nalysis of **D**ynamic **I**nformation in structural vibration) and it contains a broad set of definitions and describes several scenarios for testing a given test item. **READI** is concerned with defining which structural dynamic characteristics as well as measured responses that need to be communicated between various groups that are involved in designing and developing a specific test item that is to function satisfactorily in a given environment. Vibration test tailoring (**VTT**) is the name that has been associated with

this type of process, but is a restricted concept that ignores important interface dynamic characteristics. Properly done, **VTT** is a subset of the general concepts contained in **READI.**

Past attempts to develop such a theoretical framework have been essentially restricted to single point interface connections between structural elements. In the present theory, multiple interface connections as well as the presence of external forces acting on the test item are considered.

The ultimate goal of this work is to define realistic test environments so that meaningful vibration data can be exchanged between different working groups that will result in a cost effective design of a given test item.

Some typical questions that will be investigated are:

- What field data should be taken ? Under what conditions can the bare vehicle's response be used to define suitable test item inputs ? Is it required to have data from the combined structure (test item attached to the vehicle) ?

- How do field external forces affect the laboratory simulation results ? How can these forces be predicted in order to be properly accounted for in the laboratory ?

- How does the assumption of uncorrelated inputs affect the prediction of forces from random acceleration measurements ? How can singularity problems be reduced when solving this inverse problem ?

- How do test fixtures and enveloping techniques affect the test item dynamic response in laboratory simulations using a single vibration exciter ? How to quantify the amount of over-testing imposed to the test item under these test conditions ?

- How do motion transmissibility concepts apply to test configurations where the test item has several interface points ?

This dissertation is organized as follows. Chapter 2 discusses modal analysis principles used in the description of the field and laboratory environments. Chapter 3 describes the proposed theoretical framework where frequency domain substructuring technique concepts are employed in defining the structural interactions that occur in the field and laboratory environments. Chapter 4 shows numerical results of this theory in terms of deterministic excitations. In chapter 5 the theoretical results from chapter 3 are used to obtain new expressions to be used with random excitations and numerical results are presented in this chapter. Chapter 6 discusses the application of motion transmissibility concepts in multi connector test environments. A generalization of the well known single point transmissibility concept is presented. This transformation is called **Q** - Transmissibility matrix approach. These concepts are used to illustrate current practices in vibration testing. Chapter 7 shows experimental results regarding the force identification problem for deterministic (periodic and transient) as well as random signals. Experimental results for the **Q** - Transmissibility matrix approach are presented. Finally, Chapter 8 summarizes the main points investigated and some conclusions and recommendations are presented.

2 MODAL ANALYSIS PRINCIPLES

This chapter reviews fundamental modal analysis concepts that will be used in the remaining chapters of this dissertation.

Natural Frequencies and Normal Modes of Vibration

The finite element equations of motion of a N degrees of freedom (DOF) viscously damped linear structure can be written in matrix notation as [5, 9]

$$[M]\ \{\ddot{x}\} + [C]\ \{\dot{x}\} + [K]\ \{x\} = \{f\} \tag{2.1}$$

where the square and symmetric N x N matrices $[M]$, $[C]$, and $[K]$ contain the structure's physical mass, damping, and stiffness characteristics, respectively. The N x 1 vectors $\{f\} = \{f(t)\}$ and $\{x\} = \{x(t)\}$ contain the input forces applied to the structure and the resulting output motions due to these forces, respectively. The dots denote differentiation with respect to time.

The structure's natural frequencies and normal modes of vibration are obtained by solving the undamped free vibration problem [5]. By setting the damping matrix $[C]$ and the vector of external excitations $\{f\}$ equal to zero in Equation 2.1, the following undamped free vibration problem is obtained

$$[M]\ \{\ddot{x}\} + [K]\ \{x\} = \{0\} \tag{2.2}$$

The solution of Equation 2.2 for nonzero initial conditions can be written as a linear

combination of solutions of the type

$$\{x\} = \{\phi\}\ e^{\lambda t} \tag{2.3}$$

where $\{\phi\}$ is a N x 1 vector of real or complex entries and λ is a complex number. Substitution of Equation 2.3 in Equation 2.2 gives

$$\left[\lambda^2\ [M] + [K]\right]\{\phi\} = \{0\} \tag{2.4}$$

Equation 2.4 represents a quadratic real eigenvalue problem [48] and it presents a non-trivial solution if and only if the following relationship holds

$$det\ \left[\lambda^2\ [M] + [K]\right] = 0 \tag{2.5}$$

The solution of Equation 2.5 is composed of N pairs of pure imaginary eigenvalues and the structure's r^{th} natural frequency ω_r is obtained from the r^{th} eigenvalue λ_r through the following expression

$$\lambda_r = \pm\ j\ \omega_r \tag{2.6}$$

where $j = \sqrt{-1}$.

Once Equation 2.5 is solved for the eigenvalues, the solution for the real eigenvectors $\{\phi\}_r$ that correspond to the structure's undamped *modes of vibration* requires that Equation 2.4 be solved for each value of λ_r (or $-\omega_r^2$). Since Equation 2.4 is a homogeneous system of equations, there are an infinite number of eigenvectors $\{\phi\}_r$ satisfying this equation. Therefore, the *amplitude* of the structure's modes of vibration is indeterminate. However, the *shape* of each mode of vibration can be obtained by assuming one entry of vector $\{\phi\}_r$ to be unity [5] and solving for the remaining coordinates of that mode in terms of this unity amplitude coordinate.

The set containing all natural frequencies and mode shapes constitutes the structure's undamped *modal model* and can be written in terms of a N x N diagonal matrix containing the structure's natural frequencies squared

$$[\Omega_r] = \begin{bmatrix} \omega_1^2 & 0 & 0 & \dots & 0 \\ 0 & \ddots & \ddots & \ddots & \vdots \\ 0 & \ddots & \omega_r^2 & \ddots & 0 \\ \vdots & \ddots & \ddots & \ddots & 0 \\ 0 & \dots & 0 & 0 & \omega_N^2 \end{bmatrix} \tag{2.7}$$

and the real N x N matrix $[\Phi]$ which columns contain the mode shapes

$$[\Phi] = \begin{bmatrix} \{\phi\}_1 & \{\phi\}_2 & \dots & \{\phi\}_r & \dots & \{\phi\}_N \end{bmatrix} \tag{2.8}$$

The orthogonality conditions [5, 9] represent very important and useful properties exhibited by the mode shapes. Consider any two mode shape vectors $\{\phi\}_r$ and $\{\phi\}_s$ corresponding to distinct natural frequencies $\omega_r \neq \omega_s$. The orthogonality conditions of these mode shapes with respect to the mass and stiffness matrices are given by the following relationships [5]

$$\{\phi\}_r^T [M] \{\phi\}_s = 0 \tag{2.9}$$

$$\{\phi\}_r^T [K] \{\phi\}_s = 0 \tag{2.10}$$

For the case where $\omega_r = \omega_s$, Equations 2.9 and 2.10 result in

$$\{\phi\}_r^T [M] \{\phi\}_r = m_r \tag{2.11}$$

$$\{\phi\}_r^T [K] \{\phi\}_r = k_r \tag{2.12}$$

The constants m_r and k_r are called the *modal mass* and *modal stiffness* of the r^{th} mode shape [9]. Equations 2.11 and 2.12 can be written for all mode shape vectors as

$$[\Phi]^T [M] [\Phi] = \mathit{diag}\,[m_r] \tag{2.13}$$

$$[\Phi]^T [K] [\Phi] = \mathit{diag}\,[k_r] \tag{2.14}$$

where $[m_r]$ and $[k_r]$ are diagonal N x N matrices whose diagonals contain the modal mass and stiffness coefficients, respectively for all mode shapes. Knowledge of these modal coefficients is important since the structure's r^{th} natural frequency can be expressed in terms of the r^{th} modal mass and stiffness coefficients according to [9]

$$\omega_r = \sqrt{\frac{k_r}{m_r}} \tag{2.15}$$

In addition, the structure's r^{th} mode shape vector $\{\phi\}_r$ can be normalized by the modal mass values by using the following relationship [9]

$$\{\psi\}_r = (m_r)^{-1/2} \{\phi\}_r \tag{2.16}$$

where $\{\psi\}_r$ represents the r^{th} mass normalized mode shape.

The orthogonality conditions of Equations 2.13 and 2.14 assume a slight different form when defined in terms of the mass normalized mode shape matrix $[\Psi]$ and they are given as

$$[\Psi]^T [M] [\Psi] = [I] \tag{2.17}$$

$$[\Psi]^T [K] [\Psi] = \boldsymbol{diag} [\Omega_r] \tag{2.18}$$

where $[I]$ is the N x N identity matrix, $[\Psi]$ is the N x N mass normalized mode shape matrix, and $[\Omega_r]$ is the N x N diagonal matrix containing the structure's natural frequencies squared on the main diagonal.

Response to a Single Sinusoidal input Force: The FRF Concept

Return to Equation 2.1 and assume *zero initial conditions.* In this case, the external excitation force vector $\{f\}$ is composed by a *single harmonic* input force that is applied at a single point on the structure. Mathematically

$$\{f\} = \{f_o\} \ e^{j\omega t} \tag{2.19}$$

where

$$\{f_o\} = \{\ 0\ \ \ldots\ \ f_q\ \ \ldots\ \ 0\ \}^T \tag{2.20}$$

where f_q is the magnitude of the sinusoidal force applied at the q^{th} coordinate and ω is the excitation frequency in rad/s.

The time solution of Equation 2.1 for the excitation of Equation 2.19 is obtained by first uncoupling the structure's equations of motion through the following coordinate transformation equation [5, 9]

$$\{x\} = [\Phi]\ \{y\} \tag{2.21}$$

Equation 2.21 represents a linear transformation that relates the structure's displacements in the physical domain $\{x\}$ to the structure's displacements in the *modal domain* $\{y\}$. This coordinate transformation is mapped by the undamped mode shapes matrix.

Substitution of Equations 2.19 and 2.21 into Equation 2.1 and pre-multiplication of both sides of the resulting equation by $[\Phi]^T$ results in

$$[\Phi]^T\ [M]\ [\Phi]\ \{\ddot{y}\} + [\Phi]^T\ [C]\ [\Phi]\ \{\dot{y}\} + [\Phi]^T\ [K]\ [\Phi]\ \{y\} = [\Phi]^T\ \{f_o\}\ e^{j\omega t} \tag{2.22}$$

Equation 2.22 reduces to a set of N uncoupled single degree of freedom equations of motion in the modal coordinates if and only if the damping matrix $[C]$ obeys the following orthogonality requirement

$$[\Phi]^T[C][\Phi] = [c_r] \tag{2.23}$$

where the N x N $[c_r]$ diagonal matrix contains the structure's modal damping coefficients. This orthogonality requirement can be met if a *proportional damping distribution* is assumed. In this case, the damping matrix is expressed as combination of the mass and stiffness matrices according to [5]

$$[C] = [M] \sum_b a_b \left[[M]^{-1}\ [K]\right]^b \tag{2.24}$$

where a_b is an arbitrary constant and b is an integer. All damping matrices that are defined based on Equation 2.24 are diagonalized by the same transformation that diagonalizes $[M]$ and $[K]$. A particular and widely employed case of proportional damping distribution is the so called *Rayleigh damping* that is obtained by setting $b = 0$ and $b = 1$ in Equation 2.24. The result is

$$[C] = a_0 [M] + a_1 [K] \tag{2.25}$$

Pre and post multiplication of both sides of Equation 2.25 by $[\Phi]^T$ and $[\Phi]$ respectively, gives the following result for $[c_r]$

$$[c_r] = [\Phi]^T [C] [\Phi] = a_0 [m_r] + a_1 [k_r] \tag{2.26}$$

where the orthogonality relationships expressed in Equations 2.13 and 2.14 were used on the right hand side of Equation 2.26.

If a proportional damping distribution is assumed, Equation 2.22 reduces to

$$[m_r] \{\ddot{y}\} + [c_r] \{\dot{y}\} + [k_r] \{y\} = [\Phi]^T \{f_o\} e^{j\omega t} \tag{2.27}$$

that represents a set of N uncoupled equations of motion in the modal domain. The equation of motion for the r^{th} degree of freedom is given as

$$m_r \ddot{y}_r + c_r \dot{y}_r + k_r y_r = \{\phi\}_r^T \{f_o\} e^{j\omega t} \tag{2.28}$$

Division of both sides of Equation 2.28 by the modal mass m_r results in an alternative form for the r^{th} equation of motion in the modal coordinates

$$\ddot{y}_r + 2\zeta_r \omega_r \dot{y}_r + \omega_r^2 y_r = \mu_r e^{j\omega t} \tag{2.29}$$

where ζ_r is the *modal damping ratio* of the r^{th} mode shape and is defined in terms of the corresponding r^{th} modal mass, stiffness, and damping coefficients according to [9]

$$\zeta_r = \frac{c_r}{2\sqrt{k_r m_r}} \tag{2.30}$$

The constant μ_r that appears on the right hand side of Equation 2.29 is the *input force modal participation factor* and is defined as

$$\mu_r = \frac{1}{m_r} \{\phi\}_r^T \{f_o\} \tag{2.31}$$

This number shows how the structure's r^{th} mode shape interacts with the spatial distribution of input forces that is applied on the structure $\{f_o\}$. When $\mu_r = 0$ Equation 2.29 presents a trivial solution for all values of the excitation frequency ω for zero initial conditions. Physically, this means that the r^{th} mode of vibration has no participation in the structure's response to this particular excitation force.

If there is at least one nonzero μ_r, the time domain solution of Equation 2.28 is given as

$$y_r = Y_r \, e^{j\omega t} \tag{2.32}$$

where Y_r is the unknown r^{th} modal amplitude. Substitution of Equation 2.32 into Equation 2.28 leads to the following solution for Y_r

$$Y_r = \frac{\mu_r}{\omega_r^2 - \omega^2 + j\ 2\zeta_r\omega_r\omega} \tag{2.33}$$

The time domain solution y_r is obtained by back substitution of the expression for Y_r into Equation 2.32. The solution is

$$y_r = \frac{\mu_r}{\omega_r^2 - \omega^2 + j\ 2\zeta_r\omega_r\omega} \, e^{j\omega t} \tag{2.34}$$

Once all y_r, $r = 1 \ldots N$ are determined, the solution for the structure's displacements in the physical domain $\{x\}$ can be obtained from Equation 2.21 that can be conveniently rewritten as [5]

$$\{x\} = \sum_{r=1}^{N} \{\phi\}_r \, y_r \tag{2.35}$$

Equation 2.35 is frequently referred to as *modal superposition* [5, 6] since it indicates that the final solution $\{x\}$ is obtained by *superimposing* (summing) the contribution of each

mode shape individually to the total displacement vector. Substitution of Equation 2.34 into Equation 2.35 and the use of the definition for μ_r given in Equation 2.31 leads to

$$\{x\} = \sum_{r=1}^{N} \frac{\{\phi\}_r \{\phi\}_r^T \{f_o\}}{m_r (\omega_r^2 - \omega^2 + j\ 2\zeta_r \omega_r \omega)} e^{j\omega t} \tag{2.36}$$

From the time domain solution in the physical domain Equation 2.36 the structure's *Frequency Response Function (FRF) model* can be obtained in terms of the *Receptance FRF matrix* as

$$[R(\omega)] = \sum_{r=1}^{N} \frac{\{\phi\}_r \{\phi\}_r^T \{f_o\}}{m_r (\omega_r^2 - \omega^2 + j\ 2\zeta_r \omega_r \omega)} \tag{2.37}$$

One element of $[R(\omega)]$, $R_{pq} = R_{pq}(\omega)$ is defined as the ratio of the Fourier transforms of the structure's displacement ($X_p = X_p(\omega)$) and input force ($F_q = F_q(\omega)$) at the p^{th} and q^{th} coordinates [9, 25], respectively. Mathematically

$$R_{pq} = \frac{X_p}{F_q}(\omega) \tag{2.38}$$

and $f_k = 0,\ k = 1 \ldots N,\ k \neq q$. From Equation 2.37, R_{pq} is given as

$$R_{pq} = \sum_{r=1}^{N} \frac{\phi_{rp}\ \phi_{rq}}{m_r (\omega_r^2 - \omega^2 + j\ 2\zeta_r \omega_r \omega)} \tag{2.39}$$

where ϕ_{rp} and ϕ_{rq} are the p^{th} and q^{th} elements of the r^{th} mode shape vector, respectively.

When the excitation and response coordinate points are coincident, $p = q$, R_{pp} is called *driving point* receptance FRF [9, 25]. In this case, Equation 2.39 can be rewritten as follows

$$R_{pp} = \sum_{r=1}^{N} \frac{\phi_{pp}^2}{m_r (\omega_r^2 - \omega^2 + j\ 2\zeta_r \omega_r \omega)} \tag{2.40}$$

and when $p \neq q$, R_{pq} is called *transfer point* receptance FRF [9, 25].

Two additional FRF relationships commonly employed in vibration testing are the *Mobility* and the *Accelerance* or *Inertance* FRFs [9]. The mobility FRF $M_{pq} = M_{pq}(\omega)$ is defined as the ratio between the velocity of the structure at coordinate p to the unit force applied at coordinate point q. The accelerance FRF $A_{pq} = A_{pq}(\omega)$ is defined as the ratio between the acceleration at coordinate p to the unit force applied at the coordinate q. The relationships between the mobility FRF and the accelerance FRF to the receptance FRF are given by [9]

$$M_{pq} = j\omega \; R_{pq} \tag{2.41}$$

$$A_{pq} = -\omega^2 \; R_{pq} \tag{2.42}$$

Response to a Single Input Motion: The Motion Transmissibility Concept

Another important concept in vibration testing is the *Single Point Motion Transmissibility FRF* [25, 26]. Consider a given structure having N DOF that is subjected to an external excitation given in terms of a *single* input motion $x_b = x_b(t)$ that is applied at a *single* point. The structure's equations of motion can be written using matrix notation as

$$[M]\{\ddot{x}\} + [C]\{\dot{x}^r\} + [K]\{x^r\} = \{0\} \tag{2.43}$$

where as in the previous section, $[M]$, $[C]$, and $[K]$ are the structure's N x N mass, damping, and stiffness matrices, respectively, and the N x 1 vector $\{x\} = \{x(t)\}$ contains the structure's *absolute displacements* with respect to a fixed coordinate system. The N x 1 vector $\{x^r\} = \{x^r(t)\}$ corresponds to the structure *relative displacement* with respect to the input motion x_b. The absolute and relative displacements are related to

each other by the following equation [5]

$$\{x\} = \{x^r\} + \{\delta\}x_b \tag{2.44}$$

where $\{\delta\}$ is a constant N x 1 vector and is used to express the fact that a unit input static displacement in the direction of x_b produces a unit static displacement of all structure DOF in the same direction. In a sense, $\{\delta\}$ can be viewed as an influence coefficients vector that identifies all structure DOF that are in the direction of the input motion x_b. Thus, $\{\delta\}$ is composed of "ones" at the DOF coinciding with the direction of the input motion and "zeros" for the remaining orthogonal DOF.

Substitution of Equation 2.44 into Equation 2.43 gives the following alternative form for the structure equations of motion in terms of the relative displacement $\{x^r\}$

$$[M]\{\ddot{x}^r\} + [C]\{\dot{x}^r\} + [K]\{x^r\} = \{f\}_{eff} \tag{2.45}$$

where $\{f\}_{eff}$ is the effective input motion excitation inertia force that is given by

$$\{f\}_{eff} = \{f(t)\}_{eff} = -[M]\{\delta\}\ddot{x}_b \tag{2.46}$$

where the minus sign on the right hand side of Equation 2.46 expresses the fact that the inertia excitation force opposes the input acceleration $\ddot{x}_b$.

The solution of Equation 2.46 is obtained in a manner similar to the previous section. If it is assumed that the structure is proportionally damped, pre-multiplication of both sides of Equation 2.46 by the transpose of the undamped N x N mode shapes matrix $[\Phi]^T$ and use of the coordinate transformation relationship given in Equation 2.21 leads to a a set of N uncoupled equations of motion in the modal coordinates $\{y\}$. The equation of motion for the r^{th} coordinate is written as

$$\ddot{y}_r + 2\zeta_r\omega_r\,\dot{y}_r + \omega_r^2\,y_r = -\eta_r\,\ddot{x}_b \tag{2.47}$$

where the modal parameters that appear on Equation 2.47 were previously defined. The constant η_r on the right hand side of Equation 2.47 is the *input motion modal*

participation factor of the r^{th} mode shape and is defined as

$$\eta_r = \frac{1}{m_r}\{\phi\}_r^T [M] \{\delta\} \tag{2.48}$$

Note that the input motion modal participation factor depends on $\{\delta\}$ so that $\{\delta\}$ dictates which structure mode shapes will be excited by the input motion x_b.

Consider that the input motion x_b and the solution for the modal coordinate y_r vary harmonically according to

$$x_b = x_o\, e^{j\omega t} \tag{2.49}$$

$$y_r = Y_r\, e^{j\omega t} \tag{2.50}$$

where x_o and Y_r correspond to the amplitudes of the input motion and the solution of the r^{th} modal equation, respectively. Substitution of Equations 2.49 and 2.50 into Equation 2.47 leads to the standard result

$$Y_r = \frac{\eta_r\, \omega^2\, x_o}{\omega_r^2 - \omega^2 + j\, 2\zeta_r\omega_r\omega} \tag{2.51}$$

that is similar to the result obtained in the previous section (Equation 2.33), except that they differ in terms of the modal participation factors due to the nature of the structure's inputs in both cases.

Substitution of Equation 2.51 into Equation 2.50 leads to the time solution y_r for the r^{th} modal coordinate. Once all equations of motion are solved in the modal domain, the solution for the relative displacement vector $\{x^r\}$ in Equation 2.45 in the physical domain is obtained by modal superposition (Equation 2.35) and is given as

$$\{x^r\} = \omega^2 \sum_{r=1}^{N} \frac{\{\phi\}_r\, \{\phi\}_r^T\, [M]\, \{\delta\}}{m_r\, (\omega_r^2 - \omega^2 + j\, 2\zeta_r\omega_r\omega)}\, x_o\, e^{j\omega t} \tag{2.52}$$

The structure's absolute motion $\{x\}$ is obtained from combining Equations. 2.44, 2.49, and 2.52 and is given as

$$\{x\} = \{\Gamma(\omega)\}\, x_o\, e^{j\omega t} \tag{2.53}$$

where $\{\Gamma\} = \{\Gamma(\omega)\}$ represents the N x 1 *absolute transmissibility FRF* vector for input motion at a *single* coordinate and is given by

$$\{\Gamma\} = \omega^2 \sum_{r=1}^{N} \frac{\{\phi\}_r \{\phi\}_r^T [M]\{\delta\}}{m_r(\omega_r^2 - \omega^2 + j\ 2\zeta_r\omega_r\omega)} + \{\delta\} \tag{2.54}$$

The p^{th} element of $\{\Gamma\}$ gives the motion (displacement, velocity, or acceleration) of the p^{th} coordinate point that is due to a single input motion (displacement, velocity, or acceleration) at the r^{th} coordinate point with all remaining inputs being identically zero. Mathematically

$$\Gamma_{pr}(\omega) = \frac{X_p}{X_r}(\omega) \tag{2.55}$$

where $X_p = X_p(\omega)$ and $X_r = X_r(\omega)$ are the Fourier transforms of the structure's p^{th} absolute displacement x_p and the single *absolute* input motion $X_r = X_b$, respectively. Once the structure's transmissibility FRF vector is known, it can be used to determine the motion at all structure DOF that are due to the input motion as long as X_b represents the *only* structure input that is applied at a single point.

Although Equation 2.54 expresses the transmissibility FRF in terms of absolute motions, the transmissibility FRF can still be defined in terms of the structure relative motions $\{x^r\}$. Substitution of Equation 2.52 into Equation 2.44 gives the following expression for the relative transmissibility FRF in terms of the absolute transmissibility FRF

$$\{\Gamma^r\} = \omega^2 \sum_{r=1}^{N} \frac{\{\phi\}_r \{\phi\}_r^T [M]\{\delta\}}{m_r(\omega_r^2 - \omega^2 + j\ 2\zeta_r\omega_r\omega)} \tag{2.56}$$

or simply

$$\{\Gamma^r\} = \{\Gamma\} - \{\delta\} \tag{2.57}$$

MIMO Relationships and Loads Classification

Consider the structure shown in Figure 2.1. The input at point q consists of two vectors, a force vector and a moment vector. This input is represented by $\vec{F}_q = \vec{F}_q(\omega)$. Each input vector can be resolved in terms of the global coordinate system shown in Figure 2.1 [25, 26]. Thus, the input vector at the q^{th} location has six components. The first three components F_1, F_2, and F_3 are forces in the x, y, z directions, respectively. The remaining components F_4, F_5, and F_6 are moments about the x, y, and z directions, respectively.

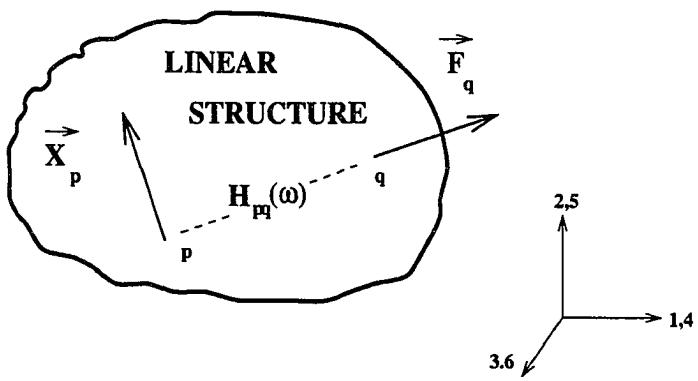

Figure 2.1 General input-output case: the input vector $\vec{F}_q$ consists of three linear forces and three moments applied at point q. The output response vector at point p, $\vec{X}_p$ consists of three linear and three angular motions.

The structure's output response at the p^{th} point consists of two vectors, a vector of linear motions (displacements, velocities, or accelerations) and a vector of angular motions (displacements, velocities, or accelerations), and it is represented in Figure 2.1 by $\vec{X}_p = \vec{X}_p(\omega)$. Each output vector can be resolved in terms of three components according to the global coordinate system shown. The linear motion vector at the p^{th} point has components X_1, X_2, and X_3 along x, y, and z, respectively. The angular motion vector has components X_4, X_5, and X_6 about x, y, and z, respectively. Thus,

the output motion vector at location p has six components like the input at location q has six components as well.

The output vector at the p^{th} point is related to the input vector at the q^{th} point through the following relationship [25]

$$\{X\}_p = [H_{uv}]_{pq} \{F\}_q \tag{2.58}$$

where u and v range from 1 to 6 and the FRF matrix (receptance, mobility, or acceleerance) $[H_{uv}]_{pq}$ has 36 entries. Thus, between each pair of input-output points p and q on the structure, there are potentially 36 input/output FRF relationships [26].

Equation 2.58 can be rewritten in partitioned form as

$$\left\{ \begin{array}{c} \{X\} \\ \{\Theta\} \end{array} \right\}_p = \left[\begin{array}{cc} [H_{FF}] & [H_{FM}] \\ [H_{MF}] & [H_{MM}] \end{array} \right]_{pq} \left\{ \begin{array}{c} \{F\} \\ \{M\} \end{array} \right\}_q \tag{2.59}$$

where $\{X\} = \{X(\omega)\}$ and $\{\Theta\} = \{\Theta(\omega)\}$ are 3x1 vectors that contain the linear and angular motions at the p^{th} location, respectively, and $\{F\} = \{F(\omega)\}$ and $\{M\} = \{M(\omega)\}$ are 3x1 vectors that contain the forces and moments applied at the q^{th} location.
Each sub-matrix in Equation 2.59 contains 9 FRFs. The sub-matrix $[H_{FF}]$ contains the FRFs regarding translational motion due to forces applied to the structure. The sub-matrix $[H_{MM}]$ contains FRFs regarding rotational motion due to moments, and the sub-matrices $[H_{FM}] = [H_{MF}]$ contain FRFs relating linear (angular) motion due to moments (forces).

In order to recognize the importance of Equation 2.59, consider the situation where there is one accelerometer at location p with its primary sensing axis oriented in the 2 direction (see Figure 2.1), and a force transducer mounted at location q with its primary sensing axis in the 1 direction. From Equation 2.59 the output acceleration at the p^{th} location due to the excitation vector at q can be expressed as

$$X_{2p} = H_{21}\ F_{1q} + H_{22}\ F_{2q} + H_{23}\ F_{3q} + H_{24}\ M_{1q} + H_{25}\ M_{2q} + H_{26}\ M_{3q} \tag{2.60}$$

where H_{uv} denotes the FRF relating the points p and q in the pq directions. The output at the p^{th} point in Equation 2.60 is the sum of six terms involving translational and rotational FRFs relative to forces and moments applied at the q^{th} point on the structure. However, in practice the sensors used to measure the input and output signals do not account for all terms shown in Equation 2.60 [25]. Instead, the following simpler equation is used

$$X_{2p} \cong H_{21}\ F_{2q} \tag{2.61}$$

or generally

$$X_p = H_{pq}\ F_q \tag{2.62}$$

and the effects of the remaining terms in Equation 2.60 are not accounted for.

The input loads that act on a given structure can be divided into three different categories [25, 26], as illustrated in Figure 2.2 for two substructures A and B that are connected together to form a combined structure. These input categories are: *Internal*, *external*, and *boundary* (interface or connector) inputs.

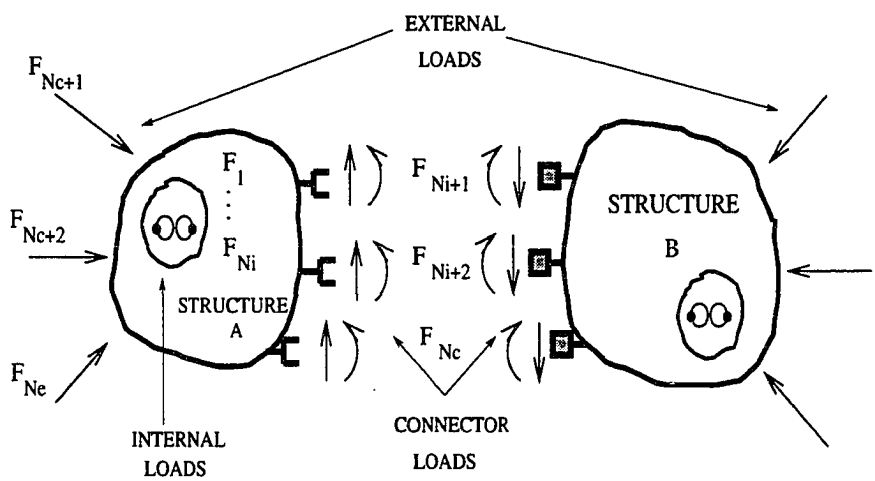

Figure 2.2 Classification of inputs to structure A: internal $(F_1, \ldots, F_{Ni})$, interface $(F_{Ni+1}, \ldots, F_{Nc})$, and external $(F_{Nc+1}, \ldots, F_{Ne})$ inputs. The output motion at the p^{th} location in structure A is due to all these inputs

The output motion exhibited by structure A can be expressed by partitioning Equation 2.58 in terms of the three types of inputs acting on the structure. This operation results in the following expression

$$\begin{Bmatrix} \{X_i\} \\ \{X_c\} \\ \{X_e\} \end{Bmatrix} = \begin{bmatrix} [H_{ii}] & [H_{ic}] & [H_{ie}] \\ [H_{ci}] & [H_{cc}] & [H_{ce}] \\ [H_{ei}] & [H_{ec}] & [H_{ee}] \end{bmatrix} \begin{Bmatrix} \{F_i\} \\ \{F_c\} \\ \{F_e\} \end{Bmatrix} \tag{2.63}$$

where subscripts i, c, and e denote internal, connector, and external forces or motions, respectively.

One element of the response vector shown on the left hand side of Equation 2.63 can be expressed as

$$X_p = \sum_{r=1}^{Ni} H_{pr}\, F_r + \sum_{s=Ni+1}^{Nc} H_{ps}\, F_s + \sum_{t=Nc+1}^{Ne} H_{pt}\, F_t \tag{2.64}$$

where N_i, N_c, and N_e denote the number of internal, connector, and external inputs on the structure, respectively. Equation 2.64 shows that *the output motion exhibited at a given point in a structure is due to all three types of applied inputs.* **Thus, the absence of any one input force or force category can significantly distort the response at any location.**

3 READI: BASIC DEFINITIONS AND TEST SCENARIOS

This chapter describes the theoretical basis for **READI** (the Rules for the Exchange and Analysis of Dynamic Information). The ultimate goal is to define a realistic basis for the exchange of dynamic information to achieve realistic test environments.

Definition of Major Structures and Dynamic Environments

As defined in Chapter1, three major structures are involved in the process of taking field data and converting it into suitable laboratory inputs: the **Test Item**, the **Vehicle**, and the **Vibration Exciter** [25, 26]. Each structure can be defined by its input-output relationship as follows:

- **The Test Item** is the structure under investigation that presents an input-output relationship that is given by

$$\{X\} = [T]\,\{F\} \tag{3.1}$$

  where $\{X\}$ denotes the test item output motion vector (either displacement, velocity, or acceleration), $[T]$ is the test item's FRF response model (receptance, mobility, or accelerance), and $\{F\}$ is the test item's input vector.

- **The Vehicle** is the structure that the test item is attached to while in service. The vehicle is usually a major source of vibration input as it transports the test item. Hence, the name vehicle. The vehicle's input-output relationship is given as

$$\{Y\} = [V]\,\{P\} \tag{3.2}$$

where $\{Y\}$ denotes the vehicle output motion vector, $[V]$ is the vehicle's FRF response model, and $\{P\}$ is the vehicle's input vector.

- **The Vibration Exciter** is the device that is used to generate test item's input while under test. The exciter input-output relationship is given as

$$\{Z\} = [E]\,\{Q\} \tag{3.3}$$

where $\{Z\}$ is the exciter's output motion vector, $[E]$ is the exciter's FRF response model, and $\{Q\}$ is the exciter's input vector.

Similarly, three dynamic environmens were defined in Chapter 1: the **Field**, the **Laboratory**, and the **Finite Element** environments. In the field environment, the test item is attached to the vehicle to create a combined structure where it is subjected to internal, connector, and external field excitations. Field test item motions are due to these three types of excitation sources. Knowledge of the forces that act on a test item while in the field environment is one of the most important issues in vibration testing since these forces are needed in both laboratory and finite element simulations.

In the laboratory environment, the test item is attached to one or more vibration exciters to create the laboratory test structure. The choice of appropriate inputs to the test item such that field measurements are reasonably simulated constitutes an important issue in laboratory testing or finite element simulations where field interface forces (and possibly motions) are natural candidates as test item inputs.

Frequency Domain Modeling

Since field and laboratory dynamic environments deal with combined structures, i.e., structures that result from the combination of two or more substructures, frequency domain substructuring concepts [6] are employed to study the structural interactions

that occur when the test item is connected to the vehicle in the field or to vibration exciters in the laboratory.

Most substructuring techniques [6] usually consider a partition of the structure's DOF in terms of *master* DOF and *slave* DOF. In the present work a similar substructuring concept will be employed where *connector (interface)* DOF are differentiated from *external (non-connector)* DOF by using the following simplified version of Equation 2.63 [14]

$$\begin{Bmatrix} \{X_c\} \\ \{X_e\} \end{Bmatrix} = \begin{bmatrix} [H_{cc}] & [H_{ce}] \\ [H_{ec}] & [H_{ee}] \end{bmatrix} \begin{Bmatrix} \{F_c\} \\ \{F_e\} \end{Bmatrix} \tag{3.4}$$

This equation can be used to describe not only the input-output relationship for a single structure, but it also can be applied to any number of independent structures that are coupled at a finite number of locations. Subscripts c and e in Equation 3.4 refer to connection (or interface) points and external points, respectively. Connection points are points on the structure that are directly connected to another structure so that connection (or interface) points are points where coupling occurs between the test item and either the vehicle or vibration exciter. External points are points on the structure that are not directly involved in the coupling process. Interface motions $\{X_c\}$ occur at connecting points while external motions $\{X_e\}$ occur at the remaining points on the structure. Interface forces $\{F_c\}$ occur at interface points and are due to coupling effects only. The external forces vector $\{F_e\}$ contains all remaining forces applied to the structure that can include acoustic and aerodynamic loads. Any excitation source due to internal forces as well as external loads applied at interface connectors are included under the broad classification of the external forces. Inclusion of these forces in the analysis requires additional matrix and vector partitions in Equation 3.4 as shown in Equation 2.63.

It is important to distinguish between motions caused by interface forces from those

caused by external forces. So, the FRF matrix $[H]$ is partitioned into four sub-matrices, as seen from Equation 3.4. In this case, $[H_{cc}]$ defines input-output FRFs for connection points, $[H_{ee}]$ defines input-output FRFs for external points, and $[H_{ce}] = [H_{ec}]^T$ defines the FRFs between connectors and external points, respectively.

An expansion of Equation 3.4 gives

$$\{X_c\} = [H_{cc}]\{F_c\} + [H_{ce}]\{F_e\} \tag{3.5}$$

$$\{X_e\} = [H_{ec}]\{F_c\} + [H_{ee}]\{F_e\} \tag{3.6}$$

The connector motions vector in Equation 3.5 is composed of two parts, the first due to interface forces and the second due to external forces. Similarly, Equation 3.6 shows that the external motion vector is formed by summing the motion due to external forces and those due to connector forces. Generally speaking, the motion of any point of the structure is composed of the sum of two motions, one part due to the connector forces and the other due to the external forces. Thus, the structure's motion can be written as

$$\{X_c\} = \{X_c\}_c + \{X_c\}_e \tag{3.7}$$

$$\{X_e\} = \{X_e\}_c + \{X_e\}_e \tag{3.8}$$

The vectors on the right hand side of Equations 3.7 and 3.8 now carry a double subscript. The first subscript refers to the location of the point on the structure (connector motions and external motions) while the second subscript refers to the location of excitation application to the structure (connector forces and external forces). Thus, terms $\{X_c\}_c$ and $\{X_e\}_c$ correspond to motions at connections and external points, respectively, that are caused by connector forces. Similarly, terms $\{X_c\}_e$ and $\{X_e\}_e$ correspond to motions at connector and external points, respectively, that are caused by external forces. Hence, $\{X_c\}_e$ and $\{X_e\}_e$ correspond to motions that occur when only external forces are active.

The Field Dynamic Environment

Figure 3.1 illustrates the field dynamic environment where the test item and vehicle are connected at N_c locations. The resulting combined structure is then subjected to field external forces, $\{F_e\}$ and $\{P_e\}$ which in turn, cause forces $\{F_c\}$ and motions $\{X_c\}$ to occur at the interface points. Knowledge of field interface forces and test item motions is vital for a successful laboratory simulation. Determination of these forces and motions requires definition of appropriate boundary conditions for the coupling points between test item and vehicle when these structures are connected in the field.

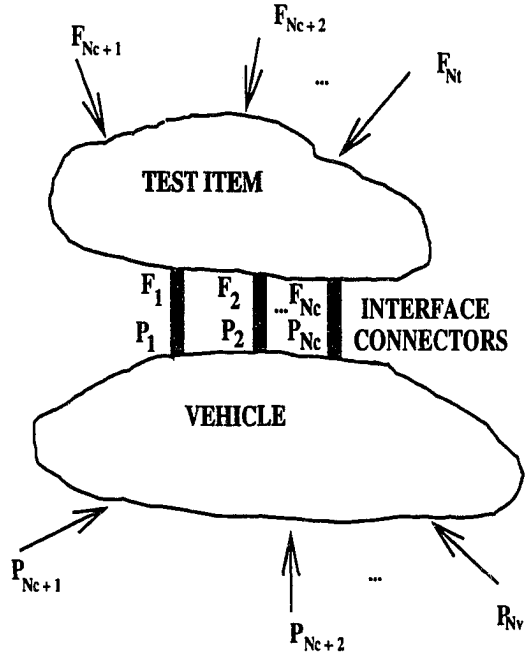

Figure 3.1 Test item attached to the vehicle in the field vibration environment

Two approaches can be used to define boundary conditions at interface points. In the first approach Equation 3.4 can be used to define input-output relationships for the connectors. In this case, connectors are independent coupling structures. In the second approach, a simpler interface boundary condition can be used, where connectors are assumed to be part of either one structure or the other. This last approach is used here to define boundary conditions at the interface points between test item and vehicle. *Connectors are considered to be part of the test item.* Since test item and vehicle are connected through a finite number of discrete points N_c, compatibility of motions at interface connecting points require

$$\{X_c\} - \{Y_c\} = \{0\} \tag{3.9}$$

where the N_c x 1 vector $\{X_c\}$ and $\{Y_c\}$ define test item and vehicle motions at the interface points, respectively. Both $\{X_c\}$ and $\{Y_c\}$ are assumed to be positive in the same direction.

The interface forces must satisfy

$$\{F_c\} + \{P_c\} = \{0\} \tag{3.10}$$

where $\{F_c\}$ and $\{P_c\}$ are N_c x 1 vectors that represent the test item and vehicle interface forces, respectively. All matching forces are positive in the same direction.

When Equation 3.5 is applied to the test item, the test item interface motions can be written as

$$\{X_c\} = [T_{cc}]\ \{F_c\} + [T_{ce}]\ \{F_e\} \tag{3.11}$$

where $\{F_e\}$ is the test item's external force vector, $\{F_c\}$ is the test item interface force, $[T_{cc}]$ is the test item interface FRF matrix, and $[T_{ce}]$ is the test item's FRF matrix relating connection and external points, respectively.

Similarly, the interface motion on the vehicle's side can be expressed as

$$\{Y_c\} = [V_{cc}]\ \{P_c\} + [V_{ce}]\ \{P_e\} \tag{3.12}$$

where $\{P_e\}$ is the external force applied to the vehicle, $[V_{cc}]$ is the vehicle interface FRF matrix, and $[V_{ce}]$ is the vehicle FRF matrix relating interface and external points, respectively.

Substitution of Equations 3.11 and 3.12 into Equation 3.9 and noting the interface force requirement of Equation 3.10 leads to

$$([T_{cc}] + [V_{cc}])\ \{F_c\} = [V_{ce}]\{P_e\} - [T_{ce}]\{F_e\} \tag{3.13}$$

The right hand side of Equation 3.13 corresponds to the relative motion at interface connecting points. The relative interface motion is caused by external forces $\{P_e\}$ and $\{F_e\}$ being applied to the vehicle and test item, respectively. Thus, using Equations 3.7 and 3.8, Equation 3.13 can be rewritten as

$$([T_{cc}] + [V_{cc}])\ \{F_c\} = \{Y_c\}_e - \{X_c\}_e \tag{3.14}$$

Matrix $([T_{cc}] + [V_{cc}])$ in Equation 3.14 is a square N_c x N_c matrix whose entries are the sum of test item and vehicle FRFs at the interface points. The main diagonal entries of this matrix are the sum of test item's and vehicle's driving point FRFs while the off-diagonal entries are the sum of test item's and vehicle's transfer point FRFs between connecting points. Solution of Equation 3.14 for interface forces $\{F_c\}$ requires inversion of this matrix at each frequency value so that Equation 3.14 becomes

$$\{F_c\} = [TV]\ (\{Y_c\}_e - \{X_c\}_e) \tag{3.15}$$

where $[TV] = ([T_{cc} + V_{cc}])^{-1}$ is the *test item-vehicle interface combined matrix.* A particular case of Equation 3.15 happens when there is no external forces acting on the test item in the field environment. In this case, $\{X_c\}_e = 0$, and Equation 3.15 reduces to

$$\{F_c\} = [TV]\ \{Y_c\}_e \tag{3.16}$$

Thus, in the absence of field external forces the interface force vector depends on the vehicle's connecting point motions only ($\{Y_c\}_e$). These are called the *bare vehicle interface motions.*

Once interface forces are determined, they can be used to calculated the test item field motions. Substitution of Equation 3.15 into Equations 3.5 and 3.6, and using Equations 3.7 and 3.8 the following results for test item motions are obtained

$$\{X_c\} = [T_{cc}][TV]\ (\{Y_c\}_e - \{X_c\}_e) + \{X_c\}_e \tag{3.17}$$

$$\{X_e\} = [T_{ec}][TV]\ (\{Y_c\}_e - \{X_c\}_e) + \{X_e\}_e \tag{3.18}$$

Equations 3.17 and 3.18 show that test item field motions depend on the relative interface motion vector and on the motions caused by external forces acting on the test item. The test item motions in Equations 3.17 and 3.18 are also dependent on the test item and vehicle FRFs, since the relative interface motion ($\{Y_c\}_e - \{X_c\}_e$) is pre-multiplied by the product of matrices containing test item FRFs $[T_{cc}]$ and $[T_{ec}]$ as well as the interface combined system matrix $[TV]$.

Equations 3.17 and 3.18 can be rewritten in matrix form as

$$\begin{Bmatrix} \{X_c\} \\ \{X_e\} \end{Bmatrix} = \begin{bmatrix} [T_{cc}][TV] & -[T_{cc}][TV] \\ [T_{ec}][TV] & -[T_{ec}][TV] \end{bmatrix} \begin{Bmatrix} \{Y_c\}_e \\ \{X_c\}_e \end{Bmatrix} + \begin{Bmatrix} \{X_c\}_e \\ \{X_e\}_e \end{Bmatrix} \tag{3.19}$$

or simply

$$\{X\} = [FED]\ \{\hat{X}_c\}_e + \{\hat{X}_e\} \tag{3.20}$$

where matrix $[FED]$, N_t x $2N_c$, is a slightly different form of the Field Environment Dynamic matrix [25].

Equations 3.19 or 3.20 express the test item motion as a function of motions caused by external forces only. The $2N_c$ x 1 vector $\{\hat{X}_c\}_e = \{\{Y_c\}_e\{X_c\}_e\}^T$, contains the

vehicle and test item interface motions due to external forces; the N_t x 1 vector $\{\hat{X}_e\} = \{\{X_c\}_e\{X_e\}_e\}^T$ contains test item's motions due to external forces for all points. The first N_c elements of $\{\hat{X}_e\}$ are connector motions and the remaining $N_t - N_c$ elements are external motions.

Equation 3.19 and 3.20 assume the following form when there are no external forces acting on the test item in the field environment

$$\begin{Bmatrix} \{X_c\} \\ \{X_e\} \end{Bmatrix} = \begin{bmatrix} [T_{cc}][TV] & -[T_{cc}][TV] \\ [T_{ec}][TV] & -[T_{ec}][TV] \end{bmatrix} \begin{Bmatrix} \{Y_c\}_e \\ \{0\} \end{Bmatrix} \tag{3.21}$$

and

$$\{X\} = [FED]\,\{\hat{X}_c\}_e \tag{3.22}$$

where $\{\hat{X}_c\}_e = \{\{Y_c\}_e\{0\}\}^T$. From Equations 3.21 and 3.22 it is obvious that when the test item is not subjected to external forces, the test item's field motions depend exclusively on the bare vehicle connecting motion $\{Y_c\}_e$. Recall that this vector corresponds to the vehicle's motion at the interface points when the test item is absent. Despite being a particular case of the field dynamic environment, this situation constitutes an important case, since it occurs often and offers a good chance for a successful laboratory simulation [26].

The Laboratory Dynamic Environment

In the laboratory environment, the test item is attached to the vibration exciter, as shown in Figure 3.2. In this case, the test item has N_t input-output points and the exciter has N_e input-output points. It is assumed that test item and vibration exciter are connected at E_c points.

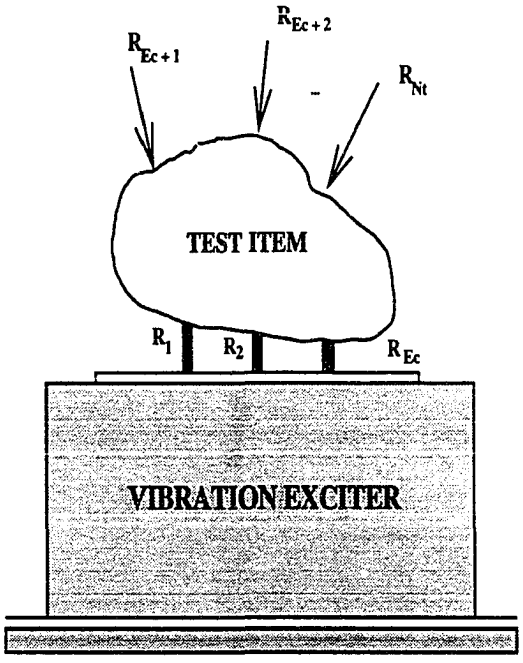

Figure 3.2 Test item attached to the vibration exciter in the laboratory vibration environment

The test item dynamic characteristics are described by Equation 3.1, written as

$$\{U\} = [\hat{T}]\ \{R\} \tag{3.23}$$

where $\{U\}$ is the test item output motion, $\{R\}$ is the test item input force in the laboratory environment, and $[\hat{T}]$ is the test item FRF matrix. Note that the laboratory test item may have different dynamic characteristics from the field test item due to manufacturing variations. Thus, the symbol $[\hat{T}]$ is used to distinguish laboratory test item from field test item ($[T]$).

Similarly, the vibration exciter input-output characteristics are given as

$$\{Z\} = [E]\ \{Q\} \tag{3.24}$$

where $\{Q\}$ and $\{Z\}$ are the exciter input and output vectors, and $[E]$ is the exciter FRF matrix, respectively.

The same frequency domain modeling technique employed in the field dynamic environment will be used in the laboratory simulation. Motions will be grouped in two distinct sets: connector motions, associated with coupling points between test item and vibration exciter, and external motions that do not have direct participation in the coupling process. The same differentiation will be used with forces: interface or connector forces apply for interface forces due to coupling, and external forces apply for external forces applied at external and connector points. As before, the goal is to obtain general expressions for interface forces between test item and vibration exciter as well as for test item's motions in the laboratory dynamic environment. This can be achieved by defining boundary conditions between test item and vibration exciter in terms of interface forces and motions. The same interface boundary condition used in the field environment will be used in laboratory simulations. The connectors are considered as being part of the test item. In this case, compatibility of motions at the E_c connecting interface points requires that

$$\{U_c\} - \{Z_c\} = \{0\} \tag{3.25}$$

where $\{U_c\}$ and $\{Z_c\}$ are E_c x 1 vectors defining test item's and exciter motions at the interface points respectively. They are positive in the same direction.

As in the field environment, interface forces satisfy the relationship

$$\{R_c\} + \{Q_c\} = \{0\} \tag{3.26}$$

where $\{R_c\}$ and $\{Q_c\}$ are E_c x 1 vectors containing the test item and exciter interface forces with the same direction being positive.

Interface motions for test item and vibration exciter in the laboratory are obtained from Equation 3.5

$$\{U_c\} = [\hat{T}_{cc}]\{R_c\} + [\hat{T}_{ce}]\{R_e\} \tag{3.27}$$

$$\{Z_c\} = [E_{cc}]\{Q_c\} + [E_{ce}]\{E_e\} \tag{3.28}$$

Substitution of Equations 3.27 and 3.28 into Equation 3.25 while using the interface force relationship from Equation 3.26 gives the following system of equations for the unknown laboratory interface forces

$$\left([\hat{T}_{cc}] + [E_{cc}]\right) \{R_c\} = \{Z_c\}_e - \{U_c\}_e \tag{3.29}$$

where $\{Z_c\}_e$ and $\{U_c\}_e$ correspond to the vibration exciter and test item interface motions, respectively. These interface motions are due to external forces only, as previously defined in Equation 3.7. The matrix $\left([\hat{T}_{cc}] + [E_{cc}]\right)$ is the sum of test item and vibration exciter FRF matrices at the interface points. Diagonal terms are the sum of driving point FRFs and off-diagonal terms are the sum of transfer point FRFs for interface points. Solution of Equation 3.29 for the laboratory interface forces can be expressed as

$$\{R_c\} = [TE] \ (\{Z_c\}_e - \{U_c\}_e) \tag{3.30}$$

where $[TE] = ([\hat{T}_{cc} + E_{cc}])^{-1}$ corresponds to the *test item-exciter interface combined matrix.*

The laboratory interface force vector $\{R_c\}$ as given by Equation 3.30 depends on the relative interface motion vector $\{Z_c\}_e - \{U_c\}_e$ between vibration exciter and test item. This relative interface motion is due to external forces that act on the vibration exciter ($\{Z_c\}_e$) and test item ($\{U_c\}_e$). In addition, calculation of laboratory interface forces requires the inversion of a square and symmetric E_c x E_c matrix.

When there are no external forces acting on the test item, the expression for the interface force becomes

$$\{R_c\} = [TE] \ \{Z_c\}_e \tag{3.31}$$

since $\{U_c\}_e = 0$. In this case, the interface force vector depends on the vibration exciter connecting points only ($\{Z_c\}_e$).

Application the same procedure adopted for the field environment, the following expression for the laboratory test item motion is obtained

$$\begin{Bmatrix} \{U_c\} \\ \{U_e\} \end{Bmatrix} = \begin{bmatrix} [\hat{T}_{cc}][TE] & -[\hat{T}_{cc}][TE] \\ [\hat{T}_{ec}][TE] & -[\hat{T}_{ec}][TE] \end{bmatrix} \begin{Bmatrix} \{Z_c\}_e \\ \{U_c\}_e \end{Bmatrix} + \begin{Bmatrix} \{U_c\}_e \\ \{U_e\}_e \end{Bmatrix} \tag{3.32}$$

or simply

$$\{U\} = [LED]\ \{\hat{U}_c\}_e + \{\hat{U}_e\} \tag{3.33}$$

where $\{U\}$ is a N_t x 1 vector that contains all test item motions. Vector $\{\hat{U}_c\}_e = \{\{Z_c\}_e\{U_c\}_e\}^T$ is $2E_c$ x 1 and contains the vibration exciter and test item interface motions due to external forces. Vector $\{\hat{U}_e\} = \{\{U_c\}_e\{U_e\}_e\}^T$ is N_t x 1 and contains test item motions due to external forces for all of the test item input-output points. Matrix $[LED]$ is the N_t x $2E_c$ Laboratory Environment Dynamic matrix [25].

When the test item is subjected to no external forces Equations 3.32 and 3.33 reduce to

$$\begin{Bmatrix} \{U_c\} \\ \{U_e\} \end{Bmatrix} = \begin{bmatrix} [\hat{T}_{cc}][TE] & -[\hat{T}_{cc}][TE] \\ [\hat{T}_{ec}][TE] & -[\hat{T}_{ec}][TE] \end{bmatrix} \begin{Bmatrix} \{Z_c\}_e \\ \{0\} \end{Bmatrix} \tag{3.34}$$

and

$$\{U\} = [LED]\ \{\hat{U}_c\}_e \tag{3.35}$$

where $\{\hat{U}_c\}_e = \{\{Z_c\}_e\{0\}\}^T$.

Thus, while in the laboratory environment, the test item undergoes motions that, according to Equations 3.32 and 3.33 depend on the test item and the exciter motions that are caused by external forces only. For the particular case where test item is subjected to no external forces, the test item motion vector is dependent on the Laboratory Environment Matrix $[LED]$ and on the bare vibration exciter interface motion $\{Z_c\}_e$.

Test Scenarios for Laboratory Simulations

This section describes four different test scenarios that can be employed in vibration testing. In each test scenario a different control strategy is used to match field data in the laboratory environment. It is *assumed* that *the number of connectors used to attach the test item to the vehicle in the field and to the vibration exciter in the laboratory is the same*, i.e., $N_c = E_c$. This is a valid assumption when defining different test scenarios but may not be the case in real situations.

In each test scenario one of the following strategies is considered:

- The bare vehicle interface motions $\{Y_c\}_e$ are used to define the test item inputs in the laboratory environment. This corresponds to the situation where the test item laboratory interface motion $\{U_c\}$ is controlled such that $\{Y_c\}_e$ is matched in the laboratory. This laboratory test scenario is frequently employed in real situations [34, 37] when a single vibration exciter is used. In this case, the test item input is generally defined by enveloping the bare vehicle interface motion $\{Y_c\}_e$.

- The exciters are controlled such that laboratory and field interface forces are matched so that

$$\{R_c\} = \{F_c\} \tag{3.36}$$

- The exciters are controlled such that laboratory and field interface motions are matched so that

$$\{U_c\} = \{X_c\} \tag{3.37}$$

- The exciters are controlled such that the motions at external points on the test item are the same in the field and laboratory environments so that

$$\{U_e\} = \{X_e\} \tag{3.38}$$

In practice, these control strategies may require multiple input controlled vibration tests, since multiple connectors are used in both the field and the laboratory environments. This, in principle requires one vibration exciter for each of the test item interface points in the laboratory simulation (as long as external forces are negligible compared with interface forces). Some issues involved in these laboratory test scenarios will be discussed next.

Test Scenario 1 - Test Item Inputs from the Bare Vehicle Interface Motions

In this case, the bare vehicle interface motion $\{Y_c\}_e$ is used to define the test item inputs in the laboratory. Recall that the bare vehicle data corresponds to field measurements obtained when the test item is not attached to the vehicle. In addition *it is assumed that no information involving the vehicle interface FRF characteristics ($[V_{cc}]$) is available.*

The set of input forces that is required to drive the test item at its N_c interface points is obtained from the solution of the following system of equations for the unknown laboratory interface forces

$$[T_{cc}]\{R_c\} = \{Y_c\}_e \tag{3.39}$$

or

$$\{R_c\} = [T_{cc}]^{-1}\ \{Y_c\}_e \tag{3.40}$$

Comparison of Equation 3.40 with Equation 3.15 that gives the true interface forces when the test item and vehicle are connected in the field reveals some important issues. First, matrix $[TV]$ in Equation 3.15 accounts for test item and vehicle interface FRF characteristics while Equation 3.40 accounts only for the test item interface FRFs. Second, field external effects ($\{X_c\}_e$) are accounted for in Equation 3.15 while they are nonexistent in Equation 3.39. Thus, it is clear that the laboratory interface forces obtained by employing Equation 3.40 will not match the field interface forces so that the

bare vehicle interface motions do not represent suitable field data for defining the test item force inputs in the laboratory environment.

However, if the vehicle interface FRF characteristics $[V_{cc}]$ are known, Equation 3.40 can be rewritten as

$$\{R_c\} = [[T_{cc}] + [V_{cc}]]^{-1} \{Y_c\}_e \tag{3.41}$$

Comparison of Equation 3.41 with the actual expression for field interface forces given by Equation 3.16 shows that $\{R_c\} = \{F_c\}$. In this case the bare vehicle interface motions can be employed to obtain the correct test item laboratory input forces, since the correct transformation matrix is used in Equations 3.39 and 3.40. This result is valid only if external forces effects are negligible, i.e., $\{X_e\}_e = 0$, see Equation 3.15.

Thus, if no significant external forces effects exist in the field and if the vehicle interface driving and transfer point FRFs are available, then the bare vehicle interface motion can be used to define suitable test item input forces in the laboratory environment. Notice that Equation 3.39 assumes that the test item has the same FRF characteristics in both the field and laboratory environments ($[\hat{T}] = [T]$).

Test Scenario 2 - Interface Forces

In this case, interface forces are matched in the laboratory environment, according to Equation 3.36. A comparison of the equations for interface forces in both the field and laboratory environments reveals additional insights into the requirements that must be fullfiled so that reasonable simulation results are obtained. Field and laboratory interface forces are given by Equations 3.15 and 3.30, that are conveniently rewritten here

$$\{F_c\} = [TV] \ (\{Y_c\}_e - \{X_c\}_e) \tag{3.42}$$

$$\{R_c\} = [TE] \ (\{Z_c\}_e - \{U_c\}_e) \tag{3.43}$$

First, it is seen that the field and laboratory interface forces depend on the test item-vehicle interface FRF matrix $[TV]$ and on the test item-exciter interface FRF matrix $[TE]$, respectively. These matrices are obtained by inverting the FRF matrix given by the sum of the test item interface FRF matrix and either the vehicle interface FRF matrix in the field or the vibration exciter interface FRF matrix in the laboratory. It is assumed that the test item has the same FRF characteristics in both environments, the problem is then matching the vehicle interface FRF matrix in the laboratory.

When a single vibration exciter is used in the laboratory simulation, the test item is usually attached to the exciter's table through a test fixture. The implications of Equations 3.42 and 3.43 are obvious. The test fixture must match the vehicle interface FRF characteristics so that $[TV] = [TE]$ and the exciter must be driven so $\{Z_c\}_e = \{Y_c\}_e$. The matching of interface FRF characteristics are nearly impossible to satisfy except in the simplest situations.

Second, a comparison is made between the relative motion vector that appears on the right hand side of Equations 3.42 and 3.43. In the field environment, the relative interface motion is given by subtracting the test item interface motion that is due to external forces $\{X_c\}_e$ from the bare vehicle interface motion $\{Y_c\}_e$. Similarly, the laboratory relative motion is obtained by subtracting the test item interface motion due to laboratory external forces $\{U_c\}_e$ from the bare exciter interface motion $\{Z_c\}_e$. The first important observation to be made from this case is that, if existing field external forces are not accounted for in the laboratory, motion $\{U_c\}_e$ is identically zero, and thus, it is clear that this simulation fails, even if $[TE] = [TV]$. Furthermore, $\{Y_c\}_e$ and $\{Z_c\}_e$ represent vehicle and exciter interface motions obtained when the test item is absent from the field and laboratory, respectively, and the chances that these motions will be the same is minimal. Thus, field external forces effects must be properly accounted for in the laboratory such that the difference $(\{Z_c\}_e - \{U_c\}_e)$ be as close as possible to $(\{Y_c\}_e - \{X_c\}_e)$. In the special case where there are no external forces acting on the test item,

the interface motions due to these forces are zero. Then, the required exciter interface motions can be obtained from Equations 3.42 and 3.43

$$\{Z_c\}_e = [TE]^{-1}[TV]\ \{Y_c\}_e \tag{3.44}$$

It is nearly impossible to satisfy Equation 3.44 through the use of a *single vibration exciter* with a *test fixture* unless all interface points have essentially the same motion. *Thus, we see that the use of multiple exciters is the only way to overcome this limitation for a single exciter and test fixture.*

Test Scenario 3 - Field Interface Motions

In this test scenario, the N_c field interface motions are matched in the laboratory environment, according to Equation 3.37. This condition can be examined by comparison of the test item field and laboratory interface motions that can be obtained from the first row of Equations 3.19 and 3.32, respectively so that

$$\{X_c\} = [T_{cc}][TV]\,(\{Y_c\}_e - \{X_c\}_e) + \{X_c\}_e \tag{3.45}$$

$$\{U_c\} = [T_{cc}][TE]\,(\{Z_c\}_e - \{U_c\}_e) + \{U_c\}_e \tag{3.46}$$

where it is assumed that $[\hat{T}_{cc}] = [T_{cc}]$.

Similarly to the previous test scenario, Equation 3.45 contains the test item-vehicle interface combined matrix $[TV]$ while Equation 3.46 contains the test item-exciter interface combined matrix, and they are different when a single exciter and test fixture are used. The effects of external forces on interface points must be properly accounted for in this case as well. *Hence, it appears that multiple exciters are required to satisfy all requirements as well.*

Test Scenario 4 - Field External Motions

In this case, the test item field external motions are matched in the laboratory as stated by Equation 3.38. Field and laboratory external motions are obtained from the

second row of Equations 3.19 and 3.32, respectively, so that

$$\{X_e\} = [T_{ec}][TV]\left(\{Y_c\}_e - \{X_c\}_e\right) + \{X_e\}_e \tag{3.47}$$

$$\{U_e\} = [T_{ec}][TE]\left(\{Z_c\}_e - \{U_c\}_e\right) + \{U_e\}_e \tag{3.48}$$

where it is assumed that the test item has the same FRFs in both environments, as was the case in the previous test scenarios. In this case, proper simulation of the external forces effects on external motions is required as well as exciter interface motions $\{Z_c\}_e$. It should be clear that this scenario has the same single test fixture problem as the other scenarios.

Test scenarios 2, 3, and 4 contain terms that involve $[TE]$ and $\{Z_c\}_e$. It is clear that it is not economical to create a single test fixture mounted on a single vibration exciter and achieve the behavior demanded by these terms, i.e, that

$$[TV]\left(\{Y_c\}_e - \{X_c\}_e\right) = [TE]\left(\{Z_c\}_e - \{U_c\}_e\right) \tag{3.49}$$

In addition, it is seen that external forces must be applied in the laboratory to simulate those experienced in the field. The only way to side step this single exciter-test fixture dilemma is to use multiple exciters at the interface points.

Chapter Summary

In this chapter, a general vibration testing model is developed that describes the variables and processes that are involved in laboratory simulations of field dynamic environments. Three structures are involved in this process: the test item, the vehicle, and the vibration exciter. The structural interactions that occur when the test item is attached to the vehicle in the field or to the vibration exciters in the laboratory are modeled by frequency domain linear input-output relationships. Substructuring concepts are used to distinguish interface properties (forces and motions) from external

properties. Suitable interface boundary conditions lead to general expressions in terms of field and laboratory interface forces and motions and for the test item external motions.

Figure 3.3 shows that there are two field environments that can be considered. Figure 3.3a corresponds to the bare vehicle case where the test item is absent. In this case the vehicle is subjected to a set of loads P_r, $r = 1, ..., (N_v - N_c)$ applied to the vehicle external DOF. The interface forces are zero in this case since the test item is absent. The field data obtained in this simulation corresponds to the N_c bare vehicle motions $\{Y_c\}_e$ that are measured at interface points Cn_p, $p = 1, ..., N_c$.

The second field environment considered here is shown in Figure 3.3b. In this case, the test item is attached to the vehicle through the N_c interface points, forming the combined structure. The test item is subjected to the interface forces F_p, $p = 1, ..., N_c$ and to the external forces F_q, $q = N_c + 1, ..., N_t$. Similarly, the vehicle is subjected to interface and external forces. The resulting data from this field environment correspond to the interface forces $\{F_c\}$, the test item interface motions $\{X_c\}$ and the test item external motions $\{X_e\}$.

Multiple exciters are required in the laboratory simulations of the field environments shown in Figure 3.3. Figure 3.4 shows the laboratory simulation corresponding to the bare vehicle field environment of Figure 3.3a. Each test item interface point is attached to a vibration exciter, and each exciter must be controlled such that the correct motion is reproduced at the control interface point. A procedure commonly employed in single exciter tests is to attach the test item to a *rigid* test fixture at N_c interface points. The exciter input is generated by enveloping the bare vehicle field data [34, 37]. Inappropriate enveloping may lead to extremely conservative tests, where the test item is over-tested at many frequencies. Thus, care should be taken when using enveloping techniques to define test item inputs in the laboratory.

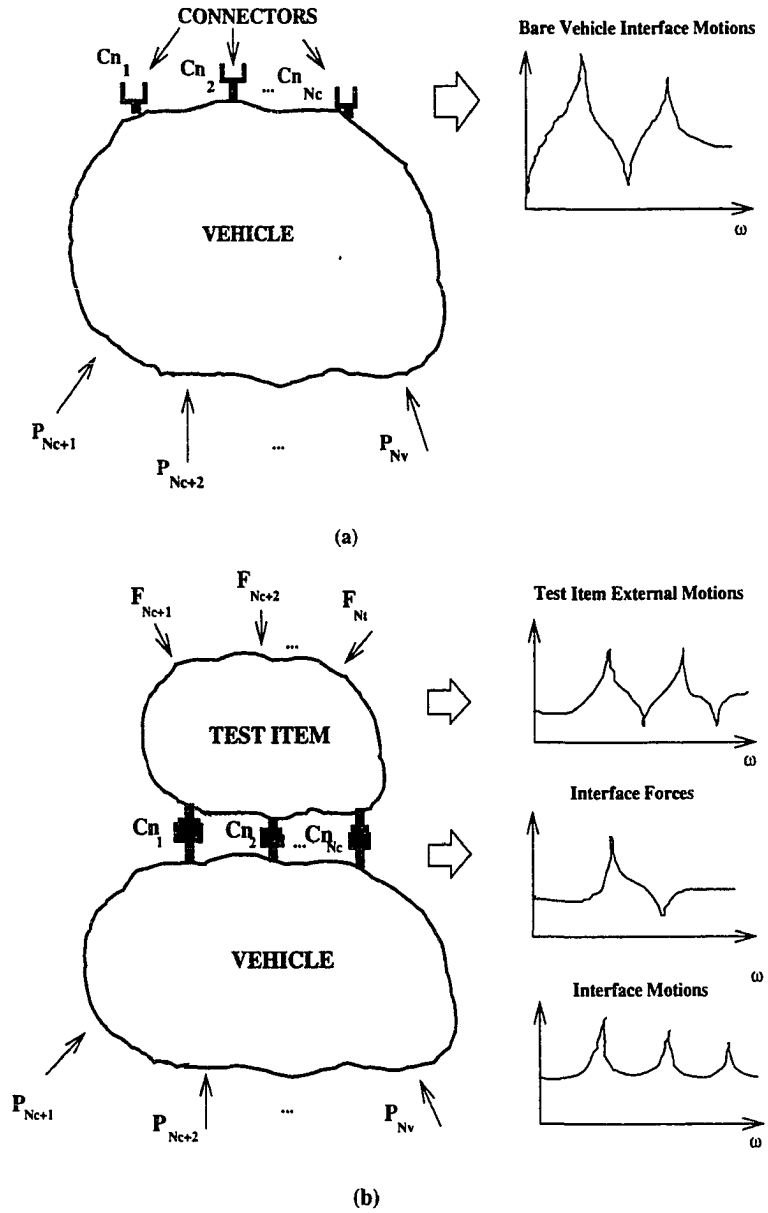

Figure 3.3 Field environments: (a) Test item is absent and field data corresponds to the bare vehicle interface motions $\{Y_c\}_e$; (b) Test item attached to the vehicle forming the combined structure and field data correspond to the interface force $\{F_c\}$, interface motion $\{X_c\}$, and test item external motion $\{X_e\}$

The required laboratory test arrangement that corresponds to the combined test item-vehicle structural system is shown in Figure 3.5. In this case, separate exciters are attached to each interface connector point as well as external loading points. It is clear that either interface motions or forces are required in order to control the connector points. Generally, the external loads are not measured in the field since they often come from sources such as acoustic or aerodynamic loadings which are difficult to measure directly. Indirect force estimation techniques [18, 15] from measured test item responses are required. This leads into an inverse problem [2] which is addressed in the following chapters for deterministic and random forces.

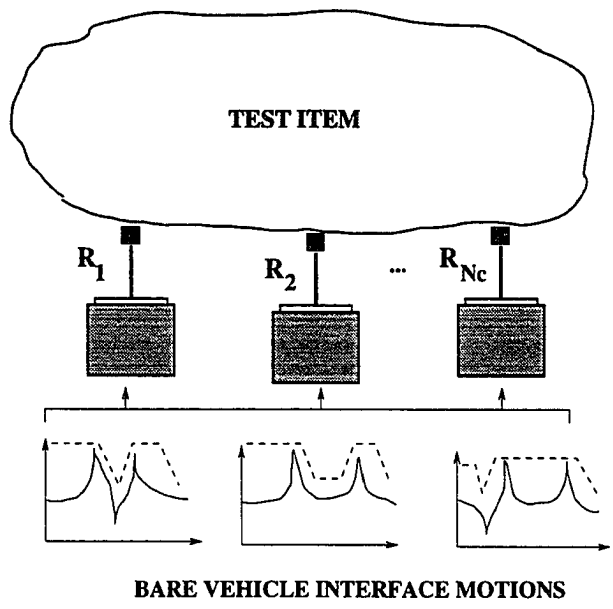

Figure 3.4 Laboratory test scenario where the test item inputs are obtained from the bare vehicle motion data $\{Y_c\}_e$

All laboratory simulations discussed in this chapter require multiple exciters operating in closed loop in order to match the corresponding field data in the laboratory. This represents a real challenge in the vibration testing context since not only the exciters must be able to generate and control a given frequency spectrum, but also cross

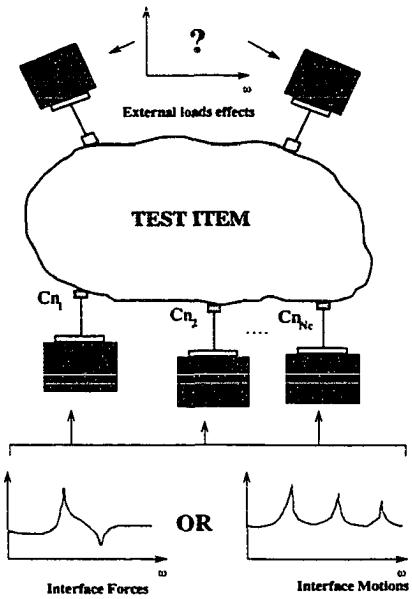

Figure 3.5 Laboratory test scenario where the test item inputs are defined from interface forces $\{F_c\}$ or external forces $\{F_e\}$ or interface motions $\{X_c\}$

correlation between excitation sources must be maintained [39, 40].

The results presented in this chapter were obtained by using an approach base on frequency spectra. This means that the several variables used to express interface and external properties are complex variables that carry both magnitude and phase information. This approach is suitable for deterministic (periodic and transient) input and output signals and are considered further in Chapter 4, but the deterministic approach is inadequate in the case of dealing with random signals. The expressions for interface forces and motions as well as for the test item external motions are derived in terms of random signals in Chapter 5 and in this case, spectral density matrices containing auto and cross spectral densities will be used with these signals.

4 NUMERICAL SIMULATION CONSIDERATIONS FOR DETERMINISTIC EXCITATIONS

This chapter presents numerical results of the vibration testing model described in Chapter 3. Two field scenarios are analyzed. In the first, the test item is absent from the field. This simulation results in the bare vehicle interface motions. In the second, the test item is attached to the vehicle in the field, being subjected to both interface and external forces. The laboratory test scenarios described in Chapter 3 are discussed for both field situations. The results of all numerical simulations presented in this dissertation were obtained by using MATLAB© software [24].

Theoretical Response Models of Test Structures

The lumped parameter models shown in Figure 4.1 are used in the numerical simulations. The test item and vehicle are each modeled by four DOF ($N_t = 4$ and $N_v = 4$) viscously damped systems. When the test item and the vehicle are connected in the field at points 1 and 3, they form the combined structure shown in Figure 4.1. The test item is attached to the vehicle through $N_c = 2$ connectors that are labeled Cn_1 and Cn_3, respectively. Coordinate acceleration variables are assigned such that interface points carry the same coordinate number in both the test item and vehicle models. Thus, according to Figure 4.1, Y_1 and Y_3 denote interface accelerations on the vehicle side and X_1 and X_3 denote interface accelerations on the test item side. The remaining coordinate variables (Y_2, Y_4, X_2, X_4) represent external accelerations. Mass and spring

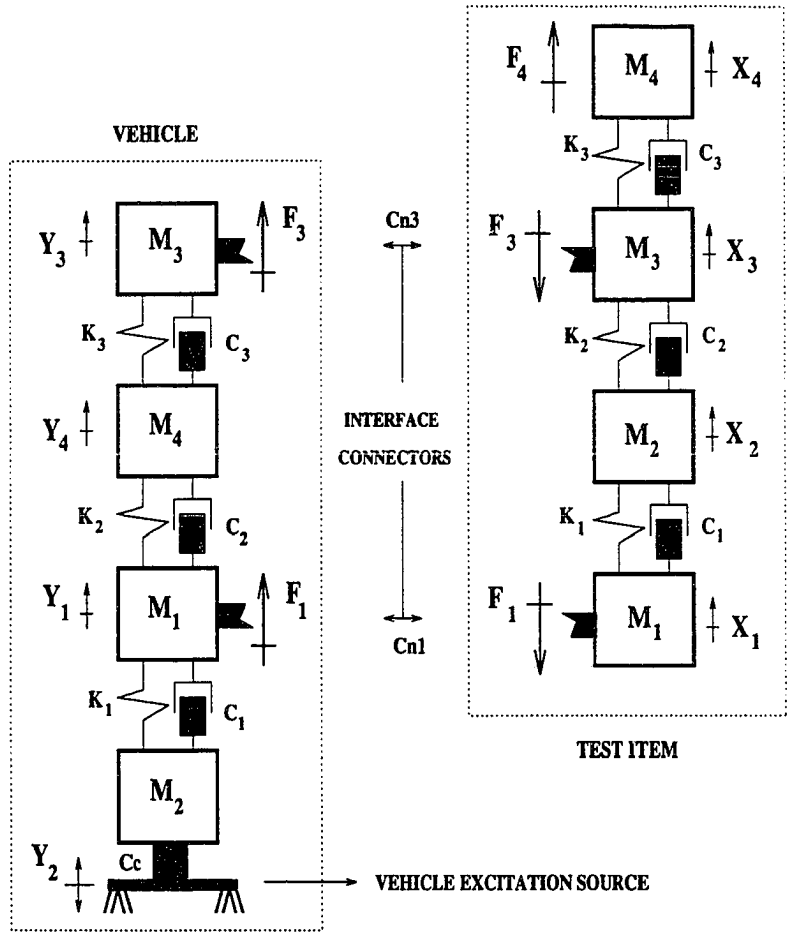

Figure 4.1 Test item attached to vehicle by connectors Cn_1 and Cn_3 in the field environment. External inputs to the combined structure given in terms of the vehicle base input acceleration Y_2 and the external force F_4 applied to the test item mass M_4

coefficients for the test item and vehicle models are given in Table 4.1.

Compatibility of interface accelerations is defined for the combined structure according to Equation 3.9 written as

$$\{X_c\} = \{Y_c\} \tag{4.1}$$

where $\{X_c\}$ and $\{Y_c\}$ are the N_c x 1 test item and vehicle interface acceleration vectors, respectively. From Equation 4.1, it is found that $X_1 = Y_1$ and $X_3 = Y_3$ so that the resulting combined structure of Figure 4.1 has $N_r = 6$ DOF.

Table 4.1 Physical parameters of test structures

Mass	Test Item (Kg)	Vehicle (Kg)
M_1	0.20	0.50
M_2	0.20	0.50
M_3	0.25	0.30
M_4	0.15	0.50
Stiffness	Test Item N/m x 10^4	Vehicle N/m x 10^4
K_1	5.00	6.00
K_2	4.00	14.00
K_3	2.00	10.00

The undamped natural frequencies and mode shapes are obtained for the test item, the vehicle, and the combined structure from the solution of the undamped eigenvalue problem of Equations 2.4 and 2.5. The test item is modeled as a free structure in space while the vehicle and combined structure are grounded through the vehicle's base mass M_2, as shown in Figure 4.1. The remaining modal parameters (modal damping ratios and modal masses) are obtained from the orthogonality conditions of Equations 2.13, 2.14, and 2.30. The modal damping ratios were obtained by assuming a proportional Rayleigh damping distribution for all test structures, as defined in Equation 2.25. In the present simulations the values $a_0 = 0$ and $a_1 = 10^{-5}$ were chosen to determine the test item's, the vehicle's, and combined structure's damping matrices. The modal parameters that are required in the FRF calculations are given in Table 4.2.

Accelerance FRF response models for the test item, the vehicle, and the combined structure were obtained by combining Equations 2.42 and 2.39 from Chapter 2. The resulting expression for the accelerance FRF $A_{pq} = A_{pq}(\omega)$ is

$$A_{pq} = -\omega^2 \sum_{r=1}^{N} \frac{\phi_{pr}\, \phi_{qr}}{m_r(\omega_r^2 - \omega^2 + j\, 2\zeta_r\omega_r\omega)} \tag{4.2}$$

Table 4.2 Modal parameters of test structures

Natural Frequency	Test Item (Hz)	Vehicle (Hz)	Combined (Hz)
f_1	0.00	30.00	23.86
f_2	52.60	86.17	58.94
f_3	85.70	164.72	85.05
f_4	131.00	-	112.00
f_5	-	-	160.21
Damping Ratio	Test Item (%)	Vehicle (%)	Combined (%)
ζ_1	0.00	0.28	0.24
ζ_2	0.50	0.81	0.56
ζ_3	0.81	1.55	0.91
ζ_4	1.23	-	1.06
ζ_5	-	-	1.54
Modal Masses	Test Item (Kg)	Vehicle (Kg)	Combined (Kg)
m_1	0.20	0.43	0.38
m_2	0.17	0.48	0.17
m_3	0.21	0.37	0.55
m_4	0.20	-	0.21
m_5	-	-	0.34

Figure 4.2 shows the test item driving point accelerance FRF at interface points 1 and 3. These FRFs are typical for a free structure with a zero natural frequency corresponding to the rigid body mode, and three non-zero natural frequencies in the $0-200\ Hz$ range as given in Table 4.2. Figure 4.3 shows the vehicle driving point accelerance FRFs at its interface points 1 and 3. There are three resonance peaks in the $0-200\ Hz$ bandwidth, corresponding to the values in Table 4.2.

The driving point accelerance FRFs for the combined structure at the interface points, VT_{11} and VT_{33}, are shown in Figure 4.4 where the FRFs show five resonant peaks in the $0-200\ Hz$ frequency range. Thus, test item and vehicle form a new structure when they are connected in the field, and this structure has unique dynamic characteristics that are different from these of the two parent structures. Figure 4.5 shows the test item and vehicle interface transfer accelerances FRFs T_{13} and V_{13}.

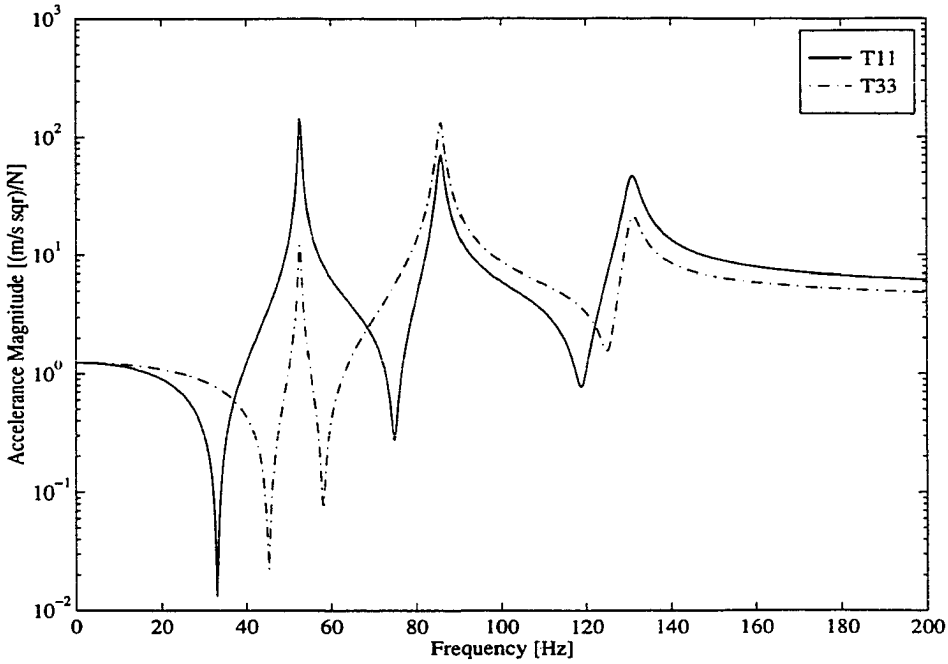

Figure 4.2 Test item interface driving point accelerances. Test item is a free structure in space

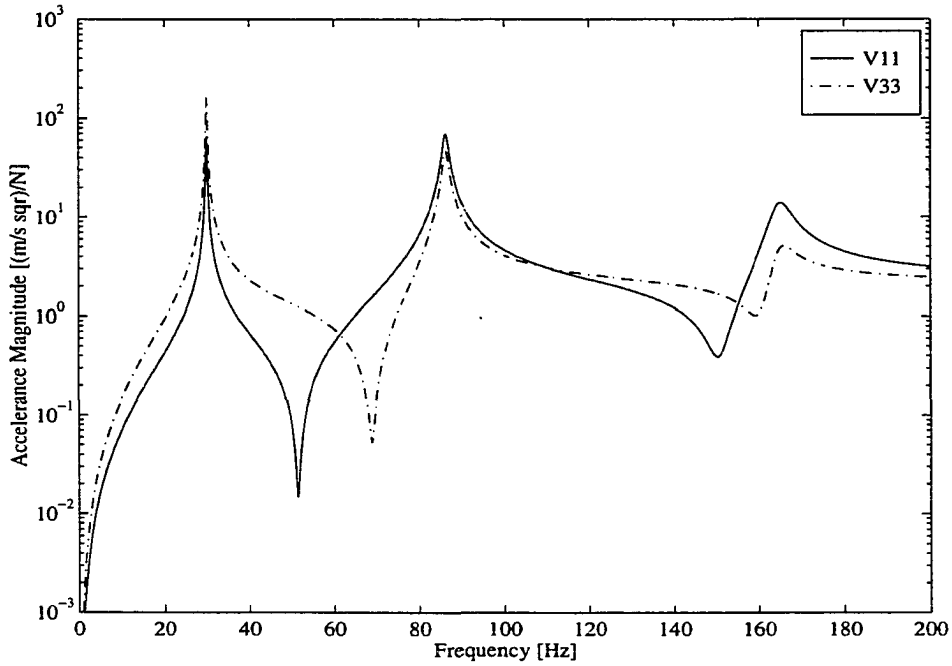

Figure 4.3 Vehicle interface driving point accelerances. The vehicle is grounded through mass M_2

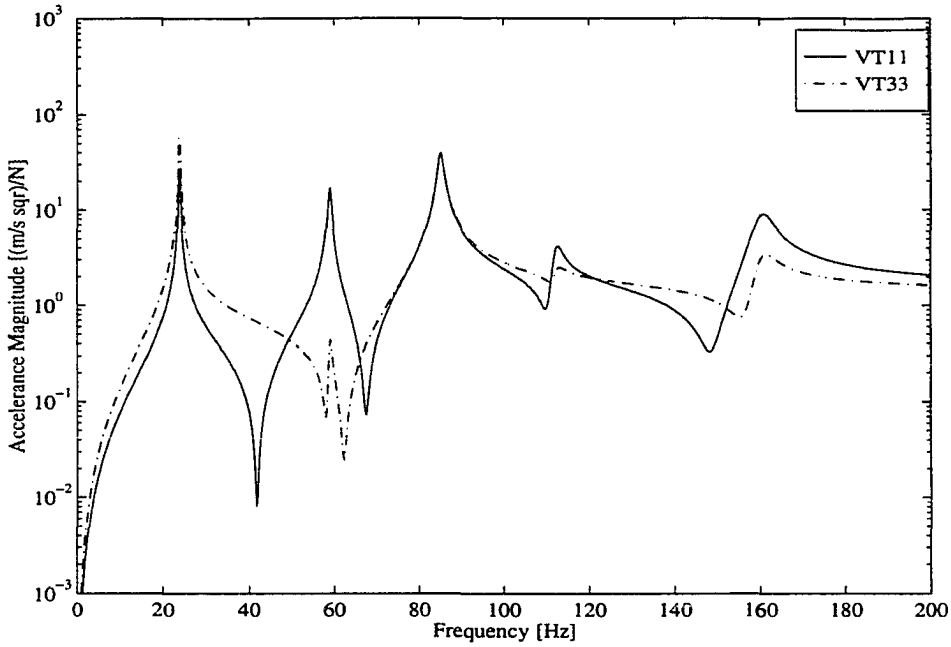

Figure 4.4 Combined structure interface driving point accelerances. The combined structure is grounded through vehicle's base mass M_2

Similarly, when the input to the structure is motion at a single coordinate, the response model is calculated in terms of the absolute transmissibility FRF vector, $\{\Gamma\} = \{\Gamma(\omega)\}$, that was defined by Equation 2.54 in Chapter 2 and that for convenience is repeated here

$$\{\Gamma\} = \omega^2 \sum_{r=1}^{N} \frac{\{\phi\}_r \{\phi\}_r^T [M]\{\delta\}}{m_r(\omega_r^2 - \omega^2 + j\, 2\zeta_r\omega_r\omega)} + \{\delta\} \tag{4.3}$$

Figure 4.6 shows the vehicle absolute acceleration transmissibility FRFs at the interface points 1 and 3, respectively. These FRFs result from the application of an input base acceleration at the vehicle's base mass M_2 in the vertical direction when the test item is absent. In this case $\{\delta\} = \{1\}$ in Equation 4.3 since all the vehicle's DOF are defined in the same direction of the base input acceleration. These transmissibility FRFs were obtained by using the modal parameters shown in Table 4.2.

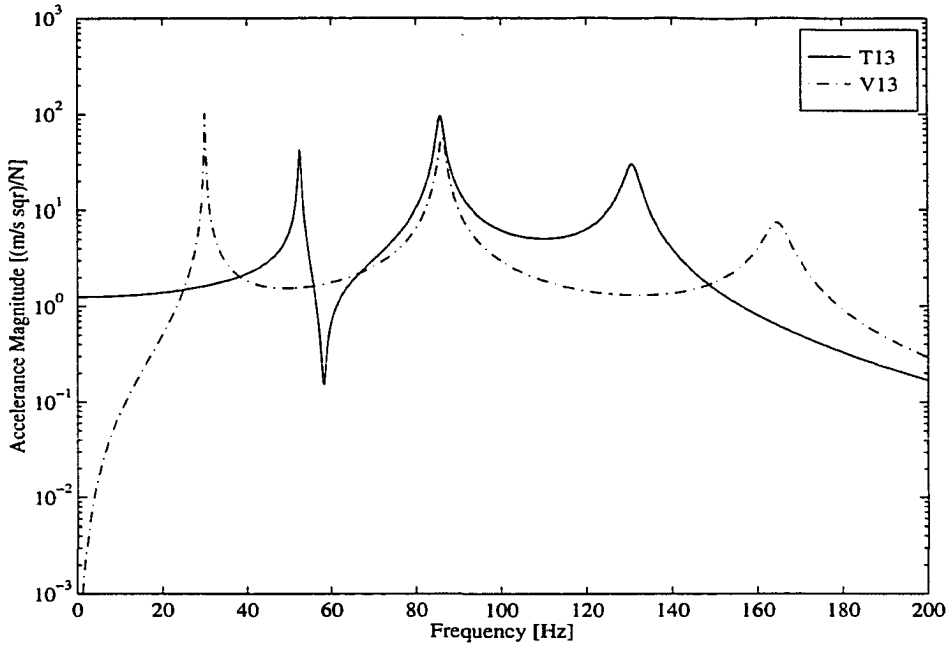

Figure 4.5 Test item and vehicle interface transfer point accelerances

Field Simulations

Two field simulations are considered in this section. *First*, the bare vehicle interface accelerations $\{Y_c\}_e$ are obtained. The bare vehicle interface accelerations represent the only field data that is available for this case. *Second*, the test item is attached to the vehicle forming the combined structure. Interface forces and accelerations as well as test item external accelerations constitute the field data in this case and they are due to the inputs applied to the combined structure.

Definition of the Vehicle and Test Item Field Excitations

Two inputs are applied to the combined structure shown in Figure 4.1. The first input corresponds to an acceleration frequency spectrum that is applied to the vehicle base mass M_2. The magnitude of the base input acceleration frequency spectrum Y_2 is shown in Figure 4.7. It increases linearly with a slope of $1.28.10^{-3}$ $(m/s^2)/Hz$ in the $0-10$ Hz

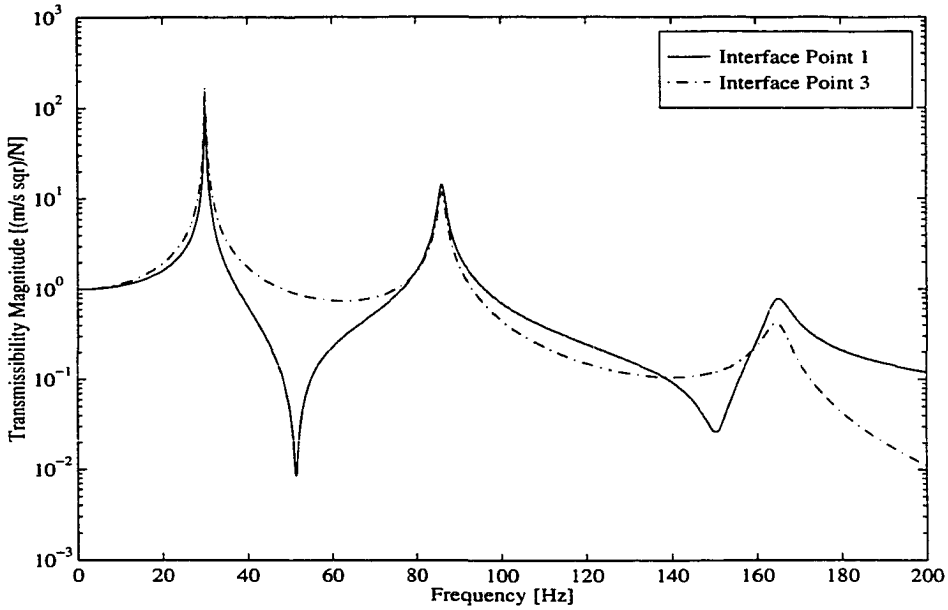

Figure 4.6 Vehicle interface absolute acceleration transmissibility FRFs Γ_{12} and Γ_{32} due to unit input acceleration at vehicle's mass M_2

frequency range and then becomes constant with a magnitude of $1.28.10^{-2}$ m/s^2 in the remaining $10 - 200$ Hz frequency range so that the total input vibration level is approximately 1.0 g_{RMS} (9.81 $(m/s^2)_{RMS}$). A total of 800 spectral lines are used in all simulations so that the frequency resolution is $\Delta f = 0.25$ Hz.

The second field input corresponds to the external force F_4 that is applied to the test item's top mass M_4 as seen in Figure 4.1. The magnitude and phase of this force frequency spectrum are shown in Figure 4.8 for the $0 - 200$ Hz frequency range where it is seen to vary significantly with frequency.

Field Simulation 1: The Bare Vehicle Interface Accelerations

The bare interface acceleration ($\{Y_c\}_e$) is the vehicle's output response due to its field inputs when the test item is absent. For the vehicle shown in Figure 4.1, the bare vehicle interface motions correspond to the acceleration frequency spectra Y_1 and Y_3 that are due to the vehicle's input acceleration Y_2 shown in Figure 4.7.

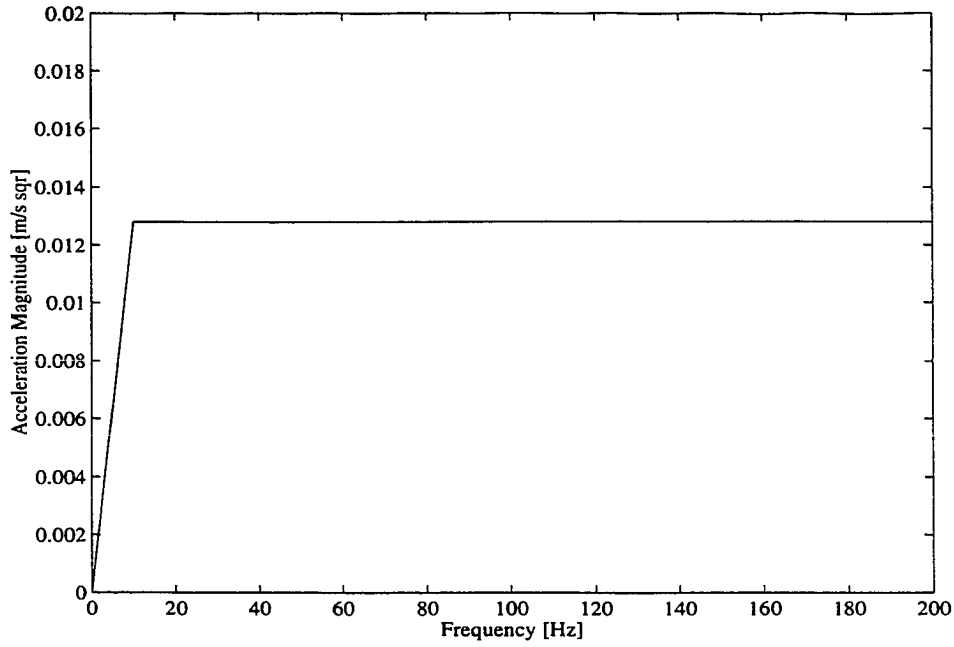

Figure 4.7 Vehicle and combined structure input base acceleration frequency spectrum Y_2 that is applied to the vehicle base mass M_2 and gives an input vibration level of 1.0 g_{RMS}

Since this acceleration frequency spectrum represents the *only* input that applied at a *single* coordinate, the accelerations Y_1 and Y_3 can be obtained from the vehicle's absolute transmissibility FRFs shown in Figure 4.6 and the input acceleration frequency spectrum of Figure 4.7 by using the definition of the transmissibility FRF of Equation 2.55 rewritten as

$$\{Y_c\}_e = \{\Gamma_{cr}\}\ Y_r \tag{4.4}$$

where $Y_r = Y_2$ and $\{Y_c\}_e = \{Y_1\ Y_3\}^T$. The bare vehicle interface accelerations Y_1 and Y_3 that are obtained from Equation 4.4 are shown in Figure 4.9. Recall that since these motions were obtained when the test item is absent from the field environment they are not affected by the external force F_4. Thus, the bare vehicle interface accelerations shown in Figure 4.9 will be used in both field simulations presented in this chapter. In addition, they will be used to illustrate the first laboratory test scenario described in

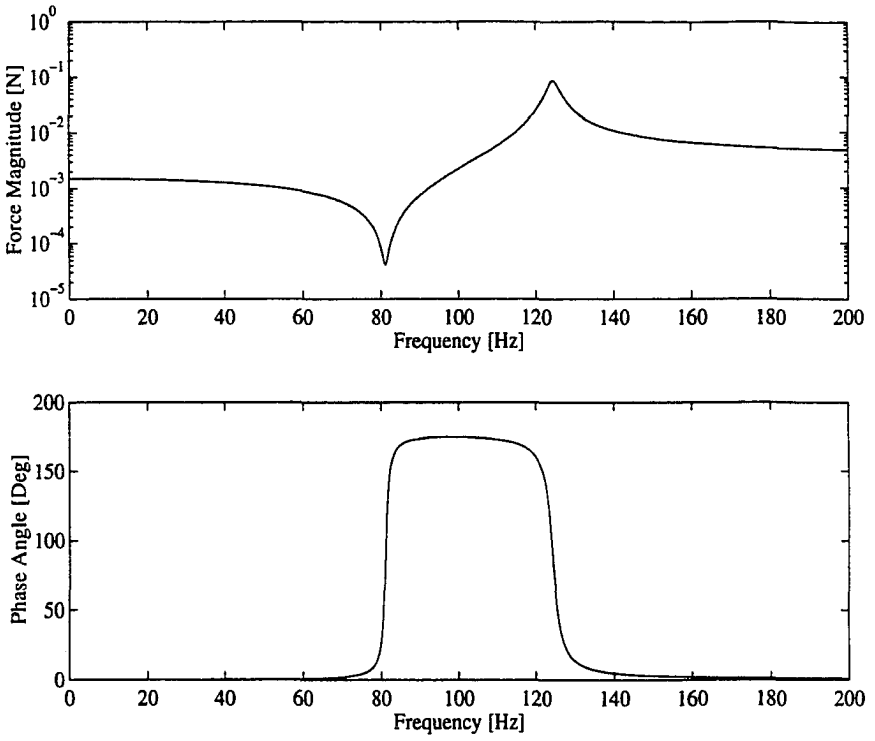

Figure 4.8 Magnitude and phase angle of the field force frequency spectrum F_4 that is applied to the test item mass M_4

the previous chapter.

Field Simulation 2: The Combined Structure Interface Forces and Interface and External Accelerations

The test item and the vehicle are connected in the field as shown in Figure 4.1. The combined structure has two inputs, the vehicle excitation acceleration spectrum Y_2 of Figure 4.7 that is applied to the vehicle base mass M_2, and the external force F_4 shown in Figure 4.8 that is applied to the test item mass M_4.

As defined in the previous chapter, field interface forces are obtained through the following expression

$$\{F_c\} = [TV]\ (\{Y_c\}_e - \{X_c\}_e) \tag{4.5}$$

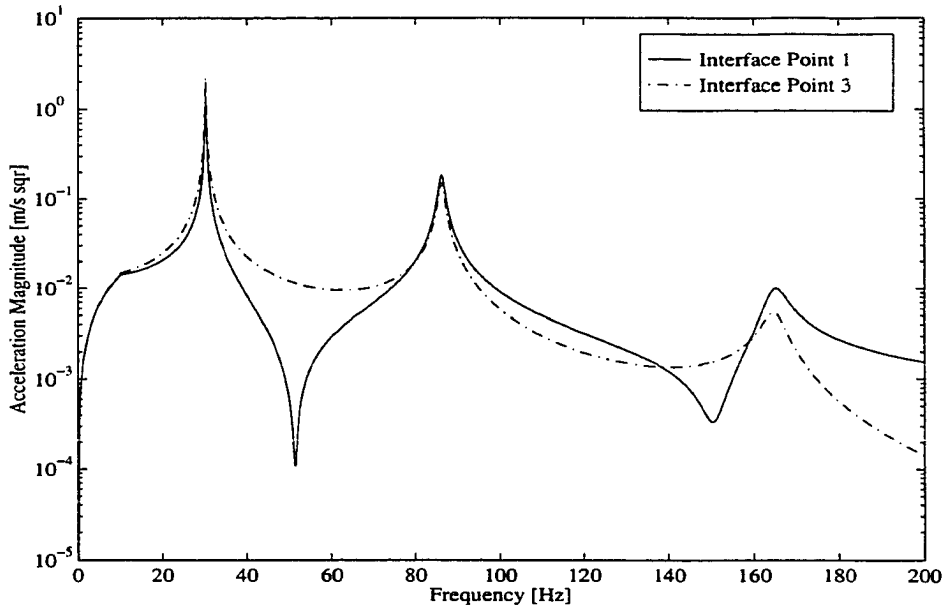

Figure 4.9 Magnitudes of the bare vehicle interface acceleration frequency spectra Y_1 and Y_3

where $\{F_c\}$ contains the N_c interface forces. Matrix $[TV] = [[T_{cc}] + [V_{cc}]]^{-1}$, N_c x N_c, is the test item-vehicle interface combined matrix and is given by the inverse of the matrix containing the sum of test item and vehicle interface accelerance FRFs T_{pq} and V_{pq} for $p, q = 1...N_c$, respectively. Vectors $\{Y_c\}_e$ and $\{X_c\}_e$, N_c x 1 represent the vehicle and the test item connector accelerations that are due to external forces, respectively. Vector $\{Y_c\}_e$ is the *bare* vehicle interface accelerations.

Similarly, the test item field accelerations are obtained through the following equation

$$\begin{Bmatrix} \{X_c\} \\ \{X_e\} \end{Bmatrix} = \begin{bmatrix} [T_{cc}][TV] & -[T_{cc}][TV] \\ [T_{ec}][TV] & -[T_{ec}][TV] \end{bmatrix} \begin{Bmatrix} \{Y_c\}_e \\ \{X_c\}_e \end{Bmatrix} + \begin{Bmatrix} \{X_c\}_e \\ \{X_e\}_e \end{Bmatrix} \tag{4.6}$$

Notice that the vector $\{X_c\}_e$ appears in both Equations 4.5 and 4.6 while the vector $\{X_e\}_e$ appears only in Equation 4.6. These vectors contain the test item interface and external accelerations that are caused by external forces applied to the test item. Thus,

prior to estimating field interface forces and motions through Equations 4.5 and 4.6, the acceleration vectors $\{X_c\}_e$ and $\{X_e\}_e$ must be determined. They are obtained through the following expression

$$\begin{Bmatrix} \{X_c\}_e \\ \{X_e\}_e \end{Bmatrix} = \begin{bmatrix} [T_{cc}] & [T_{ce}] \\ [T_{ec}] & [T_{ee}] \end{bmatrix} \begin{Bmatrix} \{0\} \\ \{F_e\} \end{Bmatrix} \tag{4.7}$$

where $\{F_e\} = \{F_4\}$. The test item accelerance FRFs used in Equation 4.7 are those obtained by considering the test item a free structure in space. The resulting interface and external accelerations are shown in Figure 4.10.

Once vectors $\{X_c\}_e$ and $\{X_e\}_e$ are determined, Equation 4.5 is used to estimate the interface forces F_1 and F_3 (see Figure 4.1) which are compared to the "exact"interface forces in Figure 4.11. These "exact" interface forces are calculated by writing the equations of motions for the interface masses on either the test item or vehicle side and then solving these equations for the desired forces. A very good fit occurs between the interface forces predicted from Equation 4.5 and those obtained through the "exact" method. Minor discrepancies are observed at frequencies around 54 Hz and 112 Hz in the result for F_1 and 6 Hz in the result for F_3.

Similarly, all four test item accelerations X_1, X_2, X_3, and X_4 are calculated from Equation 4.6. The resulting interface accelerations X_1 and X_3 are shown in Figure 4.12 while the results for the external accelerations X_2 and X_4 are shown in Figure 4.13 where "exact" test item accelerations are plotted for comparison purposes. These "exact" accelerations are obtained by solving the frequency domain equations of motion for the combined structure of Figure 4.1 when the input acceleration Y_2 and the input force F_4 are simultaneously applied. The results of Equations 4.6 and those from the "exact" procedure present a very good agreement in Figures 4.12 and 4.13.

Thus, the results presented in this section for both the bare vehicle and the com-

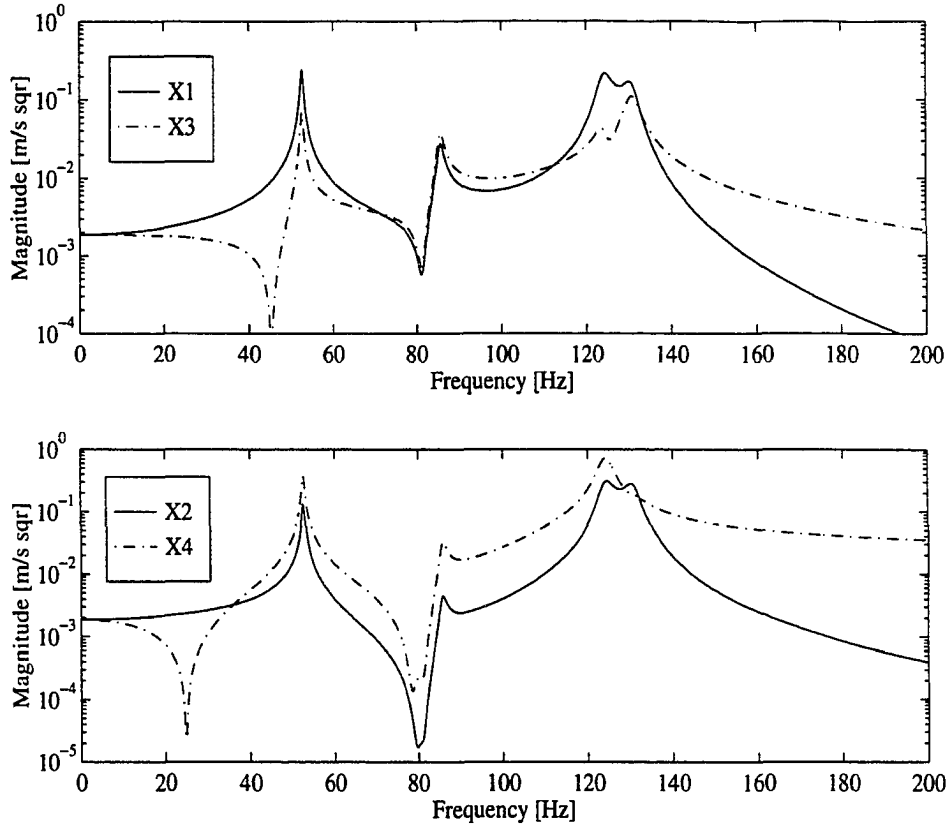

Figure 4.10 Test item interface (X_1 and X_3) and external (X_2 and X_4) accelerations due to field external force F_4 applied to M_4. The test item is a free structure in space

bined structure field simulations showed that the expressions developed in Chapter 3 for describing these two field environments were succesfully applied in generating the field data that is used in the next sections to illustrate the four test scenarios described in Chapter 3.

Laboratory Simulations Using Test Item Inputs Obtained from the Bare Vehicle Interface Accelerations

This laboratory simulation corresponds to the first test scenario discussed in Chapter 3 and uses the bare vehicle interface accelerations shown in Figure 4.9 to obtain two input

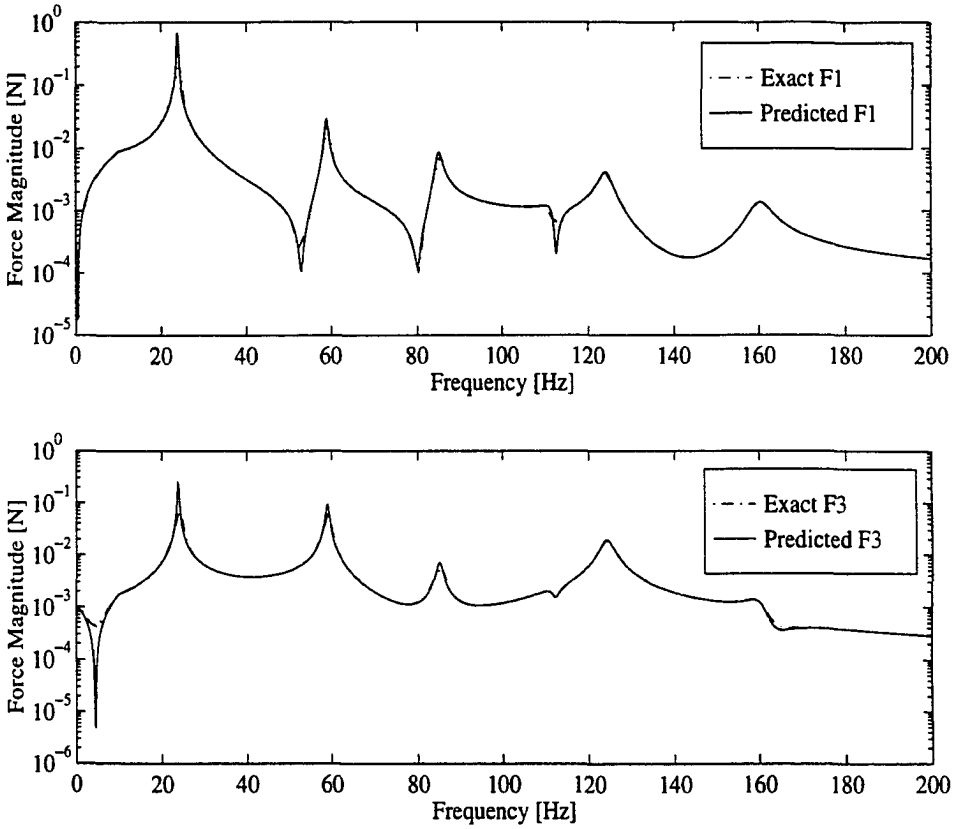

Figure 4.11 Field interface forces F_1 and F_3 due to the input acceleration frequency spectrum Y_2 and the external force frequency spectrum F_4

forces R_1 and R_3 that will be used to drive the test item's interface points 1 and 3 in the laboratory environment. It is assumed that two independently controlled vibration exciters are used to generate these input forces. This laboratory simulation is performed in order to illustrate the situation where all that is known is the bare vehicle interface accelerations Y_1 and Y_3. Thus, this laboratory simulation assumes that *the test item field external force F_4 is unknown* since the bare vehicle interface motions represent the field data in this case.

The vector containing the laboratory interface forces R_1 and R_3 is obtained from

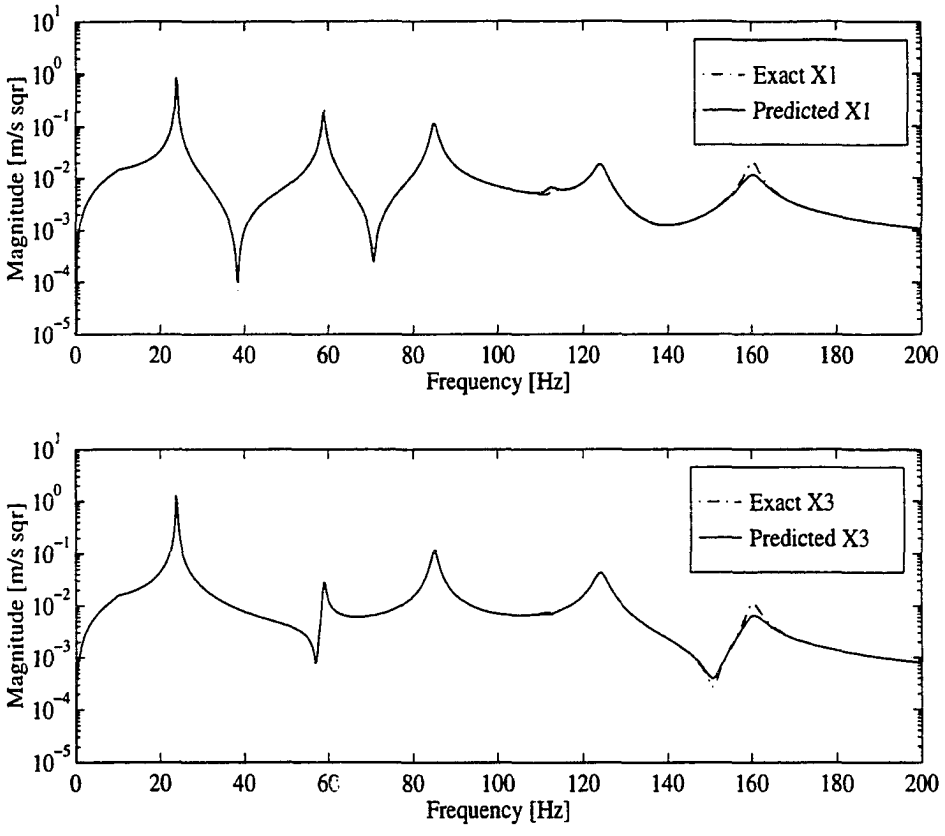

Figure 4.12 Test item *field interface* accelerations due to interface forces F_1 and F_3 and external force F_4

Equations 3.39 and 3.40 that are conveniently repeated as

$$[T_{cc}]\,\{R_c\} = \{Y_c\}_e \tag{4.8}$$

or

$$\{R_c\} = [T_{cc}]^{-1}\,\{Y_c\}_e \tag{4.9}$$

where the N_c x 1 vector $\{R_c\}$ contains the laboratory interface forces that will be applied by exciters 1 and 2 at the test item interface points 1 and 3, respectively. The N_c x 1 vector $\{Y_c\}_e$ contains the bare vehicle interface accelerations shown in Figure 4.9 and obtained from the first field simulation, and the N_c x N_c matrix $[T_{cc}]$ contains the test item interface driving point and transfer accelerance FRFs. It is assumed in this case

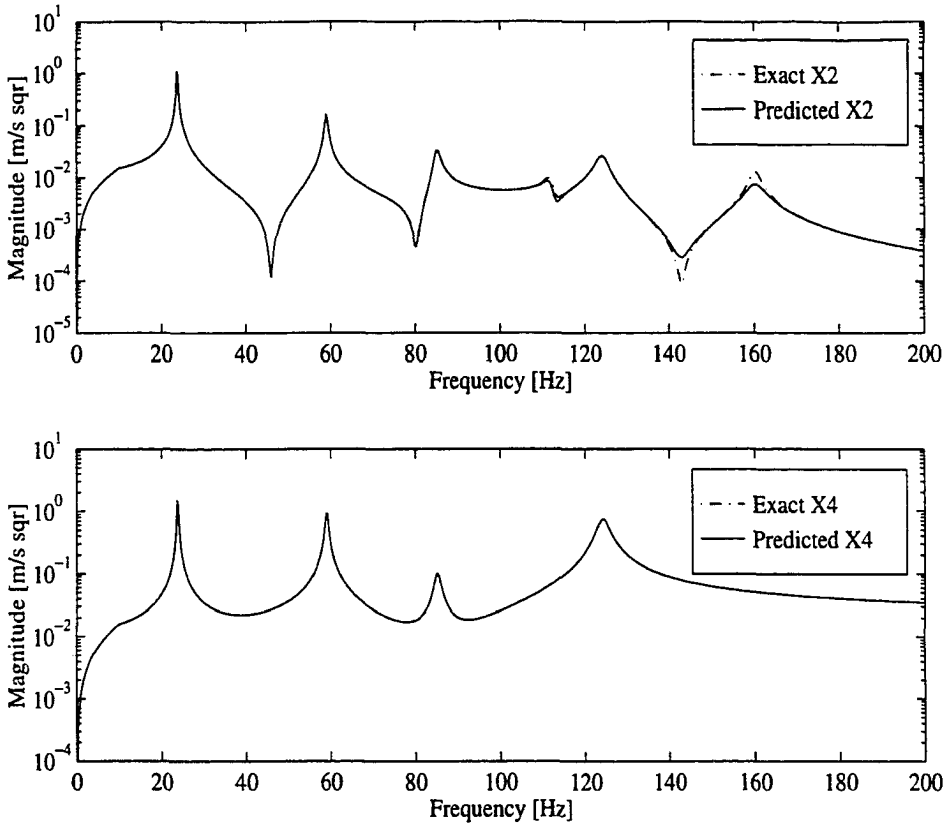

Figure 4.13 Test item *field external* accelerations due to interface forces F_1 and F_3 and external force F_4

that the test item has the same FRF characteristics in both the field and laboratory environments. This may not be always the case.

An expansion of Equation 4.8 for the model shown in Figure 4.1 gives

$$\begin{Bmatrix} R_1 \\ R_3 \end{Bmatrix} = \begin{bmatrix} T_{11} & T_{13} \\ T_{31} & T_{33} \end{bmatrix}^{-1} \begin{Bmatrix} Y_1 \\ Y_3 \end{Bmatrix} \tag{4.10}$$

It is assumed that exciters 1 and 2 can be controlled in such a way that the inputs R_1 and R_3 are generated to drive the test item interface points. When Equation 4.10 is solved for the laboratory interface force vector, the results are shown in Figure 4.14 where they are compared with the true field interface forces F_1 and F_3. It is seen that

the laboratory interface forces and the corresponding field forces do not match in this case. Figure 4.15 shows the magnitude of the ratio of the laboratory interface forces divided by the field interface forces, i.e, R_p/F_p, $p = 1, 3$ for both interface points. This ratio is seen to be greater than unity for most frequency components. In particular, there are frequencies for which $R_p/F_p > 100$, or, the force applied to the test item in the laboratory is at least 100 times larger than the corresponding field interface force. This suggests that at those frequencies the test item is being severely over-tested in the laboratory environment. In the $110 - 160$ Hz frequency range the ratio of laboratory to field interface forces is seen to be lower than unity so that the test item is being under-tested in the laboratory. This under-testing occurs due to the fact that in the field the external force F_4 increases in the $110 - 160$ Hz range, presenting a peak in the vicinity of 160 Hz, while in the laboratory the test item is being excited by interface forces *only*. Thus, the effects of F_4 not being accounted for in the laboratory leads to under-testing in the $110 - 160$ Hz range.

The N_t x 1 test item laboratory acceleration vector $\{U\}$ is obtained by

$$\{U\} = [T]\,\{R_c\} \tag{4.11}$$

where $[T]$ is the N_t x N_c test item FRF matrix. For the example shown in Figure 4.1 $N_c = 2$ and $N_t = 4$ so that Equation 4.11 expands to

$$\begin{Bmatrix} U_1 \\ U_3 \\ U_2 \\ U_4 \end{Bmatrix} = \begin{bmatrix} T_{11} & T_{13} \\ T_{31} & T_{33} \\ T_{21} & T_{23} \\ T_{41} & T_{43} \end{bmatrix} \begin{Bmatrix} R_1 \\ R_3 \end{Bmatrix} \tag{4.12}$$

The first two entries on the vector on the left hand side of Equation 4.12 correspond to the interface accelerations while the remaining entries represent external accelerations.

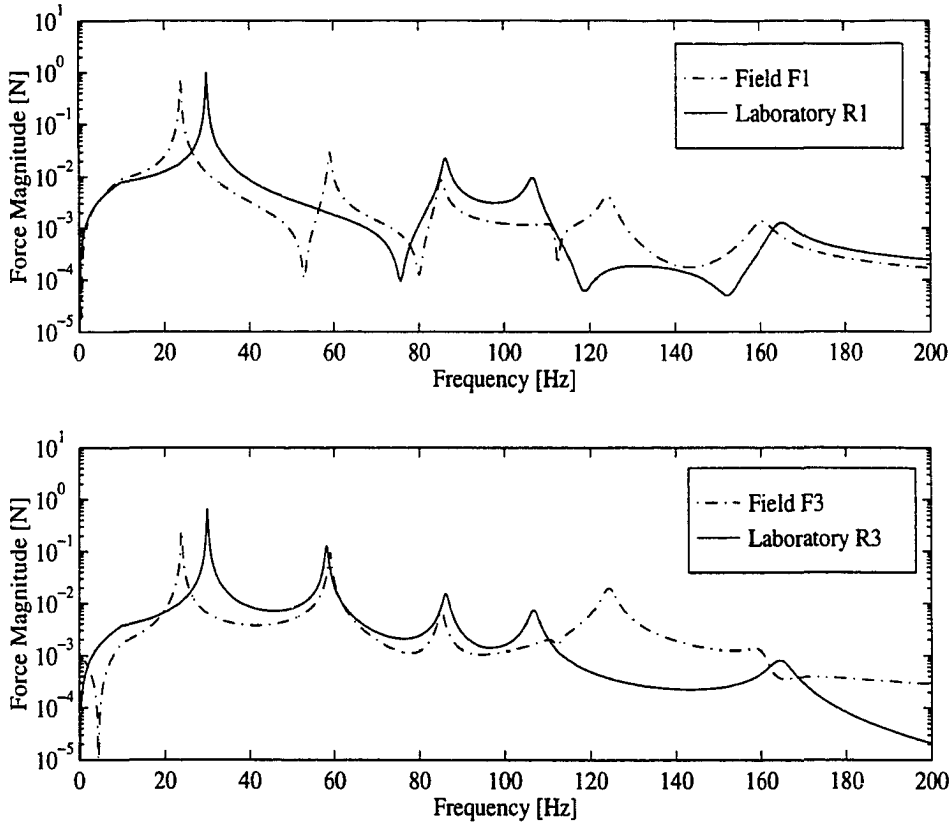

Figure 4.14 Comparison between field (F_1 and F_3) and laboratory (R_1 and R_3) interface forces for laboratory simulation using bare vehicle data

Figures 4.16 and 4.17 shows all four test item laboratory accelerations predicted from Equation 4.12 and the corresponding field accelerations obtained from Equation 4.6 when test item and vehicle are connected in the field. Clearly, there is a significant mismatch of acceleration in each case. The test item accelerations shown in Figures 4.16 and 4.17 reveal that natural frequencies and vibration levels obtained in the laboratory are not the same as those found in the field environment. Thus, a field data base composed of the bare vehicle interface accelerations only is not appropriate to define test item inputs in the laboratory for the general case. There are two reasons for this conclusion. *First*, field motion data was used to generate test item interface forces (R_1 and R_3) while in the actual field environment the test item is subjected to both interface forces (F_1 and

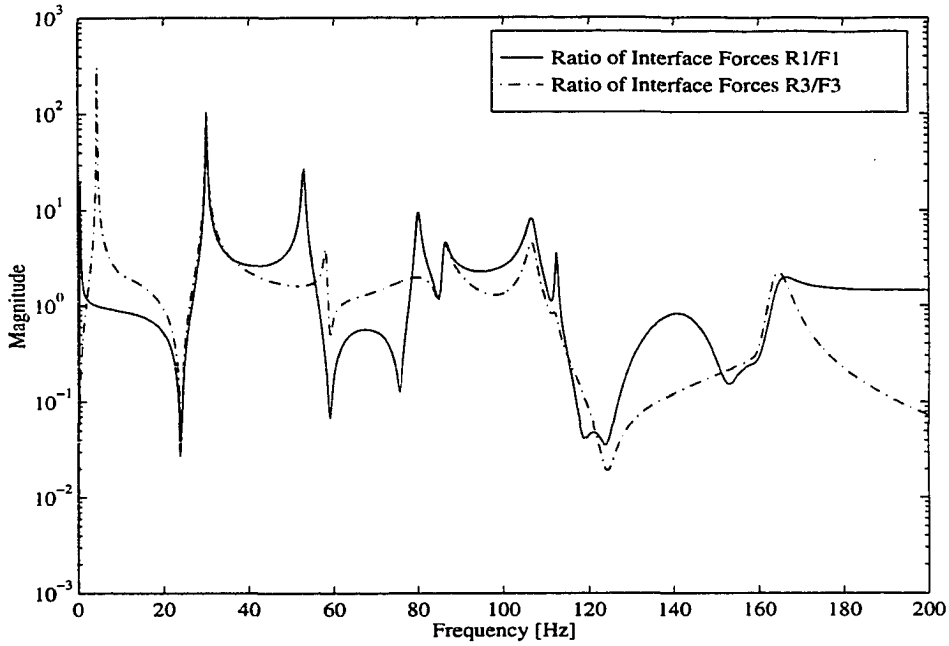

Figure 4.15 Ratio of laboratory interface forces obtained from the bare vehicle interface accelerations to the true field interface forces. No external forces applied to the test item in the laboratory while F_4 is present in the field

F_2) and an external force (F_4). *Second*, the bare vehicle interface accelerations do not contain any information regarding coupling effects between the test item and the vehicle since the test item is absent when field data is gathered. A direct comparison of the equations used to obtain field and laboratory interface forces, Equations 4.5 and 4.9 show that the vehicle's interface accelerance matrix $[V_{cc}]$ is missing from Equation 4.9. In addition, Equation 4.9 does not contain the term $\{X_c\}_e$ that shows the effects of the external force F_4 on the test item interface accelerations. This is due to the fact that only interface forces are being used to drive the test item in the laboratory.

If F_4 is removed from the field environment, then $\{X_c\}_e = \{X_e\}_e = 0$ in Equations 4.5 and 4.6. In this case, field interface forces and motions are dependent on the bare vehicle interface accelerations and on the test item and vehicle FRF characteristics. Figures 4.18 and 4.19 show that even when $F_4 = 0$ incorrect laboratory acceleration

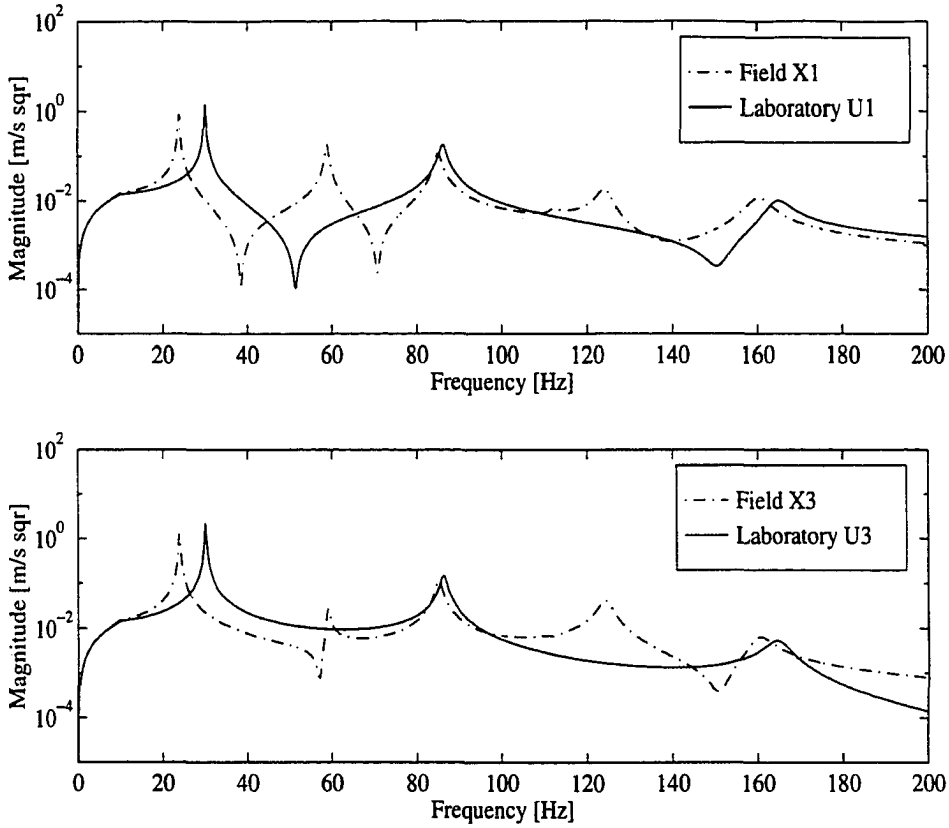

Figure 4.16 Resulting test item interface accelerations U_1 and U_3 in laboratory simulation using the bare vehicle interface data. Test item is driven by interface and external forces in the field and by interface forces obtained from the bare vehicle interface motion in the laboratory

results are obtained when using Equation 4.9. However, if $[V_{cc}]$ is used in Equation 4.8 or Equation 4.9 as shown in the true interface force expression given by Equation 4.5 (with $\{X_e\}_e = 0$), the correct transformation matrix will be applied and correct test item inputs are obtained. Thus, in the special case where the test item is subjected to no field external forces, the bare vehicle interface accelerations may be used to define suitable test item inputs in the laboratory, *provided the vehicle interface accelerance matrix* $[V_{cc}]$ *is accounted for when determining the laboratory inputs.* Otherwise, the use of the bare vehicle interface accelerations without additional information is meaningless.

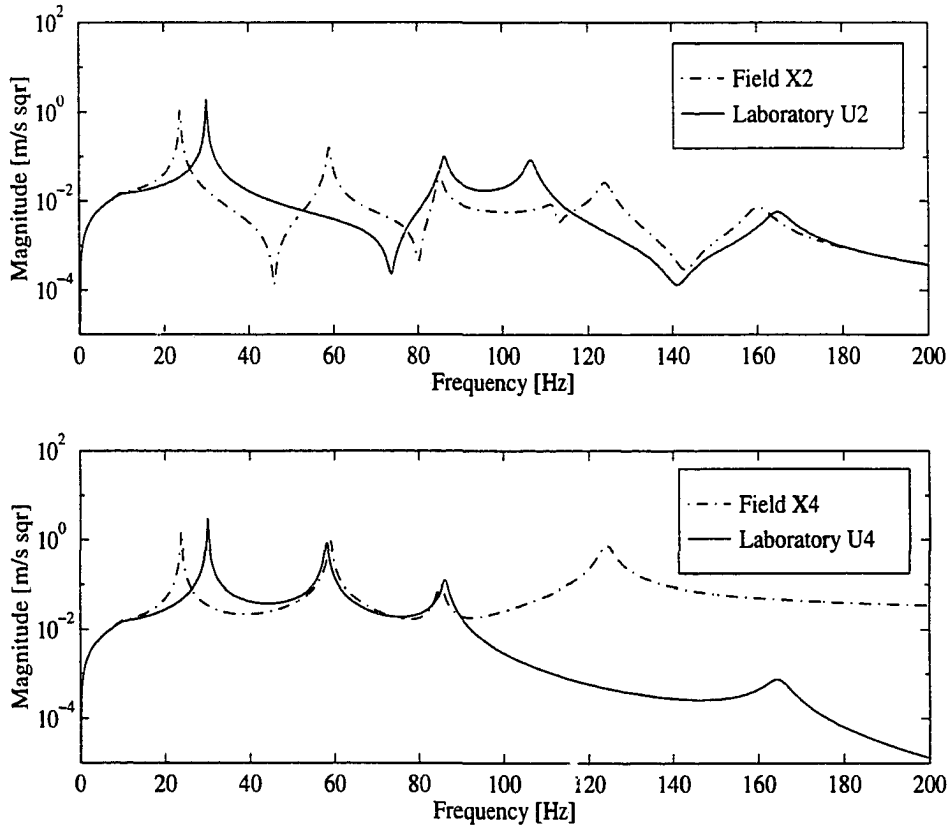

Figure 4.17 Resulting test item external accelerations U_2 and U_4 in laboratory simulation using the bare vehicle interface data. Test item is driven by interface and external forces in the field and by interface forces obtained from the bare vehicle interface motion in the laboratory

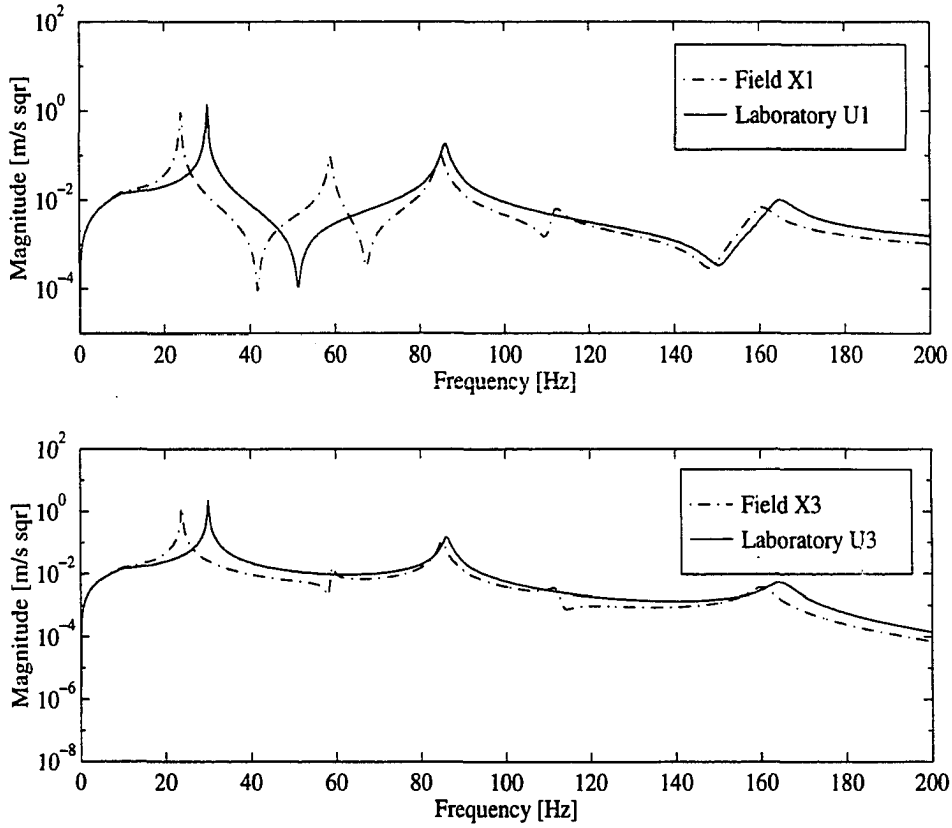

Figure 4.18 Resulting test item interface accelerations U_1 and U_3 in laboratory simulation using the bare vehicle interface data without using $[V_{cc}]$ in Equation 4.9. No external forces are applied to the test item in both environments

Laboratory Simulations Using Field Interface Forces as Test Item Inputs

This laboratory simulation corresponds to the test scenario 2 described in Chapter 3 where the field interface forces $\{F_c\}$ shown in Figure 4.11 are used as test item inputs. It is assumed that the interface forces can be generated and controlled in the laboratory environment such that field and laboratory interface forces are matched ($\{R_c\} = \{F_c\}$).

The test item acceleration response in the laboratory environment is calculated according to Equation 4.7, rewritten as

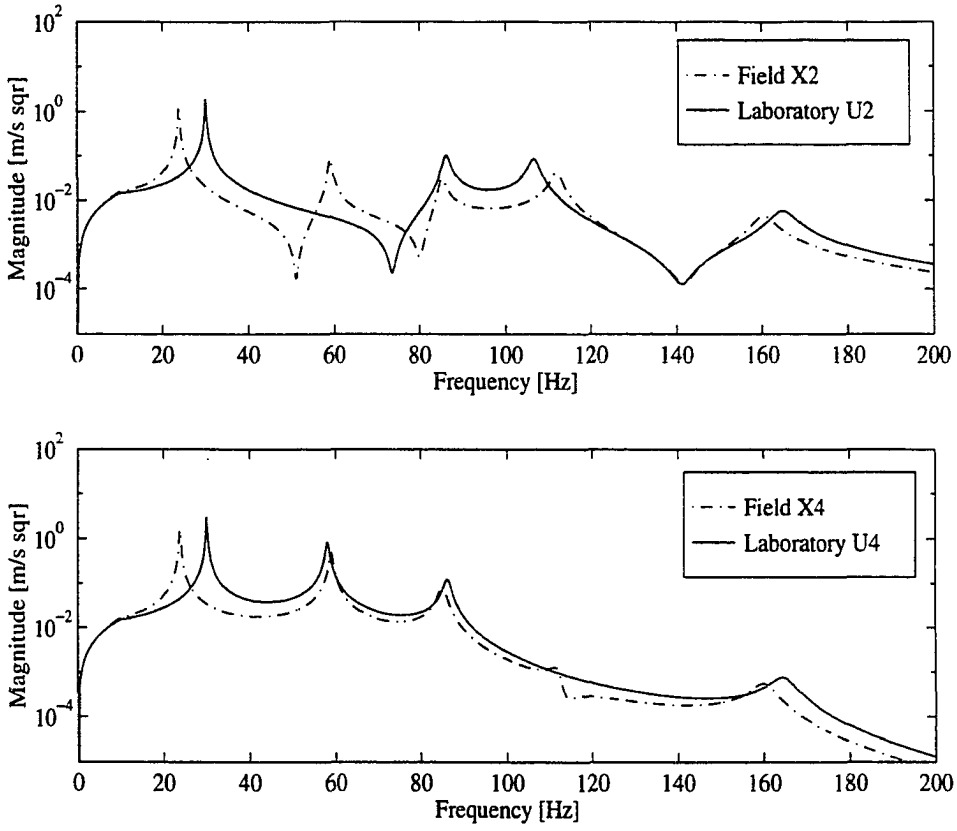

Figure 4.19 Resulting test item external accelerations U_2 and U_4 in laboratory simulation using the bare vehicle interface data without using $[V_{cc}]$ in Equation 4.9. No external forces are applied to the test item in both environments

$$\begin{Bmatrix} \{U_c\} \\ \{U_e\} \end{Bmatrix} = \begin{bmatrix} [T_{cc}] & [T_{ce}] \\ [T_{ec}] & [T_{ee}] \end{bmatrix} \begin{Bmatrix} \{F_c\} \\ \{0\} \end{Bmatrix} \tag{4.13}$$

Then, by using Equation 4.13, the test item laboratory interface and external accelerations are obtained and are shown in Figures 4.20 and 4.21, along with the test item's field accelerations. This laboratory simulation gives incorrect test item accelerations. This result is easily understood since only interface forces are applied to the test item in the laboratory and the effects of the external force F_4 are not accounted for. *Hence, matching the correct interface forces in the laboratory leads to incorrect simulation results if*

external forces effects are not accounted for in addition to interface forces.

If the external force F_4 is removed from the field environment, then the test item laboratory motions shown in Figures 4.22 and 4.23 are obtained, where in this case a different set of field accelerations are obtained since $\{X_c\}_e = 0$ and $\{X_e\}_e = 0$ in Equations 4.5 and 4.6. Field and laboratory test item accelerations are indistinguishable in this case. This result was expected since the test item inputs in the laboratory environment match the corresponding field interface forces and no field external forces were applied to the test item. Thus, controlling laboratory interface forces such that they match field interface forces leads to a successful laboratory simulation for the case where there are no external forces in both environments. *The difficulty is to get the exciters to be properly controlled since cross correlation must be maintained in these tests.*

Laboratory Simulations Using Test Item Inputs Obtained from the Field Combined Structure Accelerations When $F_4 \neq 0$

This simulation corresponds to the third and fourth scenarios described in Chapter 3. In this case, the test item field accelerations shown in Figures 4.12 and 4.13 are used to define the test item inputs in the laboratory. This constitutes a force identification problem, since a set of laboratory input forces is required to drive the test item from knowledge of field motions.

Force identification represents an inverse problem in mechanics [2]. The pseudo-inverse technique [10, 11, 13, 18, 19] is used to estimate unknown applied forces to a given structure from knowledge of motion records and the structure's FRF characteristics.

The solution for M unknown forces from knowledge of N motion records (generally $N > M$) through the pseudo-inverse technique is carried out in the frequency domain

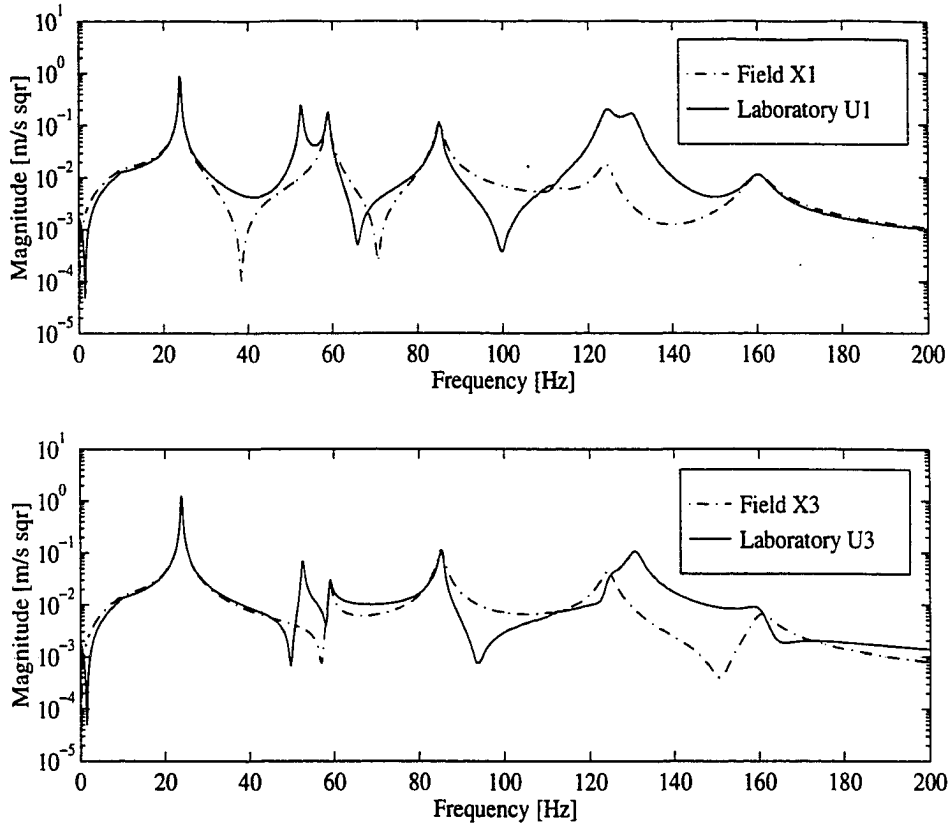

Figure 4.20 Test item interface accelerations obtained from laboratory simulation where field interface forces are used as test item inputs. The test item is driven by laboratory interface forces R_1 and R_3 that match the true field interface forces F_1 and F_3. The effects of the external field force F_4 are not accounted for in this laboratory simulation

through the following relationship [9, 10]

$$\{F\} = [A]^{+} \{X\} \tag{4.14}$$

where superscript "+" denotes the pseudo-inverse of the FRF matrix, and is given by

$$[A]^{+} = \left[[A]^{H}[A]\right]^{-1} [A]^{H} \tag{4.15}$$

where the superscript ^{H} denotes the hermitian conjugate (complex conjugate transpose) of the accelerance FRF matrix, since $[A]$ is complex for deterministic signals. Equations 4.14 and 4.15 are employed when the structure's output acceleration frequency

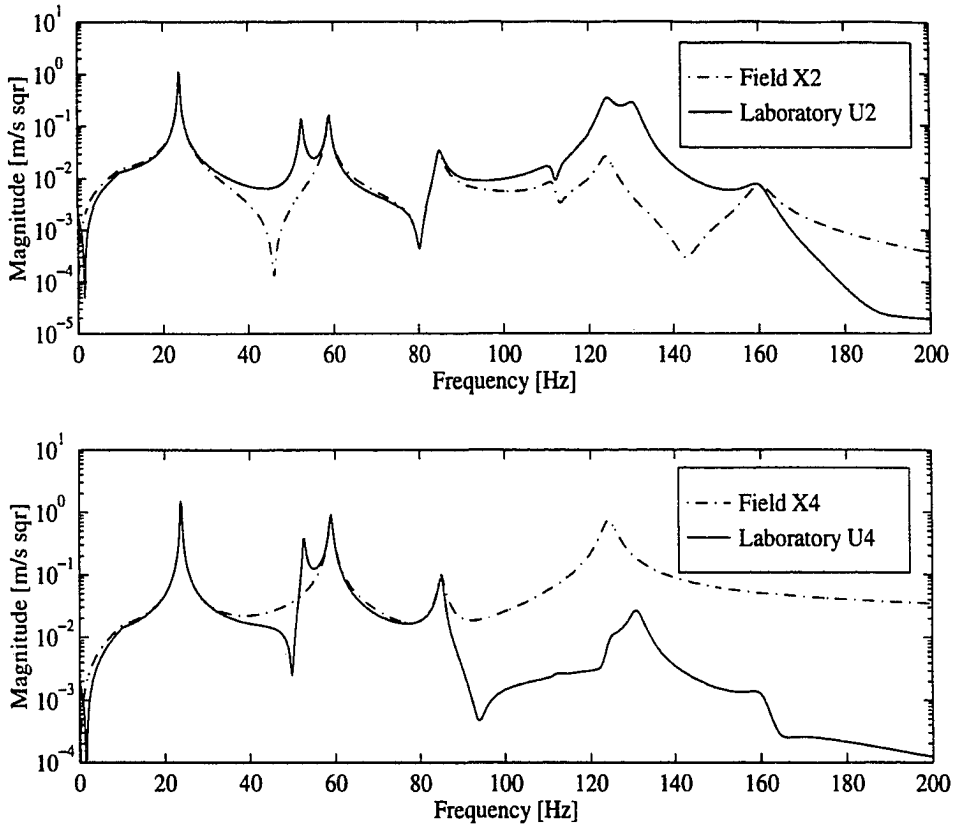

Figure 4.21 Test item external accelerations obtained from laboratory simulation where field interface forces are used as test item inputs. The test item is driven by laboratory interface forces R_1 and R_3 that match the true field interface forces F_1 and F_3. The effects of the external field force F_4 are not accounted for in this laboratory simulation

spectra (magnitude and phase) $\{X\}$ is known, and their use is restricted to deterministic (transient and periodic) signals.

As in many inverse problems, the pseudo-inverse technique is numerically ill conditioned at some frequencies [17, 18, 43]; particularly natural frequencies [10, 11] since the calculation procedure requires the inversion of the structure's FRF matrix for each frequency value. The FRF matrix is usually rectangular ($N > M$); and hence, the pseudo-inversion of the FRF matrix is required in order to solve for the unknown forces.

Some important characteristics of the pseudo-inverse technique are:

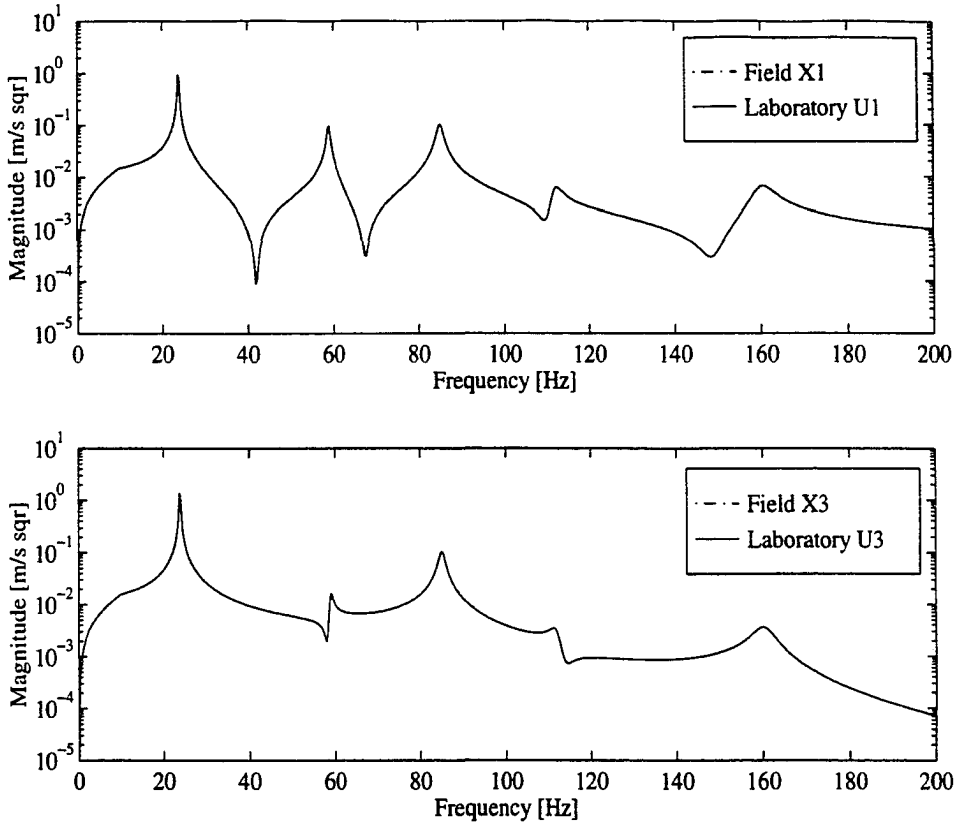

Figure 4.22 Test item interface accelerations obtained from laboratory simulation where field interface forces are used as test item inputs. The test item is driven by laboratory interface forces R_1 and R_3 that match the true field interface forces F_1 and F_3. The external field force F_4 is removed from the field environment in this simulation

- The calculation procedure is very sensitive to the accuracy of the mode shape data used in the structure's modal model [9, 18]. This affects the quality of the FRFs used in the identification process. Frequency response function curve fitting has been proposed [18] to reduce noise effects on the structure's FRF matrix, improving the numerical stability of the pseudo-inversion;

- The number of forces that can be predicted at a given frequency depends on the number of mode shapes participating in the structure's response at that fre-

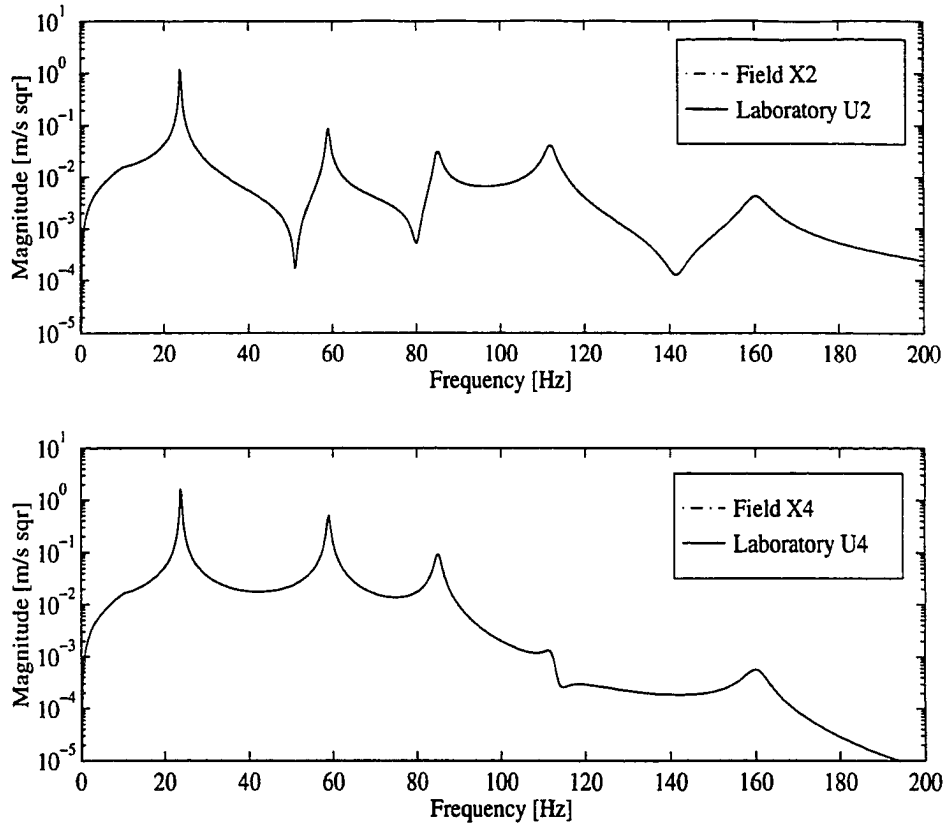

Figure 4.23 Test item external accelerations obtained from laboratory simulation where field interface forces are used as test item inputs. The test item is driven by laboratory interface forces R_1 and R_3 that match the true field interface forces F_1 and F_3. The external field force F_4 is removed from the field environment in this simulation

quency [10, 11]. In other words, the FRF matrix may be rank deficient at some frequencies.

- Experimental and numerical procedures have been proposed to improve the conditioning of the inversion problem. Hillary and Ewins [18, 19] proposed to use strain gage data instead of acceleration data in the identification of unknown forces. Han and Wicks [16] proposed to use rotational FRF data to improve the stability of the FRF matrix inversion.

A numerical study was performed on a simply supported beam in order to assess the feasibility of the pseudo-inverse technique [13]. Sinusoidal excitation at a single frequency was used. This investigation reinforced the fact that the ill conditioning is related to the number of participating modes at each frequency, since a low number of modes causes rank deficiency to the FRF matrix, which in turn, produces errors in the predicted forces. In addition, this paper points to the difference between using experimental FRFs and curve fitted FRFs in the solution of the inverse problem.

In the vibration testing context, the pseudo-inverse technique is used to calculate a set of laboratory test item inputs from knowledge of field acceleration records. Since the test item motions are divided into interface motions and external motions, a natural question that arises when using field motions to define test item inputs in this laboratory simulation is: What motions should be measured in the field such that a suitable set of test item input forces are obtained from the pseudo-inverse technique for use in the laboratory environment ?

In this simulation study, three cases are discussed. In each case the pseudo-inverse technique is employed with field accelerations to predict a set of test item laboratory input forces. These cases are summarized below:

- A set of N_c interface forces is calculated from N_c interface motions according to the following expression

$$\{R_c\} = [T_{cc}]^{+} \{X_c\} \tag{4.16}$$

  where $\{R_c\}$ is N_c x 1 and corresponds to the predicted laboratory interface forces, $\{X_c\}$ is N_c x 1 and contains field interface accelerations, and $[T_{cc}]$ is the test item interface FRF matrix. Since $[T_{cc}]$ is a square N_c x N_c matrix in this case, its pseudo-inverse coincides with the standard inverse.

- A set of N_c interface forces is calculated from all test item N_t accelerations, and in this case, Equation 4.14 gives

$$\{R_c\} = [\ [\ [T_{cc}]\ [T_{ce}]\ ]^T\ ]^+\{X\} \tag{4.17}$$

where $\{X\}$ is N_t x 1 and contains the test item laboratory interface and external accelerations and $[[T_{cc}][T_{ce}]]^T$ is the N_c x N_t test item FRF matrix.

- A set of N_t forces is calculated from N_t accelerations according to

$$\left\{ \begin{array}{c} \{R_c\} \\ \{R_e\} \end{array} \right\} = \left[\begin{array}{cc} [T_{cc}] & [T_{ce}] \\ [T_{ec}] & [T_{ee}] \end{array} \right]^+ \left\{ \begin{array}{c} \{X_c\} \\ \{X_e\} \end{array} \right\} \tag{4.18}$$

where in this case, a set of interface and external forces is obtained.

The first two cases attempt to reproduce field data by predicting interface forces only while the third case attempts to obtain interface as well as external forces. The results of these three cases will be presented for the test item described in Figure 4.1.

Simulation with N_c Interface Forces obtained from N_c Interface Accelerations and $F_4 \neq 0$

For the test item model shown in Figure 4.1, Equation 4.16 is rewritten as

$$\left\{ \begin{array}{c} R_1 \\ R_3 \end{array} \right\} = \left[\begin{array}{cc} T_{11} & T_{13} \\ T_{31} & T_{33} \end{array} \right]^+ \left\{ \begin{array}{c} X_1 \\ X_3 \end{array} \right\} \tag{4.19}$$

In this case, the test item field interface accelerations calculated according to Equation 4.6 and shown in Figure 4.12 (solid line) are used. The results for the interface forces obtained from Equation 4.19 are shown in Figure 4.24, where it is seen that the

pseudo-inverse technique gives a nearly correct result for the interface force R_1 but an incorrect result for R_3.

The test item laboratory accelerations due to the interface forces R_1 and R_3 are calculated according to

$$\begin{Bmatrix} U_1 \\ U_2 \\ U_3 \\ U_4 \end{Bmatrix} = \begin{bmatrix} T_{11} & T_{13} \\ T_{21} & T_{23} \\ T_{31} & T_{33} \\ T_{41} & T_{43} \end{bmatrix} \begin{Bmatrix} R_1 \\ R_3 \end{Bmatrix} \tag{4.20}$$

and they are shown in Figures 4.25 and 4.26 along with the corresponding field motions. Figure 4.25 shows that the interface accelerations obtained in the laboratory simulation matched the corresponding field data regardless the fact that $R_3 \neq F_3$.

Similarly, field and laboratory external accelerations X_2 and U_2 matched closely in Figure 4.26. Since there are no external forces acting on M_2, the field acceleration X_2 is governed by spring and damper forces at elements K_1, K_2, C_1, and C_2, which in turn, depend on interface displacements and velocities at points 1 and 3, respectively. Thus, if correct interface accelerations are obtained in the laboratory simulation, accelerations U_2 and X_2 will be identical. On the other hand, an incorrect result is obtained for U_4 as seen in Figure 4.26. In this case, the external force F_4 is applied to M_4 in the field, but is not accounted for in the laboratory simulation. The resulting laboratory motion U_4 is due to interface forces only while in the field X_4 is caused by the interface forces F_1 and F_3 as well as by the external force F_4.

The results of this simulation can be summarized as:

- Interface forces:

$$\begin{aligned} R_1 &= F_1 \\ R_3 &\neq R_3 \end{aligned} \tag{4.21}$$

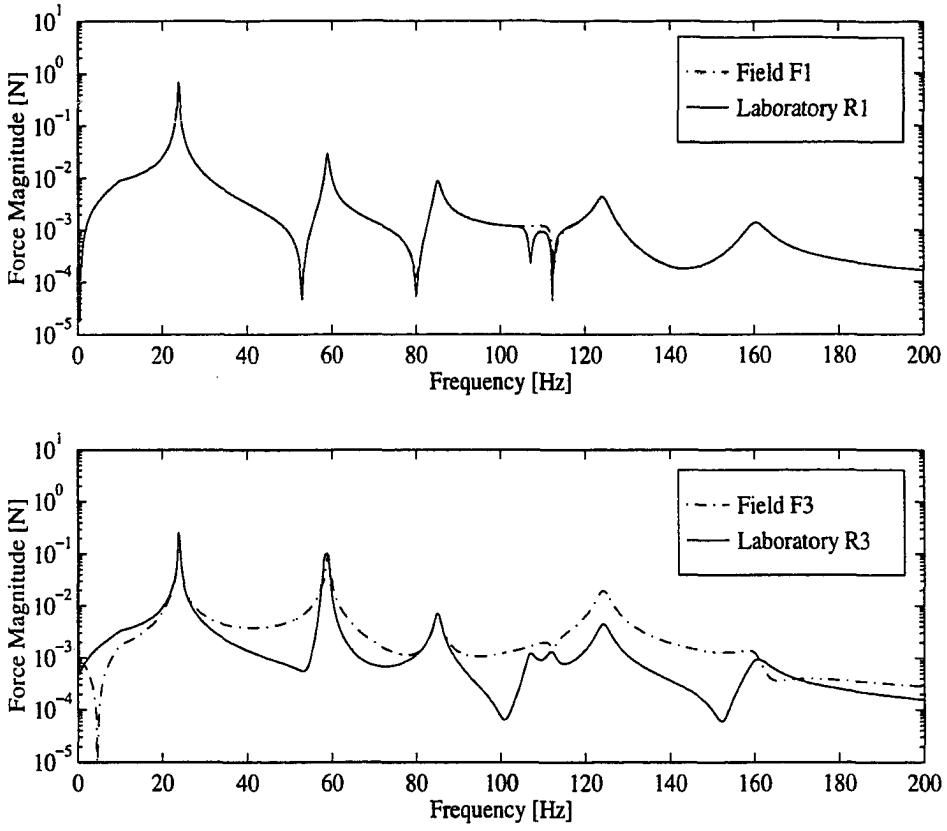

Figure 4.24 Interface forces obtained from N_c field interface motions through the pseudo-inverse technique

- Test item accelerations:

$$\begin{aligned} U_1 &= X_1 \\ U_2 &= X_2 \\ U_3 &= X_3 \\ U_4 &\neq X_4 \end{aligned} \tag{4.22}$$

Two additional simulations were performed in case 1. Both simulations employed Equations 4.19 and 4.20 but the point of application of the external force F_4 was different in each case. The results of these additional simulations are not shown here, but the following was observed:

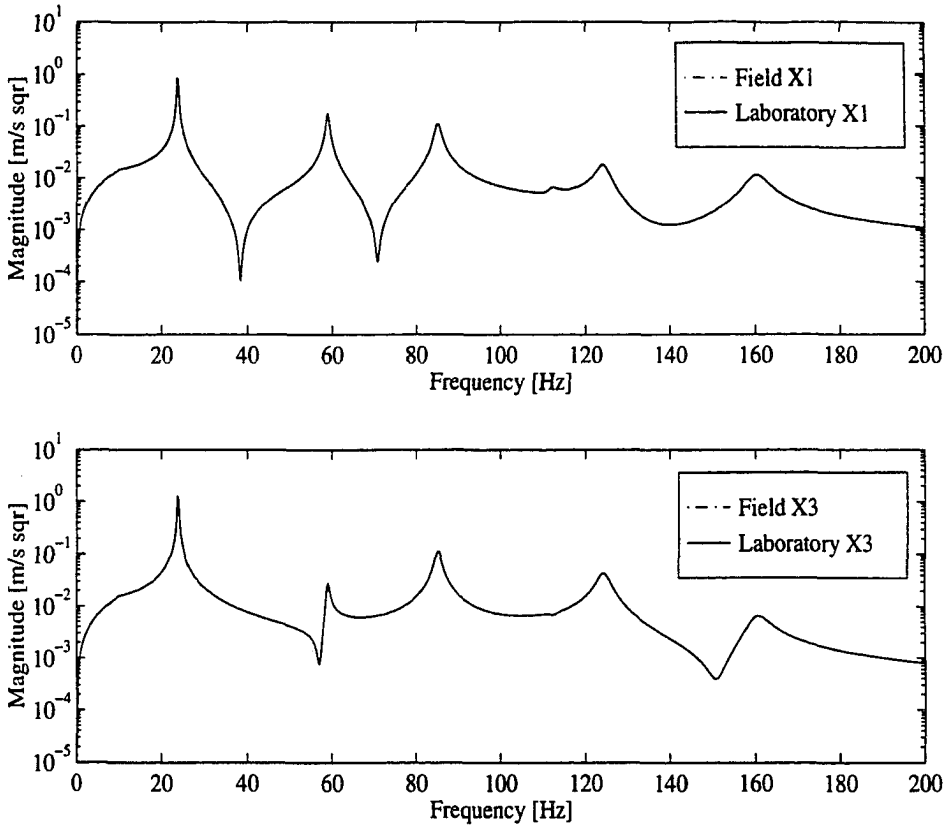

Figure 4.25 Test item interface accelerations obtained from N_c laboratory interface forces that are obtained from N_c field interface accelerations. No external forces effects are accounted for in the laboratory

(i) First, the test item external force F_4 was removed from M_4 and applied to M_2. Interface forces and test item accelerations were recalculated using Equations 4.5 and 4.6 (with $\{X_c\}_e = 0$ and $\{X_c\}_e = 0$), respectively. Then, Equations 4.19 and 4.20 were used to calculate the laboratory interface forces and test item accelerations, respectively. The results of this simulation are:

- Interface forces:

$$R_1 \neq F_1$$
$$R_3 \neq R_3 \qquad (4.23)$$

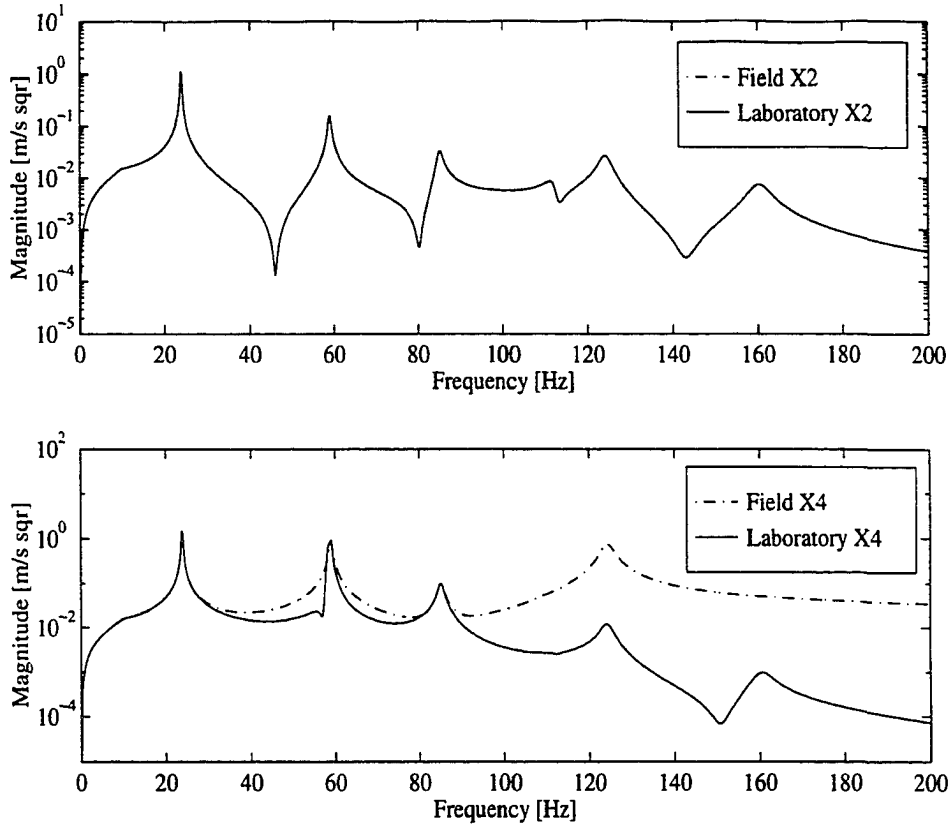

Figure 4.26 Test item external accelerations obtained from N_c laboratory interface forces that are obtained from N_c field interface accelerations. No external forces effects are accounted for in the laboratory

- Test item accelerations:

$$\begin{aligned} U_1 &= X_1 \\ U_2 &\neq X_2 \\ U_3 &= X_3 \\ U_4 &= X_4 \end{aligned} \tag{4.24}$$

(*ii*) Second, the external force F_4 is simultaneously applied to the test item masses M_2 and M_4. The results obtained are

- Interface forces:

$$R_1 \neq F_1$$
$$R_3 \neq R_3 \tag{4.25}$$

- Test item accelerations:

$$U_1 = X_1$$
$$U_2 \neq X_2 \tag{4.26}$$
$$U_3 = X_3 \tag{4.27}$$
$$U_4 \neq X_4 \tag{4.28}$$

Thus, the first laboratory simulation case employing interface motions shows the following trends: (*a*) Interface accelerations are matched in the laboratory regardless of whether the interface forces matching or not; (*b*) External accelerations corresponding to points that are subjected to external forces in the field environment are not matched in the laboratory; (*c*) In two cases the motion at an external point matched the corresponding field measurement, but this cannot be seen as a general trend, since the model used in these simulations contains only one external point free of forces.

Recall from Chapter 3 that interface and external accelerations can be broken in two parts, one due to connector forces and the other due to external forces, according to

$$\{X_c\} = \{X_{cc}\} + \{X_{ce}\} \tag{4.29}$$
$$\{X_e\} = \{X_{ec}\} + \{X_{ee}\} \tag{4.30}$$

where the first subscript in Equations 4.29 and 4.30 belongs to the motion group (connector or external) and the second subscript belongs to the force causing the corresponding acceleration. For the model shown in Figure 4.1, with the external force applied to M_4,

Equations 4.29 and 4.30 are written as

$$X_1 = X_{11} + X_{13} + X_{14} \tag{4.31}$$

$$X_3 = X_{31} + X_{33} + X_{34} \tag{4.32}$$

$$X_2 = X_{21} + X_{23} + X_{24} \tag{4.33}$$

$$X_4 = X_{41} + X_{43} + X_{44} \tag{4.34}$$

Similarly, in the laboratory simulation

$$U_1 = U_{11} + U_{13} \tag{4.35}$$

$$U_3 = U_{31} + U_{33} \tag{4.36}$$

$$U_2 = U_{21} + U_{23} \tag{4.37}$$

$$U_4 = U_{41} + U_{43} \tag{4.38}$$

Thus, by comparing Equations 4.31 and 4.32 with Equations 4.35 and 4.36, it is observed that if accelerations X_{14} and X_{34} are negligible, then the problem is reduced to matching interface accelerations X_{11}, X_{13}, X_{31}, and X_{33} that are caused by interface forces only. This condition can be achieved by applying the pseudo-inverse technique to field interface accelerations in order to get a set of forces such that application of these forces to the test item in the laboratory will give the same interface accelerations as measured in the field.

Another way of comparing field and laboratory interface characteristics is by expressing the laboratory forces as a function of field forces. By imposing $U_1 = X_1$ and $U_3 = X_3$ and using Equation 4.16 for interface points 1 and 3, the following expression is obtained for the laboratory interface forces required in this case

$$\begin{Bmatrix} R_1 \\ R_3 \end{Bmatrix} = \begin{Bmatrix} F_1 \\ F_3 \end{Bmatrix} + \begin{bmatrix} T_{11} & T_{13} \\ T_{31} & T_{33} \end{bmatrix}^{-1} \begin{Bmatrix} T_{14}F_4 \\ T_{34}F_4 \end{Bmatrix} \tag{4.39}$$

or expanding the inverse of the test item interface FRF matrix

$$\left\{ \begin{array}{c} R_1 \\ R_3 \end{array} \right\} = \left\{ \begin{array}{c} F_1 \\ F_3 \end{array} \right\} + \frac{1}{T_{11}T_{33} - T_{31}T_{13}} \left\{ \begin{array}{c} T_{33}T_{14} - T_{13}T_{34} \\ T_{11}T_{34} - T_{31}T_{14} \end{array} \right\} F_4 \qquad (4.40)$$

According to Equation 4.39 or its expanded form, Equation 4.40, field and laboratory interface forces will match if and only if there are no external forces acting on the test item while in the field, i.e., $F_4 = 0$, or if the second vector on the right hand side of Equation 4.40 equals zero. The first condition frequently occurs in real situations, but the second represents a special case that occurred for R_1 in Figure 4.24.

Simulation Using N_c interface Forces obtained from N_t Field Accelerations and $F_4 \neq 0$

In this laboratory test scenario, a set of N_c interface forces are calculated and applied to the test item according to Equation 4.17. For the system shown in Figure 4.1, Equation 4.17 is written as

$$\left\{ \begin{array}{c} R_1 \\ R_3 \end{array} \right\} = \left[\begin{array}{cc} T_{11} & T_{13} \\ T_{31} & T_{33} \\ T_{21} & T_{23} \\ T_{41} & T_{43} \end{array} \right]^+ \left\{ \begin{array}{c} X_1 \\ X_3 \\ X_2 \\ X_4 \end{array} \right\} \qquad (4.41)$$

The interface forces calculated through Equation 4.41 are shown in Figure 4.27. It is clear that the interface forces do not match in this case.

Test item accelerations are calculated according to Equation 4.20, and they are shown in Figures 4.28 and 4.29. Generally, all laboratory accelerations were incorrect in this

simulation.

Simulation Using N_t Forces Obtained from N_t Field Accelerations and $F_4 \neq 0$

In this test scenario, N_t laboratory forces are calculated from all N_t accelerations so that Equation 4.18 reduces to

$$\begin{Bmatrix} R_1 \\ R_3 \\ R_2 \\ R_4 \end{Bmatrix} = \begin{bmatrix} T_{11} & T_{13} & T_{12} & T_{14} \\ T_{31} & T_{33} & T_{32} & T_{34} \\ T_{21} & T_{23} & T_{22} & T_{24} \\ T_{41} & T_{43} & T_{42} & T_{44} \end{bmatrix}^{+} \begin{Bmatrix} X_1 \\ X_3 \\ X_2 \\ X_4 \end{Bmatrix} \tag{4.42}$$

Three significantly non zero forces were obtained from Equation 4.42, and are shown in Figures 4.30 and 4.31. It is seen that both interface forces closely match the corresponding field forces. The external force R_4 is seen to track the original force F_4 in magnitude and phase in Figure 4.31. The result for R_2 were practically zero, presenting magnitudes that vary from 10^{-16} to 10^{-19} for all frequency components since no force is applied to M_2 in the field.

The test item accelerations are obtained from

$$\begin{Bmatrix} U_1 \\ U_3 \\ U_2 \\ U_4 \end{Bmatrix} = \begin{bmatrix} T_{11} & T_{13} & T_{14} \\ T_{31} & T_{33} & T_{34} \\ T_{21} & T_{23} & T_{24} \\ T_{41} & T_{43} & T_{44} \end{bmatrix} \begin{Bmatrix} R_1 \\ R_3 \\ R_4 \end{Bmatrix} \tag{4.43}$$

and the calculated results closely match the field accelerations as shown in Figures 4.32 and 4.33.

It is clear that the pseudo-inverse technique was able to accurately predict the field interface forces in this numerical example when more motions were measured than excitation forces existed and the time signals were either transient or periodic. In addition, it is clear that the test item experiences essentially the same accelerations in the laboratory as in the field if the laboratory forces are properly controlled.

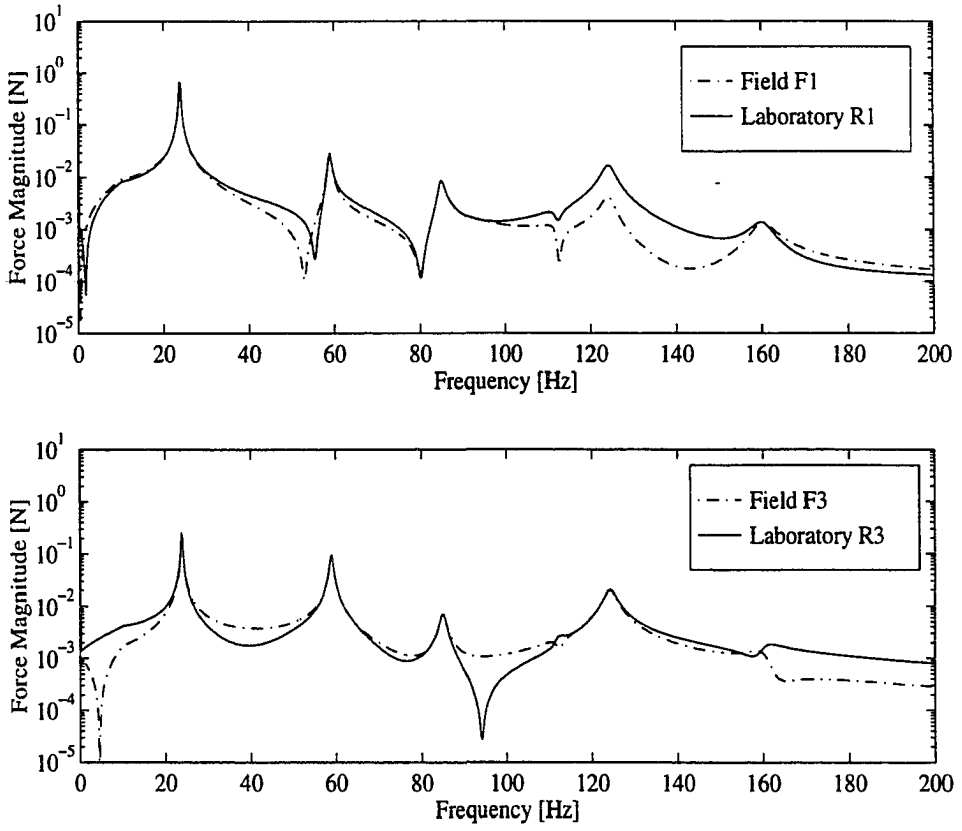

Figure 4.27 Interface forces obtained from N_t field accelerations through the pseudo-inverse technique when only two forces are obtained from four possible field accelerations. No external forces are predicted in this case

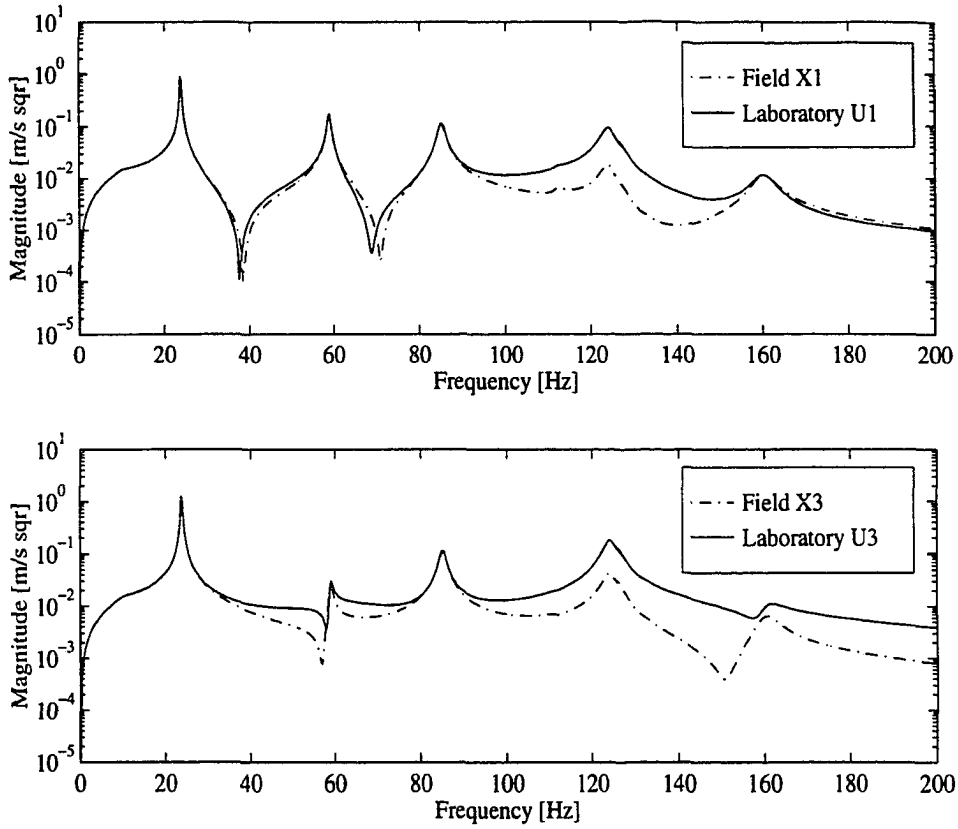

Figure 4.28 Test item interface accelerations obtained from N_c laboratory interface forces that are obtained from N_t field interface accelerations. External force F_4 is present in the field but is not accounted for in the laboratory

Chapter Summary

The results obtained in this chapter can be summarized as follows:

- The blind application of bare vehicle data without accounting for the vehicle interface FRF characteristics leads to significant test errors. If, however, these interface FRF characteristics are accounted for in transforming the bare vehicle interface accelerations, reasonable test results in terms of natural frequencies and magnitudes are obtained in *the special case where field external forces are negligible.*

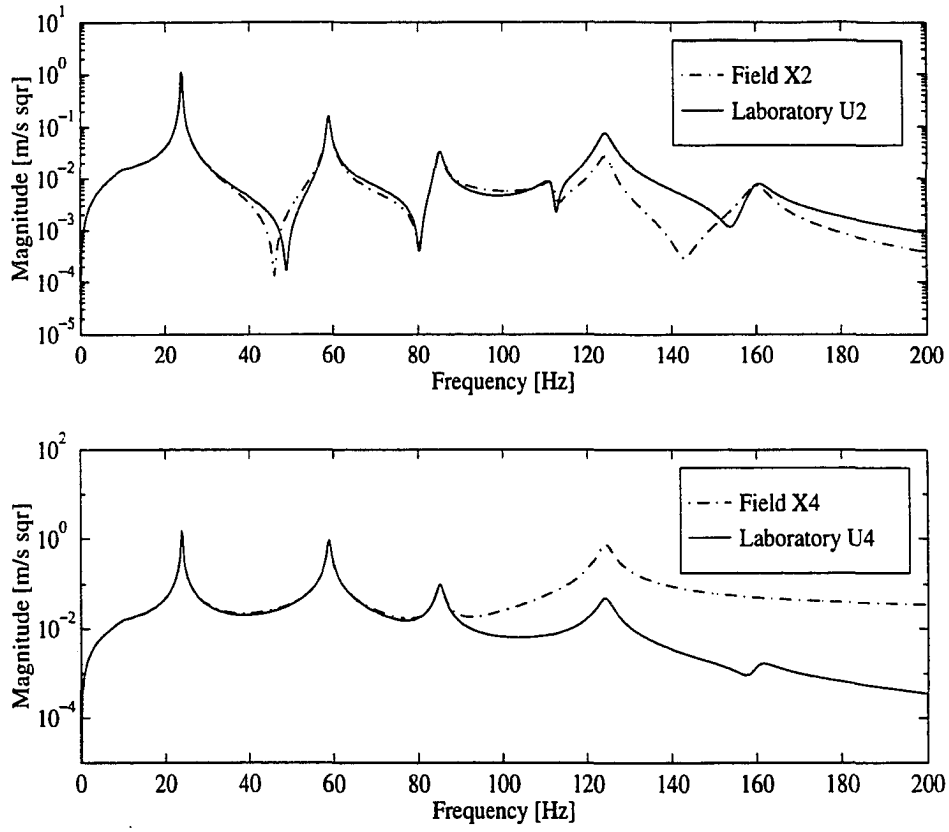

Figure 4.29 Test item external accelerations obtained from N_c laboratory interface forces that are obtained from N_t field interface accelerations. External force F_4 is present in the field but it is not accounted for in the laboratory

- Field external force effects must be accounted for in the laboratory in addition to interface forces effects in order to obtain reasonable laboratory simulation results.

- The pseudo-inverse technique was successfully applied to test item field interface and external acceleration frequency spectra in order to define the laboratory inputs.

- Note that any cross correlation requirements between variables are automatically satisfied in all of these cases since the field data contained both magnitude and phase information; that is, the signals are automatically correlated due to phase information.

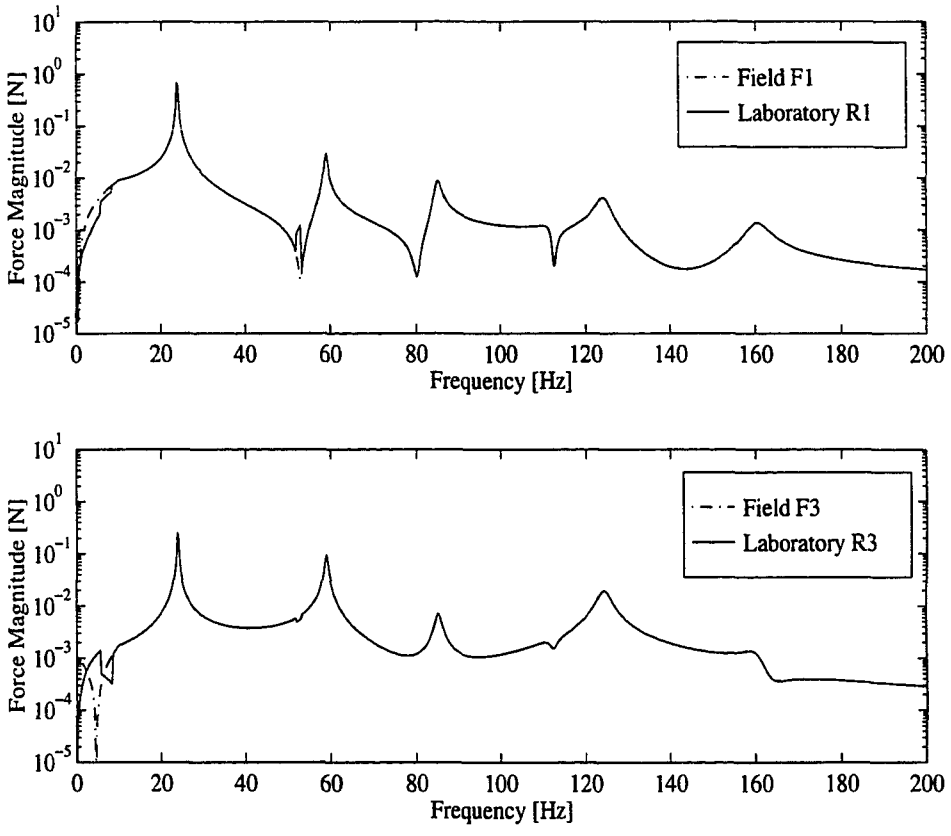

Figure 4.30 Interface forces obtained from field accelerations through the pseudo-inverse technique when N_t forces are predicted from all possible N_t field accelerations

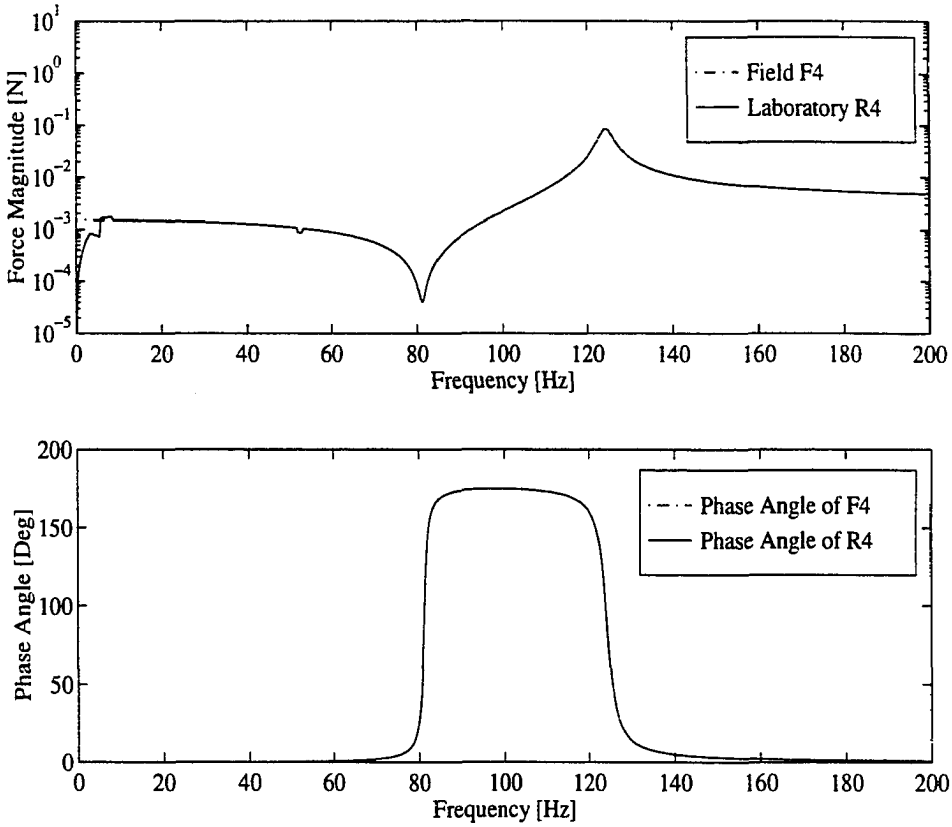

Figure 4.31 Magnitude and phase of external force R_4 that was obtained from field accelerations through the pseudo-inverse technique when N_t forces are predicted from all possible N_t field accelerations

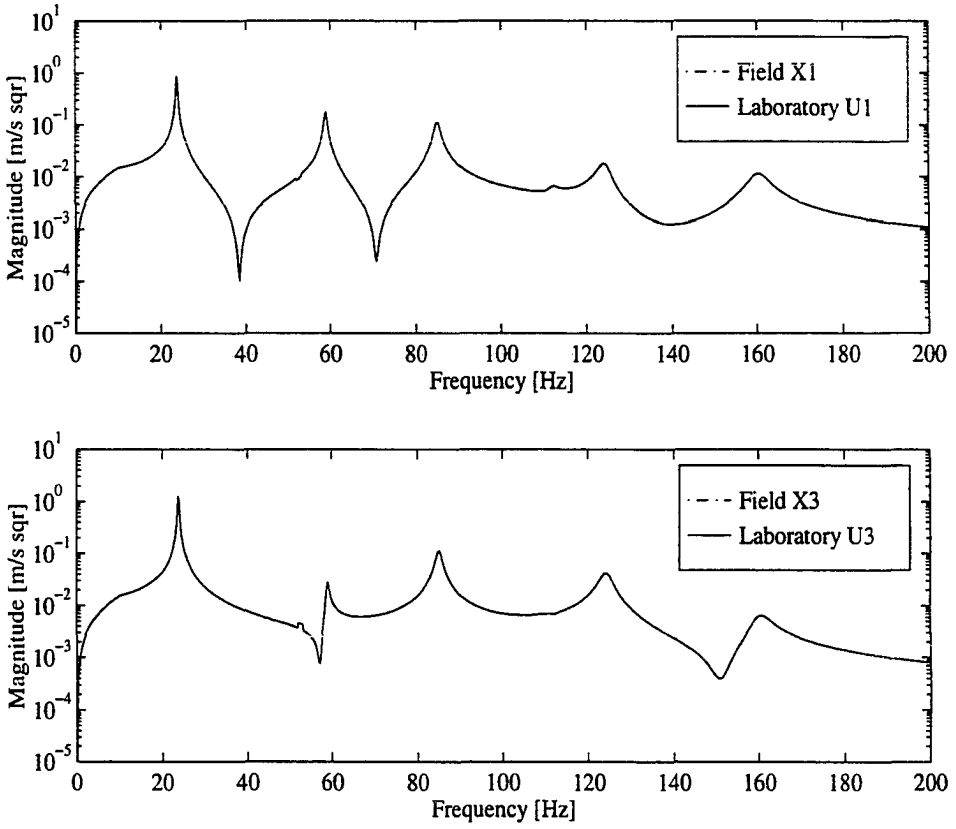

Figure 4.32 Test item interface accelerations obtained from N_t laboratory (interface and external) forces that were obtained from N_t field (interface and external) accelerations. The effects of the field external force F_4 are accounted for in the laboratory

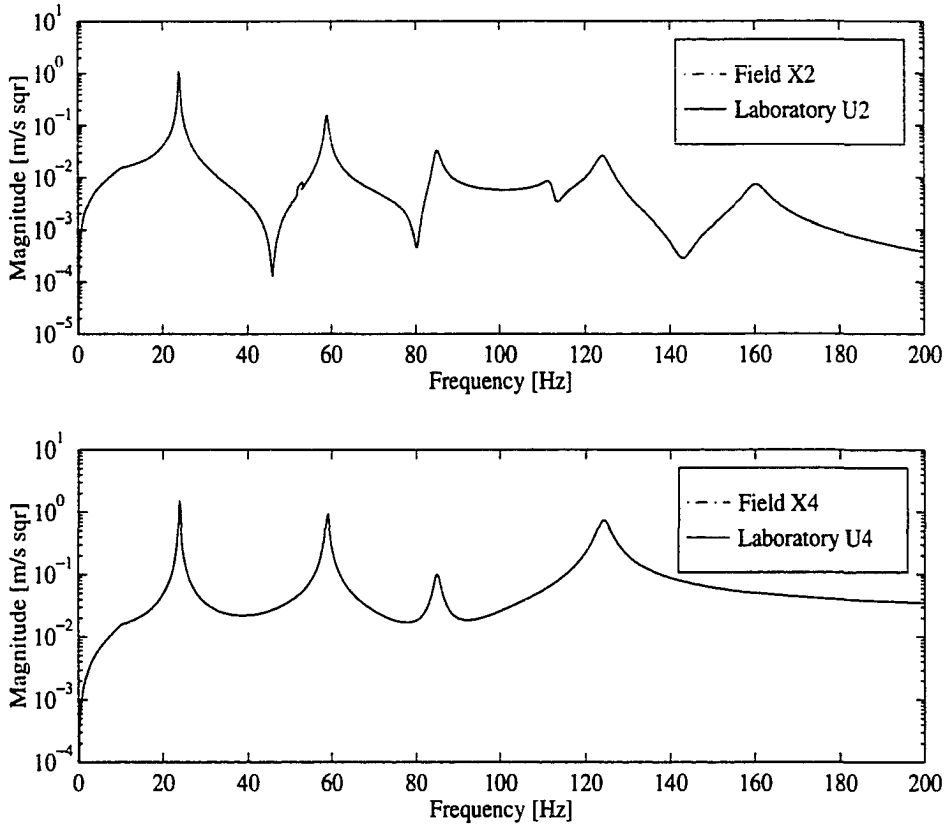

Figure 4.33 Test item external accelerations obtained from N_t laboratory (interface and external) forces that are obtained from N_t field (interface and external) accelerations. The effects of the field external force F_4 are accounted for in the laboratory

5 NUMERICAL SIMULATION CONSIDERATIONS FOR RANDOM EXCITATIONS

This chapter presents numerical results for the theoretical model presented in Chapter 3 in terms of random excitation and response signals The expressions for field interface forces and test item motions are re-derived for use with random signals. Field data is generated to be used in the laboratory simulations. The issue of correlated versus uncorrelated random signals are investigated in the laboratory simulations.

Theoretical Response Models for Random Excitations

Consider a N DOF linear structure with an acceleration FRF matrix that is denoted by $[H] = [H(\omega)]$ and is subjected to multiple random input forces. The structure input-output relationship can be expressed as [4]

$$[G_{xx}] = [H]^{*} \; [G_{ff}] \; [H]^{T} \tag{5.1}$$

where symbols "$*$" and "T" denote the complex conjugate and non conjugate transpose of the structure's FRF matrix, respectively. The N x N matrices $[G_{ff}]$ and $[G_{xx}]$ are the input and output spectral density matrices whose diagonal entries are the real valued input and output ASDs (Auto Spectral Densities) while the off-diagonal entries represent the complex valued input and output CSDs (Cross Spectral Densities), respectively. These matrices are obtained from the input and output frequency spectra

$\{F\} = \{F(\omega)\}$ and $\{X\} = \{X(\omega)\}$, according to [4] as

$$[G_{ff}] = \lim_{\tau \to \infty} \frac{2}{\tau} \epsilon \left(\{F\}^* \{F\}^T \right) \tag{5.2}$$

$$[G_{xx}] = \lim_{\tau \to \infty} \frac{2}{\tau} \epsilon \left(\{X\}^* \{X\}^T \right) \tag{5.3}$$

where τ is the analysis period and symbol "ϵ" denotes the "expected value" (in a statistical sense) of the product of vectors in Equations 5.2 and 5.3. The limit terms in Equations 5.2 and 5.3 are subsequently dropped in all equations developed for simplicity of notation.

Differentiation of interface DOF from external DOF leads to the alternative form of Equation 5.1

$$\begin{bmatrix} [G\boldsymbol{x}_{cc}] & [G\boldsymbol{x}_{ce}] \\ [G\boldsymbol{x}_{ec}] & [G\boldsymbol{x}_{ee}] \end{bmatrix} = \begin{bmatrix} [H_{cc}] & [H_{ce}] \\ [H_{ec}] & [H_{ee}] \end{bmatrix}^* \begin{bmatrix} [G\boldsymbol{f}_{cc}] & [G\boldsymbol{f}_{ce}] \\ [G\boldsymbol{f}_{ec}] & [G\boldsymbol{f}_{ee}] \end{bmatrix} \begin{bmatrix} [H_{cc}] & [H_{ce}] \\ [H_{ec}] & [H_{ee}] \end{bmatrix}^T \tag{5.4}$$

The subscripts "c" and "e" in Equation 5.4 denote connector and external points, respectively. Notice that $[H_{ce}] = [H_{ec}]^T$, but $[G\boldsymbol{f}_{ce}] = [G\boldsymbol{f}_{ec}]^H$ ($[G\boldsymbol{x}_{ce}] = [G\boldsymbol{x}_{ec}]^H$), where symbol ^{H} denotes the Hermitian (complex conjugate transpose) operator.

When the test item and vehicle are connected in the field, the interface forces frequency spectra are obtained by Equation 3.15 of Chapter 3 that is conveniently repeated here

$$\{F_c\} = [TV] \ (\{Y_c\}_e - \{X_c\}_e) \tag{5.5}$$

Application of the definitions expressed in Equations 5.2 and 5.3 to Equation 5.5 gives the following expression for the N_c x N_c *interface forces spectral density matrix* $[G\boldsymbol{f}_{cc}]$

$$[G\boldsymbol{f}_{cc}] = [TV]^* \ [\ [G\boldsymbol{y}_{cc}]_e + [G\boldsymbol{x}_{cc}]_e \ ] \ [TV] \tag{5.6}$$

The diagonal entries in $[G\boldsymbol{f}_{cc}]$ represent the interface force ASDs while the off-diagonal entries are the CSDs between interface points. The N_c x N_c matrices $[G\boldsymbol{y}_{cc}]_e$ and $[G\boldsymbol{x}_{cc}]_e$,

contain acceleration ASDs and CSDs that originated from the bare vehicle and test item interface motions, respectively. These matrices carry an extra subscript "e" since they represent contributions of external forces acting on the vehicle and test item structures. In obtaining Equation 5.6, first the complex conjugate of both sides of Equation 5.5 is post multiplied by the corresponding non conjugate transpose terms, as defined by Equations 5.2 and 5.3. When expected values are taken and the term $2/\tau$ is canceled in both sides, the left hand side of the resulting equation is the interface force spectral density matrix $[Gf_{cc}]$ while four terms appear on the right hand side of Equation 5.6. Terms $\{Y_c\}_e^*\ \{Y_c\}_e^T$ and $\{X_c\}_e^*\ \{X_c\}_e^T$ are the acceleration spectral density matrices shown on the right hand side of Equation 5.6. The two remaining terms, $\{Y_c\}_e^*\ \{X_c\}_e^T$ and $\{X_c\}_e^*\ \{Y_c\}_e^T$ are zero since *motions* $\{Y_c\}_e$ and $\{X_c\}_e$ *occur when vehicle and test item are not connected and thus they are uncorrelated.*

The test item interface and external acceleration frequency spectra are obtained in the field according to Equations 3.17 and 3.18 and are given by

$$\{X_c\} = [T_{cc}][TV]\ (\{Y_c\}_e - \{X_c\}_e) + \{X_c\}_e \tag{5.7}$$

$$\{X_e\} = [T_{ec}][TV]\ (\{Y_c\}_e - \{X_c\}_e) + \{X_e\}_e \tag{5.8}$$

where matrices $[T_{cc}]$ and $[T_{ce}] = [T_{ec}]^T$ contain the test item's interface and interface-external FRFs, respectively. The N_c x N_c matrix $[TV] = [[T_{cc}] + [V_{cc}]]^{-1}$ is the combined interface FRF matrix that was defined in Chapter 3.

Equations 5.7 and 5.8 can be converted to the random signal form by following the same procedure as was used to obtain Equation 5.6. This procedure gives the following results for the test item interface and external acceleration spectral density matrices

$$\begin{aligned}[G\boldsymbol{x}_{cc}] &= [T_{cc}]^*[TV]^*\ [\ [G\boldsymbol{y}_{cc}]_e + [G\boldsymbol{x}_{cc}]_e\ ]\ [TV][T_{cc}] \\ &- [T_{cc}]^*[TV]^*[G\boldsymbol{x}_{cc}]_e - [G\boldsymbol{x}_{cc}]_e[TV][T_{cc}] \\ &+ [G\boldsymbol{x}_{cc}]_e \end{aligned} \tag{5.9}$$

$$
\begin{aligned}
[G\boldsymbol{x}_{ee}] &= [T_{ec}]^{*}[TV]^{*}\ [\ [G\boldsymbol{y}_{cc}]_e + [G\boldsymbol{x}_{cc}]_e\ ]\ [TV][T_{ce}] \\
&- [T_{ec}]^{*}[TV]^{*}[G\boldsymbol{x}_{ce}]_e - [G\boldsymbol{x}_{ec}]_e[TV][T_{ce}] \\
&+ [G\boldsymbol{x}_{ee}]_e
\end{aligned}
\tag{5.10}
$$

Two new spectral density matrices, $[G\boldsymbol{x}_{ce}]_e = [G\boldsymbol{x}_{ec}]_e^H$ and $[G\boldsymbol{x}_{ee}]_e$ appear in Equation 5.10. The N_c x N_e matrix $[G\boldsymbol{x}_{ce}]_e$ contains CSDs relating the N_c interface and N_e external points while the N_e x N_e matrix $[G\boldsymbol{x}_{ee}]_e$ contains ASDs and CSDs relating external points only. Both matrices are originated from test item motions that are caused by field external forces *only*. Symbol "^{T}" was dropped from matrices $[TV]$ and $[T_{cc}]$ in Equations 5.6, 5.9, and 5.10 since they are symmetric matrices. In addition, the identity $[T_{ec}]^T = [T_{ce}]$ was used on the right hand side of Equation 5.10.

The results obtained in Equations 5.9 and 5.10 correspond to the N_c x N_c and N_e x N_e matrices $[G\boldsymbol{x}_{cc}]$ and $[G\boldsymbol{x}_{ee}]$ that appear on the left hand side of Equation 5.4, respectively. The remaining N_c x N_e acceleration spectral density matrix $[G\boldsymbol{x}_{ce}] = [G\boldsymbol{x}_{ec}]^H$ shown in Equation 5.4 is obtained by the same procedure used in Equations 5.9 and 5.10. Substitution of $\{X_{cc}\}^*$ obtained from Equation 5.7 and $\{X_{ee}\}^T$ given by Equation 5.8 on the right hand side of Equation 5.3 leads to the following result for the N_c x N_e CSD matrix $[G\boldsymbol{x}_{ce}]$

$$
\begin{aligned}
[G\boldsymbol{x}_{ce}] &= [T_{cc}]^{*}[TV]^{*}\ [\ [G\boldsymbol{y}_{cc}]_e + [G\boldsymbol{x}_{cc}]_e\ ]\ [TV][T_{ce}] \\
&- [T_{cc}]^{*}[TV]^{*}[G\boldsymbol{x}_{ce}]_e - [G\boldsymbol{x}_{cc}]_e[TV][T_{ce}] \\
&+ [G\boldsymbol{x}_{ce}]_e
\end{aligned}
\tag{5.11}
$$

In the previous chapter it was shown that the pseudo-inverse technique (Equations 4.14 and 4.15) was successfully employed to calculate the forces acting on the test item in the field from deterministic (real and imaginary) accelerations.

When dealing with random signals, Equation 5.1 is used in order to solve for the unknown input spectral matrix $[G_{ff}]$ based on the measured output spectral density

matrix $[G_{xx}]$. This equation is rewritten in terms of the test item field acceleration and force spectral density matrices

$$[G_{xx}] = [T]^* \; [G_{ff}] \; [T]^T \tag{5.12}$$

When both left and right hand sides of Equation 5.12 are multiplied by $[[T]^*]^+$ and $[[T]^T]^+$, the following result is obtained for the unknown input spectral density matrix

$$[G_{ff}] = [\; [T]^+ \;]^* \; [G_{xx}] \; [\; [T]^+ \;]^T \tag{5.13}$$

The resulting matrices on the left hand side of Equations 5.12 and 5.13 contain the test item acceleration and force ASDs and CSDs, respectively. These two expressions contain the correct phase relationships among the variables since the complex CSDs are accounted for in both cases. Thus, proper correlation between the corresponding time variables is accounted for when employing Equation 5.12 to obtain the acceleration spectral matrix or Equation 5.13 to solve the inverse problem for the unknown force spectral density matrix. Consequently, Equations 5.12 and 5.13 are called the *correlated* expressions for acceleration and force spectral density matrices.

A commonly accepted assumption that is used to simplify Equations 5.12 and 5.13 is to assume that the input random forces acting on the structure are statistically uncorrelated [18, 19, 49]. By this assumption, the CSDs are zero and Equation 5.12 reduces to

$$\{G_{xx}\} = [|T|^2] \; \{G_{ff}\} \tag{5.14}$$

where $\{G_{ff}\}$ and $\{G_{xx}\}$ are real valued vectors containing the input and output ASDs, respectively. Thus, Equation 5.14 shows that, under the assumption of *uncorrelated* input forces, the resulting accelerations are equally *uncorrelated* and Equation 5.14 does not provide any phase information since only output ASDs are available. Using the pseudo-inverse technique with Equation 5.14 the following result is obtained for the

unknown input force ASDs vector

$$\{G_{ff}\} = [|T|^2]^+ \{G_{xx}\} \tag{5.15}$$

A comparison of Equations 5.12 and 5.14 for the acceleration spectral density matrices as well as of Equations 5.13 and 5.15 for the solution of the inverse problem clearly shows the differences in neglecting the CSDs in both Equations 5.14 and 5.15. There is no phase information in Equations 5.14 and 5.15 so that no *correlation* exists between the time variables. Hence, these equations will be subsequently referred to as the *uncorrelated* expressions for acceleration and force spectral density matrices.

In order to further clarify this point, consider a test item being subjected to two random forces with frequency spectra respectively given by F_1 and F_2. The corresponding test item acceleration responses X_1 and X_2 can be written in terms of the test item driving and transfer point accelerances and they are respectively given by

$$X_1 = T_{11}F_1 + T_{12}F_2 \tag{5.16}$$

$$X_2 = T_{21}F_1 + T_{22}F_2 \tag{5.17}$$

Now, assume that the random forces F_1 and F_2 are statistically *uncorrelated*, i.e, $Gf_{12} = 0$. Substitution of X_1 and X_2 as given by Equations 5.16 and 5.17 into Equation 5.3 and accounting for the fact that $Gf_{12} = 0$, gives the following result for the acceleration CSD between points 1 and 2

$$Gx_{12} = T_{11}^* T_{21}\ Gf_{11} + T_{12}^* T_{22}\ Gf_{22} \tag{5.18}$$

where Gf_{11} and Gf_{22} are the input force ASDs and T_{pq}, $p, q = 1...2$ represent the test item accelerance FRFs. Thus, since Gf_{11} and Gf_{22} *are not* zero since the forces correlate with themselves, the resulting acceleration CSD Gx_{12} *is not* zero as well. Thus, there is correlation between motions at 1 and 2 independent of the input forces being either *correlated* or *uncorrelated.*

Field Simulations

The lumped parameter models used in Chapter 3 and shown here in Figure 5.1 will be used in the numerical simulations using random excitations. The test item's and vehicle's physical and modal parameters shown in Tables 4.1 and 4.2 will be used again. The accelerance and transmissibility FRF models will be generated from Equations 4.2 and 4.3, respectively. Two field simulations are performed in order to generate data for the laboratory simulations: the bare vehicle and the combined structure simulations.

Definition of the Vehicle and Test Item Field Excitations

Two excitation sources are simultaneously applied to the combined structure, as seen in Figure 5.1. The first excitation source is a base acceleration ASD Gy_{22} as shown in Figure 5.2 that is applied to the vehicle base mass M_2. This spectrum increases with a slope of 40 $dB/decade$ from 0 to 10 Hz and becomes constant at 0.00517 g^2/Hz up to 200 Hz. This amplitude level is chosen such that an overall 1.0 g_{RMS} input acceleration vibration level is obtained for the $0 - 200$ Hz frequency range. A total of 800 spectral lines is used in these simulations so that the frequency resolution is $\Delta f = 0.25$ Hz.
The second excitation source is the external force ASD Gf_{44} shown in Figure 5.2 that is applied to the test item mass M_4. Note that these two inputs are uncorrelated.

Field Simulation 1: The Bare Vehicle Interface Accelerations

When the test item is absent from the field, the input base motion ASD Gy_{22} represents the only external input to the vehicle in the model shown in Figure 5.1. Thus, the bare vehicle interface acceleration spectral density matrix $[Gy_{cc}]_e$ can be calculated by using the following expression

$$[Gy_{cc}]_e = [: \Gamma_{pq} :]^* \, [Gy_{qq}] \, [: \Gamma_{pq} :]^T \tag{5.19}$$

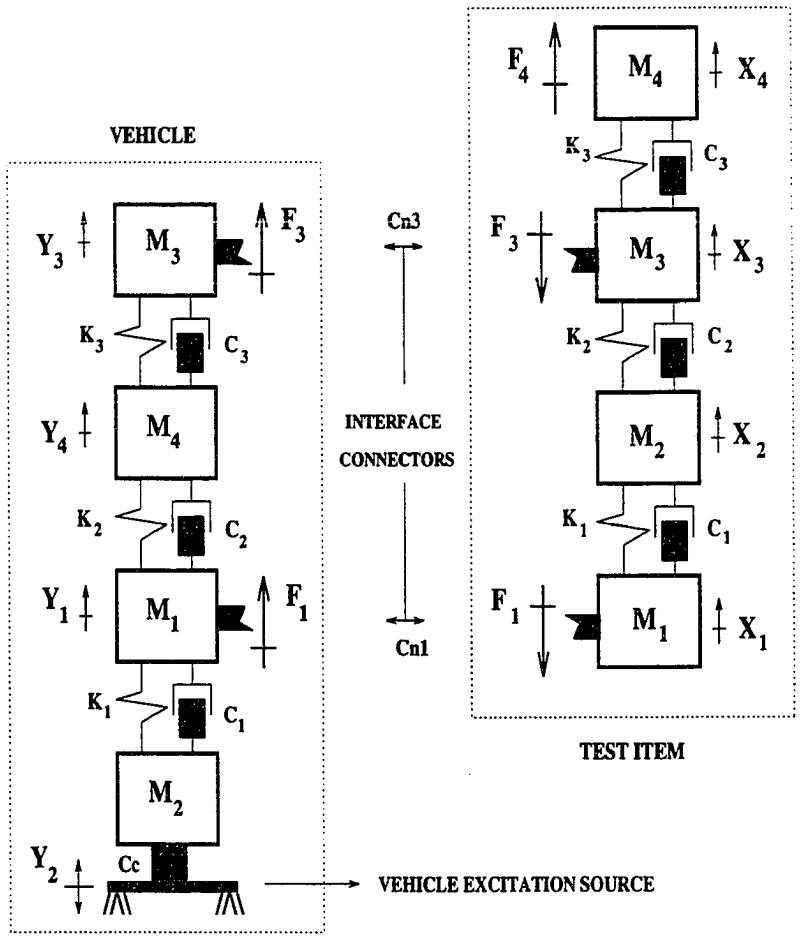

Figure 5.1 Test item attached to vehicle by connectors Cn_1 and Cn_3 in the field environment. External inputs to the combined structure given in terms of the base input acceleration ASD Gy_{22} that is applied at the vehicle's base mass M_2 and the external force ASD Gf_{44} that is applied to the test item mass M_4

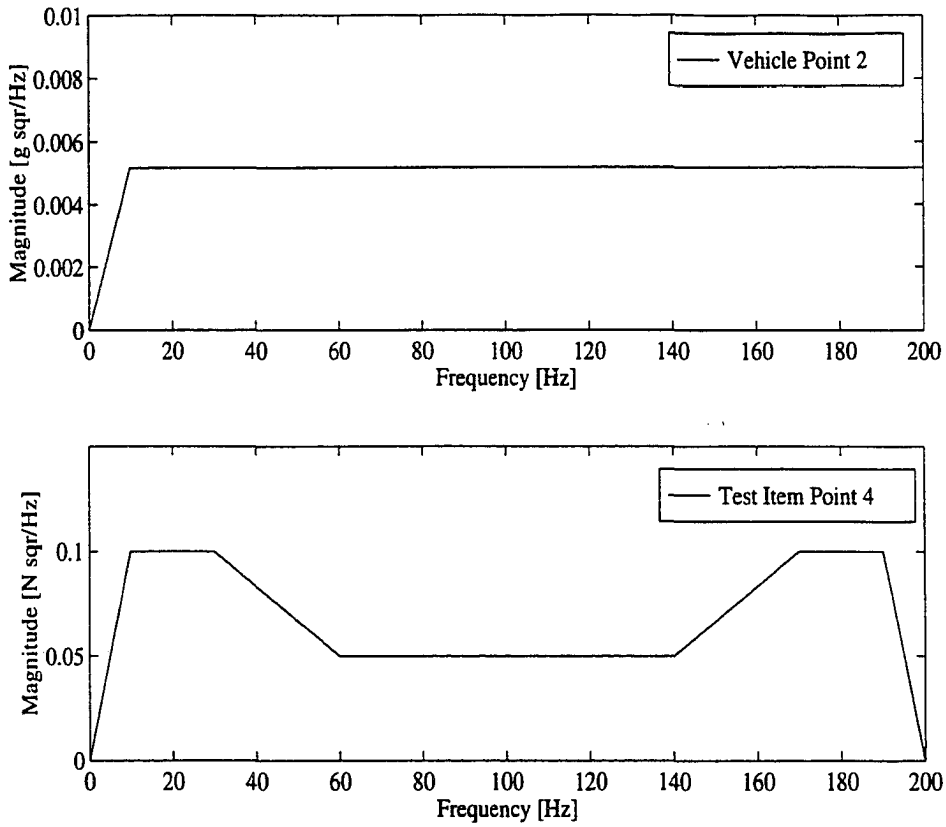

Figure 5.2 Input base acceleration ASD Gy_{22} and input force ASD Gf_{44} that are simultaneously applied to the vehicle's base mass M_2 and test item mass M_4, respectively. Top: Gy_{22}; Bottom: Gf_{44}

where index $p = 1, ..., N_c$ covers all interface points, and $q = 2$ in the case of Figure 5.1 is a fixed coordinate where the input motion Gy_{22} is applied. Matrix [: Γ_{pq} :] is a N_c x N_c matrix whose q^{th} column contains the acceleration transmissibility FRFs as defined by Equation 4.3, and all remaining entries are zero. The N_c x N_c diagonal matrix $[Gy_{qq}]$ contains zeros at all diagonal entries except at (2,2) where the input base motion Gy_{22} is applied. The diagonal elements of the resulting spectral density matrix $[Gy_{cc}]_e$ correspond to the bare vehicle interface acceleration ASDs while the off-diagonal entries are the CSDs among the vehicle interface points. The resulting bare vehicle interface accelerations ASDs Gy_{11} and Gy_{33} due to the input acceleration ASD Gy_{22}

are shown in Figure 5.3. Figure 5.4 shows the magnitude and phase of the bare vehicle acceleration CSD between coordinate points 1 and 3.

Field Simulation 2: The Combined Structure Forces and Accelerations

In this field simulation, the test item is connected to the vehicle in the field forming a combined structure and both inputs from Figure 5.2 are active.

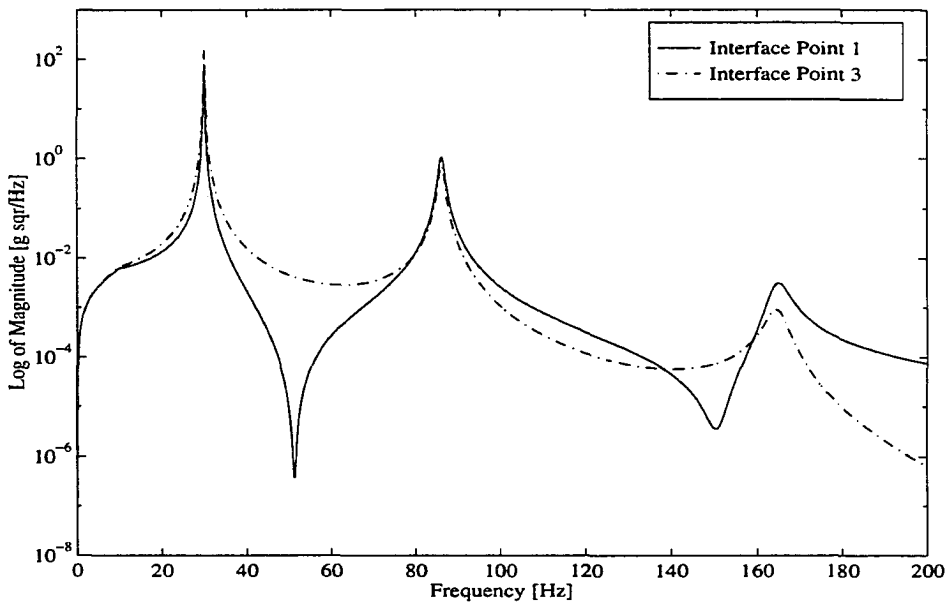

Figure 5.3 The bare vehicle acceleration ASDs representing the vehicle's response to the input acceleration ASD Gy_{22} in the absence of the test item

The N_t x N_t test item output response spectral density matrix $[Gx]_e$ due to this external random input is required in the determination of field interface forces and test item field accelerations. This acceleration spectral density matrix is calculated by Equation 5.4 for all of the N_t test item points. In this case, the input spectral density matrix $[Gf]_e$ is a N_t x N_t matrix with zeros at all entries, except at position (4,4) where Gf_{44} is used. The test item accelerance FRFs used with Equation 5.4 are those

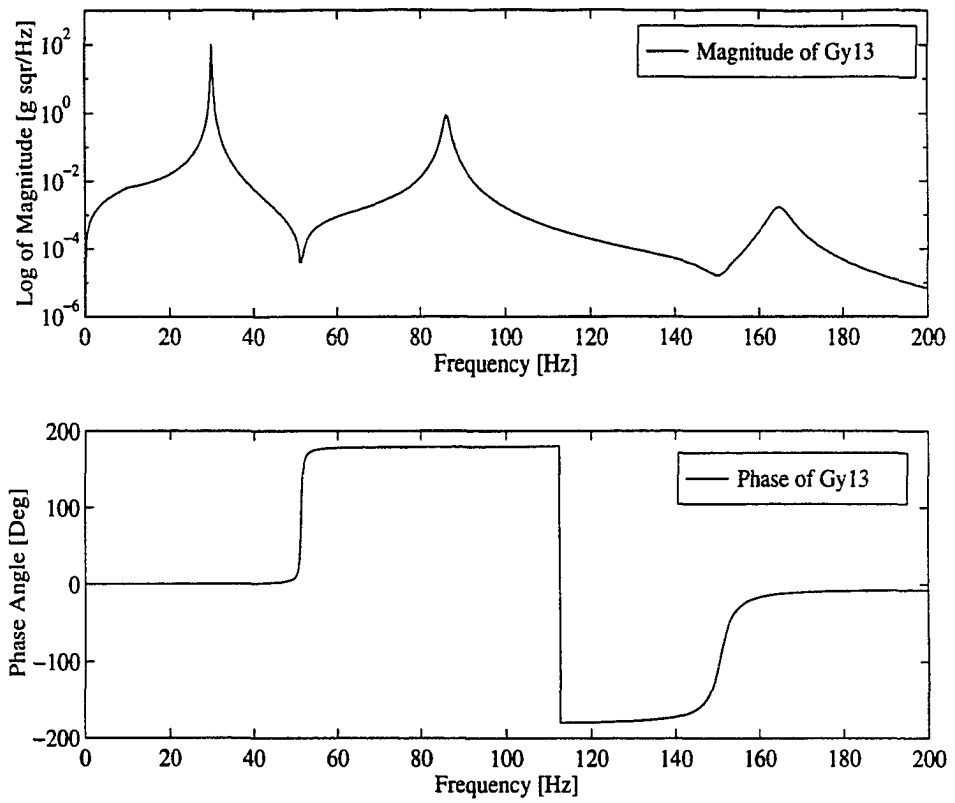

Figure 5.4 Magnitude and phase of the bare vehicle interface acceleration CSD Gy_{13} between coordinate points 1 and 3 due to the input acceleration ASD Gy_{22} in the absence of the test item

that correspond to the test item being modeled as a free structure in space since $[G\boldsymbol{x}]_e$ corresponds to the test item response due to external loads only. The test item interface and external acceleration ASDs due to Gf_{44} are shown in Figure 5.5.

The field interface force spectral density matrix is calculated from Equation 5.6 and the force ASDs are displayed in Figure 5.6 while the force CSD between interface points 1 and 3 is shown in Figure 5.7 along with the corresponding exact values for comparison. These exact values were obtained by using the same procedure employed in Chapter 4. A good magnitude fit is observed for all frequencies with only small discrepancies occurring for frequencies around 160 Hz. An inversion of the predicted phase angle Gf_{13}

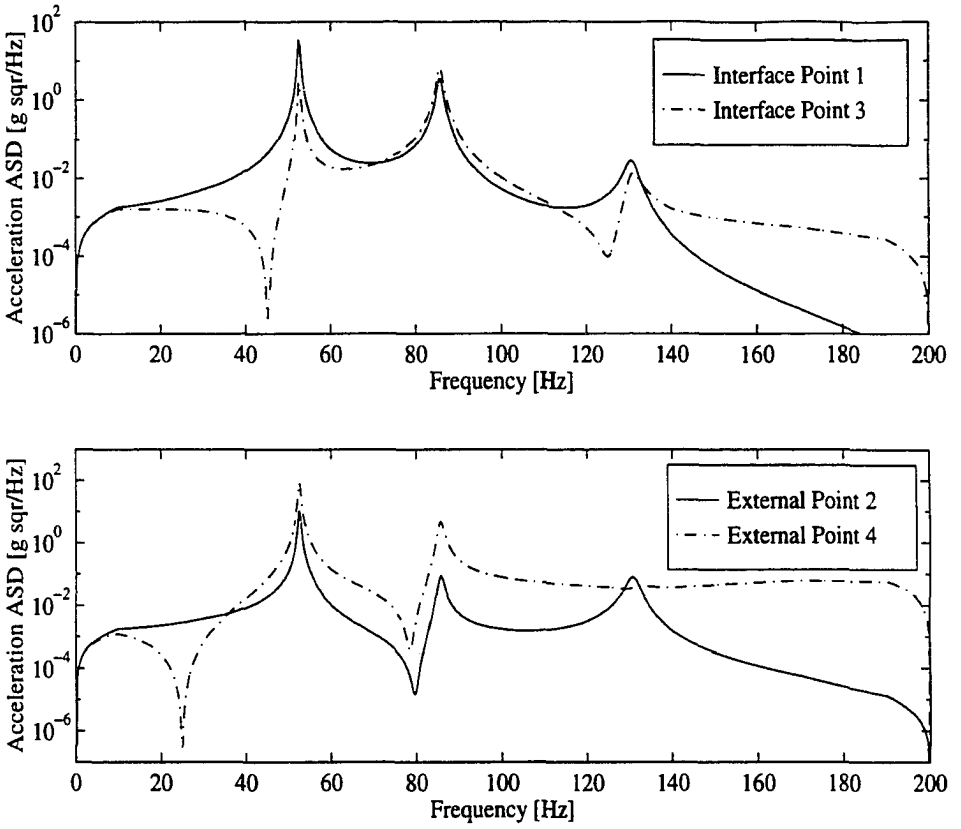

Figure 5.5 Test item interface and external acceleration ASDs due to external forces. Test item as a free structure in space and subjected to external force ASD Gf_{44} applied to M_4

in Figure 5.7 is seen to occur in the $160 - 200$ Hz frequency range.

The test item motions are calculated according to Equations 5.9, 5.10, and 5.11. The test item interface and external acceleration ASDs are shown in Figures 5.8 and 5.9, and they are seen to agree closely when compared with the exact values. Small discrepancies occur in the predicted $G\boldsymbol{x}_{22}$ for frequencies in the vicinity of 142 Hz and 160 Hz, and in $G\boldsymbol{x}_{11}$ and $G\boldsymbol{x}_{33}$ for frequencies in the vicinity of 160 Hz. The ASD and CSD for the field conditions form the basis for judging a given laboratory simulation.

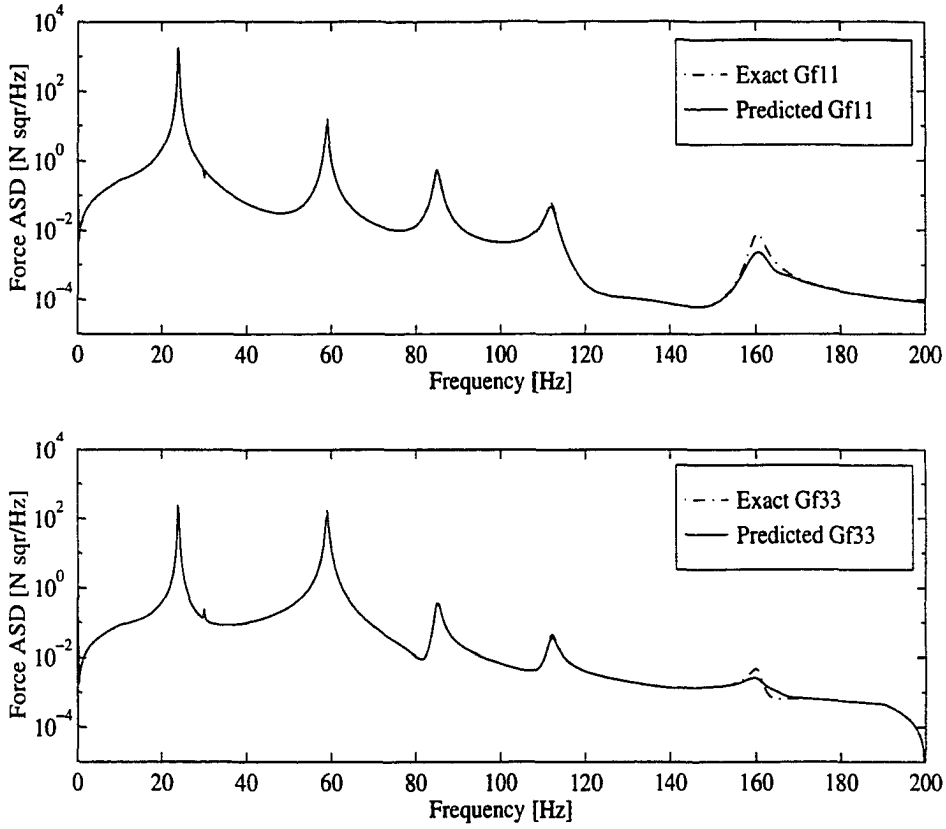

Figure 5.6 Field interface forces ASDs Gf_{11} and Gf_{33} obtained from the analysis of the combined structure and due to field input acceleration ASD $Gy_{2?}$ and input force ASD Gf_{44}

Laboratory Simulations Using Input Forces Obtained from the Bare Vehicle Interface Accelerations

This simulation corresponds to the first test scenario described in Chapter 3. In this case, the bare vehicle interface acceleration ASDs and CSD are used with Equations 5.13 and 5.15 in order to calculate a set of test item inputs in the laboratory. First, the *correlated* and *uncorrelated* Equations 5.13 and 5.15 are rewritten as a function of the bare vehicle data and the resulting expressions are

$$[Gr_{cc}] = [\ [T]^{+}\ ]^{*}\ [Gy_{cc}]_{e}\ [\ [T]^{+}\ ]^{T} \tag{5.20}$$

$$\{Gr_{cc}\} = [|T|^{2}]^{+}\ \{Gy_{cc}\}_{e} \tag{5.21}$$

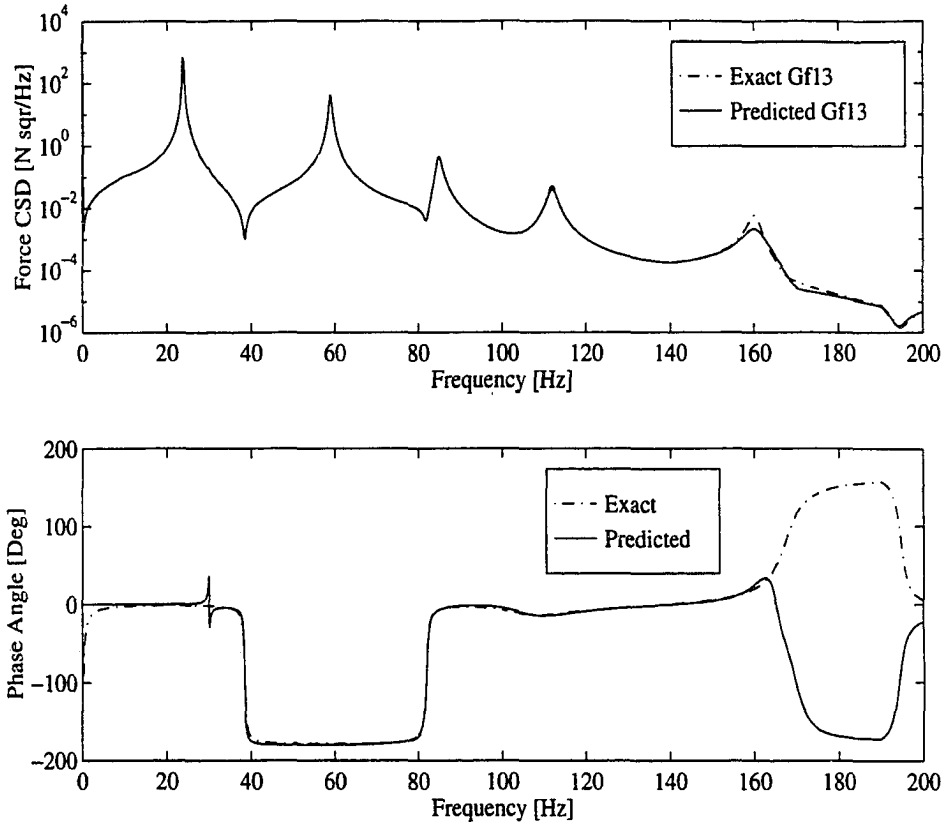

Figure 5.7 Field interface force CSD Gf_{13} between interface points 1 and 3 obtained from the analysis of the combined structure and due to the field input acceleration ASD Gy_{22} and input force ASD Gf_{44}

where the test item is assumed to have the same accelerance FRF characteristics in both the field and laboratory environments. Equation 5.20 employs the bare vehicle interface acceleration ASDs and CSD while only ASDs are used with Equation 5.21. Thus, Equation 5.20 represents the case where bare vehicle motions are assumed to be *correlated* while Equation 5.21 uses the assumption of *uncorrelated* motions.

Similarly, the test item laboratory acceleration spectral density matrix is obtained from Equation 5.1 that is rewritten as

$$[Gu] = [T]^* \ [Gr_{cc}] \ [T]^T \tag{5.22}$$

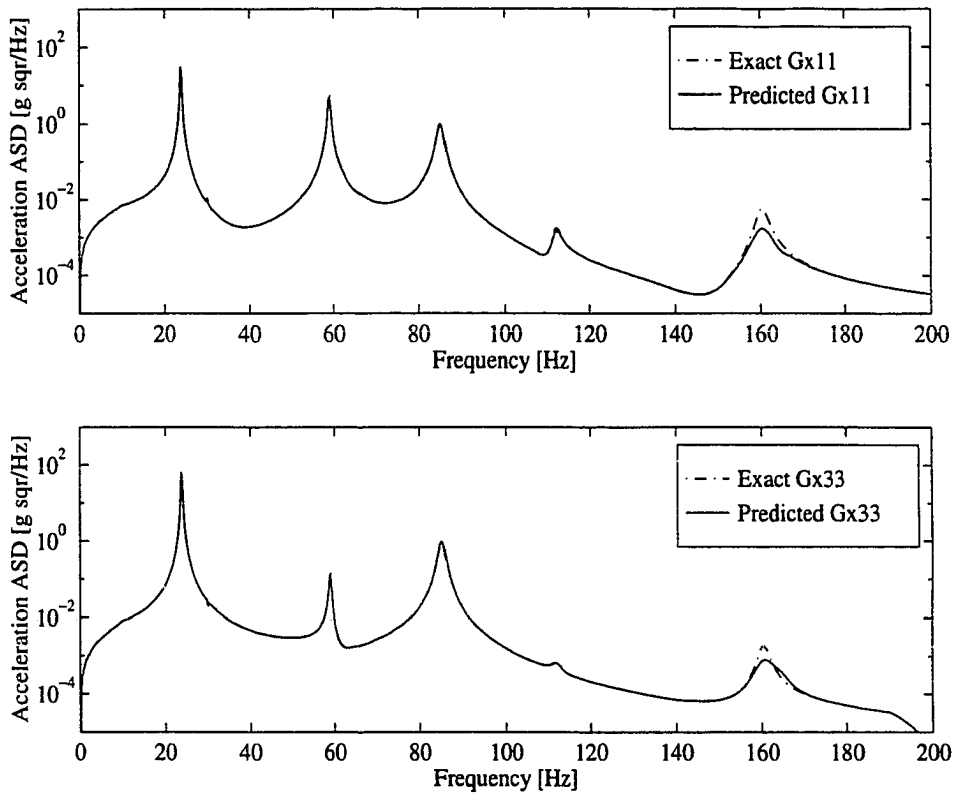

Figure 5.8 Test item field interface acceleration ASDs Gx_{11} and Gx_{33} obtained from the analysis of the combined structure and due to the input acceleration ASD Gy_{22} and input force ASD Gf_{44}

where the N_t x N_t matrix $[Gu]$ is the test item acceleration spectral density matrix in the laboratory, and the N_c x N_c matrix $[Gr_{cc}]$ is fully populated with interface force spectral densities when the *correlated* form of Equation 5.20 is used or is populated with elements of the N_c x 1 vector $\{Gr_{cc}\}$ on the main diagonal entries and zeros elsewhere when the *uncorrelated* Equation 5.21 is employed. Figures 5.10 and 5.11 show the resulting test item interface and external acceleration ASDs, respectively, that are determined from Equation 5.22 for $[Gr_{cc}]$ obtained from either Equation 5.20 and Equation 5.21. The test item field acceleration ASDs are plotted for comparison purposes.

It is evident in Figures 5.10 and 5.11 that there is more similarity between the field

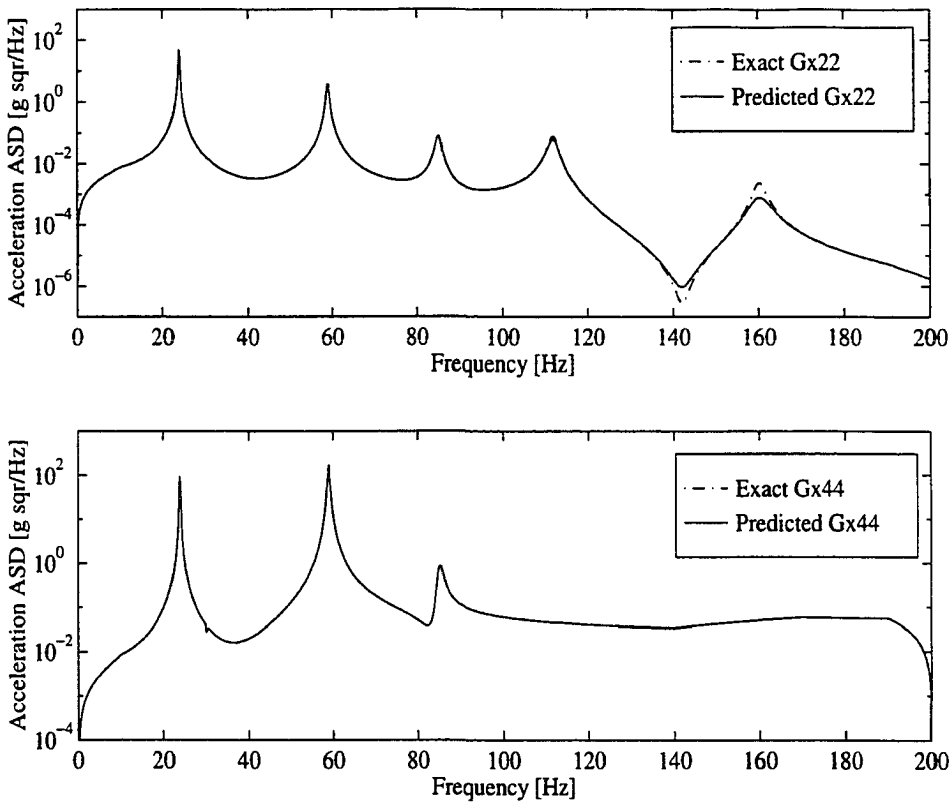

Figure 5.9 Test item field external acceleration ASDs $G\boldsymbol{x}_{22}$ and $G\boldsymbol{x}_{44}$ obtained from the analysis of the combined structure and due to the input acceleration ASD $G\boldsymbol{y}_{22}$ and input force ASD Gf_{44}

data and the results from the *correlated* inputs than there is between the field data and the *uncorrelated* inputs. The *uncorrelated* ASD results are much larger in error and represent the poorest estimates. It is clear that neither method was really successful for three reasons. *First*, it was attempted to reproduce the field data by applying forces at the test item interface points only, when in reality, the actual field environment was subjected to both test item interface forces F_1 and F_3 as well as the external force F_4 being applied to mass M_4. *Second*, the bare vehicle interface motions do not contain any information regarding coupling effects between test item and vehicle since the test item is absent when field data is obtained. *Third*, the bare vehicle interface motion

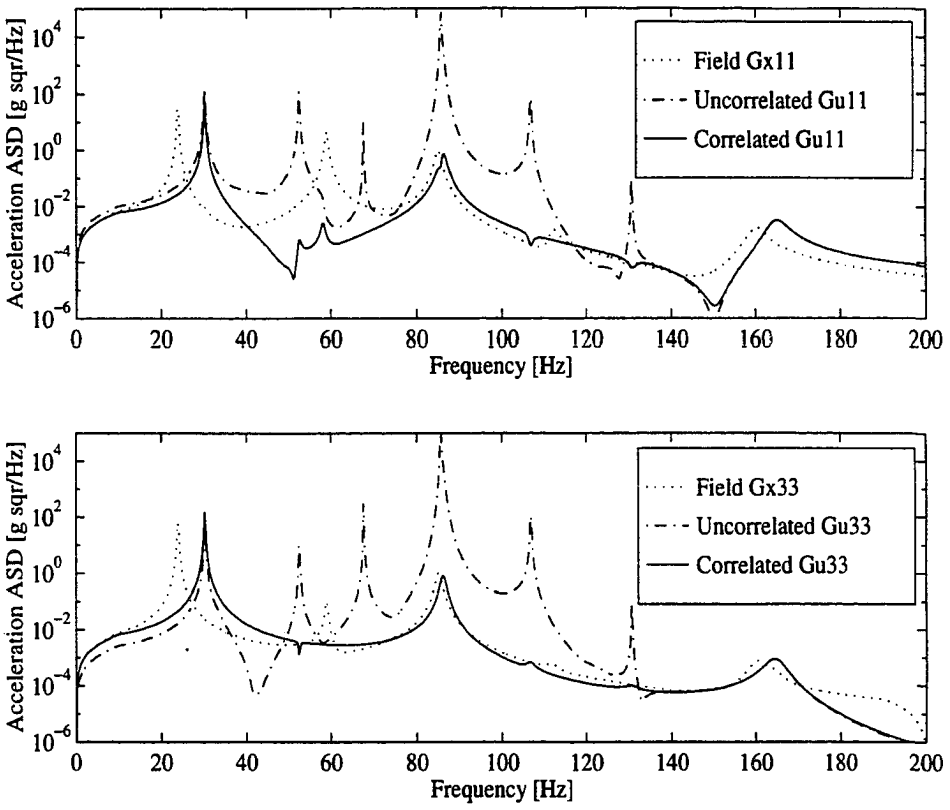

Figure 5.10 Test item laboratory interface acceleration ASDs Gu_{11} and Gu_{33} resulting from test item input interface forces that obtained from the bare vehicle interface acceleration ASDs. The effects of the external field input force Gf_{44} are not accounted for in the laboratory

shows none of the effects of the external force ASD Gf_{44}. Thus, as it was the case for deterministic signals in the previous chapter, it is concluded that the use of the bare vehicle interface acceleration data alone is inadequate for predicting how the test item will behave under field conditions unless corrections are made to take interface driving point and transfer FRFs of test item and vehicle into account.

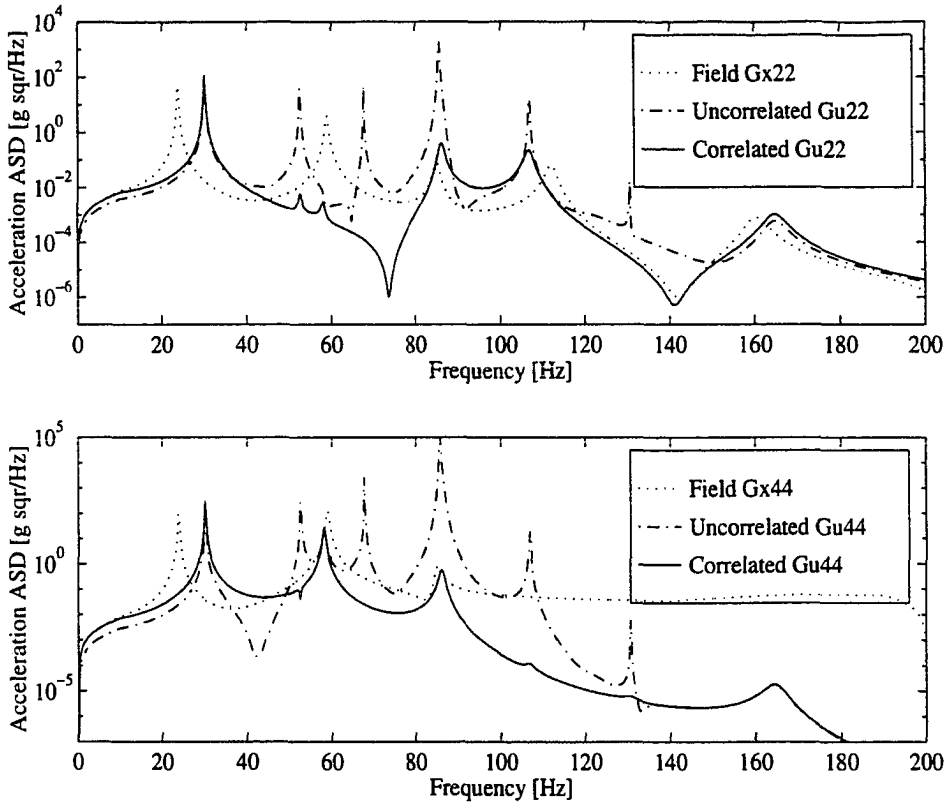

Figure 5.11 Test item laboratory external acceleration ASDs Gu_{22} and Gu_{44} resulting from test item input interface forces obtained from the bare vehicle interface acceleration ASDs. The effects of the external field input force Gf_{44} are not accounted for

Laboratory Simulations Using Field Interface Forces as Test Item Inputs

This simulation corresponds to the second test scenario described in Chapter 3. Two cases are analyzed when using field interface force as test item inputs in the laboratory. *First*, the interface forces spectral density matrix obtained from Equation 5.6 and shown in Figures 5.6 and 5.7 is applied to the test item interface points in the laboratory. These interface forces were obtained when the external random input ASD Gf_{44} shown in Figure 5.2 is applied to the test item in the field.

Second, the test item external input ASD Gf_{44} is removed from the field environment

and the interface force spectral density matrix is recalculated by Equation 5.6. The new interface force spectral density matrix is used to drive the test item in the laboratory.

These two test scenarios are used to check the accuracy of the predicted test item motions when external random forces are either present and absent from the field environment. In both cases, Equation 5.1 is rewritten as

$$[G_{\ddot{u}}] = [T]^* \ [G_{r_{cc}}] \ [T]^T \tag{5.23}$$

where $[G_{r_{cc}}] = [G_{f_{cc}}]$ represents the N_c x N_c interface force spectral density matrix obtained through Equation 5.6.

If *uncorrelated* field interface forces are assumed, Equation 5.14 is written as

$$\{G_{\ddot{u}}\} = [|T|^2] \ \{G_{r_{cc}}\} \tag{5.24}$$

where $\{G_{r_{cc}}\}$ contains the interface forces ASDs from matrix $[G_{f_{cc}}]$.

The results of the first simulation are shown in Figures 5.12 and 5.13 for interface and external laboratory acceleration ASDs, respectively. Incorrect test item motions are obtained when either the *correlated* Equation 5.23 or the *uncorrelated* Equation 5.24 are used. This is due to the fact that while in the field environment, the test item is subjected to an external force F_4 in addition to interface forces F_1 and F_3, and this external force is not accounted for in the laboratory simulation.

The results of the second laboratory simulation employing interface forces as inputs to the test item are shown in Figures 5.14 and 5.15. In this case, the external input ASD $G_{f_{44}}$ is removed from test item mass M_4 while in the field environment. Thus, the test item is subjected to interface forces *only*. The new interface forces spectral density matrix is obtained by using Equation 5.6, with $[G_{\ddot{x}_{cc}}]_e = 0$.

Also, the test item acceleration spectral density matrices given by Equations 5.9, 5.10, and 5.11 are simplified, since all matrices involving the test item accelerations ASDs and CSDs due to external forces are zero. Thus, field interface forces and test

item acceleration spectral density matrices depend only on the bare vehicle interface acceleration data $[Gy_{cc}]_e$ in the absence of field external forces applied to the test item. Similar results were obtained in the preceding chapter for deterministic signals. The test item acceleration ASDs that are obtained from the *correlated* Equation 5.23 are shown in Figures 5.14 and 5.15 and are seen to closely match the corresponding field ASDs. Small discrepancies are observed at some frequencies. Generally, the ASDs that are obtained from the *uncorrelated* Equation 5.24, which do not include CSDs, do not agree with the field data in this case.

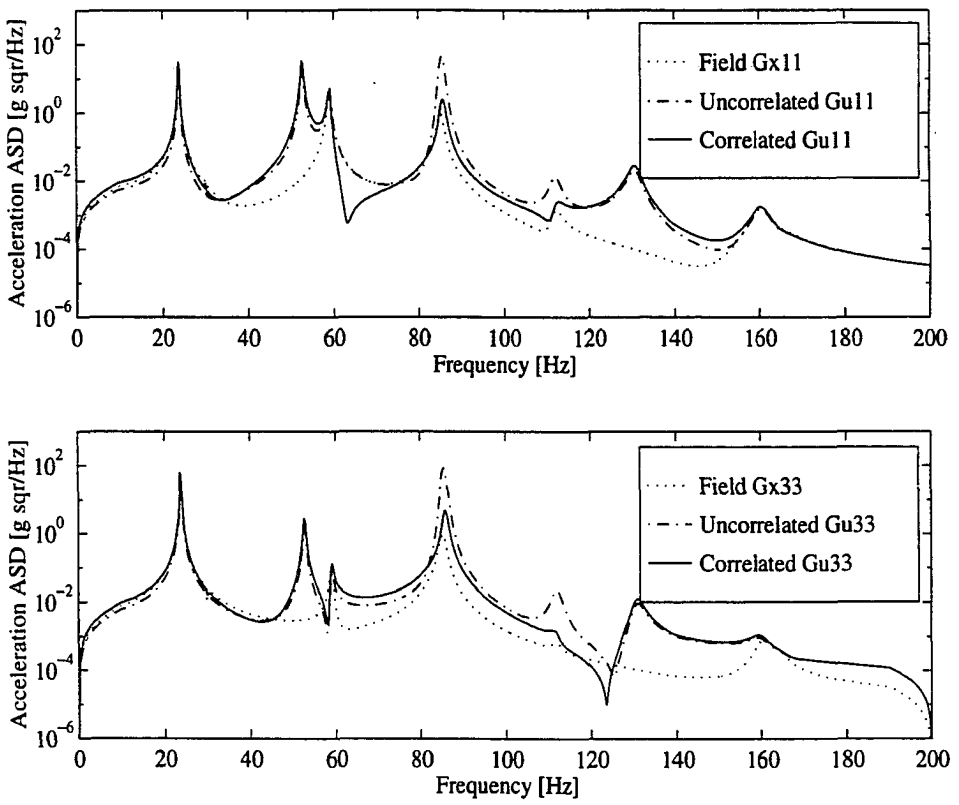

Figure 5.12 Test item laboratory interface acceleration ASDs resulting from using field interface force ASDs Gf_{11} and Gf_{33} as test item inputs. No field external forces effects accounted for even though Gf_{44} is present in the field environment

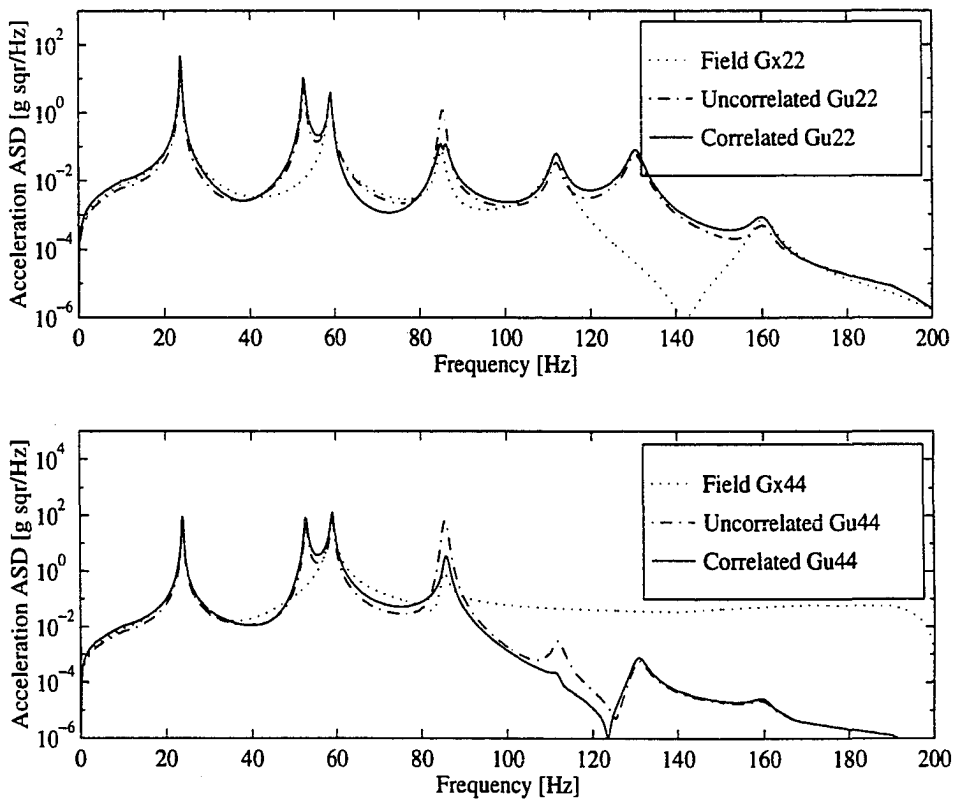

Figure 5.13 Test item laboratory external acceleration ASDs resulting from using field interface force ASDs Gf_{11} and Gf_{33} as test item laboratory inputs. No field external forces effects accounted for even though Gf_{44} is present in the field environment

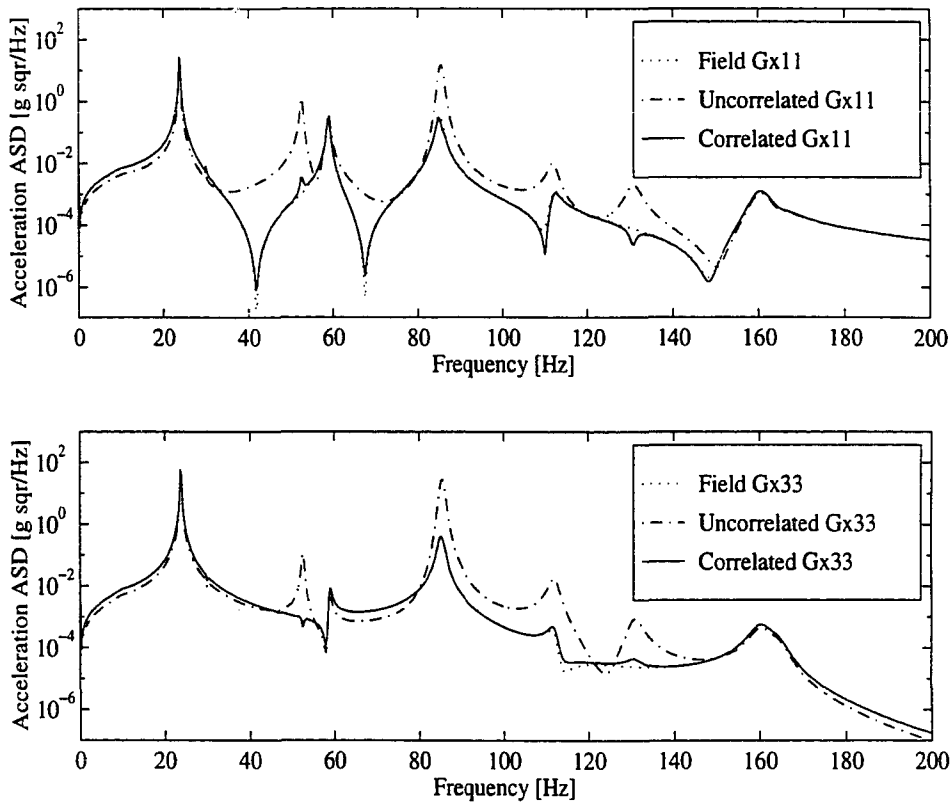

Figure 5.14 Test item laboratory interface acceleration ASDs resulting from using field interface force ASDs Gf_{11} and Gf_{33} as test item inputs. External force ASD Gf_{44} is removed from the field data

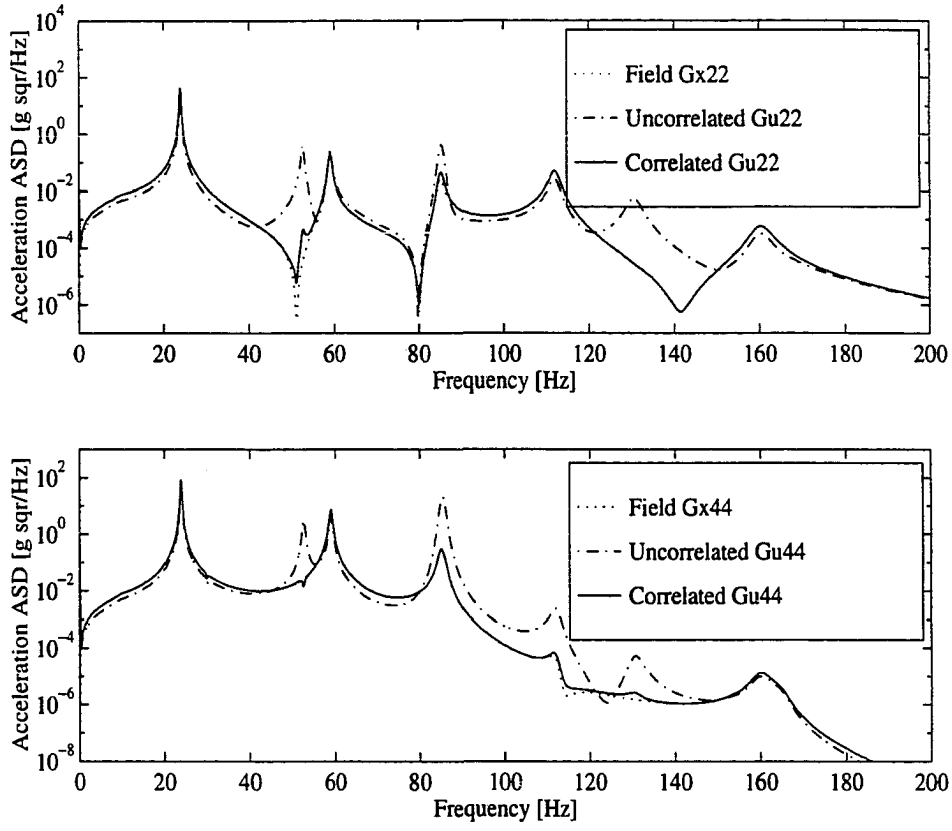

Figure 5.15 Test item laboratory external acceleration ASDs resulting from using field interface force ASDs Gf_{11} and Gf_{33} as test item laboratory inputs. External force ASD Gf_{44} is removed from the field data

Laboratory Simulations Using Inputs Obtained From Field Acceleration ASDs and CSDs

This laboratory simulation corresponds to the third and fourth test scenarios described in Chapter 3. When using the test item field accelerations to define the laboratory input forces by the pseudo-inverse technique [10, 13, 18], a natural question that arises is: Which measured accelerations should I use, and how do the predicted input forces compare with the true forces occurring in the field ? Since field data is divided in terms of interface and external forces and accelerations, the same possibilities studied in Chapter 4 will be investigated for the case of random signals. They are as follows:

- N_c interface forces are obtained from N_c interface motions.
- N_c interface forces are obtained from all N_t measured field motions.
- N_t forces are obtained from N_t motions.

These cases will be illustrated in the case of random signals for both, *uncorrelated* and *correlated* inputs and outputs.

Simulations with N_c Interface Forces Obtained from N_c Field Interface Accelerations and $F_4 \neq 0$

In this case, only field interface motions are used to solve for interface forces in the laboratory environment. Thus, Equations 5.13 and 5.15 are rewritten as

$$[G\boldsymbol{r}_{cc}] = [\ [T_{cc}]^{+}\ ]^{*}\ [G\boldsymbol{x}_{cc}]\ [\ [T_{cc}]^{+}\ ]^{T} \tag{5.25}$$

$$\{G\boldsymbol{r}_{cc}\} = [|T_{cc}|^{2}]^{+}\ \{G\boldsymbol{x}_{cc}\} \tag{5.26}$$

and since the test item item interface accelerance FRF N_c x N_c matrix $[T_{cc}]$ is square, the pseudo-inversion shown in Equations 5.25 and 5.26 reduces to the standard inverse.

The test item output response to this set of forces is obtained through Equations 5.23 and 5.24, for the case of *correlated* and *uncorrelated* inputs, respectively.

The force prediction results for this simulation are shown in Figure 5.16 in terms of the interface forces ASDs calculated through Equations 5.25 and 5.26. In this case, the *correlated* Equation 5.25 gave a good estimate for Gr_{11} when compared with the true interface force from the field but a poor estimate for Gr_{33}. The interface forces ASDs obtained from the *uncorrelated* Equation 5.26 produced significantly incorrect estimates for both Gr_{11} and Gr_{33}.

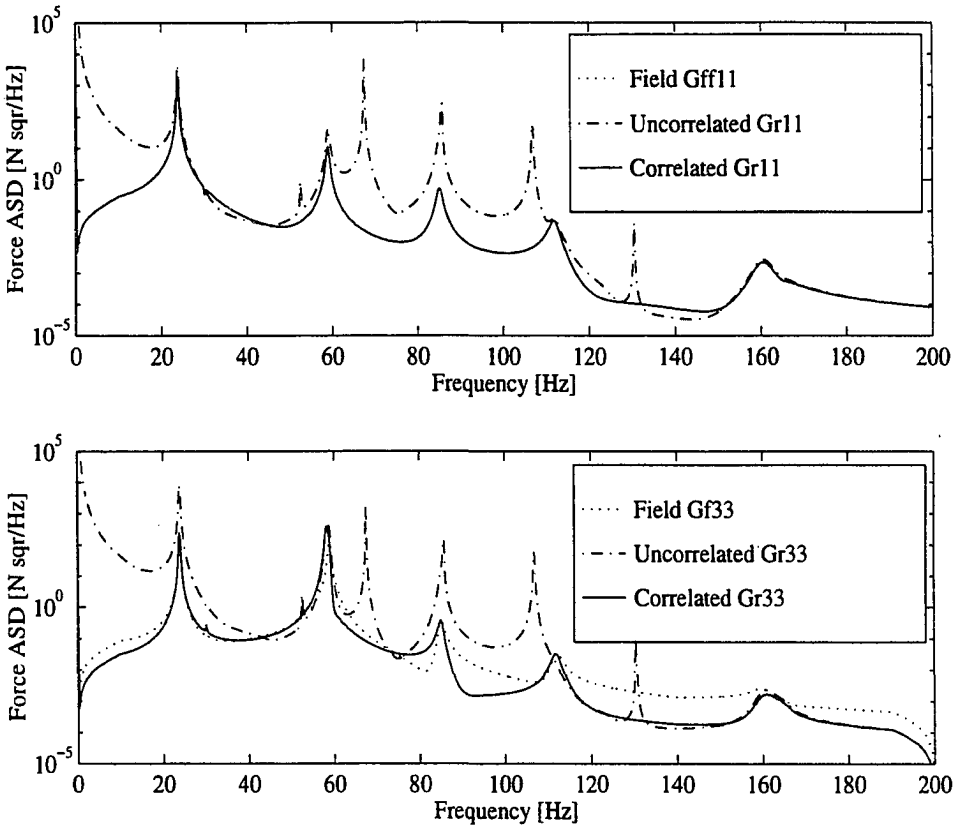

Figure 5.16 Interface force ASDs Gr_{11} and Gr_{33} predicted from N_c field interface accelerations for both the *correlated* and *uncorrelated* equations when Gf_{44} is applied in the field environment

The results for the test item acceleration ASDs are shown in Figures 5.17 and 5.18. The interface ASDs shown in Figures 5.17 match the corresponding field measurements for the case of *correlated* inputs. The external ASD Gu_{22} is seen to match the field measurement as well. This result is expected since mass M_2 is located between M_1 and M_3 which have correct motions and there is no external force applied to M_2. Thus, if the interface accelerations motions Gu_{11} and Gu_{33} are correct in the laboratory environment, then Gu_{22} should match the field Gx_{22}. The external acceleration ASD estimate $Gu44$ that is based on *correlated* inputs is seen to be seriously in error at higher frequencies. This error is due to the force Gf_{44} that is directly applied to M_4 in the field but is unaccounted for in this simulation. In all cases, the laboratory estimates based on ASD field information without using CSD for both interface forces (Figure 5.16) and test item acceleration ASDs (Figures 5.17 and 5.18) are seriously in error. It is noted that the use of *correlated* inputs caused the interface force inputs to be adjusted so that the correct interface acceleration occurred at locations 1 and 3. Acceleration of mass M_2 is correct since the only forces acting on M_2 in this case are those due to the motions of masses M_1 and M_3. Similarly, the motion of M_4 is incorrect since an unaccounted for external force is acting on mass M_4. Thus, the motion of M_2 is isolated from the external force applied to M_4 by the distorted interface force acting on M_3.

This laboratory simulation employing only interface motions to obtain the test item input forces fails due to the fact that the external effects caused by F_4 are not accounted for. In the absence of external forces, the procedure of generating N_c interface forces from N_c interface accelerations could result in correct laboratory predictions as long as the *correlated* relationship of Equation 5.25 is used. However, this simulation case should be viewed with caution since the pseudo-inversion of the test item interface FRF matrix in Equation 5.25 reduces to the standard inversion. This occurs since the number of motions is the same as the number of input forces that are predicted. In this case, the inversion of $[T_{cc}]$ can cause numerical problems due to rank deficiency at some frequen-

cies [10, 11]. In these cases, the solution for the input forces must be obtained in least squares sense where more motions are used than forces predicted [18]. This procedure not only improves the numerical stability of the pseudo-inversion process but also helps to reduce experimental noise effects when dealing with actual data.

Simulations Using N_c Interface Forces Obtained form N_t Field Accelerations and $F_4 \neq 0$

In this simulation, N_c interface forces are calculated from all N_t field motions. Equations 5.25 and 5.26 are rewritten as

$$[G\boldsymbol{r}_{cc}] = [[[[T_{cc}][T_{ce}]]^T]^+]^* \; [G\boldsymbol{x}] \; [[[[T_{cc}][T_{ce}]]^T]^+]^T \tag{5.27}$$

$$\{G\boldsymbol{r}_{cc}\} = [|[[T_{cc}][T_{ce}]]^T|^2]^+ \; \{G\boldsymbol{x}\} \tag{5.28}$$

where the N_t x N_t matrix $[G\boldsymbol{x}]$ contains all measured accelerations in the field. The results for the interface force ASDs calculated from the *correlated* (Equation 5.27) and *uncorrelated* (Equation 5.28) relationships are shown in Figure 5.19. Both the correlated and uncorrelated results do not match the corresponding field interface force ASDs.

The test item output accelerations for *correlated* and *uncorrelated* inputs are obtained through Equations 5.23 and 5.24, respectively with the results being shown in Figure 5.20 for interface acceleration ASDs and in Figure 5.21 for external acceleration ASDs. In this case, both the *correlated* and the *uncorrelated* estimates present surprisingly good agreement when compared one to another, but both results deviate from the true field measurement. The assumption of *uncorrelated* inputs does not appear to be totally inadequate in this case. However, the fact that the test item is subjected to interface forces only in the laboratory while in the field both interface and external forces exist is the cause for the incorrect laboratory simulation results.

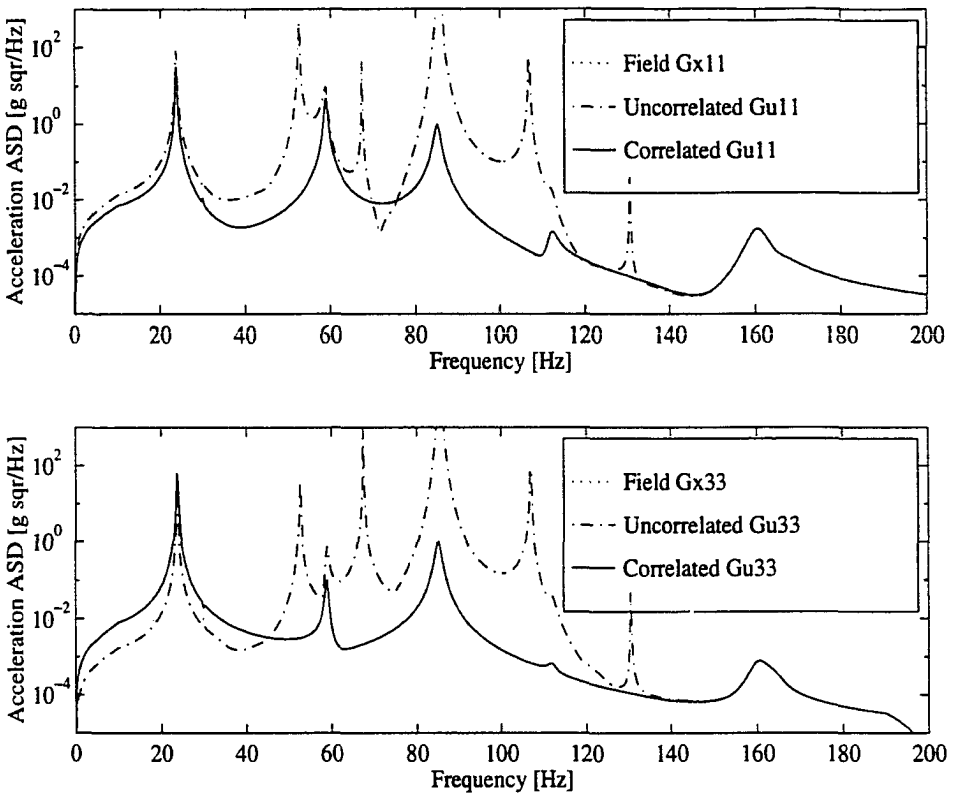

Figure 5.17 Test item laboratory interface acceleration ASDs resulting from using laboratory interface force ASDs Gr_{11} and Gr_{33} obtained from N_c field interface accelerations. External force ASD Gf_{44} is not accounted for even though it is present in the field environment

Simulations Using N_t Forces Obtained from N_t Field Accelerations and $F_4 \neq 0$

This laboratory simulation corresponds to determining N_t forces from N_t measurements. Thus, in addition to calculating interface forces, possible external forces acting on test item external points where motion measurements were taken are identified. In this case, the *correlated* (Equation 5.13) and the *uncorrelated* (Equation 5.15) relationships are used with the full N_t x N_t test item accelerance FRF matrix. The full N_t x N_t

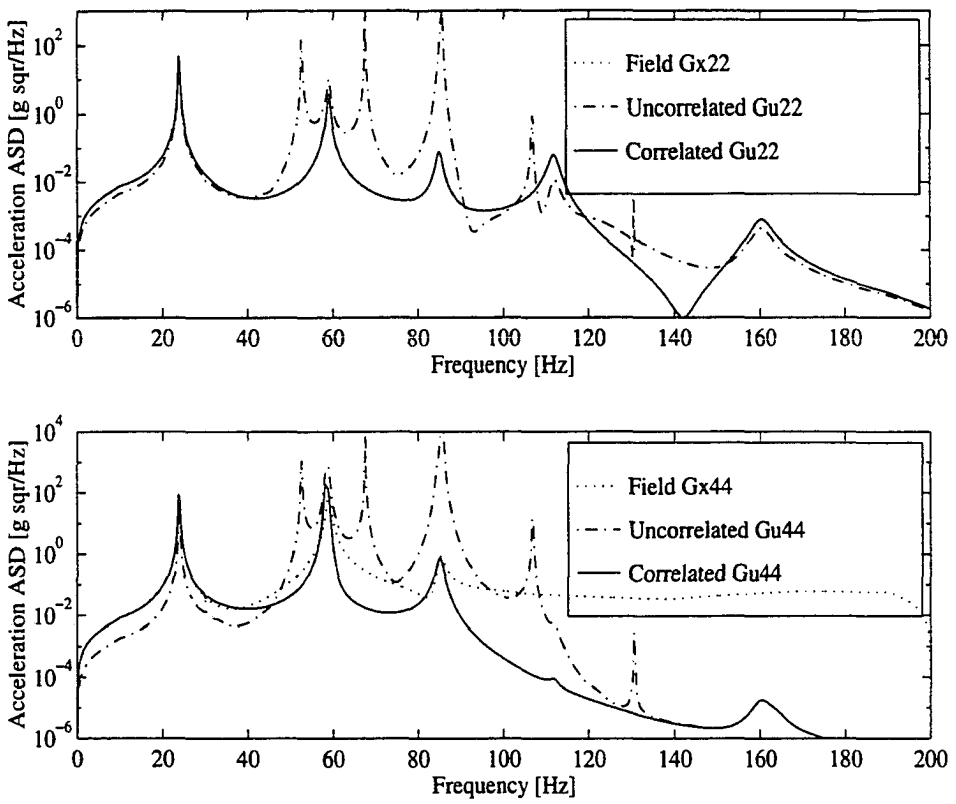

Figure 5.18 Test item laboratory external acceleration ASDs resulting from using laboratory interface force ASDs Gr_{11} and Gr_{33} obtained from N_c field interface accelerations. External force ASD Gf_{44} is not accounted for even though it is present in the field environment

output spectral density matrix is used with Equation 5.13 while only the output ASD functions are used in Equation 5.15. The results for the predicted forces are shown in Figures 5.22 and 5.23. Figure 5.22 shows the interface forces ASDs. In this case, the results when CSDs are accounted for (*correlated outputs*) match the corresponding field measurements.

The results from the *uncorrelated* Equation 5.15 are not in agreement with the field measurements in the $0 - 50$ Hz frequency range but the agreement is considerably improved in the remaining $50 - 200$ Hz frequency range. The results for the external

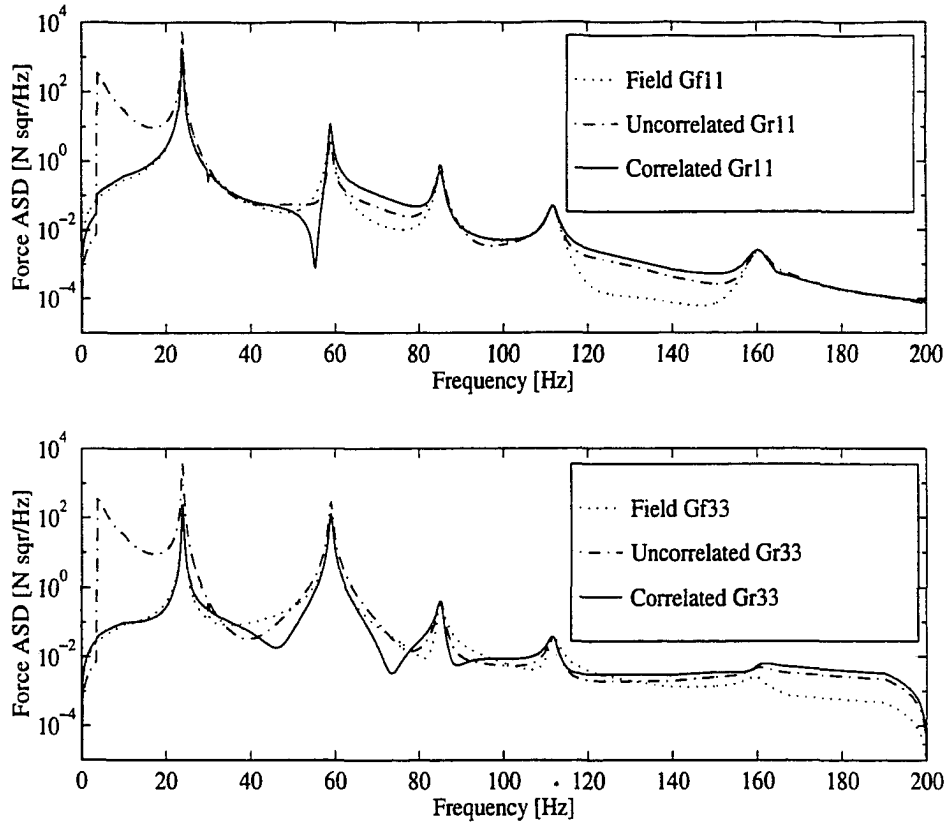

Figure 5.19 Interface force ASDs Gr_{11} and Gr_{33} predicted from N_t field interface accelerations for both the *correlated* and *uncorrelated* equations

force F_4 applied to the test item in the field is shown in Figure 5.23. In this case, the result for correlated inputs match the corresponding Gf_{44} (see Figure 5.23 for a plot of the estimated Gf_{44} in linear scale) while the result for uncorrelated inputs do not present a good agreement in the $0-120$ Hz frequency range, but improves in the $120-200$ Hz range.

The test item output spectral density N_t x N_t matrix $[\boldsymbol{Gu}]$ is obtained by using the corresponding interface and external force ASDs in Equation 5.23 and the resulting acceleration ASDs are shown in Figures 5.24 and 5.25. In this case, all field acceleration ASDs are matched in the laboratory. This is due to the fact that the external force

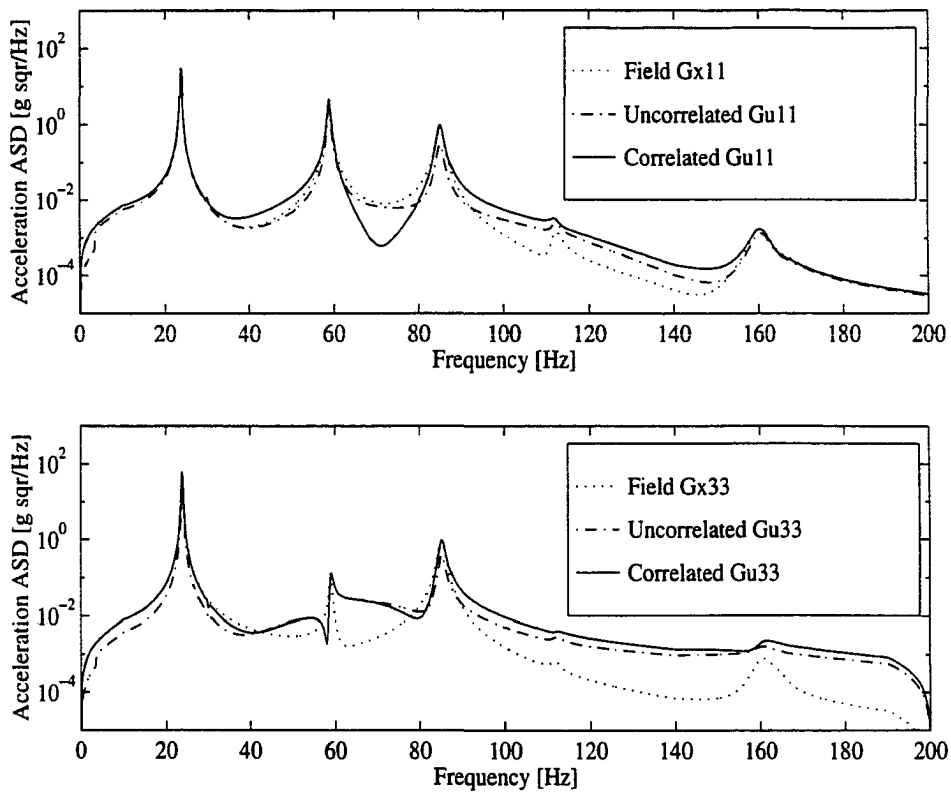

Figure 5.20 Test item laboratory interface acceleration ASDs resulting from using laboratory interface force ASDs Gr_{11} and Gr_{33} obtained from N_t field interface accelerations. External force ASD Gf_{44} is not accounted for even though it is present in the field environment

effects from Gf_{44} were accounted for in the laboratory. It is interesting to notice that, although the predicted *uncorrelated* input ASDs did not yield good results along the entire $0 - 200$ Hz range in Figures 5.22 and 5.23, the resulting test item accelerations ASDs matched closely with the field measurements. However, it should be recalled that when assuming *uncorrelated* inputs, Equations 5.15 and 5.22 are used to obtain the forces and resulting acceleration ASDs, respectively, and no information about the force and acceleration CSDs are obtained when the assumption of uncorrelated inputs is used. Although not shown here, the resulting force and acceleration CSDs match the

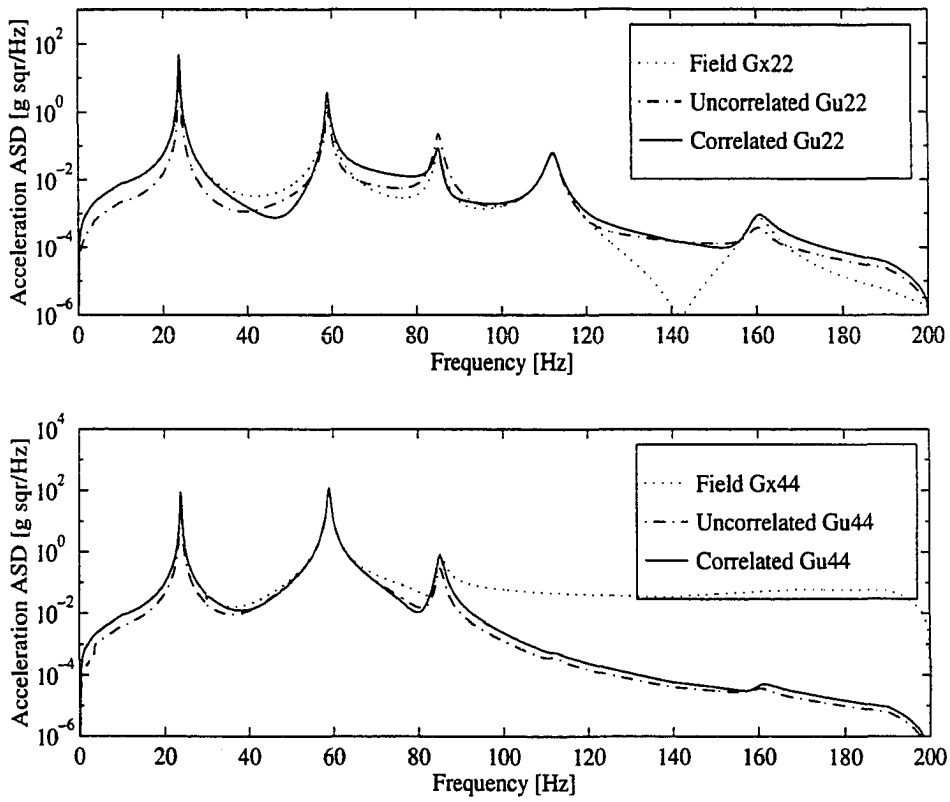

Figure 5.21 Test item laboratory external acceleration ASDs resulting from using laboratory interface force ASDs Gr_{11} and Gr_{33} obtained from N_t field interface accelerations. External force ASD Gf_{44} is not accounted for even though it is present in the field environment

corresponding field measurements.

This last simulation case represents a good example of the difficulties involved in obtaining the correct test item excitation forces from knowledge of accelerations when using the pseudo-inverse technique. The *uncorrelated* predicted interface and external force ASDs do not match the actual forces experienced by the test item in the field as shown in Figures 5.22 and 5.23. However, when this set of predicted forces are applied to the test item, the exact field accelerations are reproduced in the laboratory. The solution for the laboratory forces was reduced to the standard inversion of the N_t x N_t

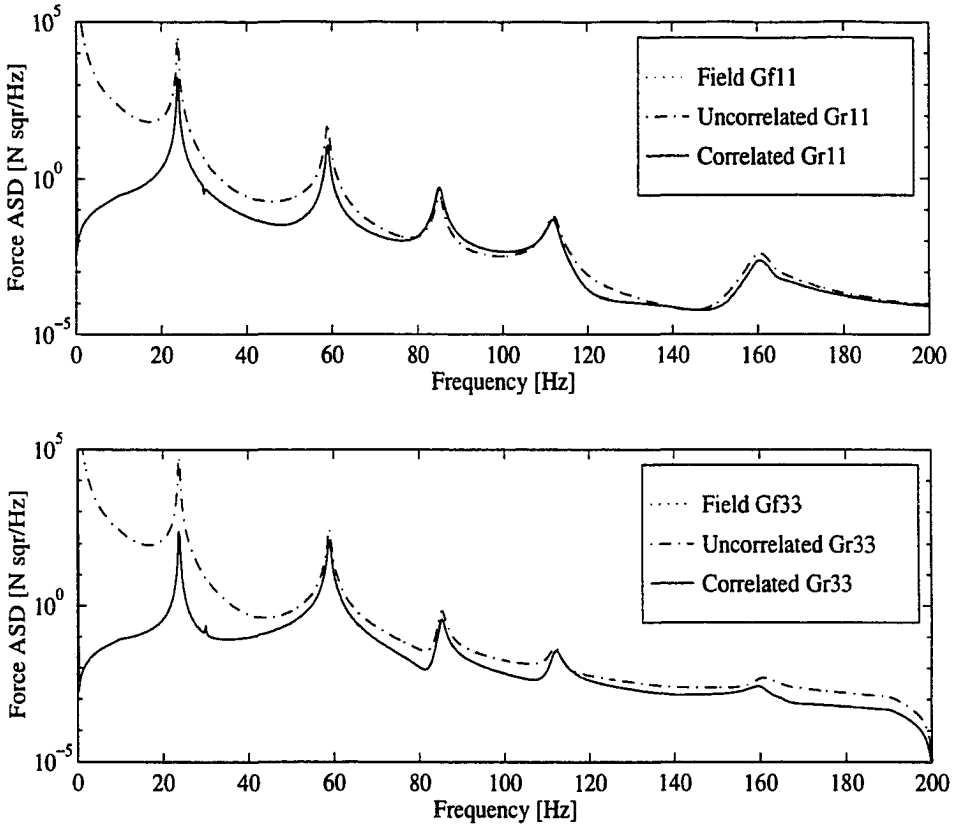

Figure 5.22 Interface force ASDs Gr_{11} and Gr_{33} obtained when N_t forces are predicted from N_t accelerations

test item FRF matrix since the number of motions and the number of forces are the same. Thus, it appears that FRF matrix rank deficiency problems occurred in employing Equation 5.15. These numerical difficulties caused distortions on the predicted set of forces but, when these *pseudo-forces* were applied to the test item, the correct motions were obtained. This is a classical example of a *non unique* set of forces that produced the correct motions and it reinforces the idea that by *over-determining* Equations 5.13 and 5.15 (more motions than forces), a *unique* set of forces can be obtained in a least squares sense.

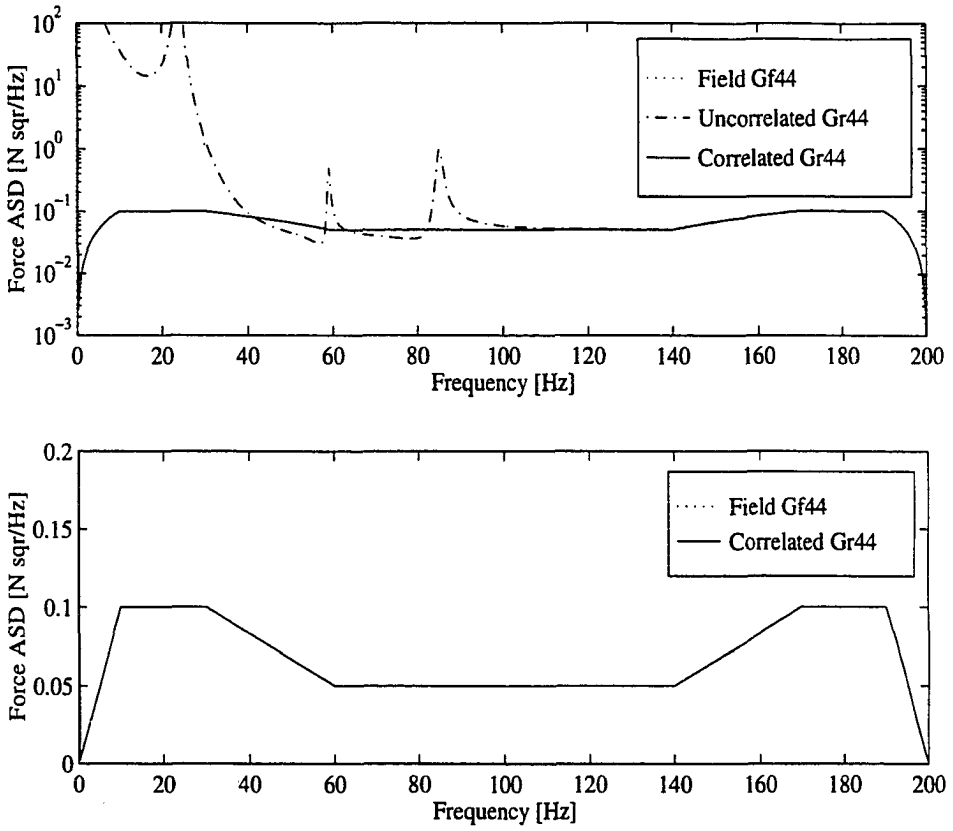

Figure 5.23 External force ASD Gr_{44} in logarithmic and linear scales obtained when N_t forces are predicted from N_t accelerations

Chapter Summary

The results obtained in the numerical simulations can be summarized as follows:

- Acceleration CSDs must be accounted for in addition to acceleration ASDs when obtaining the test item inputs from knowledge of field motions through the pseudo-inverse technique. This is due to the fact that motions are always correlated independent of the input forces being correlated or uncorrelated. Numerical problems can occur when employing the pseudo-inverse technique due to rank deficiency of the test item FRF matrix in some frequencies. These difficulties can be overcome by seeking a set of pseudo-forces in a least squares sense. This set of pseudo-forces

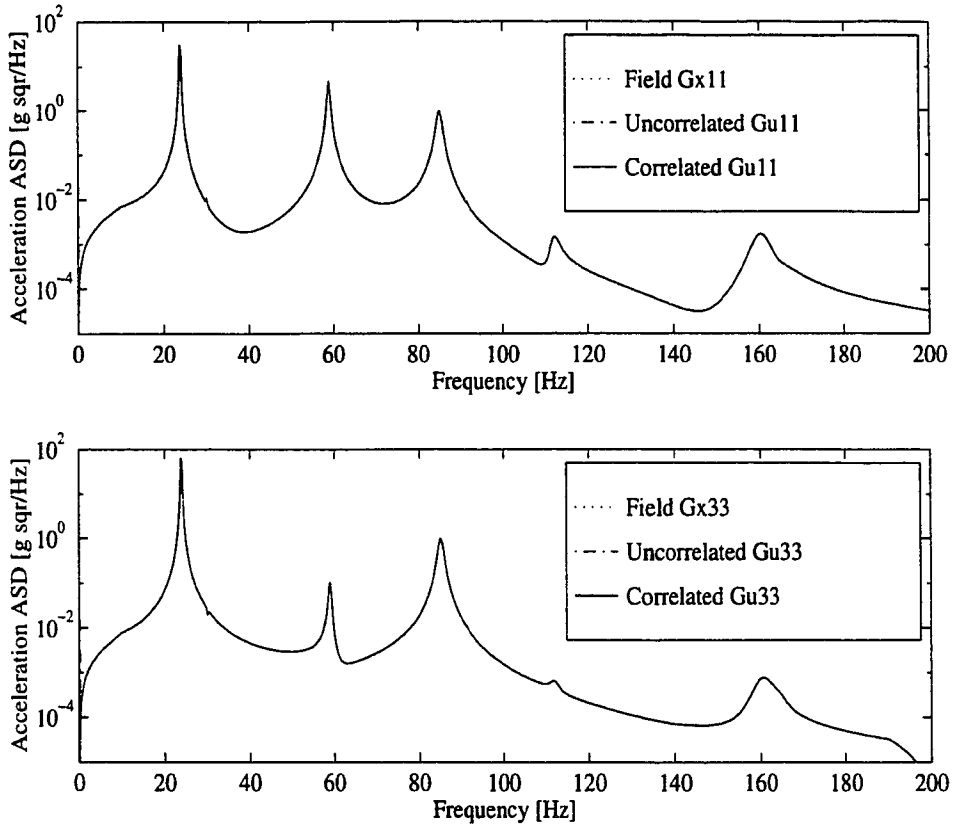

Figure 5.24 Test item laboratory interface acceleration ASDs resulting from using laboratory interface force ASDs Gr_{11} and Gr_{33} and external Gr_{44} obtained from N_t field interface accelerations. External force ASD Gf_{44} is accounted for in the laboratory

will in some cases resemble the actual forces acting on the test item depending primarily on the locations where the accelerations and FRFs were measured.

- The bare vehicle interface acceleration ASDs do not represent suitable test item inputs in laboratory simulations. These accelerations can give reasonable simulation results in the absence of field external forces and if the vehicle driving and transfer point FRFs are known. Otherwise, the bare vehicle data alone is meaningless.

- Field external forces must be accounted for in laboratory simulations so that the reasonable acceleration predictions can be obtained.

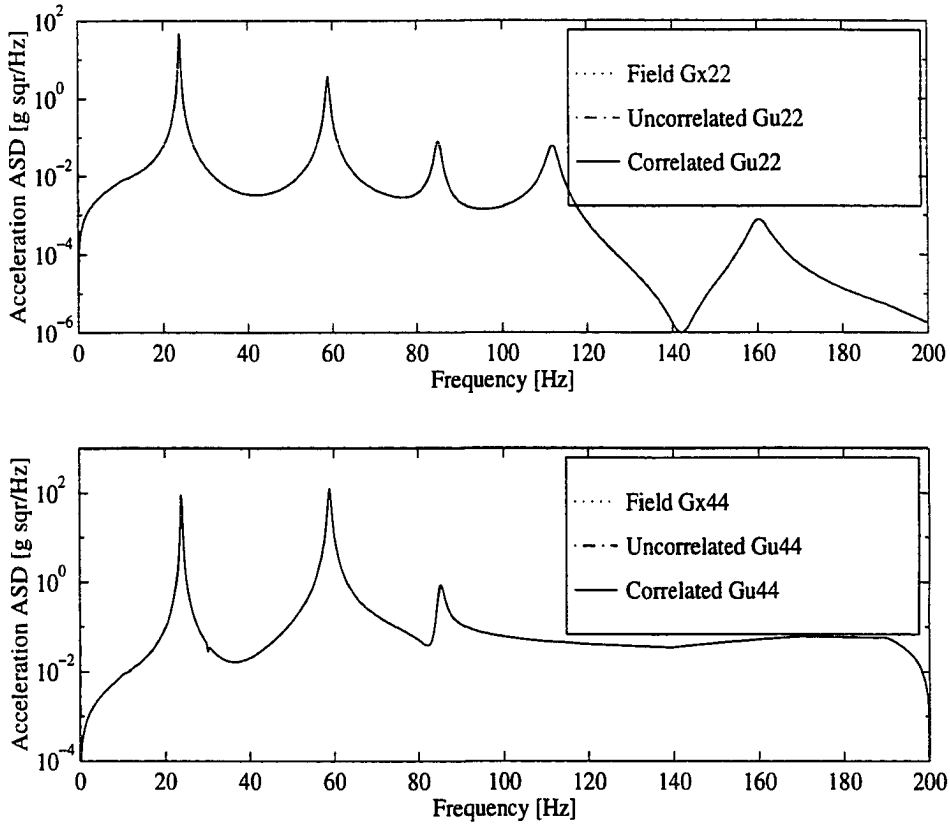

Figure 5.25 Test item laboratory external acceleration ASDs resulting from using laboratory interface force ASDs $\boldsymbol{Gr}_{11}$ and $\boldsymbol{Gr}_{33}$ and external $\boldsymbol{Gr}_{44}$ obtained from N_t field interface accelerations. External force ASD $\boldsymbol{Gf}_{44}$ is accounted for in the laboratory

6 TRANSMISSIBILITY CONCEPTS IN MULTIPLE CONNECTOR TEST ENVIRONMENTS

In this chapter, the single point transmissibility FRF concept discussed in Chapter 2 is extended to the case where the inputs are given in terms of a set of multiple interface motions that are *simultaneously* applied to the test item. A transformation called **Q**-transmissibility matrix (**Q-T** matrix) is defined. Current practices used in vibration testing are discussed using transmissibility concepts.

The Q-Transmissibility Approach for Deterministic Excitations

The single point transmissibility FRF concept discussed in Chapter 2 represents a useful tool for determining external motions when the test item is subjected to an input motion at a single interface point as shown in Figure 6.1. In this case, Equation 2.55 is rewritten as

$$X_p = \Gamma_{pr}\, X_r \tag{6.1}$$

where $X_p = X_p(\omega)$ and $X_r = X_r(\omega)$ are the Fourier transforms of the structure's p^{th} absolute displacement x_p and the single *absolute* input motion $X_r = X_b$, respectively. Thus, if test item and vehicle are attached one to another by a single interface connector [26], Equation 6.1 the test item external accelerations X_p is obtained from the test item single point interface acceleration transmissibility FRF Γ_{pr} and the interface acceleration X_r.

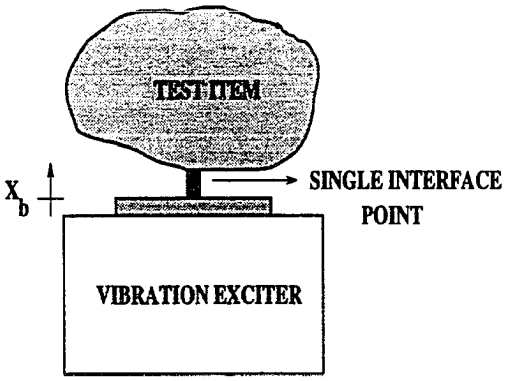

Figure 6.1 Test item attached to a vibration exciter and subjected to a single interface input motion x_b

However, in many cases, the test item is attached to the vehicle in the field or to the vibration exciter in the laboratory at several interface points as shown in Figure 6.2. In these cases, the transmissibility input-output relationship defined by Equation 6.1 is not applicable.

This section describes a procedure that can be used to predict the test item responses at external points when the test item excitation consists of multiple interface motions that are simultaneously applied at its interface points in the absence of external forces.

This procedure is called the **Q-T** matrix and it involves multiple interface inputs and multiple external motion outputs. The **Q-T** matrix is defined by

$$\{X_e\} = [Q]\ \{X_c\} \tag{6.2}$$

where the N_e x 1 vector $\{X_e\}$ represents the test item external motions, the N_c x 1 vector $\{X_c\}$ contains the measured interface motions, and the N_e x N_c matrix $[Q]$ is the **Q-T** matrix that defines the linear transformation between measured interface motions and the unknown external motions. Equation 6.2 is similar to the well known force input-output motion linear transformation

$$\{X\} = [T]\ \{F\} \tag{6.3}$$

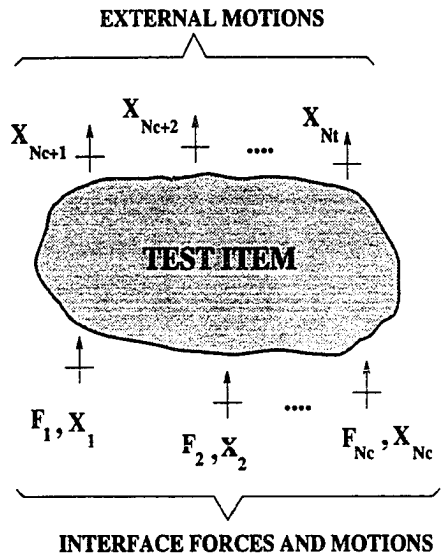

Figure 6.2 Test item subjected to multiple interface input motions

where the input force vector $\{F\}$ is transformed into the motion vector $\{X\}$ by the test item FRF matrix $[T]$. In the following discussion, *it is assumed that* $[T]$ *represents accelerance.*

The entries of the **Q-T** matrix in Equation 6.2 are obtained from the test item driving point and transfer point accelerance FRFs by writing Equation 6.3 as a partitioned matrix that separates *connector* and *external* points according to Equation 3.4 from Chapter 3, that is conveniently repeated here

$$\left\{ \begin{array}{c} \{X_c\} \\ \{X_e\} \end{array} \right\} = \left[\begin{array}{cc} [T_{cc}] & [T_{ce}] \\ [T_{ec}] & [T_{ee}] \end{array} \right] \left\{ \begin{array}{c} \{F_c\} \\ \{F_e\} \end{array} \right\} \tag{6.4}$$

where as before, the N_c x 1 vector $\{X_c\}$ contains the test item interface (connector) accelerations while the N_e x 1 vector $\{X_e\}$ contains the test item external accelerations. Similarly, the excitation force vector $\{F\}$ on the right hand side of Equation 6.3 is broken in two components, the N_c x 1 vector of interface forces $\{F_c\}$ that occur at the test item N_c connector points, and the N_e x 1 vector of external forces $\{F_e\}$. Interface forces

are assumed to result from coupling effects *only*, i.e., the force interactions that occur when the test item is attached to a second structure. The partition of input force and output acceleration vectors in terms of interface and external variables requires that the test item accelerance FRF N_t x N_t matrix $[T]$ be broken in the four submatrices $[T_{cc}]$ (N_c x N_c), $[T_{ee}]$ (N_e x N_e), and $[T_{ce}] = [T_{ec}]^T$ (N_c x N_e), as before.

Expansion of Equation 6.4 leads to the following expressions for interface and external motions

$$\{X_c\} = [T_{cc}]\{F_c\} + [T_{ce}]\{F_e\} \tag{6.5}$$

$$\{X_e\} = [T_{ec}]\{F_c\} + [T_{ee}]\{F_e\} \tag{6.6}$$

where it is clear that both the interface and external motions $\{X_c\}$ and $\{X_e\}$ are caused by both interface and external forces that are applied to the test item. Equations 6.5 and 6.6 can be simplified if *it is assumed that the test item is subjected to no external forces*, i.e. $\{F_e\} = 0$. In this case, the interface force can be obtained from Equation 6.5 as

$$\{F_c\} = [T_{cc}]^{-1}\{X_c\} \tag{6.7}$$

Substitution of Equation 6.7 into Equation 6.6 with the assumption that $\{F_e\} = 0$ leads to the following equation relating the unknown external motions $\{X_e\}$ to the measured interface motions $\{X_c\}$

$$\{X_e\} = [T_{ec}][T_{cc}]^{-1}\{X_c\} \tag{6.8}$$

which is the same as equation 6.2 with

$$[Q] = [T_{ec}][T_{cc}]^{-1} \tag{6.9}$$

Thus, in principle the test item external accelerations can be obtained from Equation 6.8 from knowledge of the test item interface accelerations and the test item interface $[T_{cc}]$ and interface-external $[T_{ce}]$ accelerance FRF characteristics.

Limiting Case of a Single Deterministic Input Motion

If the test item has a single interface point ($N_c = 1$) that is subjected to an input motion X_r, then Equation 6.8 reduces to

$$\{X_e\} = \frac{X_r}{T_{rr}} \{T_{er}\} \tag{6.10}$$

The external motion at the p^{th} coordinate point is seen to be given by

$$X_p = \frac{T_{pr}}{T_{rr}} X_r = \Gamma_{pr} X_r \tag{6.11}$$

In this simple case, the ratio of the test item external-connector FRF T_{pr} to the connector-connector FRF T_{rr} is the *single point transmissibility* FRF Γ_{pr} between points p and r as given by Equation 6.1. This simple result is only valid for the case where the test item is subjected to a single input motion.

Effects of Rigid Test Fixtures

Now consider the situation where $N_c > 1$ so that the test item is subjected to multiple input motions that are simultaneously applied to its interface points. In this case, the external motion at the p^{th} coordinate point is given by

$$X_p = Q_{p1}X_1 + Q_{p2}X_2 + ... + Q_{pNc}X_{Nc} \tag{6.12}$$

where the Q_{pr}, $r = 1, ..., N_c$ are the entries of the p^{th} row of the **Q-T** matrix defined by Equation 6.9, and X_r, $r = 1, ..., N_c$, $r \neq p$ are the input interface accelerations. Standard laboratory testing procedures [8] recommend that the test item be attached to a *single* exciter through a *rigid test fixture.* In this case, the excitation motion that is generated by the exciter system is transmitted to the test item through each interface point causing all input motions to the test item to be the same, i.e, $X_1 = X_2 = ... = X_{Nc} = X_o$. Thus, Equation 6.12 reduces to

$$X_p = \left(\sum_{r=1}^{Nc} Q_{pr} \right) X_o \tag{6.13}$$

Thus, when the same input motion is applied to all of the interface points, the test item acceleration response at the external point X_p is given by the product of the input motion X_o and the sum of the p^{th} row of the **Q-T** matrix. In this case, the right hand side of Equation 6.13 *does not* reduce to the transmissibility FRF that is experienced under field conditions. The only exception occurs when multiple interface points all have the same field motions. The implications of using Equation 6.13 in laboratory simulations will be investigated in the next section.

Numerical Results for Deterministic Excitations

This section presents results of numerical simulations for deterministic excitation and response signals. The **Q-T** matrix approach outlined in the previous section will be employed in laboratory simulations with the lumped models shown in Figure 6.3.

The Test Item Field Acceleration Data

The test item field acceleration frequency spectra is obtained From Equation 3.21 as

$$\begin{Bmatrix} \{X_c\} \\ \{X_e\} \end{Bmatrix} = \begin{bmatrix} [T_{cc}][TV] & -[T_{cc}][TV] \\ [T_{ec}][TV] & -[T_{ec}][TV] \end{bmatrix} \begin{Bmatrix} \{Y_c\}_e \\ \{0\} \end{Bmatrix} \tag{6.14}$$

Recall that in the absence of external force effects, the test item accelerations depend exclusively on the bare vehicle interface accelerations $\{Y_c\}_e$ and on the test item and vehicle interface accelerance FRFs.

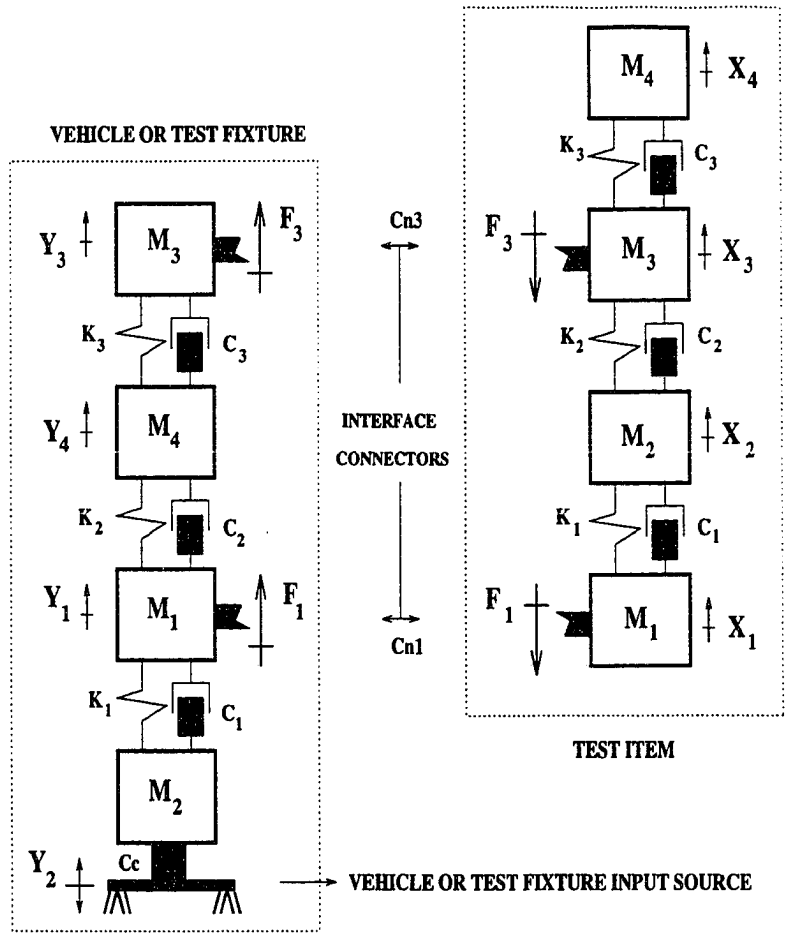

Figure 6.3 Test item attached to the vehicle in the field by connectors Cn_1 and Cn_3. In the laboratory environment the vehicle becomes the test fixture

The numerical simulations presented in this chapter employed the same lumped models used in the previous chapters and shown in Figure 6.3. The models' physical and modal parameters are shown in Tables 4.1 and 4.2, respectively.

The test item external force frequency spectrum F_4 shown in Figure 4.8 that was applied to the test item's mass M_4 is made zero so that the test item is subjected to interface forces (F_1 and F_3), as assumed in the development of Equation 6.8. Thus, the only field excitation is the input acceleration frequency spectrum Y_2 shown in Figure 4.7 and that is applied to the vehicle's base mass M_2.

The bare vehicle interface acceleration frequency spectrum $\{Y_c\}_e$ is obtained by using the single point transmissibility relationship given by Equation 6.1. These accelerations are shown in Figure 4.9.

The test item's interface and external acceleration frequency spectra are obtained from Equation 6.14 and they are shown in Figures 6.4 and 6.5.

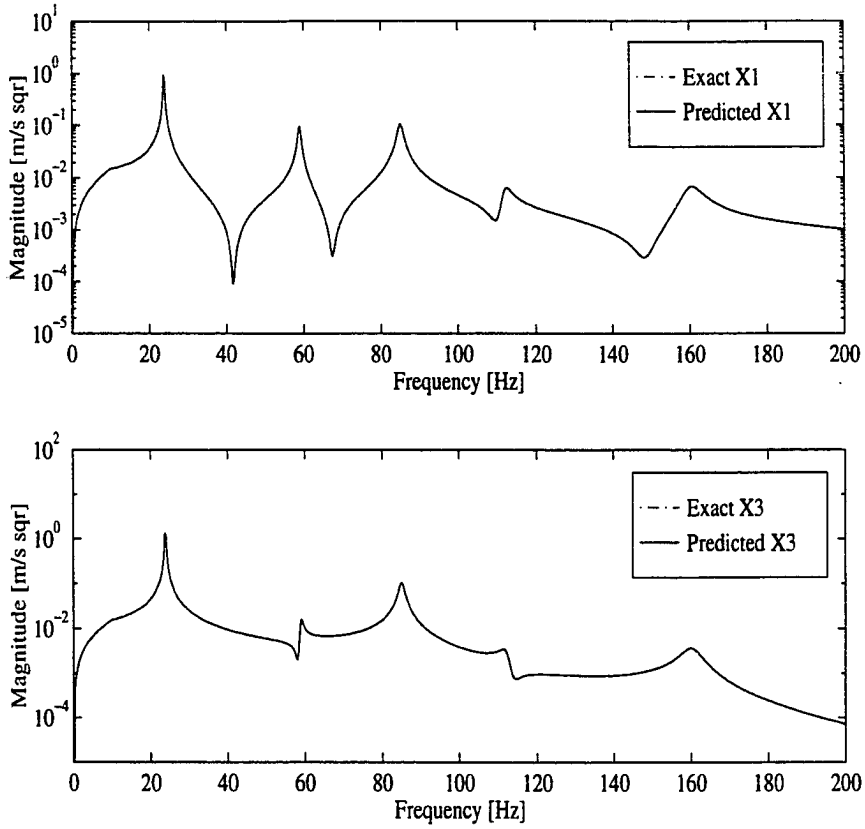

Figure 6.4 Test item field interface acceleration frequency spectra X_1 and X_3 due to field interface forces F_1 and F_3

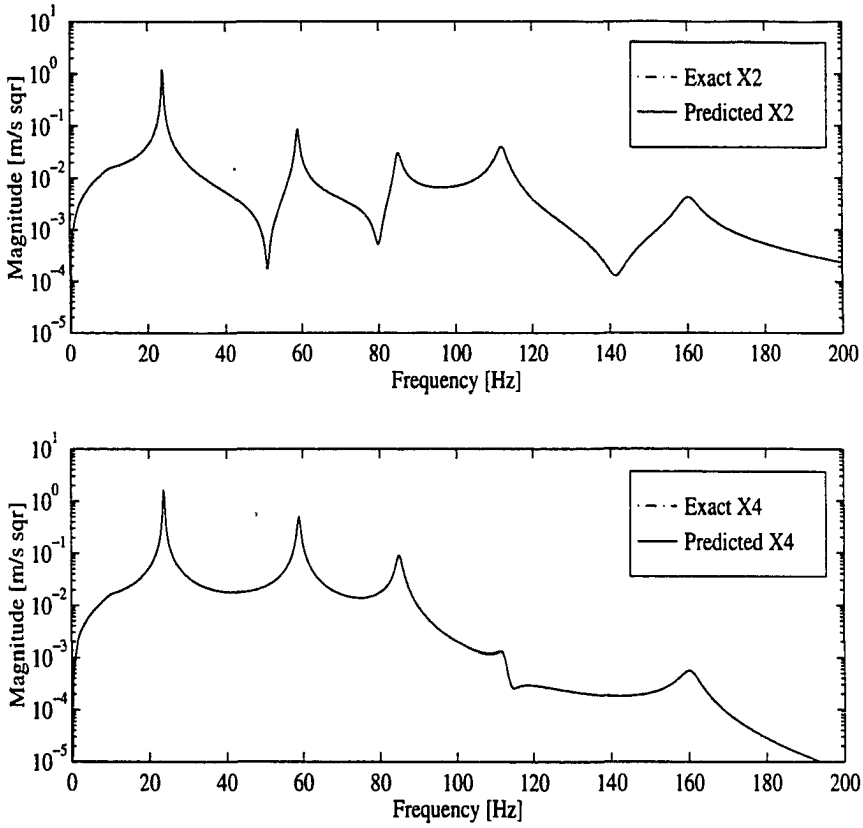

Figure 6.5 Test item field external acceleration frequency spectra X_2 and X_4 due to field interface forces F_1 and F_3

Laboratory Simulation Using a Single Vibration Exciter

The test item is attached to the vibration exciter table through a rigid test fixture. The vehicle becomes the test fixture in this case as shown in Figure 6.3. New spring constants are chosen so that a *rigid test fixture* is obtained as recommended by the MIL-STD 810D [8]. The test fixture spring constants are $K_1 = 9.10^6\ N/m$, $K_2 = 14.10^7\ N/m$, and $K_3 = 10^8\ N/m$. The test fixture masses are the same as the vehicle masses shown in Table 4.1. The resulting fixture natural frequencies are respectively $f_1 = 410\ Hz$, $f_2 = 2,464\ Hz$, and $f_3 = 5,161\ Hz$. These natural frequencies are located well above the $0 - 200\ Hz$ test frequency range. The test item is assumed to be the same in both environments. Similarly to the field, the test item and the test fixture are connected at

interface points 1 and 3. The excitation signal is generated by a single vibration exciter that is attached to the test fixture mass M_2.

- Choice of the test item input in this case constitutes a problem since a single vibration exciter is employed in the simulation while there are two interface accelerations in the actual field environment as shown in Figure 6.3. Thus, a natural question that arises in simulations where a single vibration exciter is used is: *Which field motion should be used as the test item input ?* Two cases are considered here:

  - **Case 1** The vibration exciter is controlled to reproduce either of the interface accelerations shown in Figure 6.4.

  - **Case 2** The vibration exciter is controlled to generate an input acceleration that is a combination of the measured field interface accelerations shown in Figure 6.4.

Note that in both cases, the input accelerations applied at the test item interface points 1 and 3 will be the same due to the rigid test fixture. Thus, Equation 6.13 must be employed in order to obtain the resulting test item external accelerations.

In the first case described above, the acceleration frequency spectrum at the interface point 1 X_1 is used to drive the test fixture and test item. Equation 6.13 is rewritten as

$$U_p = \left(\sum_{r=1}^{Nc} Q_{pr} \right) X_1 \tag{6.15}$$

where U_p, $p = 2, 4$ is p^{th} external test item acceleration. The **Q-T** matrix is obtained from Equation 6.9. Figure 6.6 shows the resulting test item external acceleration magnitudes U_2 and U_4 obtained in this test scenario as well as the field acceleration magnitudes X_2 and X_4 that are used for comparison purposes. Both external motions are incorrect since the *same* interface input motion X_1 is applied to *both* test item interface points 1 and 3 while in the field the actual interface motions are different due to the flex-

ibility characteristics of the vehicle structure. It is clear that both over-testing and under-testing occur in this test arrangement.

In the second test scenario described above, a single test item input is obtained by using the average of the field interface accelerations X_1 and X_3 such that

$$X_o = \frac{X_1 + X_3}{2} \tag{6.16}$$

This acceleration is transmitted to the test item through the test fixture so that Equation 6.13 is used again. The resulting external acceleration frequency spectra U_2 and U_4 are plotted in Figure 6.7 along with the field response. The laboratory external acceleration U_2 shows good agreement with field data occurs for frequency components in the $0 - 70$ Hz test frequency range, a poor agreement between field and laboratory data occurs in the $70 - 105$ Hz frequency range, and a nearly perfect agreement occurs between U_2 and X_2 for the remaining spectral lines. The external acceleration U_4 has good agreement with X_4 in the $0 - 30$ Hz frequency range while there is poor agreement in the remaining $30 - 200$ Hz frequency range. It is clear that both over-testing and under-testing occur in this testing arrangement as well.

Laboratory Simulation Using Multiple Vibration Exciters

In this case, each of the test item N_c interface points is attached to a single vibration exciter. The vibration exciters are controlled so that the test item is driven by a set of accelerations that match the field interface accelerations in magnitude and phase and are simultaneously applied to the test item interface points. This means that each of the N_c interface points will be subjected to a different input acceleration. Then, the test item external acceleration at the p^{th} location is calculated by Equation 6.12 where X_1, X_2, ..., X_{Nc} represent the N_c input accelerations that are generated by the vibration exciters and Q_{p1}, Q_{p2}, ..., Q_{pNc} is the p^{th} row of the **Q-T** matrix that is obtained from Equation 6.9.

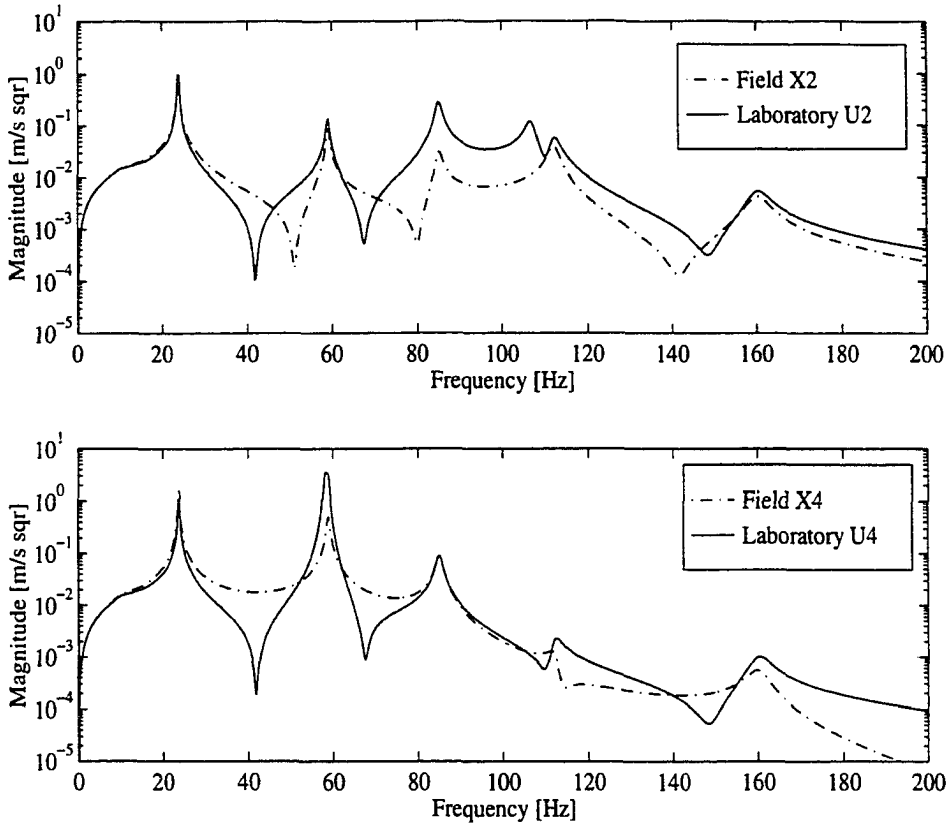

Figure 6.6 Magnitudes of test item external acceleration frequency spectra for laboratory simulation employing a single exciter with rigid a test fixture and input acceleration matching field motion X_1

For the test item in Figure 6.3, the external motions are obtained by expanding Equation 6.8 as

$$\begin{Bmatrix} U_2 \\ U_4 \end{Bmatrix} = \begin{bmatrix} T_{21} & T_{23} \\ T_{41} & T_{43} \end{bmatrix} \begin{bmatrix} T_{11} & T_{13} \\ T_{31} & T_{33} \end{bmatrix}^{-1} \begin{Bmatrix} X_1 \\ X_3 \end{Bmatrix} \tag{6.17}$$

In this simple case, Equation 6.17 can be easily expanded to

$$U_2 = \frac{1}{\Delta_{cc}} \left[(T_{11}T_{23} - T_{33}T_{21})X_1 - (T_{13}T_{21} - T_{31}T_{23})X_3 \right] \tag{6.18}$$

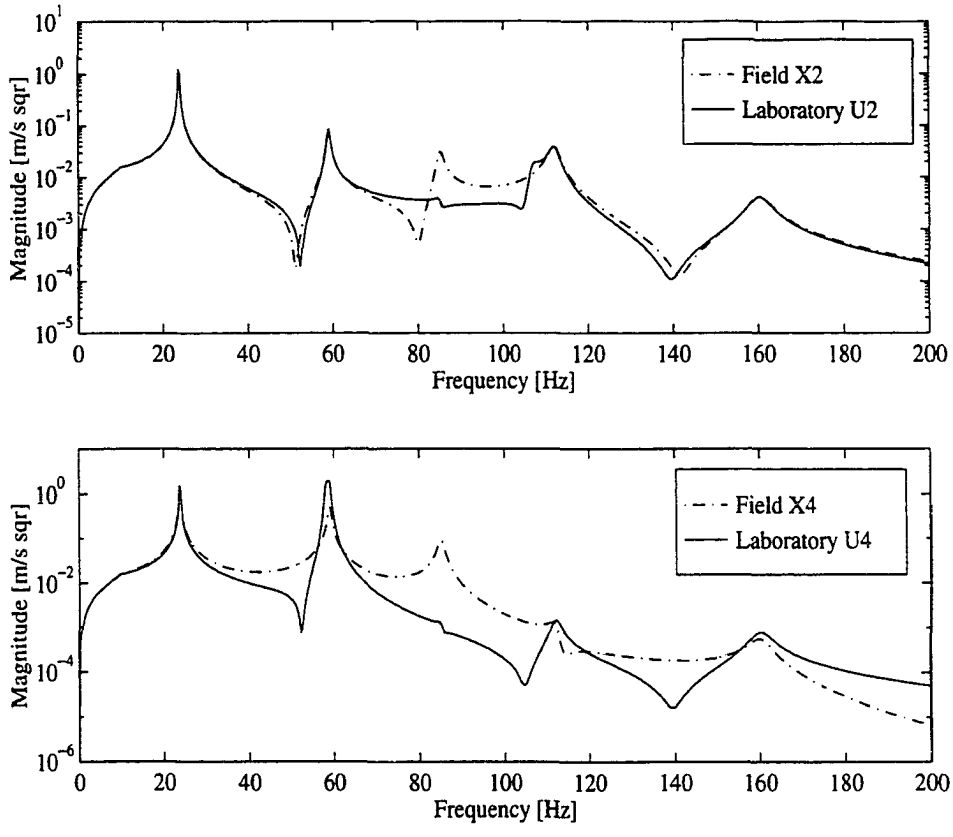

Figure 6.7 Magnitudes of test item external acceleration frequency spectra for laboratory simulation employing a single exciter with rigid a test fixture and input acceleration matching the average of field interface accelerations X_1 and X_3

$$U_4 = \frac{1}{\Delta_{cc}} [(T_{11}T_{43} - T_{33}T_{41})X_1 - (T_{13}T_{41} - T_{31}T_{43})X_3] \tag{6.19}$$

where Δ_{cc} is the determinant of the test item interface accelerance matrix ($\Delta_{cc} = T_{11}T_{33} - T_{13}T_{31}$). From Equations 6.18 and 6.19, the **Q-T** matrix for the test item can be obtained as

$$[Q] = \frac{1}{\Delta_{cc}} \begin{bmatrix} T_{11}T_{23} - T_{33}T_{21} & T_{13}T_{21} - T_{31}T_{23} \\ T_{11}T_{43} - T_{33}T_{41} & T_{13}T_{41} - T_{31}T_{43} \end{bmatrix} \tag{6.20}$$

and is noticed that each entry of the **Q-T** matrix has Δ_{cc} as the denominator.

The test item external accelerations obtained from Equations 6.18 and 6.19 are shown in Figure 6.8. An excellent agreement is seen to occur between the accelerations obtained through the **Q-T** matrix approach (U_2 and U_4) and the corresponding field data (X_2 and X_4).

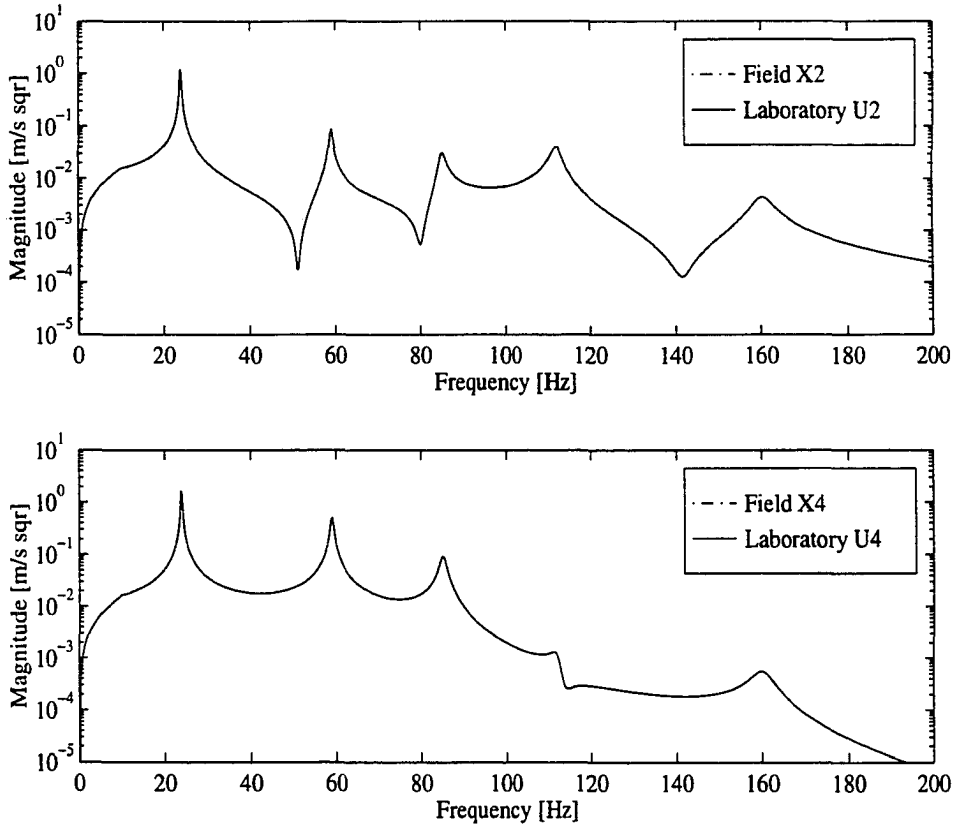

Figure 6.8 Magnitudes of test item external acceleration frequency spectra for laboratory simulation employing multiple exciters and inputs matching the field interface acceleration frequency spectra X_1 and X_3

The Q-Transmissibility Approach for Random Excitations

In order to use the **Q-T** matrix approach with random excitation and response signals, Equation 6.8 must be reformulated since it was originally derived in terms of deterministic frequency spectra. In order to obtain the corresponding **Q-T** matrix expression for random signals, the following definition employed in the previous chapter is used [4]

$$[G\boldsymbol{x}_e] = \lim_{\tau \to \infty} \frac{2}{\tau} \epsilon \left(\{X\}_e^* \{X\}_e^T \right) \tag{6.21}$$

where the N_e x N_e spectral density matrix $[G\boldsymbol{x}_e]$ contains the external acceleration ASDs in the main diagonal and the corresponding CSDs in the remaining off-diagonal entries and τ represents the analysis period. The symbol * denotes the conjugate of the complex external acceleration frequency spectrum $\{X_e\}$.

The application of this fundamental definition from Equation 6.21 to both sides of Equation 6.8 gives the following result for the external acceleration spectral density matrix

$$[G\boldsymbol{x}_e] = [T_{ec}]^*[[T_{cc}]^{-1}]^* \; [G\boldsymbol{x}_c] \; [[T_{cc}]^{-1}]^T[T_{ec}]^T \tag{6.22}$$

where the the N_c x N_c spectral density matrix $[G\boldsymbol{x}_c]$ contains the interface acceleration ASDs and CSDs. The right hand side of Equation 6.22 can be simplified by using the identities: $[T_{ce}] = [T_{ec}]^T$ and $[[T_{cc}]^{-1}]^T = [[T_{cc}]^T]^{-1} = [T_{cc}]^{-1}$, since $[T_{cc}]$ is symmetric. The resulting expression for the external acceleration spectral density matrix is

$$[G\boldsymbol{x}_e] = [T_{ec}]^*[[T_{cc}]^{-1}]^* \; [G\boldsymbol{x}_c] \; [T_{cc}]^{-1}[T_{ce}] \tag{6.23}$$

or simply

$$[G\boldsymbol{x}_e] = [Q]^* \; [G\boldsymbol{x}_c] \; [Q]^T \tag{6.24}$$

where in this case, the interface acceleration spectral density matrix $[G\boldsymbol{x}_c]$ is multiplied on the left by the complex conjugate of the **Q-T** matrix and on the right by the transpose of the **Q-T** matrix $[Q] = [T_{ec}][T_{cc}]^{-1}$, respectively.

Limiting Case of a Single Random Input Motion

Application of the definition expressed in Equation 6.21 to Equation 6.10 gives the following result in terms of random excitation and response signals for the case of a single interface motion

$$[G\boldsymbol{x}_e] = \frac{G\boldsymbol{x}_{rr}}{|T_{rr}|^2}\,[\beta_{er}] \tag{6.25}$$

where $G\boldsymbol{x}_{rr}$ is the interface input motion ASD and T_{rr} is the interface driving point FRF. The N_e x N_e matrix $[\beta_{er}]$ is given by

$$[\beta_{er}] = \begin{bmatrix} |T_{2r}|^2 & T_{2r}^* T_{3r} & T_{2r}^* T_{4r} & \dots & T_{2r}^* T_{Ner} \\ T_{3r}^* T_{2r} & |T_{3r}|^2 & \dots & \dots & T_{3r}^* T_{Ner} \\ \ddots & \ddots & |T_{pr}|^2 & \ddots & \vdots \\ \vdots & \ddots & \ddots & \ddots & \vdots \\ T_{Ner}^* T_{2r} & \dots & \ddots & \ddots & |T_{Ner}|^2 \end{bmatrix} \tag{6.26}$$

where the first $r = 1 \dots N_c$ subscripts ($N_c = 1$) denote interface DOF and the remaining subscripts ($p = 2 \dots N_e$) denote external DOF. It can be easily shown that the matrix $[\beta_{er}]$ is related to the single point transmissibility FRFs Γ_{pr}, that relate the external DOF to the single interface point. Thus, Equation 6.25 can also be expressed as as

$$[G\boldsymbol{x}_e] = \left[\, [: \Gamma_{pr} :]^* \, [\delta_{rr}] \, [: \Gamma_{pr} :]^T \,\right] G\boldsymbol{x}_{rr} \tag{6.27}$$

where the matrix $[\delta_{rr}]$ denotes the Dirac-delta function matrix ($\delta_{rr} = 1$ for $r = 1$, and $\delta_{rr} = 0$ for $r \neq 1$). Symbols ":" are used in Equation 6.27 to express the fact that the matrices $[: \Gamma_{pr} :]^*$ and $[: \Gamma_{pr} :]^T$ have zeroes in all entries except in the column (p,r), where the transmissibility FRFs are used.

Effects of Rigid Test Fixtures

In this case, Equation 6.13 should be used with the definition shown in Equation 6.21. The resulting expression for the p^{th} external motion ASD is

$$G\boldsymbol{x}_{pp} = \left[\left(\sum_{r=1}^{Nc} Q_{pr}^{*} \right) \left(\sum_{r=1}^{Nc} Q_{pr} \right) \right] G\boldsymbol{x}_{oo} \tag{6.28}$$

where $G\boldsymbol{x}_{oo}$ denotes the input motion ASD. Note that, as it was the case for deterministic signals, Equation 6.28 does not reduce to the standard single point transmissibility FRF.

Numerical Results for Random Excitations

In this section, motion transmissibility concepts are used in numerical simulations involving random excitation and response signals to show the consequences of using current vibration testing procedures.

The Test Item Field Random Acceleration Data

The same lumped models used in the previous section and shown in Figure 6.3 will be used when employing the **Q-T** matrix approach with random excitations. The test item is attached to the vehicle in the field and physical and modal parameters for both structures are shown in Tables 4.1 and 4.2, respectively.

The random acceleration ASD $G\boldsymbol{y}_{22}$ used in Chapter 5 is used as the vehicle input source in both field simulations. This acceleration ASD is applied to the vehicle base mass M_2 and it is shown in Figure 6.9. This base motion is the only input used in the field environment. No external inputs are applied to the test item in this example.

Recall from Chapter 5 that in the absence of field external forces, the test item

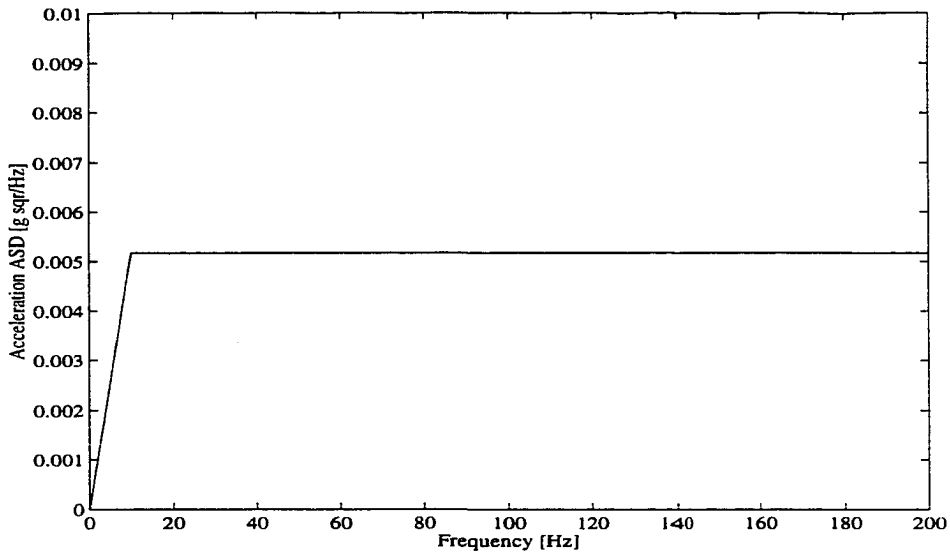

Figure 6.9 Vehicle and combined structure field input base acceleration ASD Gy_{22} that is applied to the vehicle base mass M_2 and gives an input vibration level of 1.0 g_{RMS}

interface and external acceleration spectral density matrices are respectively given by

$$[G\boldsymbol{x}_{cc}] = [T_{cc}]^*[TV]^* \left[[G\boldsymbol{y}_{cc}]_e \right] [TV][T_{cc}] \tag{6.29}$$

$$[G\boldsymbol{x}_{ee}] = [T_{ec}]^*[TV]^* \left[[G\boldsymbol{y}_{cc}]_e \right] [TV][T_{ec}]^T \tag{6.30}$$

where the diagonal entries in $[G\boldsymbol{x}_{cc}]$ and in $[G\boldsymbol{x}_{ee}]$ represent the interface and external acceleration ASDs and the off-diagonal entries are the interface and external CSDs, respectively. The N_c x N_c matrix $[TV] = [[T_{cc}]+[V_{cc}]]^{-1}$, is the test item-vehicle combined matrix and is given by the inverse of the matrix formed by the sum of the test item and vehicle connector accelerance FRF matrices, $[T_{cc}]$ and $[V_{cc}]$, respectively.

Note that, similarly to the previous section, the test item interface and external motions depend on the test item's and vehicle's accelerance FRF characteristics and on the N_c x N_c bare vehicle interface acceleration spectral density matrix $[G\boldsymbol{y}_{cc}]_e$ that is obtained when the test item is absent and that is due to the input acceleration ASD shown in Figure 6.9. These motions are obtained in the same exact way as it was done

in Chapter 5, i.e., by using the vehicle's single point transmissibility FRFs and the input acceleration ASD Gy_{22}. The bare vehicle interface acceleration ASDs are shown in Figure 6.10.

The results obtained from Equations 6.29 and 6.30 for the combined structure shown in Figure 6.3 are shown in Figure 6.11.

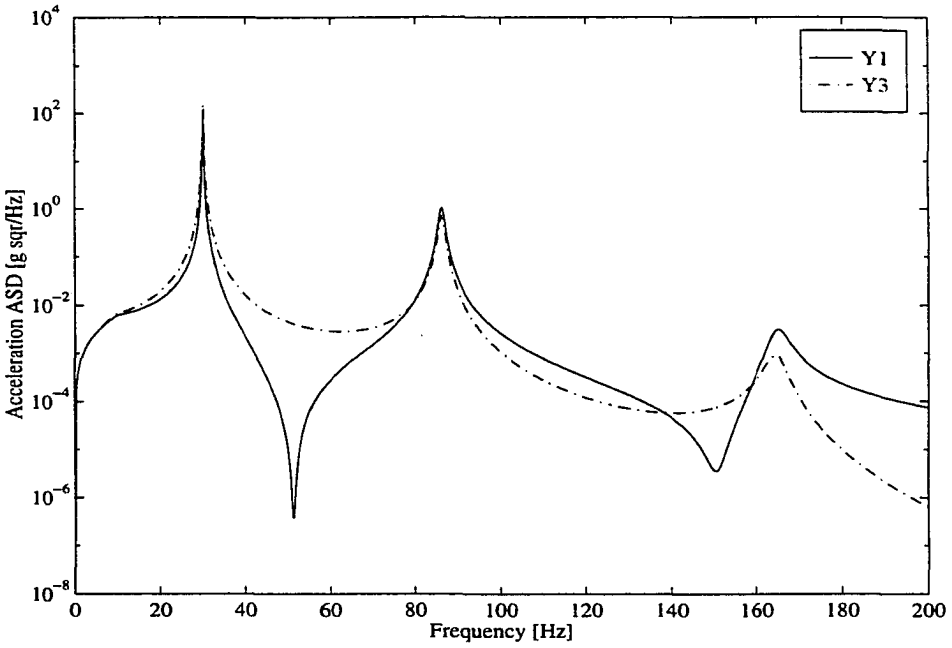

Figure 6.10 The bare vehicle acceleration ASDs representing the vehicle's response to the input acceleration ASD Gy_{22} in the absence of the test item

Laboratory Simulation Considerations

Often standard testing practice is to use a single vibration exciter and test fixture where the test item is attached to the test fixture at N_c points [8, 33, 34, 41, 42]. It is necessary to examine how this arrangement affects the test outcome. It was previously shown in Chapters 3, 4 and 5 that certain requirements must be satisfied in order to have a successful simulation when there are multiple interface connections. *First*, multiple

exciters must be used, one for each connection point. *Second*, each exciter must be controlled such that either the corresponding interface motion or force occurs at each interface point that has the correct phasing relative to the other inputs. *Third*, the external loads must be properly applied to the test item. Now the question is, "can the test fixture and exciter input be specified so that the desired results are obtained?" To begin to answer this question, Equations 6.29 and 6.30 are re-examined.

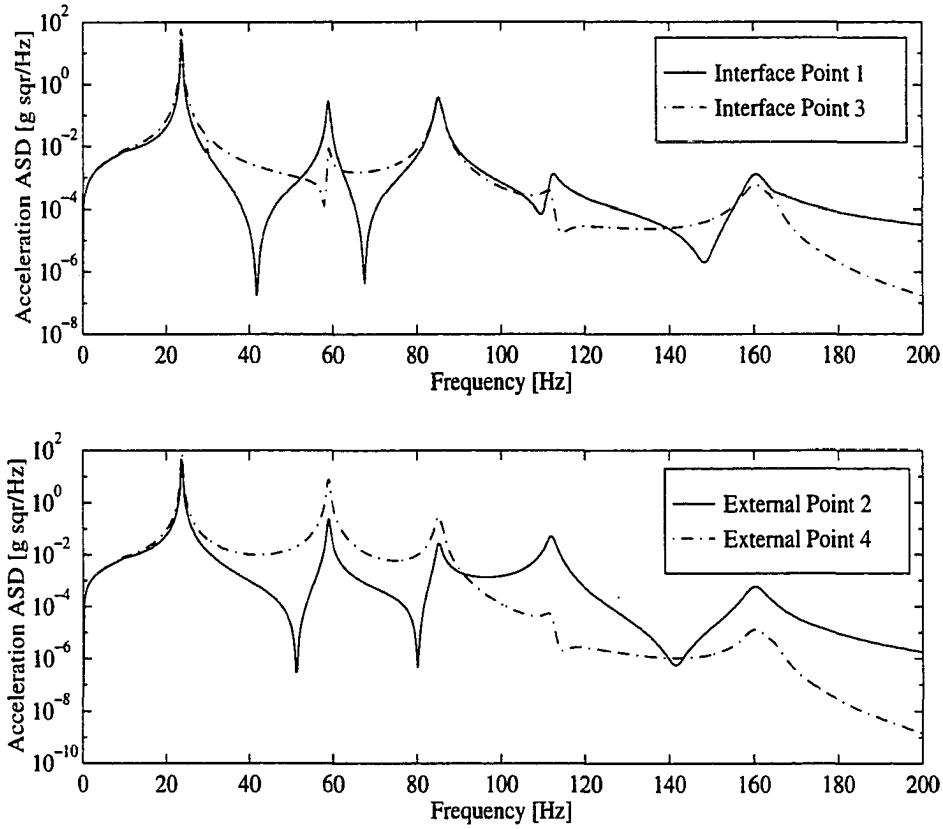

Figure 6.11 Test item field interface and external acceleration ASDs. The test item is subjected to field interface forces only

Equations 6.29 and 6.30 require that the test fixture have the same driving and transfer point accelerance as the vehicle so that the $[TV]$ matrices are the same in the field and laboratory environments. This matching of driving and transfer point accelerances is a very difficult requirement to achieve in the first place and extremely

expensive to implement. Thus, there is a little chance of meeting this requirement in general.

Current practice [8] requires that the test fixture be "rigid" over the range of frequencies tested. In this study, the test fixture is simulated as a four DOF system as shown in Figure 6.3. Two test fixture designs are used where one is rigid and the other has a single resonance in the middle of the test frequency range. These two different test fixture conditions are achieved by changing the spring constants that were given in Chapter 4, Table 4.1. The actual spring constant values are given in Table 6.1 along with the corresponding test fixture natural frequencies.

Equations 6.29 and 6.30 require that there be multiple inputs, but the test situation in Figure 6.3 shows only a single input Gy_{22}. Hence, the automatic question of what to do when using a single exciter with a test fixture and multiple connector or interface points are present appears in the context of the system shown in Figure 6.3. So, how is this question answered in test standards ?

Table 6.1 Parameters for test fixtures

Stiffness (N/m)	Rigid x 10^8	Flexible x 10^8
K_1	0.09	0.005
K_2	1.40	14.00
K_3	1.00	10.00
Natural Frequency (Hz)	Rigid x 10^2	Flexible x 10^2
f_1	4.10	1.00
f_2	24.64	76.57
f_3	51.61	162.98

MIL-STD810D [8] recommends that field data is used if it is available. It also recommends that the highest interface motion peaks be used in drawing a flat envelope (similar to the one shown in Figure 5.2) over all bare vehicle peaks. For this simulation, the bare vehicle interface acceleration ASDs from Figure 6.10 were enveloped with the

same shape as that shown in Figure 6.9. This means that the exciter acceleration ASD in Figure 6.9 is multiplied by a scale factor of $140^2 = 1.96.10^4$ to obtain the test item laboratory input.

It is immediately clear from this discussion and Figure 6.3 that the requirements for an adequate simulation are not being met by using a single test fixture and input motion. Now, the consequences of using these test standard recommendations for this test setup will be discussed.

First, the *bare test fixture* acceleration ASDs must be calculated from Equation 6.27 for the laboratory environment when the test fixture characteristics given in Table 6.1 are used and the desired input acceleration ASD that envelopes the bare vehicle interface ASD curves in in Figure 6.10. Then Equation 6.27 becomes

$$[Gz_{cc}]_e = [: \Gamma_{pq} :]^* \, [Gz_{qq}] \, [: \Gamma_{pq} :]^T \tag{6.31}$$

where $[Gz_{cc}]_e$ represents the bare fixture interface acceleration spectral density matrix and Γ_{pq} represents the test fixture acceleration transmissibility FRFs. The diagonal N_c x N_c matrix $[Gz_{pq}]$ has zeros at all entries except at $q = 2$ where the test fixture input acceleration ASD that is obtained by enveloping the bare vehicle interface ASD curves is used. The test item acceleration spectral density matrices are obtained by rewriting Equations 6.29 and 6.30 as

$$[Gu_{cc}] = [T_{cc}]^*[TF]^* \, [\, [Gz_{cc}]_e \,] \, [TF][T_{cc}] \tag{6.32}$$

$$[Gu_{ee}] = [T_{ec}]^*[TF]^* \, [\, [Gz_{ec}]_e \,] \, [TF][T_{ec}] \tag{6.33}$$

where $[Gu_{cc}]$ and $[Gu_{ee}]$ represent the test item connector and external acceleration spectral densities that include both ASDs on the diagonal and CSDs on the off diagonals. Notice that when the rigid test fixture is used, the test item laboratory response is governed by the **Q-T** matrix relationship given in Equation 6.28, i.e., all test item interface points are driven by the same input motion due to the rigidity of the fixture.

However, since the vehicle's model shown in Figure 6.3 became the test fixture in the laboratory environment, Equations 6.31 are used with Equations 6.32 and 6.33 to obtain the the test item acceleration ASD responses for both the *rigid* and *flexible* test fixture cases. These motions are shown in Figures 6.12, 6.13, 6.14, and 6.15. Figures 6.12 and 6.13 show the interface acceleration ASDs Gu_{11} and Gu_{33}, respectively, while Figures 6.14 and 6.15 show the external acceleration ASDs Gu_{22} and Gu_{44}, respectively for both the *rigid* and *flexible* test fixture cases. The original field ASDs are shown by the dotted lines, but these curves were multiplied by a factor of 10^4 in order to plot in the same range as the laboratory data. This indicates that the acceleration ASDs are significantly in error in terms of levels of magnitude.

The two interface motions for the *rigid* case (Gu_{11} and Gu_{33}) are depicted by the dashed-dotted and are essentially flat with a value near 100 as required to envelope the bare vehicle input motion shown in Figure 6.10. This is the expected result and serves as a good indication that the inputs were correctly calculated. In the *rigid* test fixture case, each of the two test item external points show a single resonance with one at 58.0 Hz in the Gu_{44} ASD where mass M_4 resonates on spring K_4 and one at 106.2 Hz in the Gu_{22} ASD where mass M_2 resonates on springs K_2 and K_3 since interface points 1 and 3 have the same motion due to test fixture rigidity.

The *flexible* test fixture case is shown by the solid line curves in Figures 6.12, 6.13, 6.14, and 6.15. In this case, three resonances are present in each ASD. These resonances occur at 56.0 Hz, 80.0 Hz, and 119.5 Hz and correspond to the natural frequencies of the combined test fixture and test item.

It is clearly evident from these resulting laboratory motions that poor estimates of either the test item acceleration levels or its natural frequencies were achieved in this example. The excessive vibration levels are due to using a flat input envelope that equals or exceeds the highest bare vehicle interface acceleration ASD peaks. The resulting inaccurate natural frequencies is due to the use of a *rigid* or *nearly rigid* fixture that

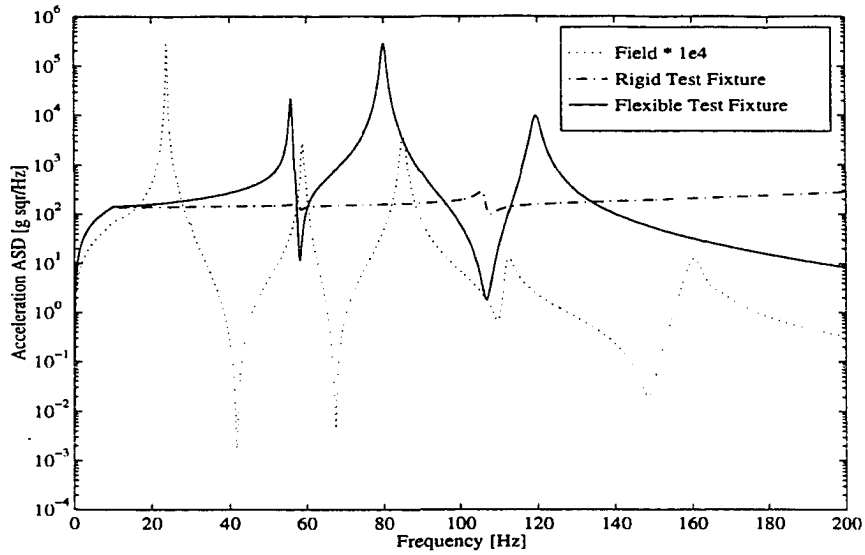

Figure 6.12 Test item acceleration ASD at interface point 1 due to excitation Gz_{22} applied to rigid and flexible test fixtures; Dotted line: Field*10^4, Dashed-Dotted: Rigid Fixture, Solid Line: Flexible Fixture

does not match the vehicle driving point and transfer accelerances as required. Hence, a significant over-test has occurred in this case and an estimate of just how significant of an over-test actually occurred is needed.

Exploring the Amount of Over-test

A direct measure of the amount of over-test that occurred during the laboratory simulation shown in the previous section can be determined by comparing the strain levels that occur in the test item when in the field environment to those obtained in the laboratory environment when both *rigid* and *flexible* test fixtures are employed. The basic definition of strain is the relative displacement of two adjacent points divided by the original distance between the points. Hence, relative displacements between adjacent points in the test item while in the field and laboratory environments can be used as a direct measure of test item strain.

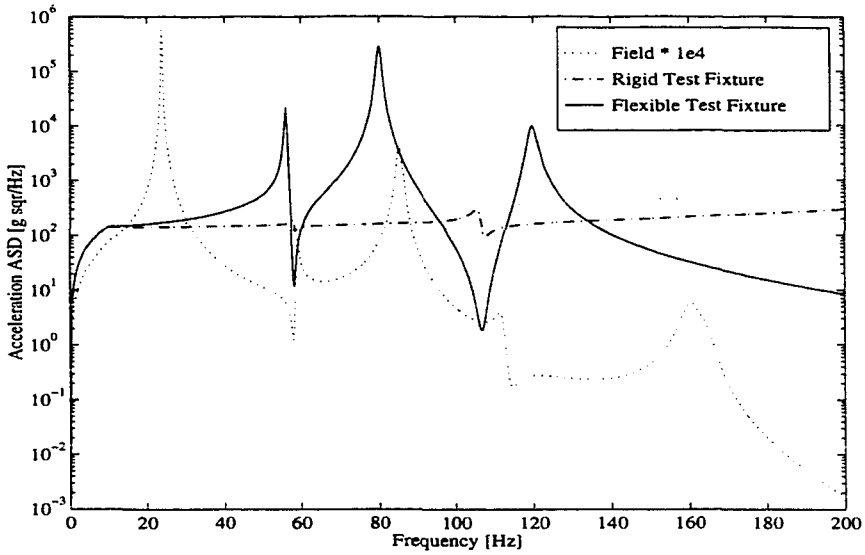

Figure 6.13 Test item acceleration ASD at interface point 3 due to excitation Gz_{22} applied to rigid and flexible test fixtures; Dotted line: Field*10^4, Dashed-Dotted: Rigid Fixture, Solid Line: Flexible Fixture

The relative displacement frequency spectra between two adjacent points p and q, X_{pq}, can be obtained from the acceleration ASDs Gx_{pp} and Gx_{qq} for each point and the real part of the acceleration CSD Gx_{pq} by the relationship

$$X_{pq} = \frac{g_o}{\omega^2} \left[\Delta f(Gx_{pp} + Gx_{qq} - 2\ Re(Gx_{pq}))\right]^{1/2} \tag{6.34}$$

where g_o is the acceleration of gravity in units of 9.81 $m/s^2/g$, Δf is the frequency component spacing in Hz, and ω is the corresponding frequency. Equation 6.34 is used to calculate the relative displacements X_{12}, X_{23}, and X_{34} for the field and laboratory environments which are plotted in Figures 6.16, 6.17, and 6.18. There are three things to note about the field relative displacements. First, they must be multiplied by a factor of 100 in order to plot in the same range as the laboratory relative displacements. Second, they tend to drop off with a slope of about $1/\omega^3$ while the laboratory relative

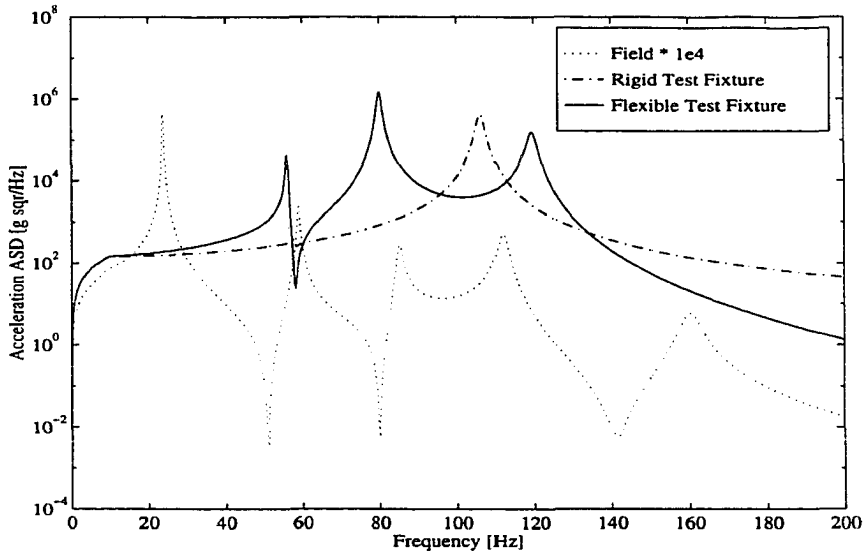

Figure 6.14 Test item acceleration ASD at external point 2 due to excitation Gz_{22} applied to rigid and flexible test fixtures; Dotted line: Field*10^4, Dashed-Dotted: Rigid Fixture, Solid Line: Flexible Fixture

displacements have a much shallower slope. Third, there are five resonant peaks in each relative field motion while the laboratory relative motions have fewer resonant peaks. It is clear that laboratory and field strains are significantly different.

The *rigid* test fixture case shows only one resonant frequency for X_{12} and X_{23} at 106 Hz while X_{34} shows a single resonance at 58 Hz. The *flexible* test fixture case shows the same three resonant peaks in each relative displacement since the test fixture motion of point 3 allows the motion of point 4 to communicate with the motion of points 1 and 2 in this case compared to the *rigid* test fixture case.

It is difficult to compare these relative displacements and decide the relative damage potential since these damage estimates depend on the variables involved in the fatigue theory used. Among these variables are the distribution of peak strains in terms of amplitude and frequency in the frequency domain and the probability density distribution of peaks in the time domain. In this work, a figure of merit is used to explain the amount

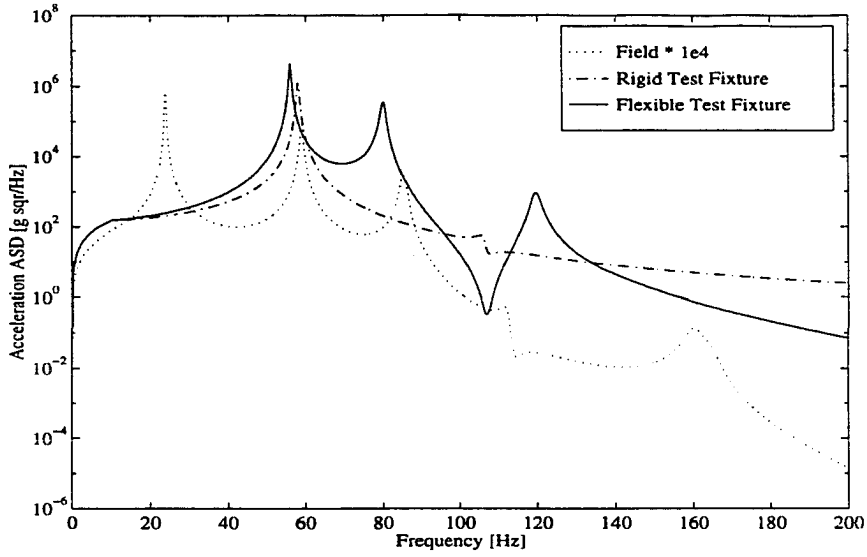

Figure 6.15 Test item acceleration ASD at external point 4 due to excitation Gz_{22} applied to rigid and flexible test fixtures; Dotted line: Field*10^4, Dashed-Dotted: Rigid Fixture, Solid Line: Flexible Fixture

of over-test.

A Figure of Merit to Access the Amount of Over-Test

A simple *Figure of Merit* (FOM) for comparing the potential fatigue damage of the three cases cited is proposed. This FOM is obtained by taking the product of each relative displacement FRF peak amplitude times its corresponding frequency in Hz

$$FOM = (X_{pq})_{peak}\ f_{peak} \tag{6.35}$$

This FOM is a measure of how fast damage is accumulated at each peak. In addition, each FOM from each resonant frequency can be added up and comparisons of this sum between test environments can be made.

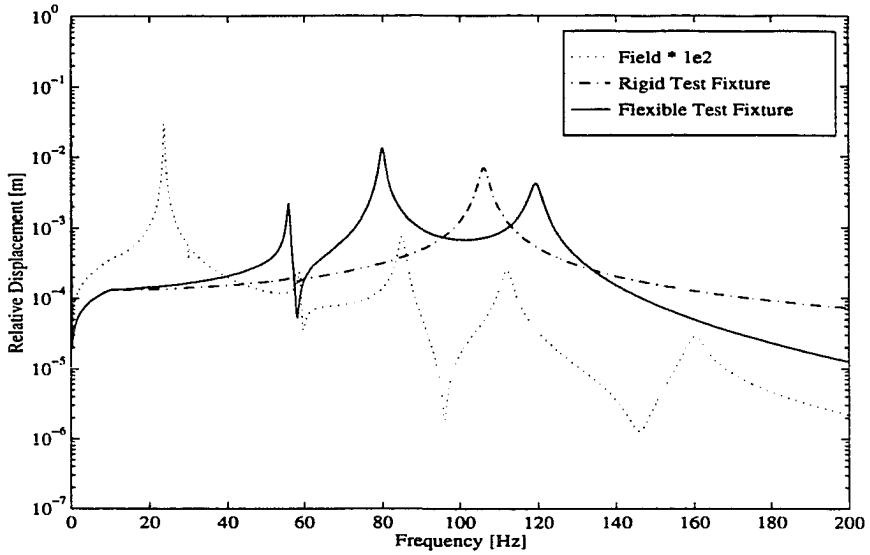

Figure 6.16 Test item relative displacement U_{12} both rigid and flexible laboratory simulations Dotted line: Field*10^2, Dashed-Dotted: Rigid Fixture, Solid Line: Flexible test fixture

Comparing Relative Displacements X_{12}

It is clear from Table 6.2 that the first natural frequency is the dominant strain damage element in the field environment with a relative amplitude of 302 x 10^{-6} m at 23.9 Hz while other significant damage situation occurs at the third resonance (85 Hz at 7.52 x 10^{-6} m). The other field peaks should contribute little to field fatigue in this case. For the *rigid* test fixture case, there is only one resonant component at 106.7 Hz with an amplitude of $7,411$ x 10^{-6} m. In the *flexible* test fixture case, there are three strain peaks. The 80 Hz peak of $14,020$ x 10^{-6} m is the largest with the other two being $2,340$ x 10^{-6} m and $4,450$ x 10^{-6} m at 56 Hz and 119.5 Hz, respectively.

The corresponding results in Table 6.2 shows that the total FOM for the field case is 8.33 x 10^{-3} mHz while the *rigid* test fixture has a total FOM of 791 x 10^{-3} mHz and the flexible test fixture has a FOM of $1,783$ x 10^{-3} The ratio of the total FOM to that in the field shows that the *rigid* test fixture is about 95 times more severe and the *flexible*

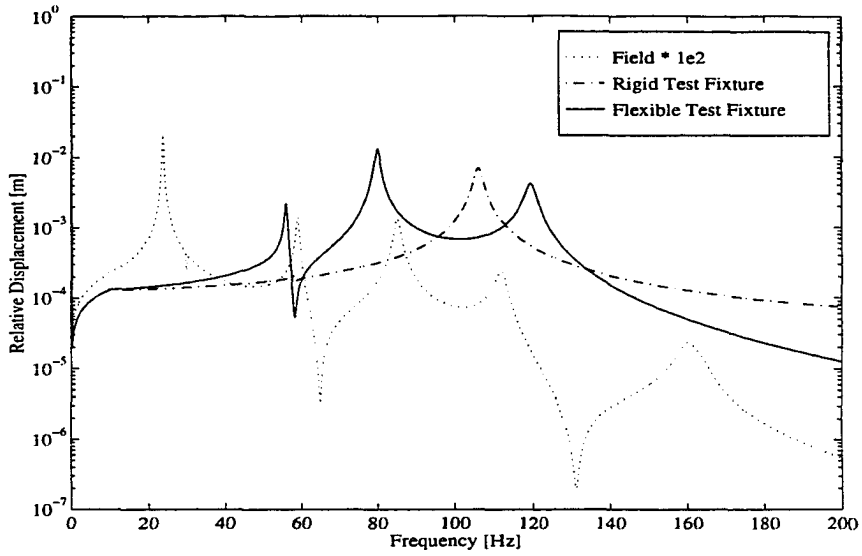

Figure 6.17 Test item relative displacement U_{23} both rigid and flexible laboratory simulations Dotted line: Field*10^2, Dashed-Dotted: Rigid Fixture, Solid Line: Flexible test fixture

test fixture case is about 214 times more severe than the field environment.

Comparing Relative Displacements X_{23}

The results for the relative displacement X_{23} is shown in Table 6.3. In this case, the field total FOM is 7.39 x 10^{-3} mHz while the *flexible* test fixture case has a total FOM of 1,784 x 10^{-3} mHz. The ratio of the total FOM to that in the field shows that the *rigid* test fixture is about 107 times more severe and the *flexible* test fixture case is about 242 times more severe than the field environment.

Comparing Relative Displacements X_{34}

The results for the relative displacement X_{34} is shown in Table 6.4. In this case the field total FOM is 15.88 x 10^{-3} mHz while the *rigid* test fixture case has a total FOM of 2,530 x 10^{-3} mHz and the *flexible* test fixture case has a total FOM of 6,440 x 10^{-3} mHz. The ratio of the total FOM to that in the field shows that the *rigid* test fixture is about

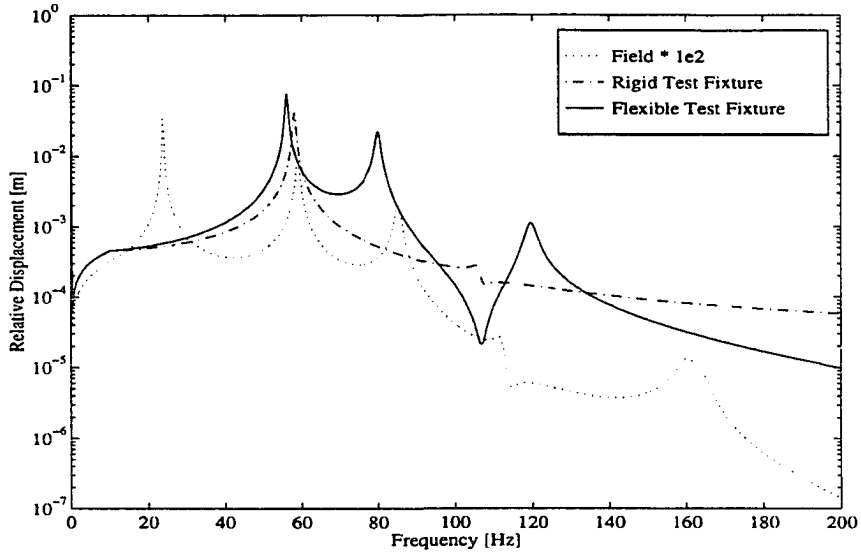

Figure 6.18 Test item relative displacement U_{34} both rigid and flexible laboratory simulations Dotted line: Field*10^2, Dashed-Dotted: Rigid Fixture, Solid Line: Flexible test fixture

159 times more severe and the *flexible* test fixture case is about 405 times more severe than the field environment.

Comparing the Different Relative Displacement FOM Results

It is clear that the displacement FOM values for X_{12} and X_{23} are nearly equal (8.30 x 10^{-3} mHz and 7.39 x 10^{-3} mHz) while X_{34} has nearly twice these values (15.88 x 10^{-3} mHz) when in the field environment. This implies that fatigue failure should occur due to X_{34} strains. Similarly, a comparison of the FOM for the *rigid* test fixture case it is seen that the FOM has increased about 100 times for relative displacements X_{12} and X_{23} and about 160 times for relative displacement X_{34}. Now, a comparison of the FOM for the *flexible* test fixture case it is seen that the FOM has increased about 214 to 241 times for relative displacements X_{12} and X_{23} and about 405 times for X_{34}. These results imply that failure should occur in the correct location in the test item structure but at a much faster rate than would occur in the field. In addition,

Table 6.2 Analysis of relative displacement X_{12}

	FIELD			
No.	Frequency $[Hz]$ $.10^0$	Amp. $[m]$ $.10^{-6}$	FOM $[mHz]$ $.10^{-3}$	Ratio
1	23.9	302.00	7.22	
2	58.9	2.36	0.14	
3	85.0	7.52	0.64	
4	112.0	2.52	0.28	
5	160.2	0.28	0.04	
Total			8.33	1
	RIGID			
1	106.7	7,411	791	
Total			791	95
	FLEXIBLE			
1	56.0	2,340	131	
2	80.0	14,020	1,120	
3	119.5	4,450	532	
Total			1,783	214

it is noted that the rigid test fixture can significantly alter both natural frequencies and mode shapes. Thus, a correlation between field fatigue life and laboratory fatigue lives may be purely coincidental as in this case.

Chapter Summary

This chapter discusses motion transmissibility concepts and it applications to test situations where multiple connectors exist between the test item and either the vehicle or test fixture. The single point transmissibility concept is extended for the case of multiple connectors when no external forces act on the test item. A transformation called the **Q-T** matrix transformation is defined. This transformation is used to estimate the test item motions at external points from knowledge of the interface motions. The **Q-T** Matrix is used in numerical simulations involving deterministic and random signals. The results obtained from the application of this multi-connector transmissibility approach

Table 6.3 Analysis of relative displacement X_{23}

	FIELD			
No.	Frequency $[Hz]$ $.10^0$	Amp. $[m]$ $.10^{-6}$	FOM $[mHz]$ $.10^{-3}$	Ratio
1	23.9	214.00	5.11	
2	58.9	14.12	0.83	
3	85.0	13.40	1.14	
4	112.0	2.40	0.27	
5	160.2	0.23	0.04	
Total			7.39	1
	RIGID			
1	106.7	7,400	790	
Total			790	107
	FLEXIBLE			
1	56.0	2,330	130	
2	80.0	14,020	1,122	
3	119.5	4,450	532	
Total			1,784	242

to deterministic excitation and response signals can be summarized as follows

- *Both* simulations, where the test item is attached to a *rigid* test fixture and a *single* vibration exciter is employed to excite the test item, gave inaccurate external acceleration results. Equation 6.13 was used to predict the test item external motions U_2 and U_4 by using two different combinations of field interface accelerations as test item inputs.

- When the test item is attached to multiple vibration exciters, the **Q-T** matrix approach gave good estimates of external accelerations for both U_2 and U_4. In this case, Equation 6.12 is used to calculate each external motion where each entry of the **Q-T** matrix is multiplied by a different interface acceleration. The resulting **Q-T** matrix in this example is given by Equation 6.20 where it is seen that it is a function of Δ_{cc}, i.e, the determinant of the test item interface accelerance FRF matrix.

Table 6.4 Analysis of relative displacement X_{34}

	FIELD			
No.	Frequency $[Hz]$ $.10^0$	Amp. $[m]$ $.10^{-6}$	FOM $[mHz]$ $.10^{-3}$	Ratio
1	23.9	336.0	8.03	
2	58.9	103.5	6.10	
3	85.0	14.81	1.69	
4	112.0	0.27	0.03	
5	160.2	0.13	0.02	
Total			15.88	1
	RIGID			
1	58.0	43,100	2,500	
2	106.7	292	31.2	
Total			2,530	159
	FLEXIBLE			
1	56.0	79,200	4,400	
2	80.0	23,200	1,856	
3	119.5	1,182	141	
Total			6,440	405

Simulation results involving the application of motion transmissibility concepts in random vibration test environments using current vibration testing procedures can be summarized as follows

- The test fixture dramatically alters the dynamic response characteristics of the test item, i.e, natural frequencies and mode shapes when compared to its field characteristics where it is attached to the vehicle.

- The enveloping of the bare vehicle interface acceleration ASD creates excessive input levels that are certainly conservative.

- Test item fatigue accumulates at significantly faster rates when using rigid test fixtures and enveloped inputs.

- Flexible test fixtures can produce excessively high fatigue levels when compared with rigid test fixtures.

7 EXPERIMENTAL INVESTIGATION

The simulated results presented in Chapters 4 and 5 indicated that the pseudo-inverse technique [9, 10, 11] yields good estimates of both field interface and external forces for both deterministic and random excitation signals. This chapter presents an experimental analysis of a simple structure in order to access the feasibility of using the pseudo-inverse technique to predict input forces from measured field acceleration data. This pseudo-inverse technique is employed with both deterministic and random type of response signals in the force identification problem as well as with random response signals when using the **Q-T** matrix approach.

Description of the Experimental Setup

The test item used in this experimental investigation is a 2.3 x 0.03175 x 0.0254 m (92 x 1.25 x 1.0 in) cold rolled steel beam that is supported by flexible cords in order to simulate the free free boundary condition. Two slightly different test setups were employed as shown in Figure 7.1. Figure 7.1a shows the first experimental setup where the beam is excited at two locations by two vibration exciters. The first exciter is attached at the beam's mid point (MB Dynamics model Modal 50) while the second exciter is attached at the beam's left end (B&K model 4808). The second setup is shown in Figure 7.1b and employs the same excitation arrangement as in Figure 7.1a, except that in this case two 0.22 Kg ($\cong$ 0.5 lb) rigid masses are attached to the beam's right end (point 1). These masses are used to introduce a third external force to the

beam which is an inertia force that is calculated from Newton's second law since the acceleration is measured at location A_1.

Input and output vibration signals were gathered by a 486 PC computer equipped with the Data Physics Dp420© data acquisition and signal processing board [7].

Frequency response function (FRF) measurements were performed on the bare beam in the $0-625$ Hz frequency range which contains the first seven natural frequencies. A total of 984 spectral lines were used so that the frequency resolution is $\Delta f = 0.6357$ Hz and the analysis period is $\Delta t = 1.57$ s. A single exciter driven by pseudo-random excitation was used in the FRF measurements so that rectangular windows can be employed in both the input and output channels since there is no filter leakage in this case. Table 7.1 gives the first seven bending natural frequencies in the $0-625$ Hz frequency range that were obtained by curve fitting the experimental accelerance FRFs using ICATS© modal analysis software [20]. The experimental natural frequencies are compared with values obtained analytically from a continuous model [25]. Figures 7.2 and 7.3 show both the experimental and curve-fitted driving point accelerances for the excitation points 3 and 4, respectively, while Figure 7.4 shows the experimental and curve-fitted transfer accelerances between points 3 and 4. Note that each curve has a low frequency rigid body pendulum type of vibration below 10 Hz that is ignored in the analysis.

Table 7.1 Beam's natural frequencies

Number	Continuous Model Hz	Experimentally Curve-fitted Hz
1	24.30	25.30
2	67.60	67.98
3	132.40	131.22
4	218.00	216.60
5	327.00	322.53
6	457.00	450.60
7	608.00	597.62

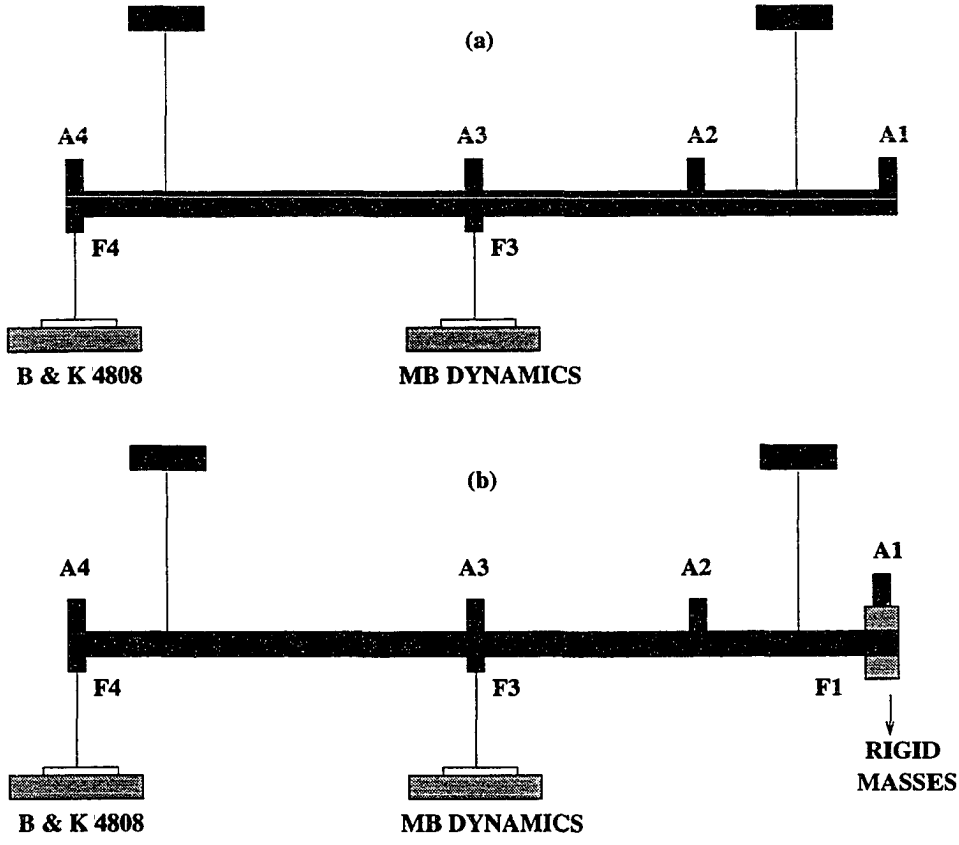

Figure 7.1 Experimental setups for force prediction: (a) Two external forces applied to the beam; (b) Three external forces applied to the beam

Excitation forces were applied at the beam's mid and end point (F_3 and F_4) and were measured by piezoelectric force transducers in order to have a comparison basis for the predicted forces. The beam's output acceleration was measured at four locations (A_1, A_2, A_3, and A_4) as indicated in Figures 7.1a and b. Table 7.2 contains the specifications of the transducers used for each measurement.

Table 7.2 Characteristics of sensors used in tests

Sensor Type	Position on Beam	Sensor Model	Sensitivity	Unit
Force	F3	PCB 208/A03	2.57	mv/N
Force	F4	PCB 208/A03	2.57	mv/N
Accel.	A1	PCB 302A	10.09	mv/g
Accel.	A2	Endveco 2222C	1.70	pc/g
Accel.	A3	PCB 302A	10.18	mv/g
Accel.	A4	PCB 302A02	10.04	mv/g

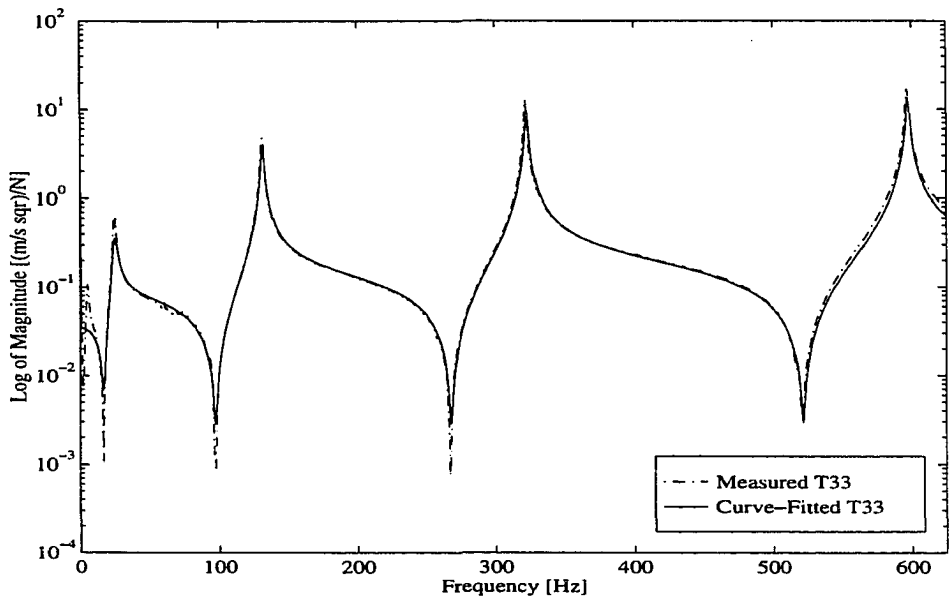

Figure 7.2 Free free beam's experimental and curve fitted driving point accelerance T_{33}. The experimental T_{33} was obtained by driving the beam with a single exciter with pseudo-random excitation

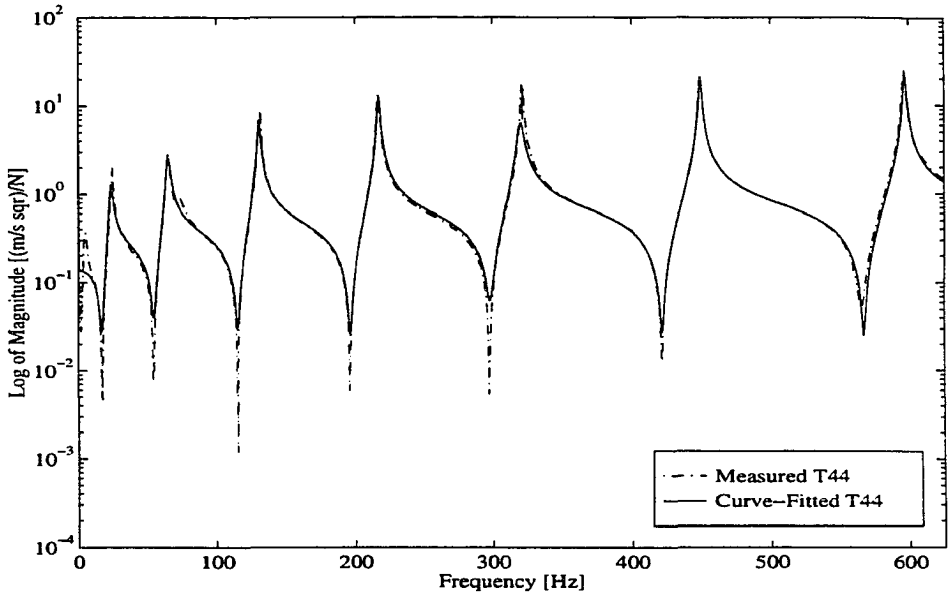

Figure 7.3 Free free beam's experimental and curve fitted driving point accelerance T_{44}. The experimental T_{44} was obtained by driving the beam with a single vibration exciter with pseudo-random excitation

Force Prediction Results When the Excitations are Deterministic With and Without External Loads

In this section, multiple sinusoidal and transient excitations are applied to the free free beam at locations 3 and 4. Since these signals are deterministic (with real and imaginary parts), the input and output signals are measured by the Dp420 in terms of frequency spectra. For this deterministic situation, Equations 4.14 and 4.15 from Chapter 4 are used and are rewritten for the free free beam as

$$\{R\} = [T]^{+} \{X\} \tag{7.1}$$

where superscript "+" denotes the pseudo-inverse of the FRF matrix, and is given by

$$[T]^{+} = \left[[T]^{H}[T]\right]^{-1} [T]^{H} \tag{7.2}$$

where the superscript ^{H} denotes the hermitian conjugate (complex conjugate transpose)

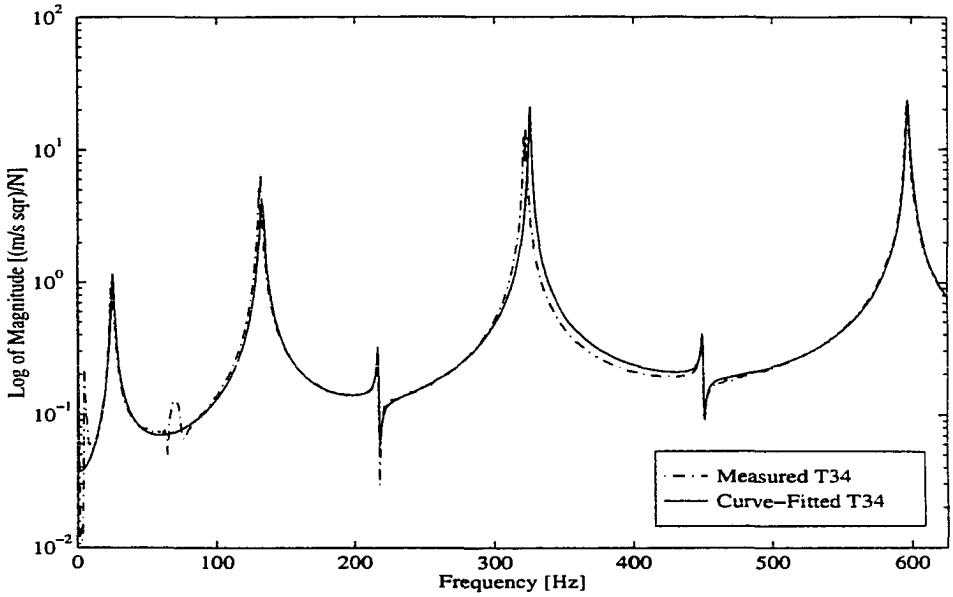

Figure 7.4 Free free beam's experimental and curve fitted transfer accelerance T_{34}. The experimental T_{34} was obtained by driving the beam with a single vibration exciter with pseudo-random excitation

of the beam's accelerance FRF matrix, since $[T]$ is complex.

A potential problem when calculating the pseudo-inverse of the beam's FRF matrix is instrumentation noise. In this case, the beam's curve fitted FRFs could be used to improve the numerical conditioning in the pseudo-inverse process [18]. However, curve fitting errors can also distort the predicted forces [13]. **All force prediction results shown in this chapter were obtained using the beam's measured FRFs.** Curve fitting as well as numerical ill-conditioning of the pseudo-inverse process are investigated at the end of this chapter.

Sinusoidal Excitation Signal

In the first set of measurements, two sinusoidal signals having approximately the same magnitude but different frequencies are used to drive the beam in both setups

shown in Figures 7.1a and b. A single frequency sinusoidal signal at $f_3 = 200\ Hz$ is applied to the beam through the vibration exciter to drive the beam's mid point and its corresponding frequency spectrum is measured by the force transducer $F3$ mounted at point 3. Simultaneously, a second single frequency sinusoidal excitation signal at $f_4 = 350\ Hz$ is applied by the vibration exciter at point 4 and its frequency spectrum is measured by the force transducer $F4$. Hanning windows are used with the input and output channels in order to reduce filter leakage. The beam's output acceleration frequency spectra are measured at all four positions shown in Figures 7.1a and b.

Chirp Excitation Signal

Chirp excitation was employed in the second set of measurements. In this case, both vibration exciters were driven by the same chirp pulse that was generated by the Dp420 system. This chirp was designed to sweep the $0 - 625\ Hz$ frequency range with a duration of $\Delta t_c = 100\ ms$, thus occupying less than 10% of the total analysis period ($\Delta t = 1.57\ s$). Rectangular windows are used with input and output channels in this transient input case.

The acceleration frequency spectra obtained from these experiments were used along with the beam's FRFs in Equations 7.1 and 7.2 in order to predict the beam's input forces when sinusoidal or chirp excitations are used. Table 7.3 summarizes the tests performed as well as the forces obtained in each test.

Table 7.3 Measured and predicted deterministic forces

Case	Setup	Rigid Mass	Input	Measured	Predicted
a	Fig. 7.1 a	No	Sinusoidal	F_3, F_4	R_3, R_4
b	Fig. 7.1 b	Yes	Sinusoidal	F_1, F_3, F_4	R_1, R_3, R_4
c	Fig. 7.1 a	No	Chirp	F_3, F_4	R_3, R_4
d	Fig. 7.1 b	Yes	Chirp	F_1, F_3, F_4	R_1, R_3, R_4

Case a - Two Sinusoidal Input Forces (200 Hz and 350 Hz) with No Rigid Mass

In this case, Equation 7.1 is written as

$$\begin{Bmatrix} R_1 \\ R_2 \\ R_3 \\ R_4 \end{Bmatrix} = \begin{bmatrix} T_{11} & T_{12} & T_{13} & T_{14} \\ T_{21} & T_{22} & T_{23} & T_{24} \\ T_{31} & T_{32} & T_{33} & T_{34} \\ T_{41} & T_{42} & T_{43} & T_{44} \end{bmatrix}^{+} \begin{Bmatrix} X_1 \\ X_2 \\ X_3 \\ X_4 \end{Bmatrix} \tag{7.3}$$

where R_q, $q = 1 \ldots 4$ are the unknown input force frequency spectra, X_p, $p = 1 \ldots 4$ are the measured output acceleration frequency spectra, and T_{pq} are the beam's accelerance FRFs. Equation 7.3 corresponds to the situation where the number and location of inputs are unknown; and hence, as many input forces as output measurements are calculated. On the other hand, when the input forces locations are known, as it is the case for the forces applied by the exciters in Figure 7.1a, then Equation 7.3 can be simplified to

$$\begin{Bmatrix} R_3 \\ R_4 \end{Bmatrix} = \begin{bmatrix} T_{13} & T_{14} \\ T_{23} & T_{24} \\ T_{33} & T_{34} \\ T_{43} & T_{44} \end{bmatrix}^{+} \begin{Bmatrix} X_1 \\ X_2 \\ X_3 \\ X_4 \end{Bmatrix} \tag{7.4}$$

The results for sinusoidal forces R_3 and R_4 predicted through Equation 7.4 and corresponding to case (a) are shown in Figures 7.5 and 7.6. Figure 7.5 shows the measured and predicted force at location 3 as a function of frequency in the 200 Hz and 350 Hz regions. The excitation force at location 3 is at 200 Hz and causes the *primary* response at 200 Hz as well as digital filter leakage. The *secondary* response at 350 Hz is due to the force applied at location 4 which causes motion at location 3. This motion produces

a secondary smaller force to occur that is an inertia force caused by acceleration of the exciter armature.

Figure 7.6 shows the measured and predicted force at location 4 as a function of frequency around 200 Hz and 350 Hz regions. The excitation force at location 4 is at 350 Hz and causes the *primary* response at 350 Hz as well as digital filter leakage. The *secondary* response at 200 Hz is due to the force applied at location 3 which causes motion and a small force due to the exciter armature at location 4.

The *primary response* predicted forces in both Figures 7.5 and 7.6 closely fit the measured values at the peaks and over a $\pm$ 10 Hz region. The *secondary response* predicted forces are not as consistent with location 4 having a better prediction than location 3. Since these were sinusoidal single frequency excitations, only the values at 200 Hz and 350 Hz should be compared since the off excitation frequency components are due to digital filter leakage.

Case b - Two Sinusoidal Input Forces (200 Hz and 350 Hz) with Rigid Masses

In this case the two 0.22 Kg rigid masses were attached to the beam's free end at location 1 as shown in Figure 7.1b in order to introduce a third inertia type of force to act on the beam. The forces are calculated by rewriting Equation 7.4 as

$$\begin{Bmatrix} R_1 \\ R_3 \\ R_4 \end{Bmatrix} = \begin{bmatrix} T_{11} & T_{13} & T_{14} \\ T_{21} & T_{23} & T_{24} \\ T_{31} & T_{33} & T_{34} \\ T_{41} & T_{43} & T_{44} \end{bmatrix}^{+} \begin{Bmatrix} X_1 \\ X_2 \\ X_3 \\ X_4 \end{Bmatrix} \tag{7.5}$$

The results for test case (b) are shown in Figures 7.7, 7.8 and 7.9. Figure 7.7 shows the results for the inertia load F_1 where both the measured and predicted forces have

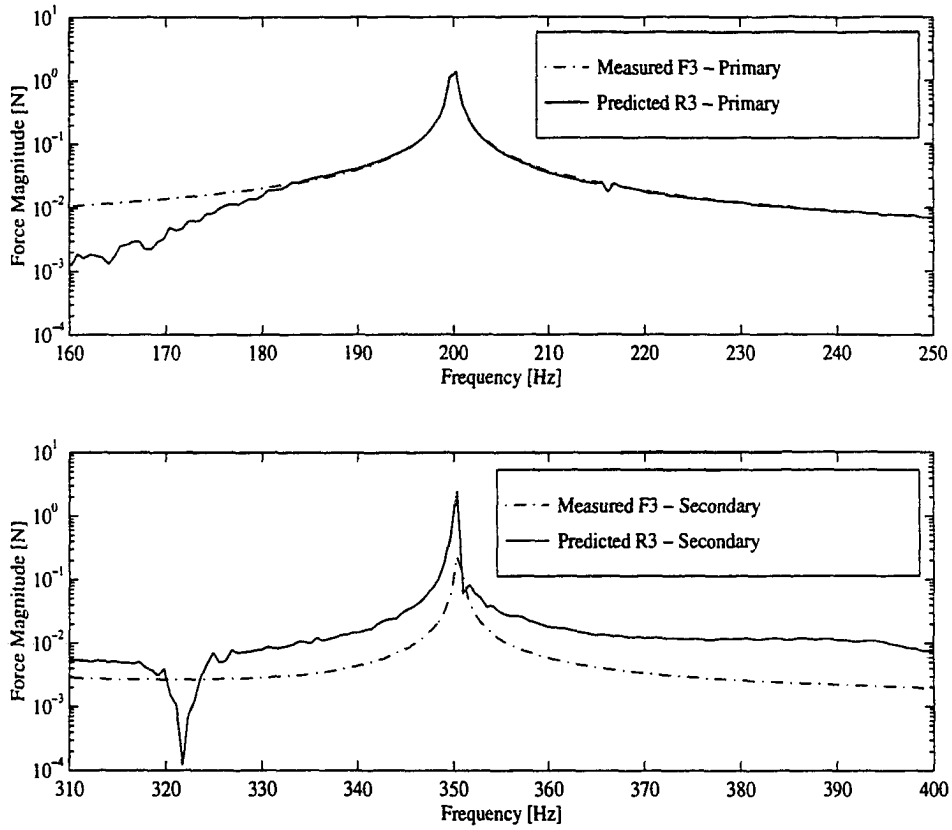

Figure 7.5 Comparison of measured and predicted beam's excitation forces at point 3 that correspond to case (a) when no lumped mass is attached to the beam. Top: Primary; Bottom: Secondary

two peaks in the $0 - 625$ Hz frequency range. In both cases, the inertia loads used for comparison (dashed line) are calculated from the measured acceleration at location 1 (A_1) and the rigid masses attached to the beam through Newton's second law in order to avoid problems with direct force measurement. Measured and predicted results for forces at points 3 and 4 are shown in Figures 7.8 and 7.9, respectively. In general, predicted force results for this case present a good agreement with the corresponding measured forces. However, secondary components in Figures 7.8 and 7.9 were predicted to be larger than the measured forces.

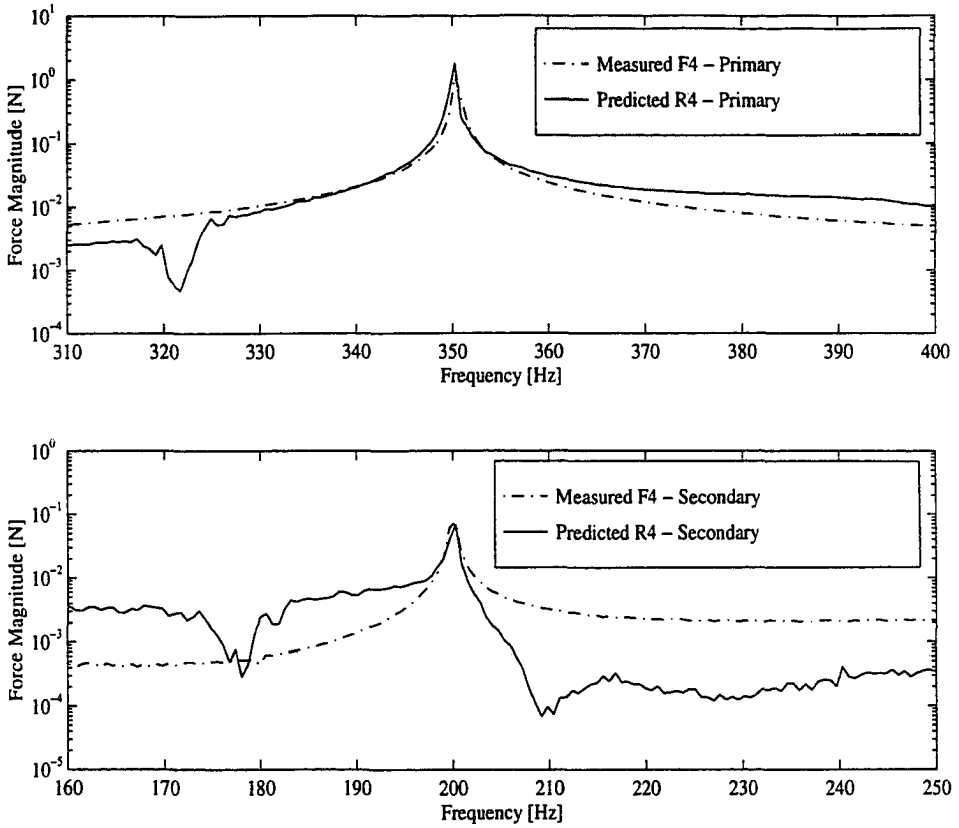

Figure 7.6 Comparison of measured and predicted beam's excitation forces at point 4 that correspond to case (a) when no lumped mass is attached to the beam. Top: Primary; Bottom: Secondary

Case c - Two Simultaneous Chirp Forces at Points 3 and 4 and No Rigid Mass

The $0 - 625\ Hz$ chirp excitation was used in this case. The predicted forces were obtained through Equation 7.4 and they are shown in Figure 7.10 for the chirp applied at the beam's mid point and at the end point. In this case, measured and predicted forces do not give good agreement in the $0 - 50\ Hz$ bandwidth. The measured force F_3 shows a notch at $f \cong 20\ Hz$ while the predicted R_3 shows a peak at this frequency. This behavior was observed before [18, 19]. For frequencies above 50 Hz, both the measured

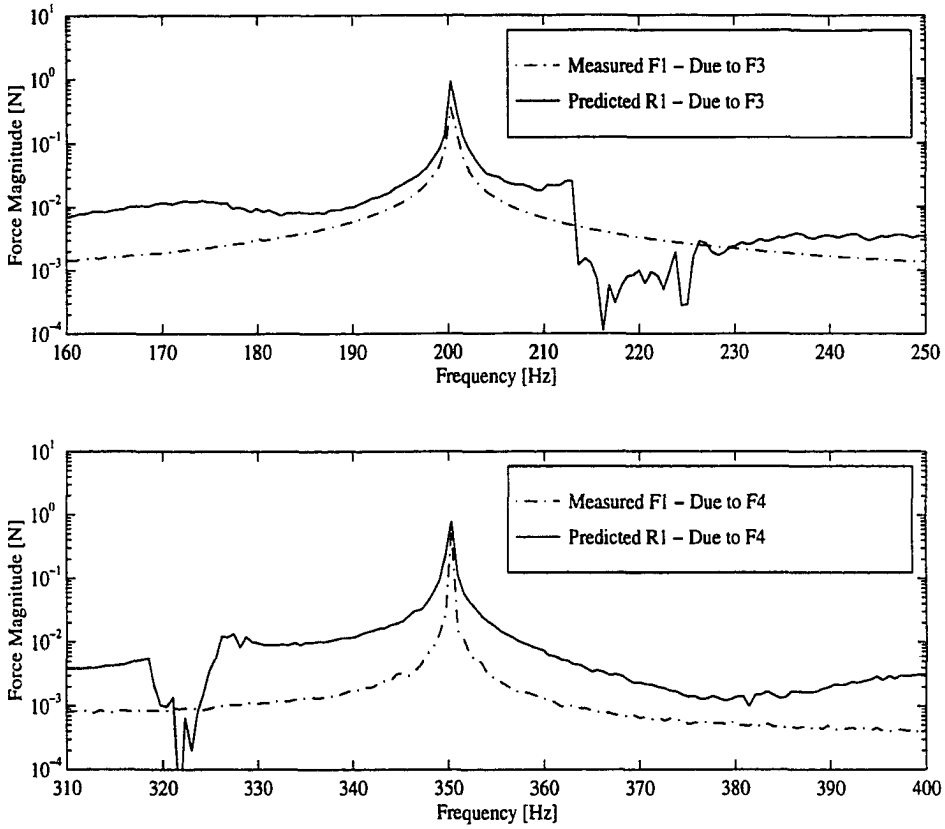

Figure 7.7 The inertia force at location 1 for case (b) due to F_3 at 200 Hz and due to F_4 at 350 Hz. Measured force is obtained from the beam's acceleration frequency spectrum at point 1 through Newton's second law. Top: Inertia force due to F_3; Bottom: Inertia force due to F_4

and pseudo-inverse predicted forces F_3 and F_4 are in close agreement.

Case d - Two Simultaneous Chirp Forces at Points 3 and 4 with Rigid Masses at Location 1

In this case, the experimental setup of Figure 7.1b is used with the same chirp signal being fed to both exciters at 3 and 4. The predicted inertia force at point 1 and the input excitation forces at points 3 and 4 are obtained through Equation 7.5 and they are shown along with the corresponding measured signals in Figures 7.11, 7.12, 7.13,

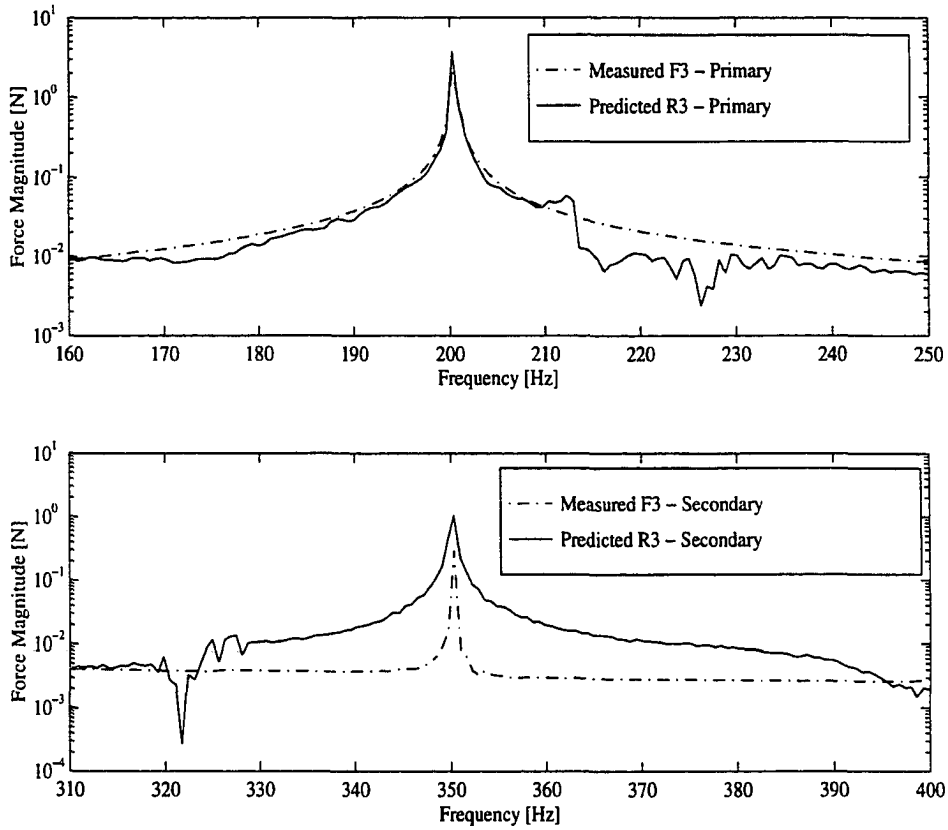

Figure 7.8 Comparison of primary and secondary components of the measured and predicted beam's excitation force at point 3 for case (b). The rigid masses are attached at the beam's right end at point 1. Top: Primary; Bottom: Secondary

and 7.14, respectively. Figure 7.11 shows the results for the inertia load. In this case, measured and predicted results agree closely for frequencies in the neighborhood of the peak forces. At frequencies away from the peak forces, the measured and predicted inertia loads follow the same trend except at the beam's natural frequencies where the predicted force shows significant notches. These notches are caused by the pseudo-inversion of the FRF matrix in Equation 7.5 since this matrix is generally rank deficient at frequencies that coincide with the structure's natural frequencies. This rank deficiency causes numerical difficulties in the calculation of the pseudo-inverse at these frequencies.

The measured and predicted forces at points 3 and 4 are compared in Figures 7.12

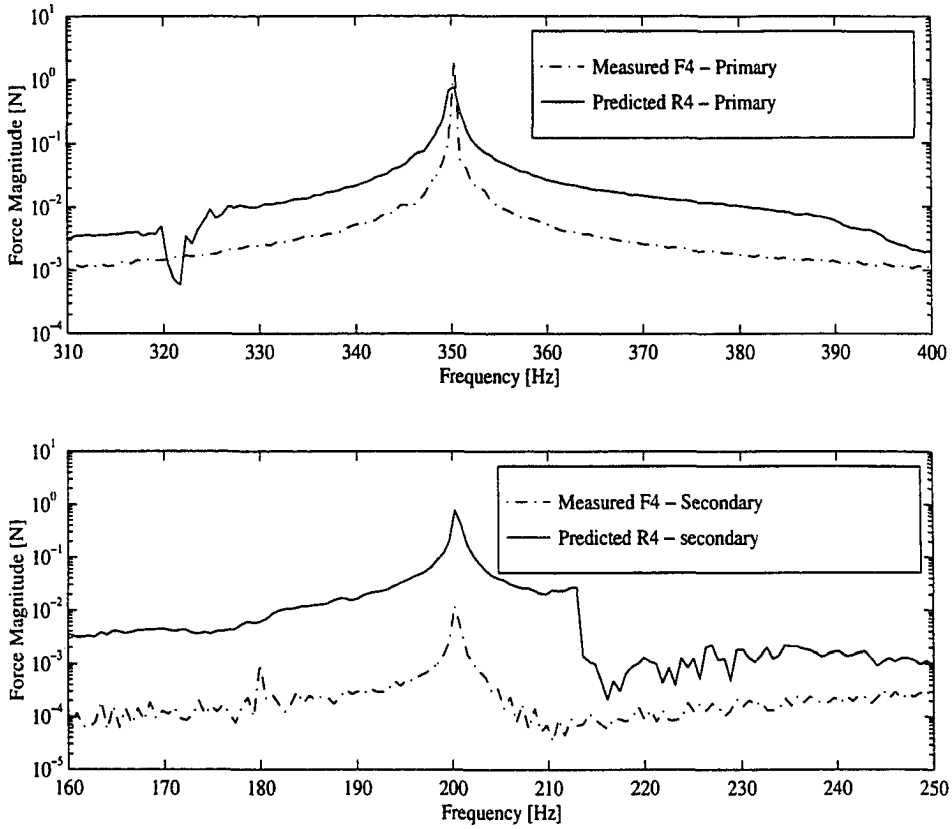

Figure 7.9 Comparison of primary and secondary components of the measured and predicted beam's excitation force at point 4 for case (b). The rigid masses are attached at the beam's right end at point 1. Top: Primary; Bottom: Secondary

and 7.13, respectively. In both cases, it is noticed that measured and predicted forces follow basically the same trend of good agreement except in $0 - 50\ Hz$ frequency range where they do not show good agreement. The presence of notches in the predicted forces that coincide with the beam's natural frequencies are particularly evident in Figure 7.13 which is a point that shows all of the beam's natural frequencies. Figure 7.12 shows fewer notches since only half of the natural frequencies appear at point 3.

Finally, Figure 7.14 shows the measured and predicted results for F_4 in case d when a different vibration exciter is employed at point 4 in the setup of Figure 7.1b. In this case, the B&K 4808 vibration exciter was replaced by an Unholtz-Dickie T206 vibration

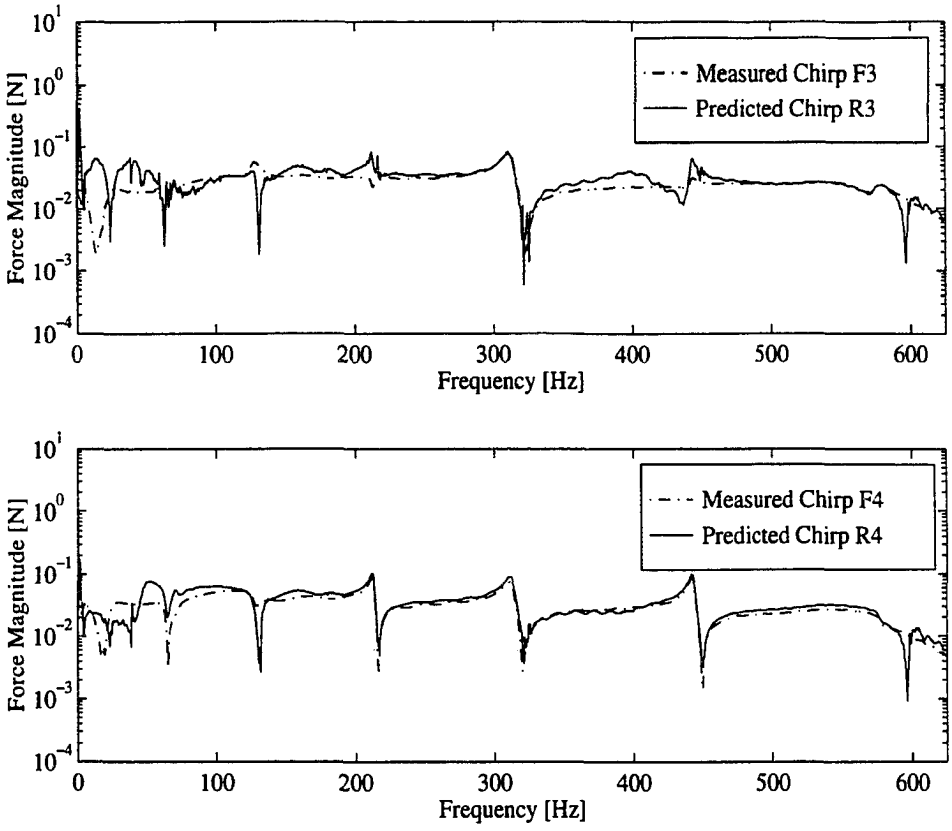

Figure 7.10 Comparison of measured and predicted forces at locations 3 and 4 for the chirp excitation case (c). Both exciters at points 3 and 4 are driven by the same transient chirp and no rigid mass is attached at the beam's right end at location 1

exciter. The Unholtz-Dickie vibration exciter's armature is approximately 9 Kg while the MB Dynamics 50 and the B&K exciters have armature masses of approximately 0.18 Kg. Thus, a large discrepancy in armature masses occurs when the UD T206 is attached at point 4 and the MB Dynamics at point 3, since the first has an armature that is about 50 times more massive than the other.

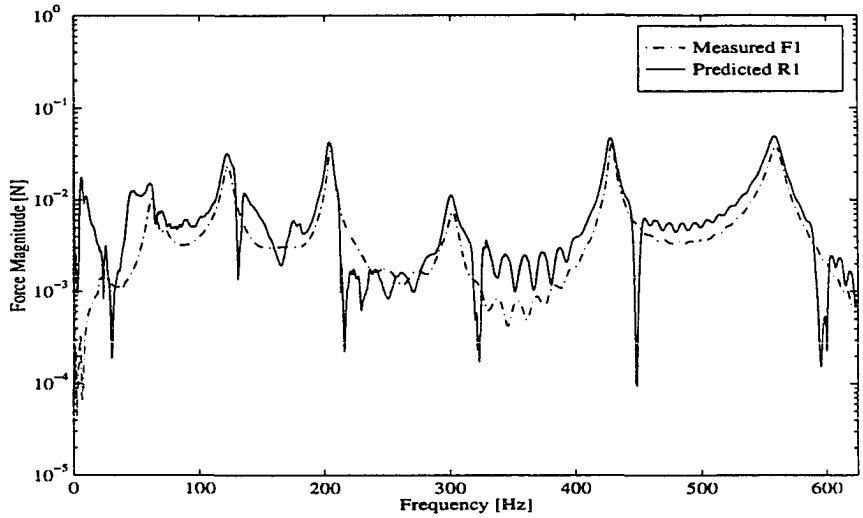

Figure 7.11 Comparison of transient inertia forces F_1 (measured) and R_1 (predicted) through the pseudo-inverse technique for case (d). Both exciters at points 3 and 4 are driven by the same transient chirp signal and the rigid mass is attached at the beam's right end

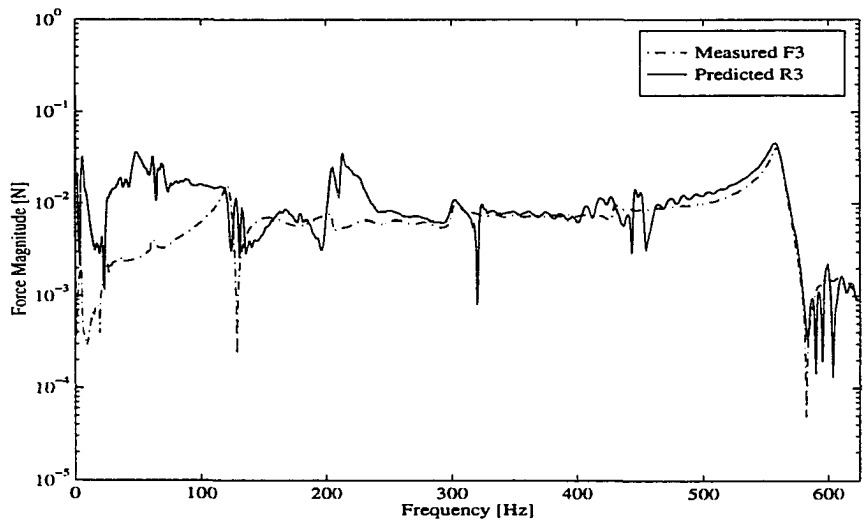

Figure 7.12 Comparison of transient inertia forces F_3 (measured) and R_3 (predicted) through the pseudo-inverse technique for case (d). Both exciters at points 3 and 4 are driven by the same transient chirp signal and the rigid mass is attached at the beam's right end

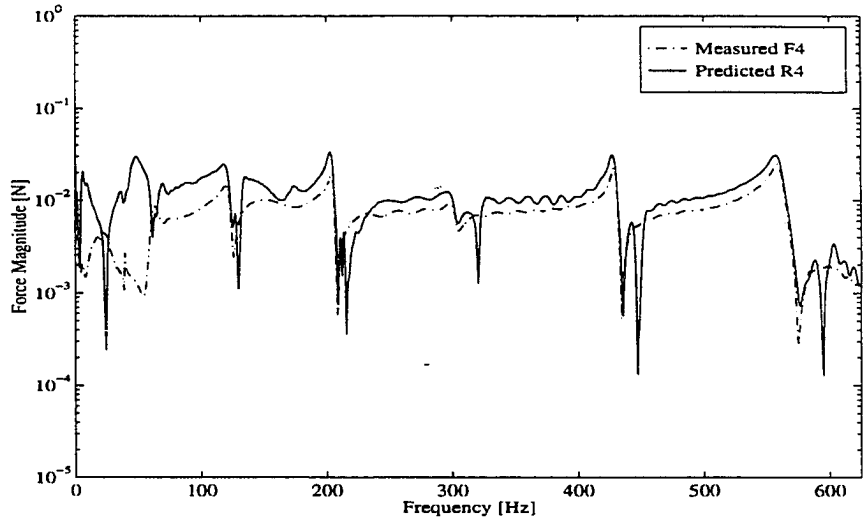

Figure 7.13 Comparison of transient inertia forces F_4 (measured) and R_4 (predicted) through the pseudo-inverse technique for case (d). Both exciters at points 3 and 4 are driven by the same transient chirp signal and the rigid mass is attached at the beam's right end

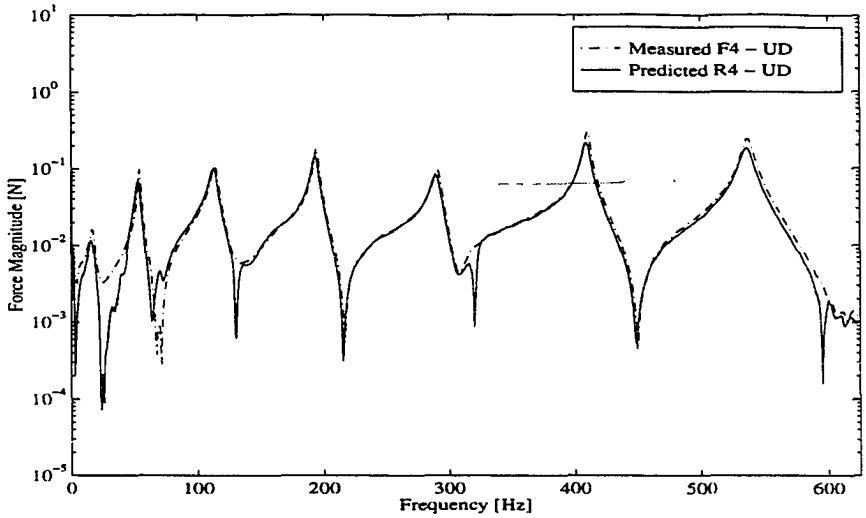

Figure 7.14 Comparison of transient forces f_4 (measured) and R_4 (predicted) predicted through the pseudo-inverse technique for case (d). Both exciters at points 3 and 4 are driven by the same transient chirp signal and the rigid mass is attached at the beam's right end. The excitation at point 4 was applied by the Unholtz-Dickie vibration exciter

By comparing the results for force F_4 when using the Unholtz-Dickie at point 4 instead of the B&K 4808 with the previous result of Figure 7.13, it becomes clear that vibration exciter armature mass can significantly influence the results in laboratory simulations.

Force Prediction When Excitations are Random With and Without External Loads

Two tests are performed with each experimental setup shown in Figure 7.1. In the first test, the random signals that are used to feed the exciters at points 3 and 4 are generated by two independent random signal generators. This is done in order to simulate the case where the input forces are statistically uncorrelated. In the second test, the same random signal is used to feed both vibration exciters at points 3 and

4. This corresponds to the case where the input signals to the vibration exciters are correlated. Table 7.4 summarizes the tests performed as well as the forces identified in each test.

The same data acquisition and processing system as well as force and acceleration transducers used in the previous section are employed in this section.

Table 7.4 Measured and predicted forces for all test cases

Case	Setup	Rigid Mass	Sources	Measured	Predicted
a	Fig. 7.1 a	No	Two	F_3, F_4	F_3, F_4
b	Fig. 7.1 a	No	One	F_3, F_4	F_3, F_4
c	Fig. 7.1 b	Yes	Two	F_1, F_3, F_4	F_1, F_3, F_4
d	Fig. 7.1 b	Yes	One	F_1, F_3, F_4	F_1, F_3, F_4

The experimental data gathered in all four tests listed in Table 7.4 were used in the force prediction process in two different ways. *First*, the input forces and accelerations are assumed to be correlated. This means that the random pseudo-inverse technique equations that were used in the numerical simulations of Chapter 5 are used to predict the beam's input random forces so that

$$[G_{rr}] = [\ [T]^{+}\ ]^{*}\ [G_{xx}]\ [\ [T]^{+}\ ]^{T} \tag{7.6}$$

where $[G_{rr}]$ represents the predicted input force spectral density matrix, $[T]$ contains the free free beam's accelerance FRFs, and $[G_{xx}]$ is the measured output acceleration spectral density matrix that results from the application of the input random forces at points 3 and 4. Application of Equation 7.6 requires the measurement of the beam's acceleration CSDs among the four output accelerations shown in Figures 7.1a and 7.1b. Equation 7.6 will be referred to as the *correlated equation.*

Second, the input forces and consequently the output accelerations are assumed to be uncorrelated. In this case, the following expression from Chapter 5 is used in the force prediction process

$$\{G_{rr}\} = [|T|^{2}]^{+}\ \{G_{xx}\} \tag{7.7}$$

where in this case, only acceleration ASDs are used to predict the input force ASDs. Equation 7.7 is referred to as the *uncorrelated equation.*

The *correlated* (Equation 7.6) and *uncorrelated* (Equation 7.7) relationships are used in each case shown in Table 7.4.

Case a - Two Uncorrelated Random Forces at Points 3 and 4 With No Rigid Mass

The experimental setup of Figure 7.1a is used with two independent random signal generators feeding exciters at 3 and 4. The predicted random force ASDs and CSDs from the *correlated* (Equation 7.6) expression are shown in Figures 7.15 and 7.16. The predicted ASDs from the *uncorrelated* (Equation 7.7) expression are shown in Figure 7.17. By comparing predicted ASD results from Figure 7.15 with those shown in Figure 7.17, it is seen that even when two independent random sources are used with exciters at points 3 and 4, the *correlated* (Equation 7.6) expression gave significantly better results than the *uncorrelated* (Equation 7.7) expression. As seen in Figure 7.16, a reasonable prediction for Gf_{34} was obtained from Equation 7.6 while Equation 7.7 yields no CSD results.

Case b - Two Correlated Random Forces at Points 3 and 4 With No Rigid Masses

Both vibration exciters at 3 and 4 are driven by the same input random excitation signal. The *correlated* Equation 7.6 and *uncorrelated* Equation 7.7 are used to obtain the predicted forces. Figure 7.18 shows a comparison of the measured and predicted force ASDs Gr_{33} and Gr_{44} when the correlated inverse equation is used.

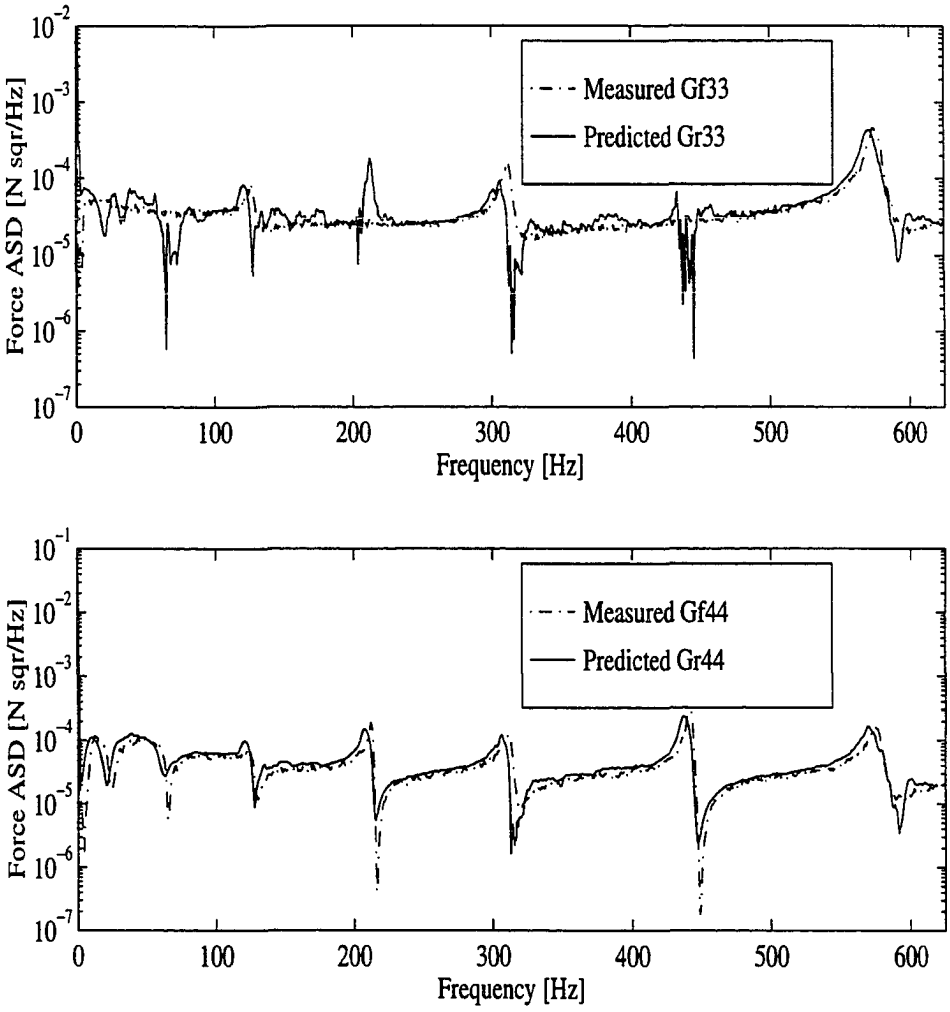

Figure 7.15 Comparison of measured and predicted random force ASDs Gr_{33} and Gr_{44} for case (a) using measured acceleration ASDs and CSDs (*correlated motions*). Predicted force ASDs from the pseudo-inverse technique (solid line) are compared with measured force ASDs (dashed-dotted line). Two independent input random signals are used to drive both exciters and no rigid mass is attached to the beam's right end

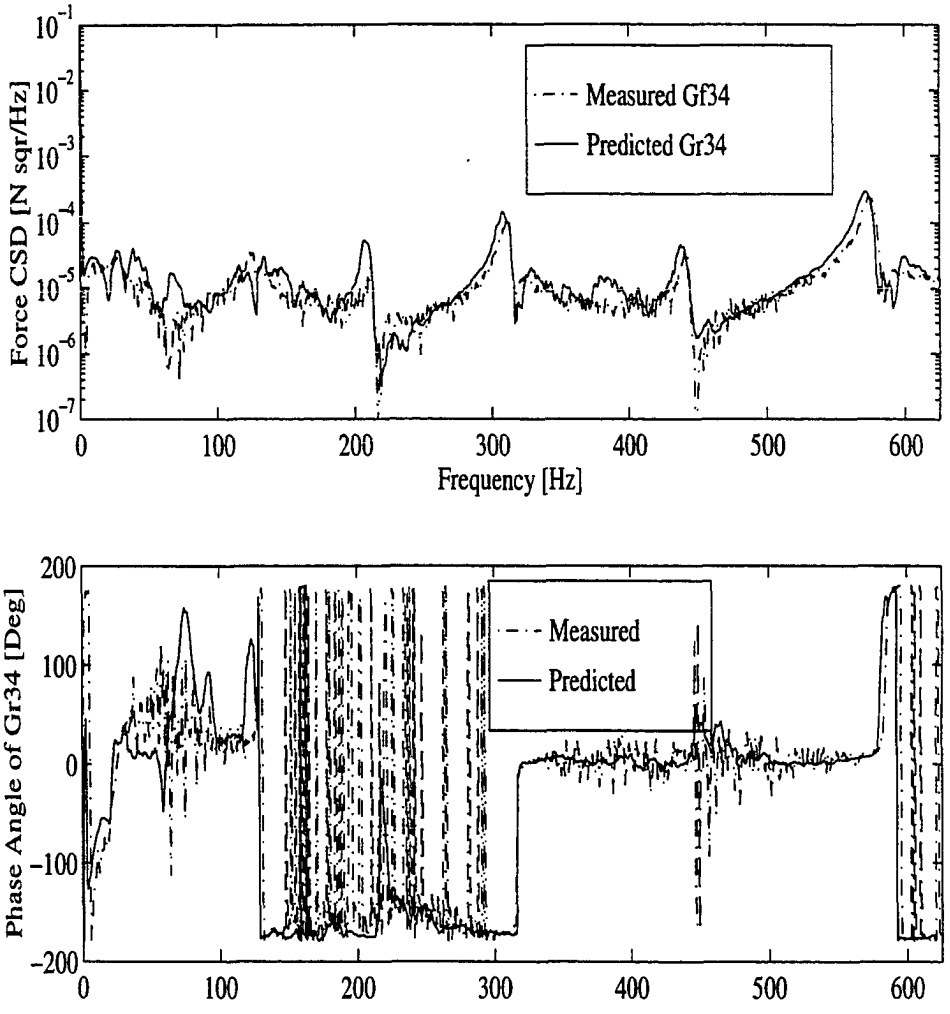

Figure 7.16 Comparison of magnitude and phase angle of measured and predicted random force CSD Gr_{34} for case (a) using measured acceleration ASDs and CSDs (*correlated motions*). The predicted force CSD from the pseudo-inverse technique (solid line) is compared with measured force CSD (dashed-dotted line). Two independent input random signals are used to drive both exciters and no rigid mass is attached to the beam's right end

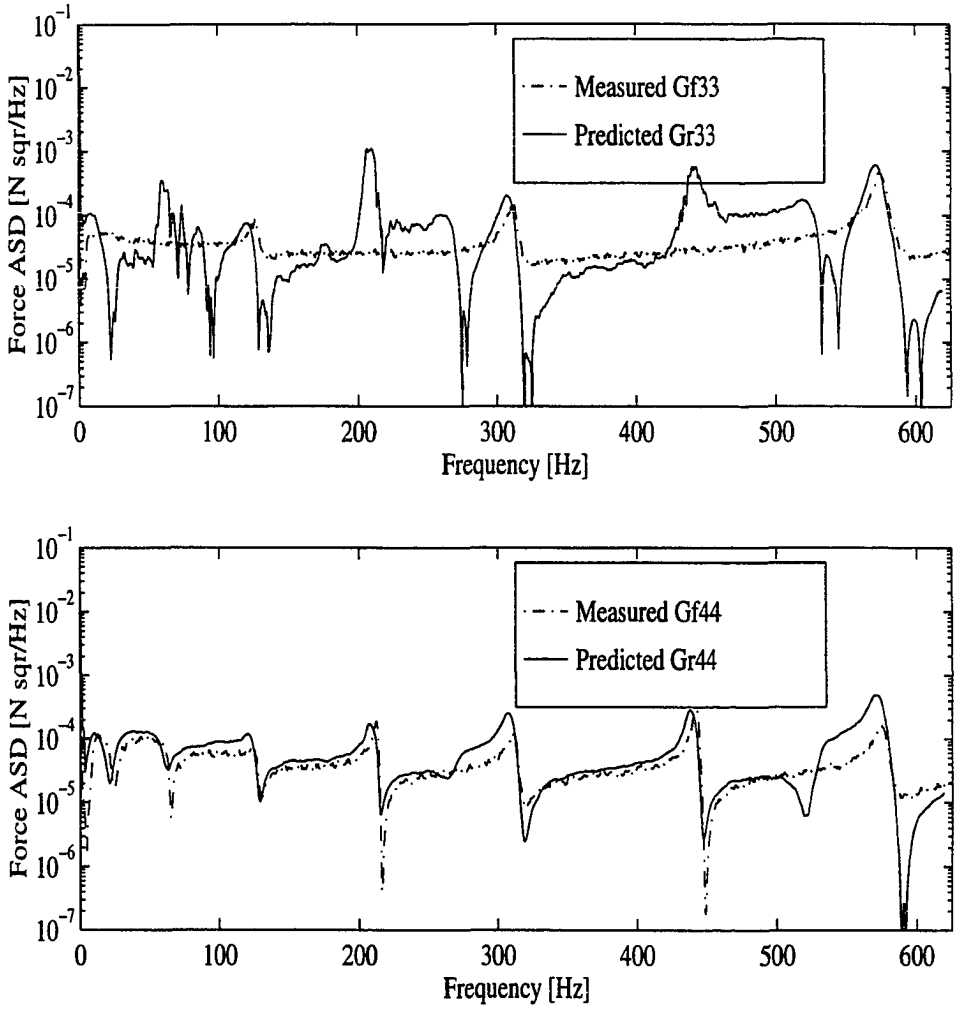

Figure 7.17 Comparison of measured and predicted random force ASDs Gr_{33} and Gr_{44} for case (a) using measured acceleration ASDs (*uncorrelated motions*). Predicted force ASDs from the pseudo-inverse technique (solid line) are compared with measured force ASDs (dashed-dotted line). Two independent input random signals are used to drive both exciters and no rigid mass attached to the beam's right end

Figure 7.19 shows a comparison of the measured and predicted magnitude and phase of the random CSD Gr_{34}. It is clear that there is close agreement over the entire frequency range. The uncorrelated equation is used to predict the force ASDs in Figure 7.20 where it is abundantly clear that significant errors occur at most frequencies. A comparison of Figure 7.18 and 7.20 shows that the correlated equation (Equation 7.6) is superior to the uncorrelated equation (Equation 7.7).

Case c - Two Uncorrelated Random Forces at Points 3 and 4 With Rigid Mass

This test employs the setup shown in Figure 7.1b. Two independent random excitation signals are used as inputs to the exciters at positions 3 and 4. Three forces are predicted in this case, namely, the two measured forces at locations 3 and 4, and the inertia load at location 1 that is applied to the beam by the rigid masses attached to the beam end at 1.

Figures 7.21, 7.22, and 7.23 show a comparison of the measured and predicted force ASDs Gr_{11}, Gr_{33}, and Gr_{44} when the correlated Equation 7.6 is used in the force prediction. The inertia force ASD Gf_{11} was obtained from the acceleration ASD Gx_{11} by using Newton's second law with the rigid masses. Figure 7.24 shows a comparison of the measured and predicted magnitude and phase angle of the force CSD Gf_{34}. This CSD comparison is typical of the results obtained for Gr_{13} and Gr_{14} as well. The predicted force ASDs from the uncorrelated Equation 7.7 are shown in Figures 7.25, 7.26, and 7.27. As in the two previous tests, the force estimates from the *correlated* Equation 7.6 gave far better results than those obtained from the *uncorrelated* Equation 7.7.

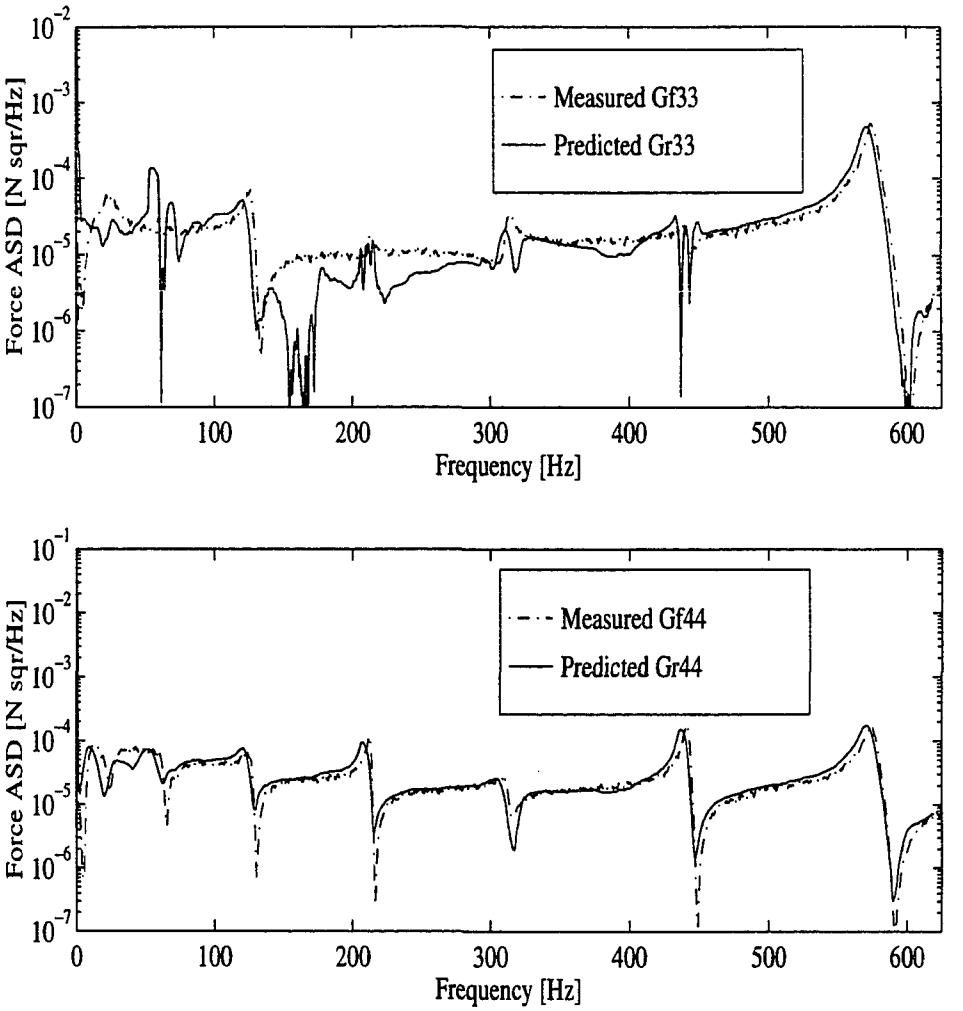

Figure 7.18 Comparison of measured and predicted random force ASDs Gr_{33} and Gr_{44} for case (b) using measured acceleration ASDs and CSDs (*correlated motions*). Predicted force ASDs from the pseudo-inverse technique (solid line) are compared with measured force ASDs (dashed-dotted line). A single random input signal is used to drive both exciters and no rigid mass is attached to the beam's right end

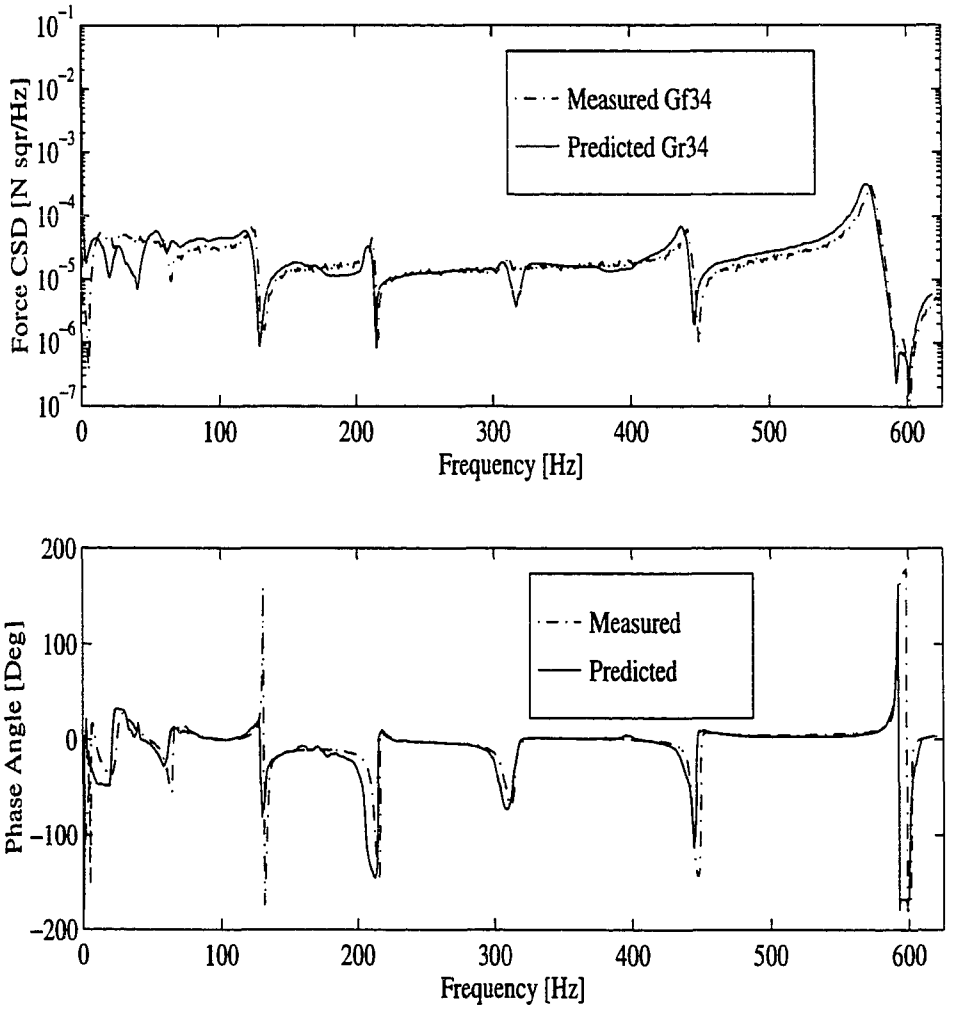

Figure 7.19 Comparison of measured and predicted magnitude and phase angle of the random force CSD Gr_{34} for case (b) using measured acceleration ASDs and CSDs (*correlated motions*). The predicted force CSD from the pseudo-inverse technique (solid line) is compared with measured force CSD (dashed-dotted line). A single random input signal is used to drive both exciters and no rigid mass is attached to the beam's right end

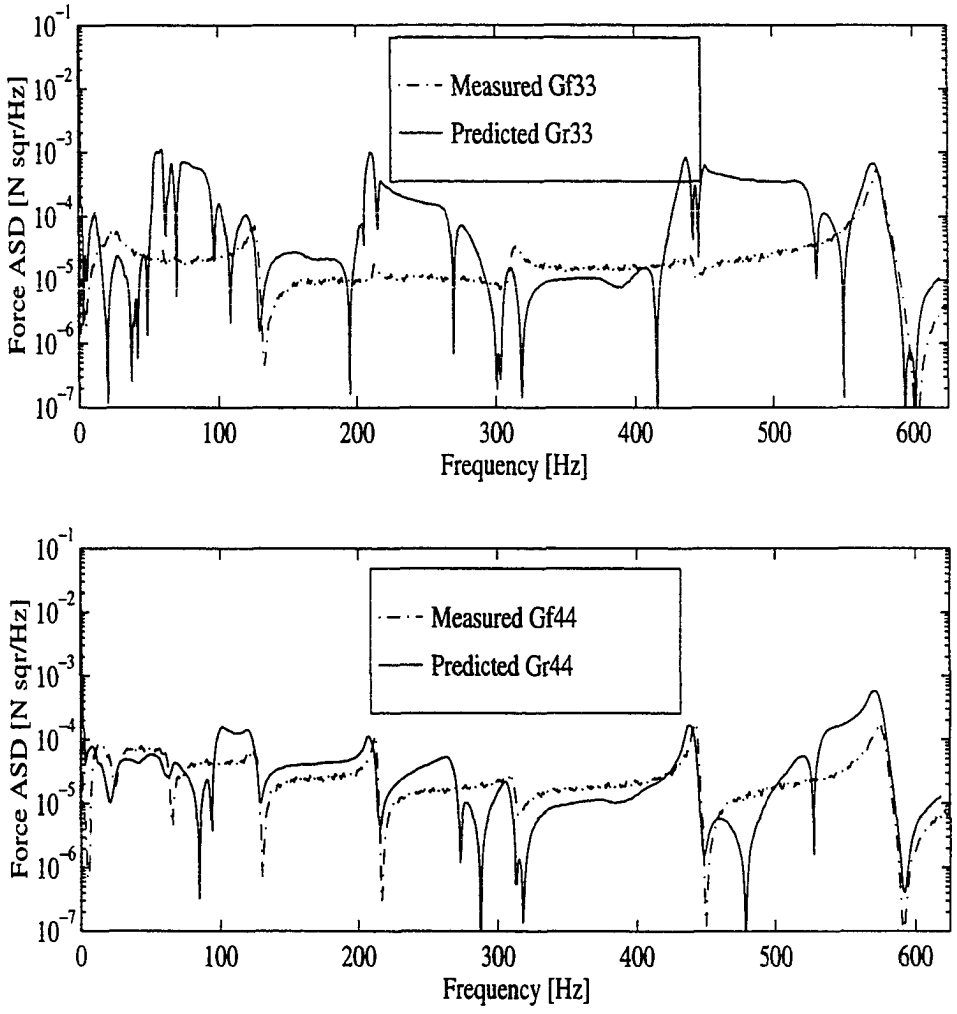

Figure 7.20 Comparison of measured and predicted random force ASDs Gr_{33} and Gr_{44} for case (b) using measured acceleration ASDs (*uncorrelated motions*). Predicted force ASDs from the pseudo-inverse technique (solid line) are compared with measured force ASDs (dashed-dotted line). A single random input signal is used to drive both exciters and no rigid mass is attached to the beam's right end

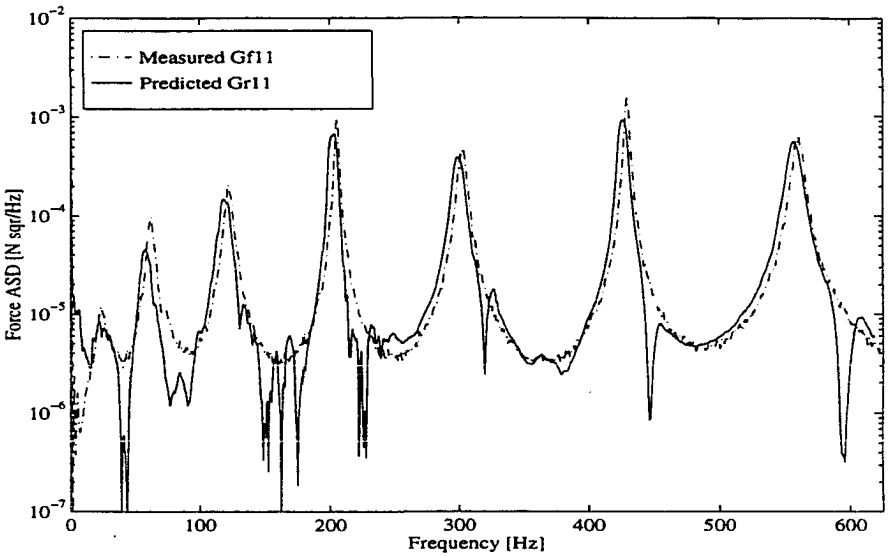

Figure 7.21 Comparison of measured and predicted random inertia force ASD Gr_{11} for case (c) using acceleration ASDs and CSDs (*correlated motions*). Two independent random signals are used to drive both exciters and the rigid mass is attached to the beam's right end

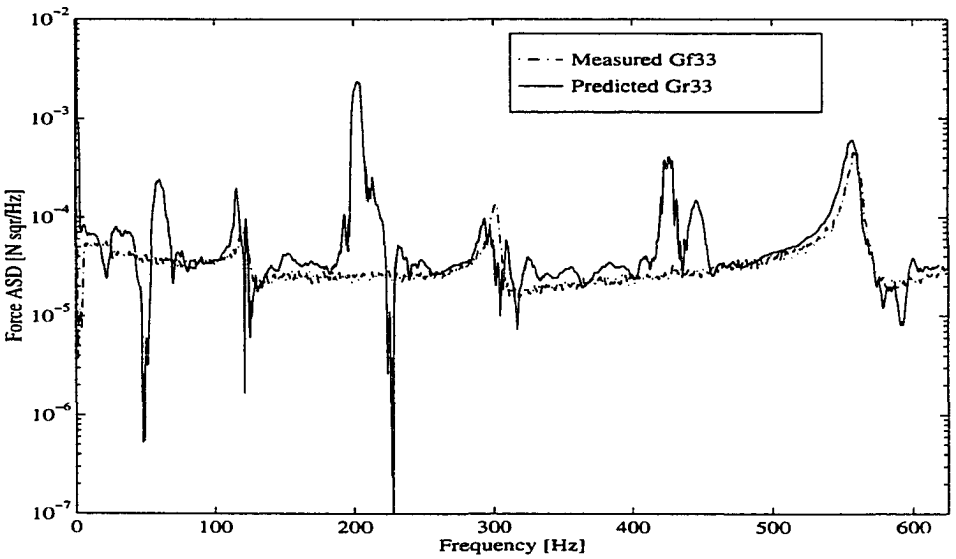

Figure 7.22 Comparison of measured and predicted random force ASD Gr_{33} for case (c) using acceleration ASDs and CSDs (*correlated motions*). Two independent input random signals are used to drive both exciters and the rigid mass is attached to the beam's right end

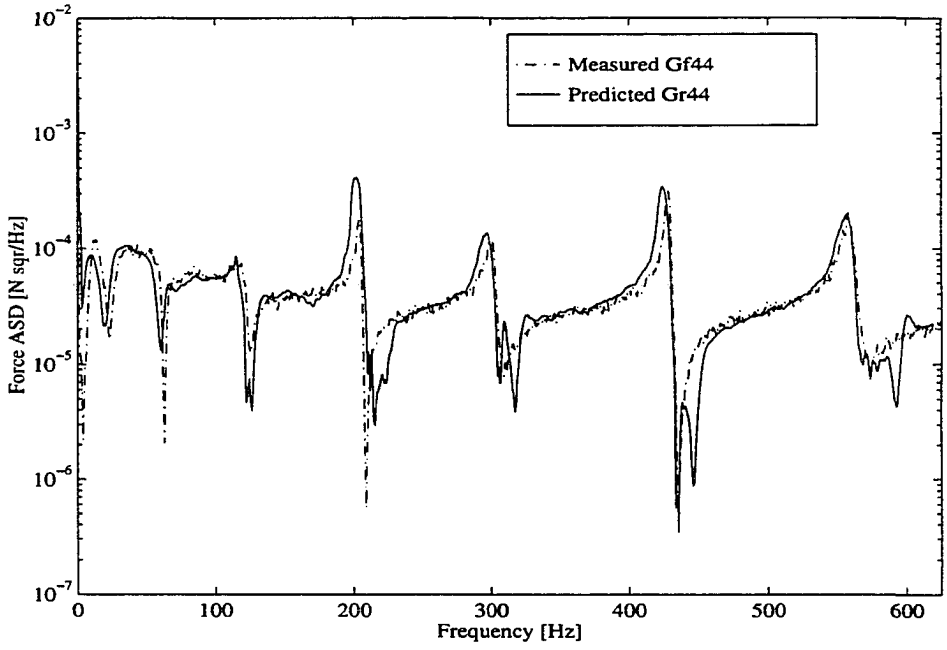

Figure 7.23 Comparison of measured and predicted random force ASD Gr_{44} for case (c) using acceleration ASDs and CSDs (*correlated motions*). Two independent input random signals are used to drive both exciters and the rigid mass is attached to the beam's right end

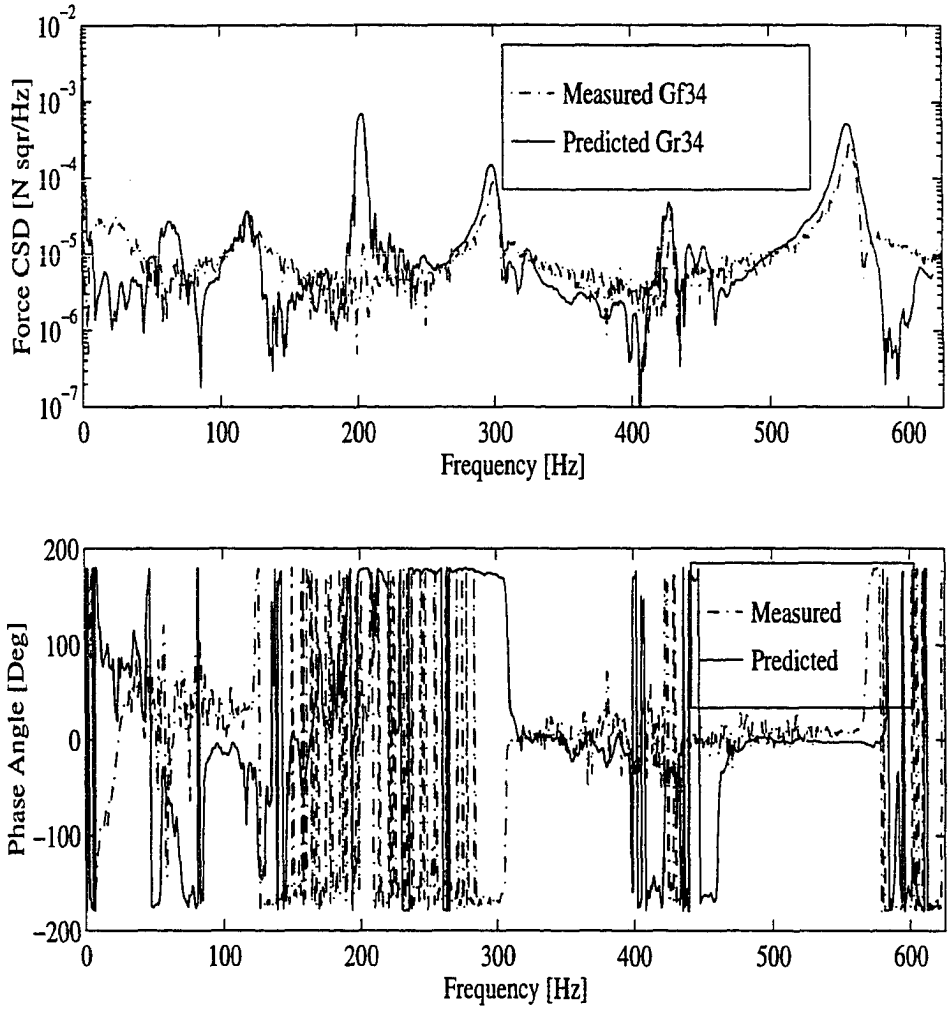

Figure 7.24 Comparison of measured and predicted magnitude and phase angle of force CSD Gr_{34} for case (c) using acceleration ASDs and CSDs (*correlated motions*).Two independent input random signals are used to drive both exciters and the rigid mass is attached to the beam's right end

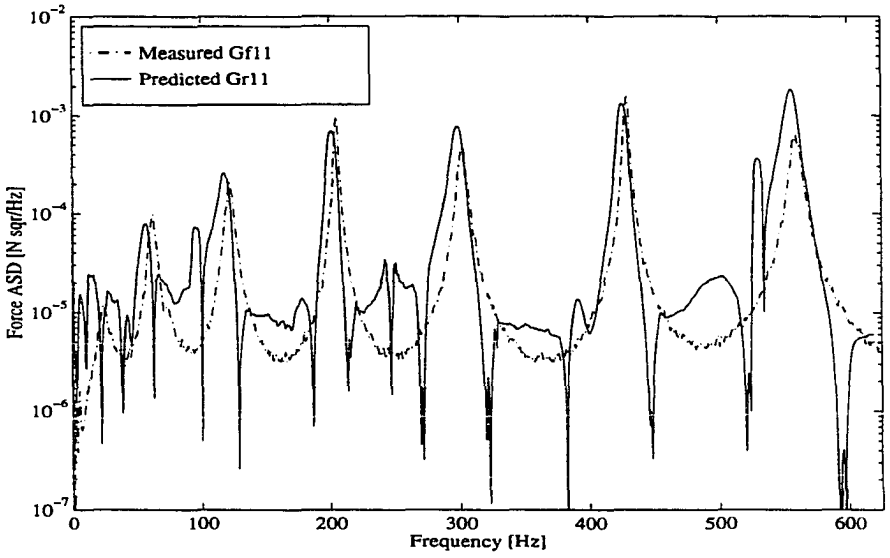

Figure 7.25 Comparison of measured and predicted random force ASD Gr_{11} for case (c) using acceleration ASDs (*uncorrelated motions*). Two independent input random signals are used to drive both exciters and the rigid mass is attached to the beam's right end

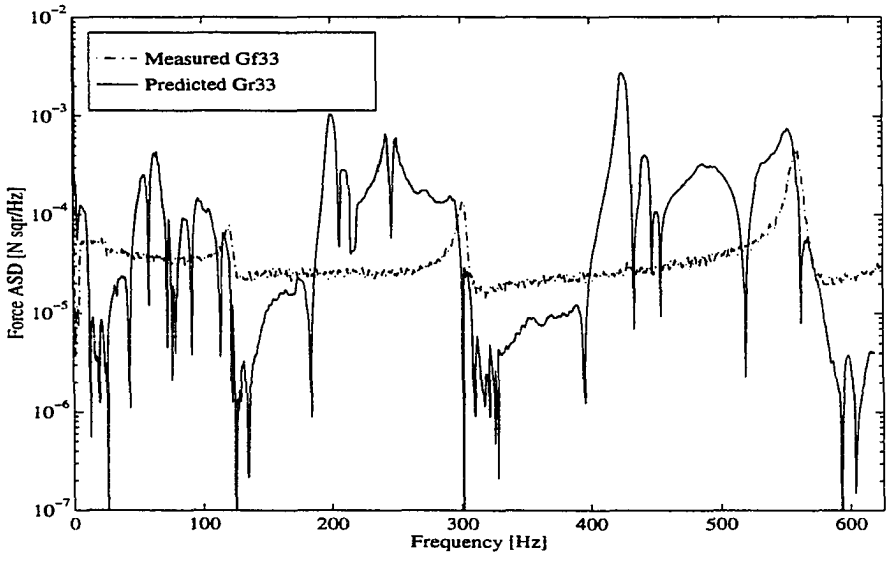

Figure 7.26 Comparison of measured and predicted random force ASD Gr_{33} for case (c) using Acceleration ASDs (*uncorrelated motions*). Two independent input random signals are used to drive both exciters and the rigid mass is attached to the beam's right end

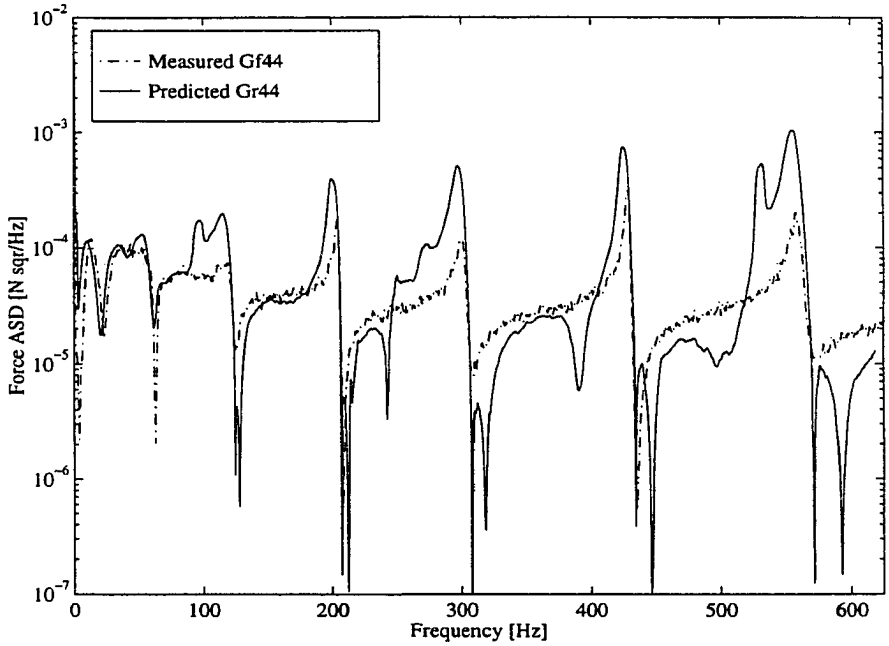

Figure 7.27 Comparison of measured and predicted random force ASD Gr_{44} for case (c) using acceleration ASDs (*uncorrelated motions*). Two independent input random signals are used to drive both exciters and the rigid mass is attached to the beam's right end

Case d - Two Correlated Random Forces at Points 3 and 4 With Rigid Mass

This test employed a single signal that drove both exciters in the setup of Figure 7.1b. The force ASDs Gr_{11}, Gr_{33}, Gr_{44}, and CSD Gr_{34} were predicted based on the *correlated* Equation 7.6 and are compared with the measured forces in Figures 7.28, 7.29, 7.30, and 7.31, respectively. Similarly, Figures 7.32, 7.33, and 7.34 show the predicted force ASDs based on the *uncorrelated* Equation 7.7 compared to the measured forces. As in the previous cases, the predicted force that is obtained from the *correlated* (Equation 7.6) expression have much better agreement with measured forces than those obtained from the *uncorrelated* (Equation 7.7) expression.

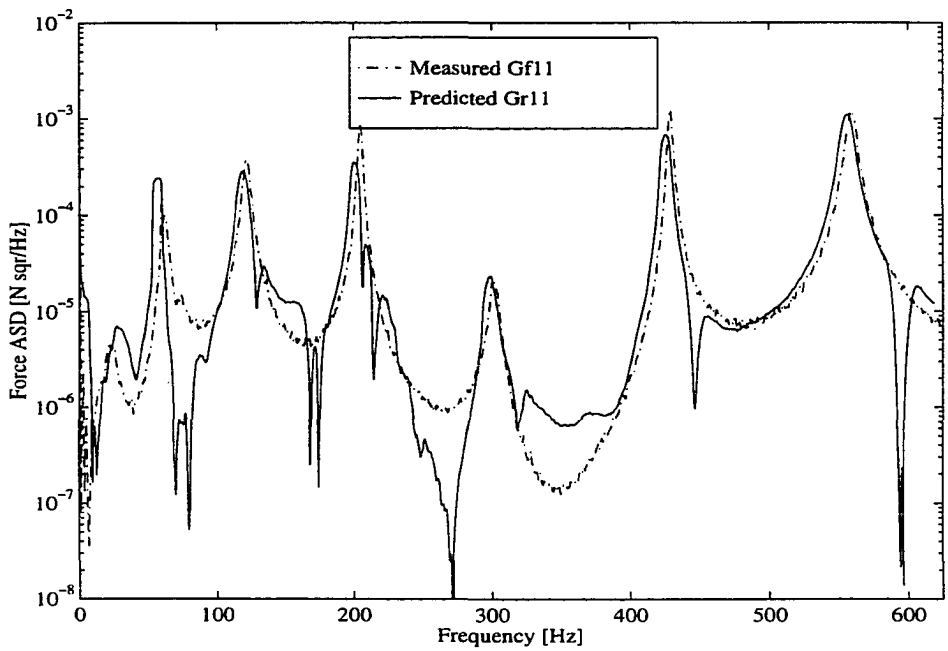

Figure 7.28 Comparison of measured and predicted random force ASD Gr_{11} for case (d) using acceleration ASDs and CSDs (*correlated motions*). A single input random signal is used to drive both exciters and the rigid mass is attached to the beam's right end

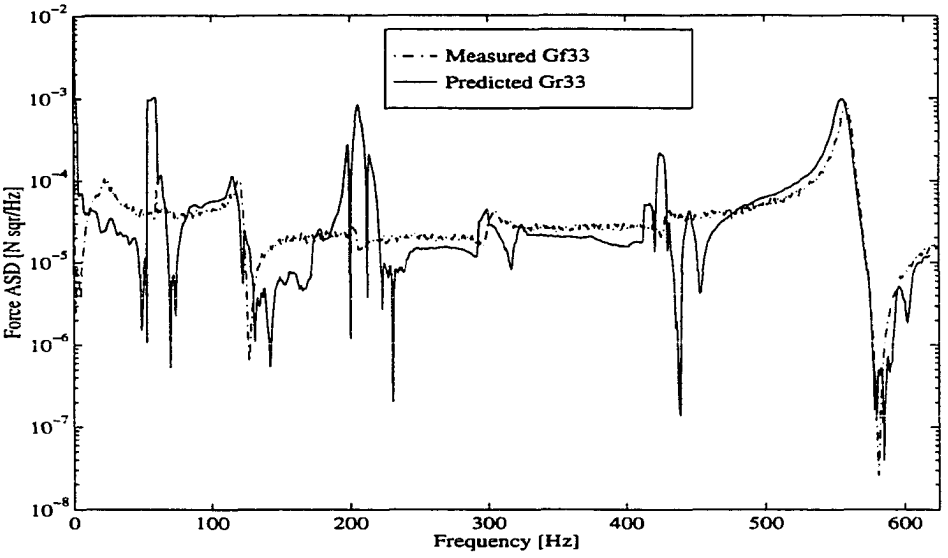

Figure 7.29 Comparison of measured and predicted random force ASD Gr_{33} for case (d) using acceleration ASDs and CSDs (*correlated motions*). A single input random signal is used to drive both exciters and the rigid mass is attached to the beam's right end

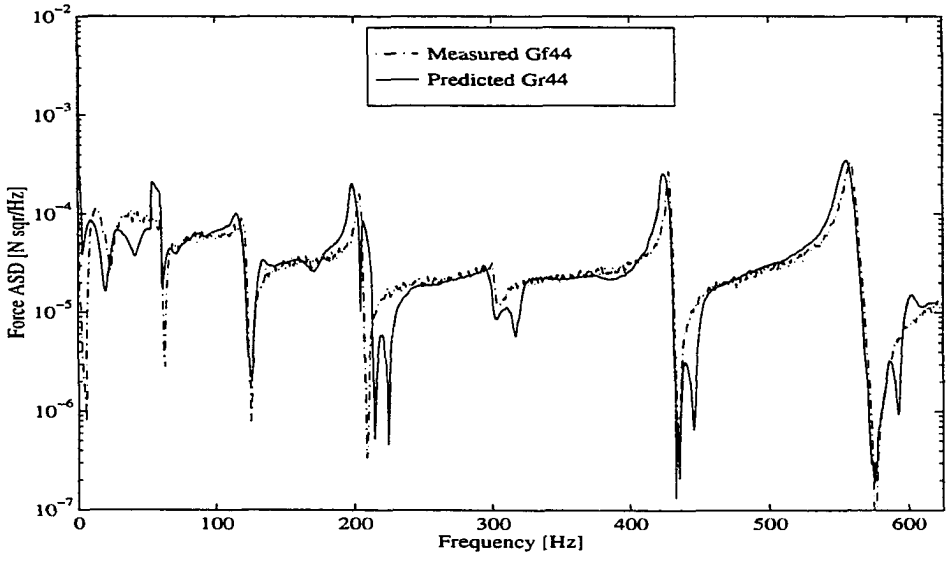

Figure 7.30 Comparison of measured and predicted random force ASD Gr_{44} for case (d) using acceleration ASDs and CSDs (*correlated motions*). A single input random signal is used to drive both exciters and the rigid mass is attached to the beam's right end

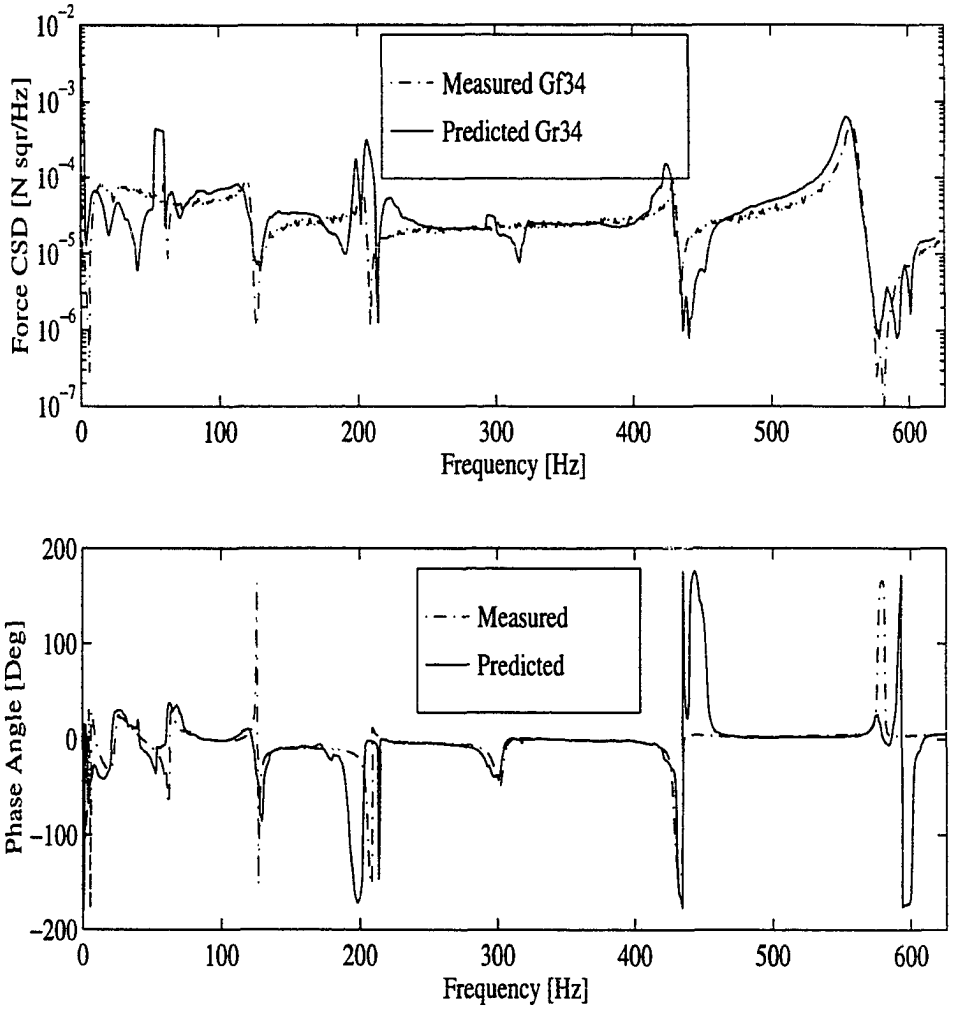

Figure 7.31 Comparison of measured and predicted magnitude and phase angle of force CSD Gr_{34} for case (d) using acceleration ASDs and CSDs (*correlated motions*). A single input random signal is used to drive both exciters and the rigid mass is attached to the beam's right end

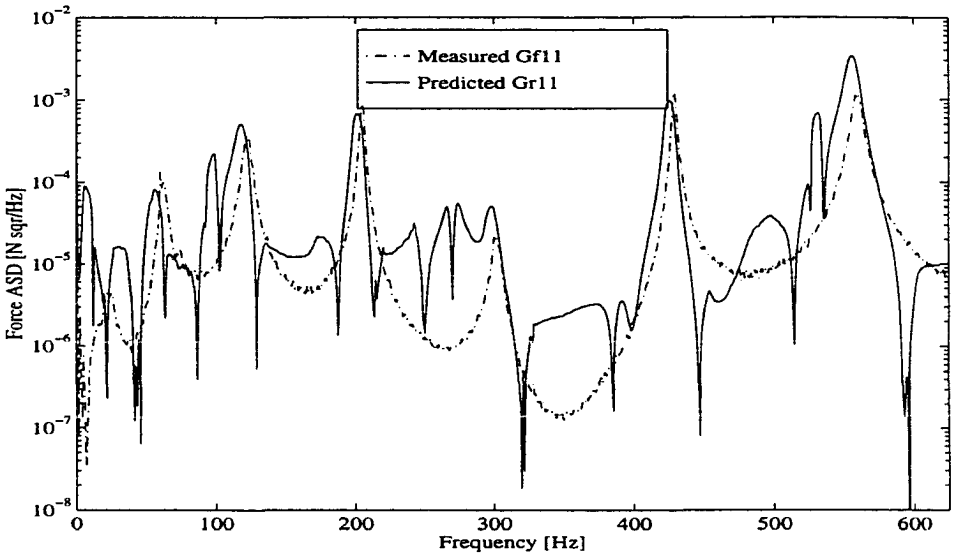

Figure 7.32 Comparison of measured and predicted random force ASD Gr_{11} for case (d) using acceleration ASDs (*uncorrelated motions*). A single input random signal is used to drive both exciters and the rigid mass is attached to the beam's right end

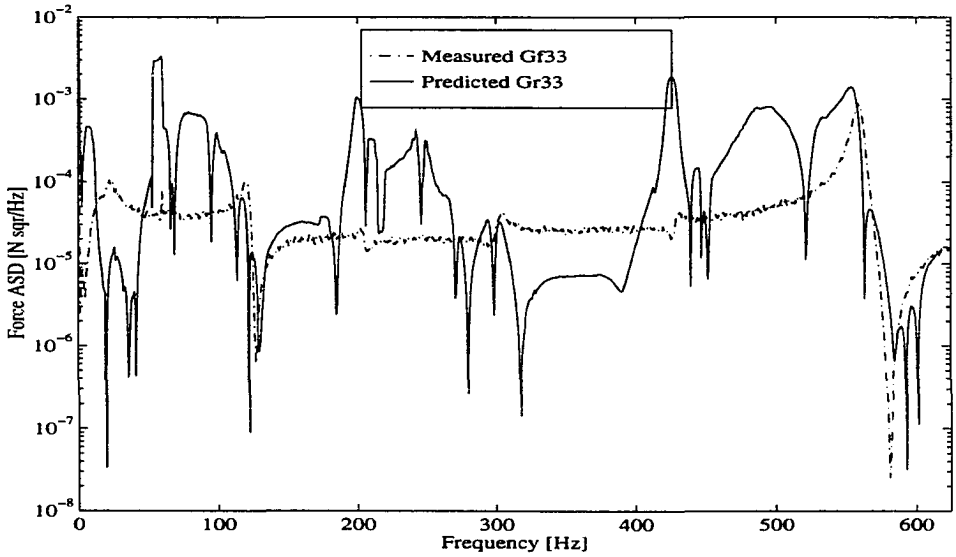

Figure 7.33 Comparison of measured and predicted random force ASD Gr_{33} for case (d) using acceleration ASDs (*uncorrelated motions*). A single input random signal is used to drive both exciters and the rigid mass is attached to the beam's right end

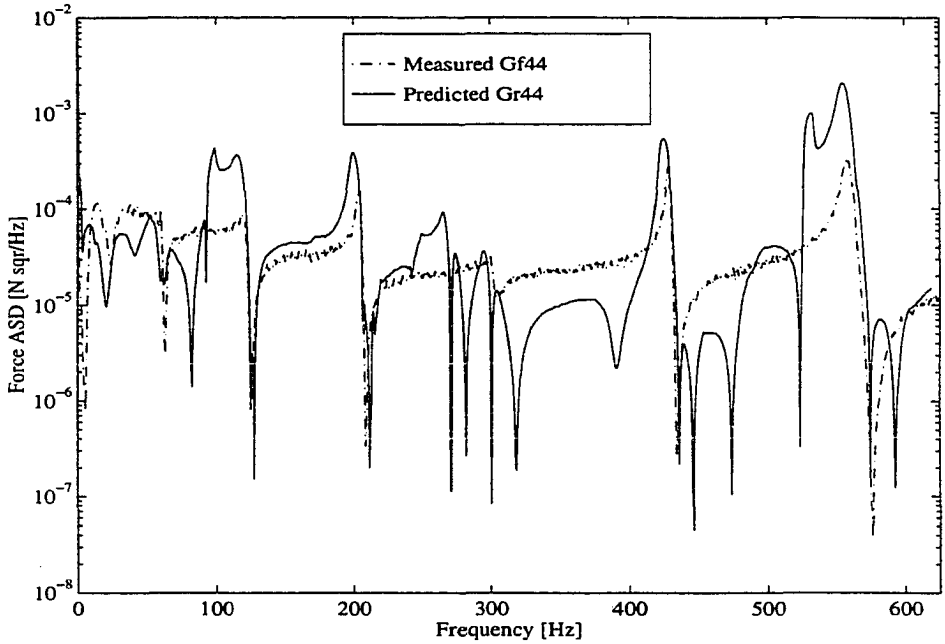

Figure 7.34 Comparison of measured and predicted random force ASD Gr_{44} for case (d) using acceleration ASDs (*uncorrelated motions*). A single input random signal is used to drive both exciters and the rigid mass is attached to the beam's right end

The force prediction results for all cases shown in Table 7.4 demonstrate that both acceleration ASDs and CSDs must be accounted for in the random force estimate calculation when using the pseudo-inverse technique. This means that the *correlated* Equation 7.6 should be employed in solving this inverse problem for random signals, and that the assumption of *uncorrelated* test item motions is untrue even when the exciters are driven by statistically *uncorrelated* random signals. There are two reasons for this correlation requirement. *First*, the motion at each point in a structure is due to all forces applied to the structure. When the cross correlation between any two points is examined, it is found that these motions are correlated because each force is perfectly correlated with itself even when it is completely uncorrelated with the other forces. *Second*, the force signals measured by force transducers at 3 and 4 will present some correlation even when independent input signals are used with each exciter due to the

mechanical coupling between the exciters by the beam. This results in the so called cross coupling effect among excitation sources that is due to exciter armature inertia [39, 40].

Prediction of External Accelerations Using the Q-T Matrix Approach

In this section, the experimental setup shown in Figure 7.1a is employed. Random excitation is used with both vibration exciters to drive the beam. The beam's output acceleration ASDs are measured by the piezoelectric sensors listed in Table 7.2 at locations A_1, A_2, A_3, and A_4 as shown in Figure 7.1a. The corresponding acceleration CSDs between all measurement locations are also measured since the resulting motions are *correlated.* The acceleration ASDs from the locations where the input excitation signals are applied (points A_3 and A_4) will be referred to as the *interface accelerations* while the acceleration ASDs at A_1 and A_2 will correspond to the *external accelerations.*

The goal in this section is to use the **Q-T** matrix approach described in Chapter 6 to predict the external acceleration ASDs and CSDs at points 1 and 2 from the measured interface accelerations ASDs and CSDs at points 3 and 4. In this case, the external acceleration ASDs and CSDs are measured in order to provide a comparison basis for the resulting motions predicted through the **Q-T** matrix.

Recall from Chapter 6 that when dealing with random excitation and response signals, the expression for the **Q-T** matrix is given by Equation 6.23

$$[G\boldsymbol{u}_e] = [T_{ec}]^*[[T_{cc}]^{-1}]^* \, [G\boldsymbol{x}_c] \, [T_{cc}]^{-1}[T_{ce}] \tag{7.8}$$

where $[G\boldsymbol{u}_e]$ is the matrix containing the predicted external acceleration ASDs and CSDs and $[G\boldsymbol{x}_c]$ denotes the measured interface acceleration ASDs and CSDs.

Results for External Random Accelerations Predicted by the Q-T Matrix Approach

Equation 7.8 is used with the experimental beam data from the interface acceleration ASDs and CSD at locations 3 and 4 in order to predict the external acceleration ASDs and CSDs at points 1 and 2. In order to reduce the experimental noise in the calculation procedure, the curve fitted interface accelerances shown in Figures 7.2, 7.3 and 7.4 and the curve fitted external-interface accelerances T_{13}, T_{14}, T_{23}, and T_{24} (not shown) are used to construct the FRF matrices $[T_{cc}]$ and $[T_{ec}]$, respectively. These curve fitted accelerance FRFs were generated by using the beam's identified modal parameters from the FRFs curve fitting [20].

Figures 7.35 and 7.36 show a comparison of the measured and predicted external acceleration ASDs ($\boldsymbol{Gx}_{11}$ and $\boldsymbol{Gu}_{11}$, and $\boldsymbol{Gx}_{22}$ and $\boldsymbol{Gu}_{22}$) from Equation 7.8, respectively. In both cases, the predicted external acceleration ASD is in good agreement with the corresponding measured data for frequency components in the vicinity of the acceleration peaks while a poor agreement is observed in the valleys located between two consecutive acceleration peaks. In these valleys, the estimated acceleration ASD is seen to have a fictitious acceleration peak followed by a notch or a notch followed by an acceleration peak. This fictitious behavior could cause a false impression that a structure has additional natural frequencies in the $0 - 625\ \boldsymbol{Hz}$ that were not detected in the FRF measurements. These uncertainties were not observed in the numerical simulation results employing the **Q-T** matrix approach given in the Chapter 6.

Returning to Equation 7.8, a matrix inversion is required for all frequency components in the frequency bandwidth covered by the tests. The matrix that must be *explicitly* inverted corresponds to the test item interface accelerance N_c x N_c FRF matrix $[T_{cc}]$ that is *square* and *symmetric*.

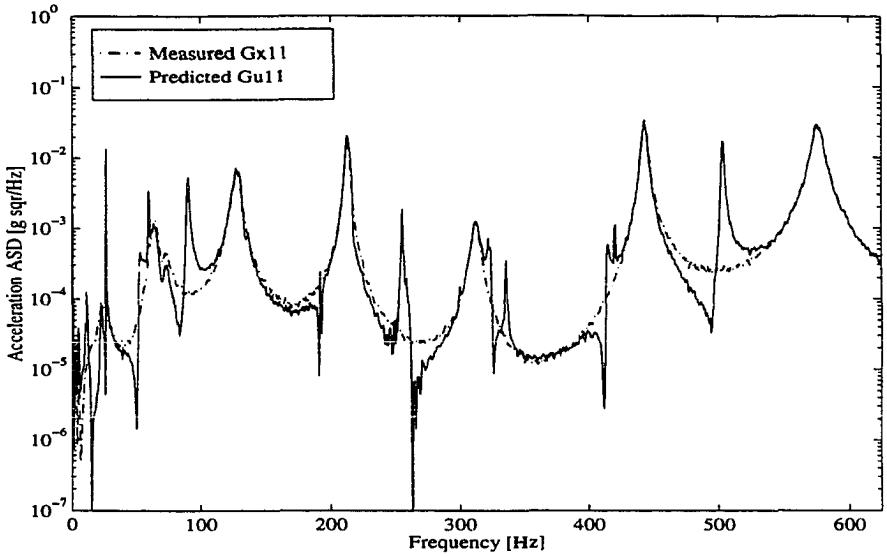

Figure 7.35 Comparison of experimental and predicted external accelerations ASDs $\boldsymbol{Gx}_{11}$ and $\boldsymbol{Gu}_{11}$ at location A_1 when calculated from the Q-T matrix. The curve-fitted test item accelerances are used in this case

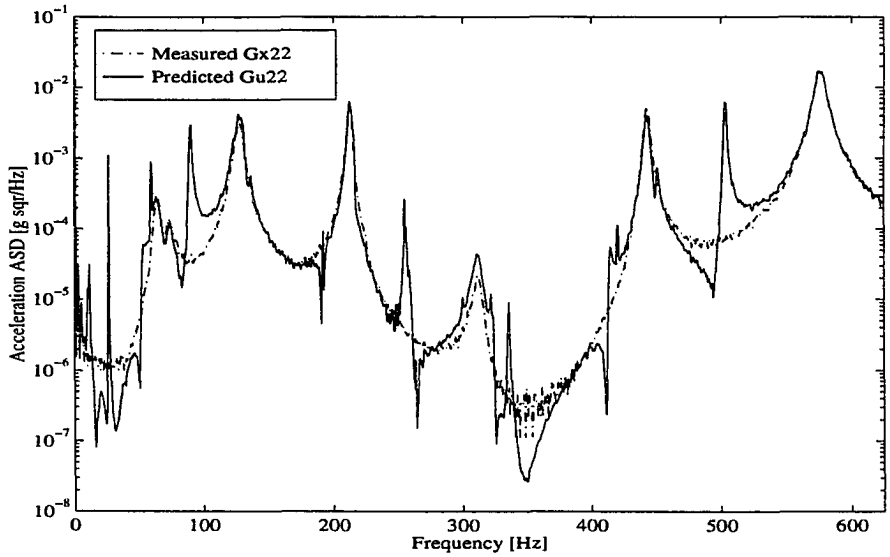

Figure 7.36 Comparison of experimental and predicted external acceleration ASDs $\boldsymbol{Gx}_{22}$ and $\boldsymbol{Gu}_{22}$ at location A_2 when calculated from the Q-T matrix. The curve-fitted test item accelerances are used in this case

Since this analysis is based on the assumption that the test item is subjected to interface forces *only*, the external motion spectral density matrix $[G\boldsymbol{x}_e]$ in Equation 7.8 is due to interface forces *only*. Thus, Equation 7.8 can be rewritten as

$$[G\boldsymbol{u}_e] = [T_{ec}]^*[Gf_{cc}][T_{ce}] \tag{7.9}$$

where the N_c x N_c matrix $[Gf_{cc}] = [[T_{cc}]^{-1}]^*[G\boldsymbol{x}_c][T_{cc}]^{-1}$ contains the interface force spectral densities. Thus, in a sense although Equation 7.8 expresses the test item input in terms of interface motions, the *inverse* solution for the interface forces in terms of interface motions is *implicitly* implied in this equation as seen in Equation 7.9.

As discussed in Chapters 4 and 5, the solution for the excitation forces from knowledge of measured motions corresponds to an *inverse* problem, and is well known to be case dependent and to offer numerical difficulties when dealing with actual experimental data, since the inversion of the structure's FRF matrix for each frequency spectral line is required in solving for the unknown forces [10, 18, 19, 43]. These numerical difficulties occur due to the fact that the system FRF matrix tends to be rank deficient in the vicinity of the natural frequencies and this rank deficiency is caused by an insufficient number of modes participating at the structure's response at those frequencies [10, 11]. This rank deficiency of the FRF matrix causes numerical problems and affects the uniqueness of the solution at frequencies close to the natural frequencies.

The pseudo-inverse technique is frequently employed to give a least squares solution for the N excitation forces from knowledge of M acceleration records when $M > N$, i.e, more motions are used than forces predicted. This over-determination of the system of equations that must be solved for each frequency component requires the pseudo-inversion process of the M x N structural FRF matrix in order to obtain a unique solution for the unknown forces in a least squares sense. The predicted forces may or may not resemble the actual forces acting on the structure depending on the information contained in the measured motions and on the structure's FRF matrix. The least

squares solution of the inverse problem also helps to reduce measurement noise effects at frequencies where the measured data has a poor signal to noise ratio. However, numerical difficulties may still persist even when seeking an approximate least squares solution for the unknown forces since the solution process may be affected by a number of factors such as an unsuitable selection of measurement location [21], motions caused by unknown external forces, and moments that are not accounted for in the solution process. Several procedures have been proposed to reduce the ill conditioning of the inversion process [16, 17, 19, 43, 49].

The external acceleration ASDs predictions shown in Figures 7.35, and 7.36 indicate that the free free beam interface accelerance FRF matrix $[T_{cc}]$ is rank deficient at those frequencies where false peaks and valleys are observed in the predicted acceleration ASDs. Since the interface accelerance FRF matrix is 2x2 in this case, Equations 6.20 can be used to obtain the inverse of the beam interface FRF matrix. The determinant of $[T_{cc}]$ is $\Delta_{cc} = T_{33}T_{44} - T_{34}T_{43}$ and is shown in Figure 7.37 for both the experimental and curve fitted interface accelerance FRF matrices. These determinants present amplitude variations in terms of peaks and notches in the $0 - 625\ Hz$ frequency range that vary from approximately $10^{-4}\ (g/N)^2$ to $10^{3}\ (g/N)^2$. A close inspection at the notch frequencies of Δ_{cc} and the corresponding frequencies where the false peaks and valleys occur in Figures 7.35 and 7.36, reveals that they are essentially the same. Thus, what is happening is that the pseudo-inverse of $[T_{cc}]$ in the present case coincides with standard inversion and the determinant Δ_{cc} that is in the denominator of $[T_{cc}]^{-1}$ in Equation 6.23 becomes very small (in the order of $\cong\ 10^{-3}$ for the experimental FRFs or even $\cong\ 10^{-4}$ in the case of the curve fitted FRFs) at the frequencies where unwanted variations on the predicted motions are seen to occur. An alternative approach to explain the singularities presented by the beam's interface FRF accelerance matrix $[T_{cc}]$ is to plot the singular values [48] of this matrix as a function of the excitation frequency. The singular values are obtained by performing a decomposition called the singular value de-

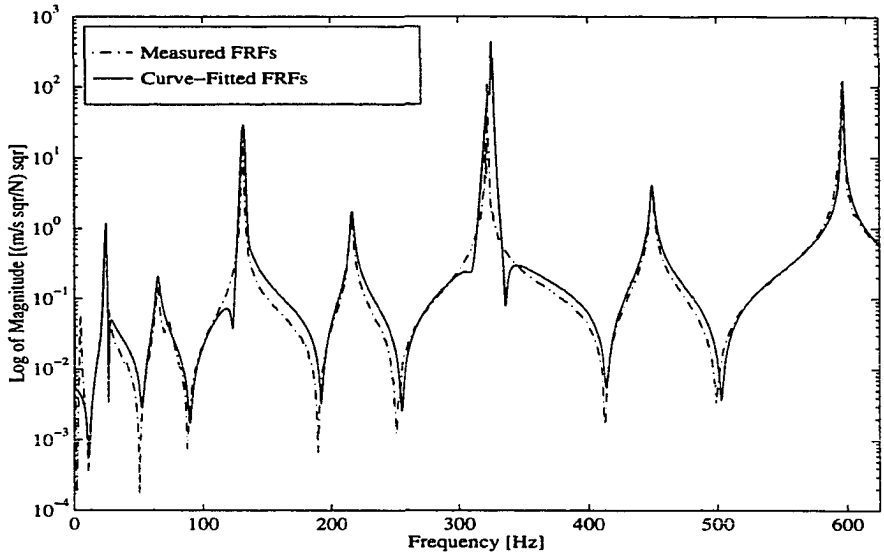

Figure 7.37 · Comparison of the determinant of the free free beam interface accelerance FRF matrix $[T_{cc}]$ as a function of the excitation frequency based on measured and curve-fitted FRF data

composition (SVD) of the matrix [23, 48]. Since the pseudo-inverse of the FRF matrix is usually calculated by the SVD technique [23, 47], the pseudo-inverse of the FRF matrix can be expressed as a function of a diagonal matrix whose main diagonal entries are the reciprocals of the singular values as shown in the Appendix of this dissertation. Thus, if at any frequency one of the singular values of the structure's FRF matrix becomes very small, the FRF matrix becomes rank deficient at that frequency, and the pseudo-inversion process becomes ill-conditioned. Thus, in order for the numerical inversion of the FRF matrix in Equation 7.8 be stable over the entire frequency range, it must present a minimum number of singular values that are greater than zero or greater than a given precision set in the inversion algorithm. In applications involving the pseudo-inversion of the structure's mode shape matrix [47], this requirement can be met by solving the inverse problem in a least squares sense, i. e., by increasing the order of the matrix to be inverted so that a minimum number of singular values is achieved.

In order to improve the conditioning of the inversion process shown in Equation 7.8, it

is proposed to increase the order of the input acceleration spectral density matrix $[G\ddot{x}_{cc}]$ in Equation 7.8 such that the solution for the unknown external motions is obtained in a least squares sense. Since the input acceleration spectral density matrix $[G\ddot{x}_{cc}]$ is formed by *all interface* motions, the only way of increasing the order of this input matrix is if *external* motions are introduced as test item inputs in Equation 7.8. In this case, Equation 7.8 is rewritten as

$$[G\ddot{u}_e] = [T_{ec}]^*[[\hat{T}_{cc}]^+]^* \; [\hat{G}\ddot{x}_c] \; [\hat{T}_{cc}]^+[T_{ce}] \tag{7.10}$$

where the hat symbol "$\hat{}$" is used to denote the fact the interface and external accelerations form the input motions frequency spectra and spectral densities in Equation 7.10. Although this new formulation of the **Q-T** matrix approach essentially violates the initial assumption that only interface motions would be used as test item inputs, it is expected that it can reduce the numerical ill conditioning of the problem since a least squares solution is now obtained from Equation 7.10. The pseudo-inverse of the FRF matrix $[\hat{T}_{cc}]$ is required in this case as denoted by symbol $^+$ in Equation 7.10. In this case, the singular value decomposition described in the Appendix is used to calculate the pseudo-inverse of the FRF matrix when it is required.

The consequences of this new formulation for the **Q-T** matrix can be seen in Figures 7.38 and 7.39 where the singular values of the free free beam's matrices $[T_{cc}]$ and $[\hat{T}_{cc}]$ are plotted as a function of the excitation frequency. In this case, an additional row formed by the beam's accelerances T_{13} and T_{14} is appended to matrix $[T_{cc}]$ thus giving the augmented 3 x 2 $[\hat{T}_{cc}]$. Recall that $[T_{cc}]$ is 2 x 2 and contains T_{33}, T_{44}, and $T_{34} = T_{43}$. It is observed in Figure 7.38 that the singular value σ_1 of $[T_{cc}]$ presents deep notches at frequencies that are close to the beam's natural frequencies as shown in the beam's FRFs and in Table 7.1. The uncertainties presented by the predicted external acceleration ASDs of Figures 7.35 and 7.36 are seen to occur in the vicinity of these σ_1 notches, i.e., $[T_{cc}]$ becomes nearly singular in the vicinity of the beam's natural frequencies. The

singular value $\hat{\sigma}_1$ obtained from the SVD of $[\hat{T}_{cc}]$ and also shown in Figure 7.38 does not present the notches observed in σ_1. A similar behavior is observed to occur for the singular values σ_2 and $\hat{\sigma}_2$ shown in Figure 7.39. In this case, the original singular value σ_2 does not present serious singularity problems and when the order of $[T_{cc}]$ is increased, the magnitudes of $\hat{\sigma}_2$ become even larger than σ_2. Thus, it is expected that by increasing the order of the test item interface matrix $[T_{cc}]$, the numerical problems observed in the predicted accelerations of Figures 7.35 and 7.36 can be reduced.

Equation 7.10 is employed with the experimental data obtained in the free free beam experiments. The following two cases are considered:

- The measured external acceleration ASD $\boldsymbol{Gu}_{22}$ and CSDs $\boldsymbol{Gu}_{23}$ and $\boldsymbol{Gu}_{24}$ are used in Equation 7.10 and it is then solved for $\boldsymbol{Gu}_{11}$. This means that $[\hat{T}_{cc}]$ contains the additional T_{23} and T_{24} FRFs.

- The measured external acceleration ASD $\boldsymbol{Gu}_{11}$ and CSDs $\boldsymbol{Gu}_{13}$ and $\boldsymbol{Gu}_{14}$ are used in Equation 7.10 and then it is solved for $\boldsymbol{Gu}_{22}$. This means that $[\hat{T}_{cc}]$ contains the additional T_{13} and T_{14} FRFs.

The results for both cases 1 and 2 are shown in Figures 7.40 and 7.41, respectively. These results were obtained by using the beam accelerance FRFs obtained in the curve fitting process. It is seen that the results for both $\boldsymbol{Gu}_{11}$ and $\boldsymbol{Gu}_{22}$ are greatly improved when employing the least squares version of the **Q-T** matrix approach, Equation 7.10. Small discrepancies are seen to occur in the predicted $\boldsymbol{Gu}_{11}$ and $\boldsymbol{Gu}_{22}$ for frequency components in the $0 - 25$ Hz and $320 - 340$ Hz regions. A possible reason for these discrepancies is that the experimental and curve fitted FRFs are not in good agreement for frequencies that are close to the first and fifth natural frequencies as it is shown in Figure 7.3. In this case, the first and fifth natural frequency peaks of the experimental T_{44} are sharper and have higher amplitude values than the corresponding T_{44} obtained by curve fitting (see Figure 7.3).

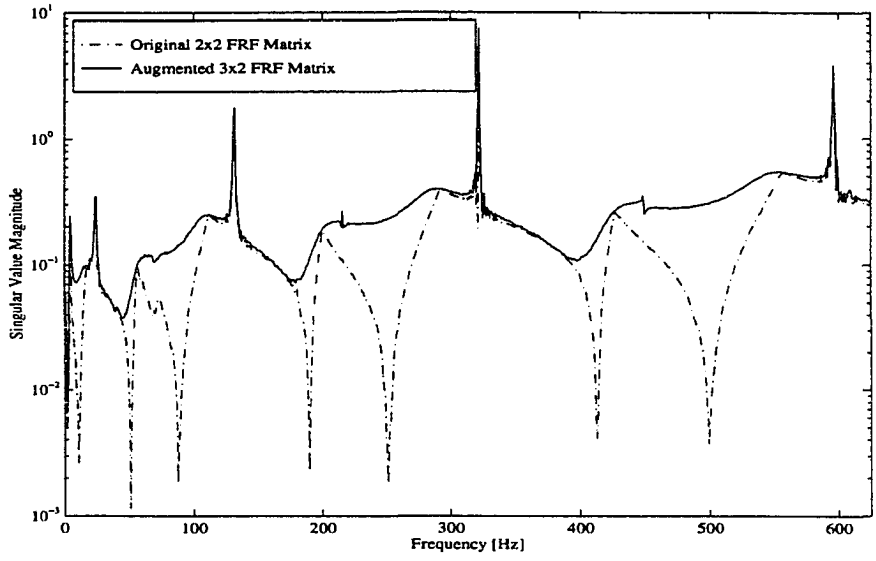

Figure 7.38 Singular values σ_1 (dashed-dotted line) and $\hat{\sigma}_1$ (solid line) of the free free beam's original 2x2 ($[T_{cc}]$) and augmented 3x2 ($[\hat{T}_{cc}]$) interface FRF matrices

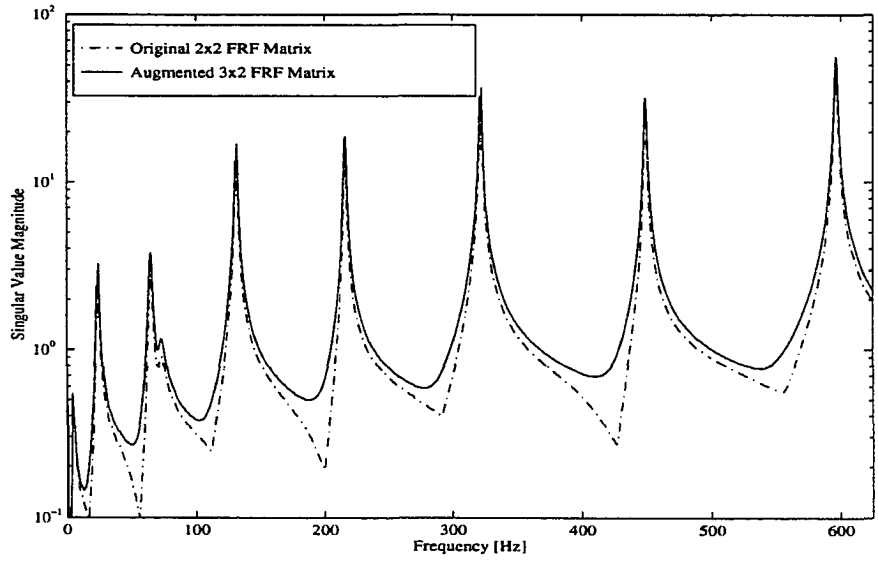

Figure 7.39 Singular values σ_2 (dashed-dotted line) and $\hat{\sigma}_2$ (solid line) of the free free beam's original 2x2 ($[T_{cc}]$) and augmented 3x2 ($[\hat{T}_{cc}]$) interface FRF matrices

In order to check how sensitive Equation 7.10 is to curve fitting errors, the same two cases are repeated by using the beam experimental FRFs without curve fitting to perform the calculations required by Equation 7.10. The results for cases are shown in Figures 7.42 and 7.43, respectively. Figure 7.42 shows the results for the predicted Gu_{11} when the measured Gu_{22} is used as an input in Equation 7.10. The result for this acceleration ASD shows that the uncertainties that were obtained in the $0 - 25$ Hz and $320 - 340$ Hz regions when the curve fitted FRFs were used are considerably reduced. The same trends are observed in the predicted acceleration ASD Gu_{22} of Figure 7.43 for frequencies in the $0 - 25$ Hz and $320 - 340$ Hz regions.

The point of this experimental exercise is that a reasonable estimate of test item external acceleration will result when the correct interface input accelerations are applied to the test item. The real problem is to develop a multi-exciter control system that can handle the required ASD and CSD requirements since the inversion problem is automatically handled by the test item.

Chapter Summary

The results presented in this chapter can be summarized as follows

Summary of Deterministic Force Predictions

The results obtained in the experimental analysis for deterministic excitation and response signals can be summarized as follows:

- The pseudo-inverse technique is feasible when working with experimental *deterministic* signals. Acceleration frequency spectra containing magnitude and phase information were used with this technique to predict the external forces applied to the test item. This means that a specific cross correlation exists between each time

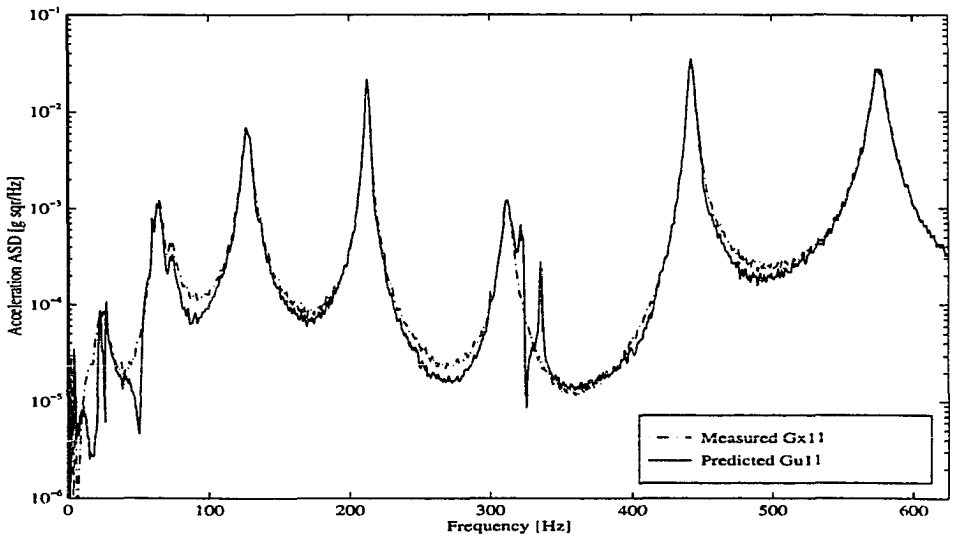

Figure 7.40 Comparison of measured and least squares prediction of external acceleration ASD $\boldsymbol{Gu}_{11}$ when the measured $\boldsymbol{Gx}_{22}$ is used to formulate the over-determined problem. The curve-fitted FRFs are used in this case

variable pair even though no such function was explicitly calculated or measured.

- The solution for the external forces was obtained in a least squares sense since more accelerations were measured than forces were predicted. This least squares formulation of the inverse problem helps in obtaining an unique solution for the unknown forces and helps to reduce measurement noise problems.

- The solution obtained from the pseudo-inverse technique appears to be sensitive to the acceleration measurement locations. Additional laboratory tests on the free free beam were performed where the acceleration measurement locations were changed. The results of these tests are not shown in this dissertation but considerably different results from those shown here were obtained. In particular, it was observed that the ill conditioning of the pseudo-inversion process of the FRF matrix tends to become worse when one or more accelerometers are mounted close

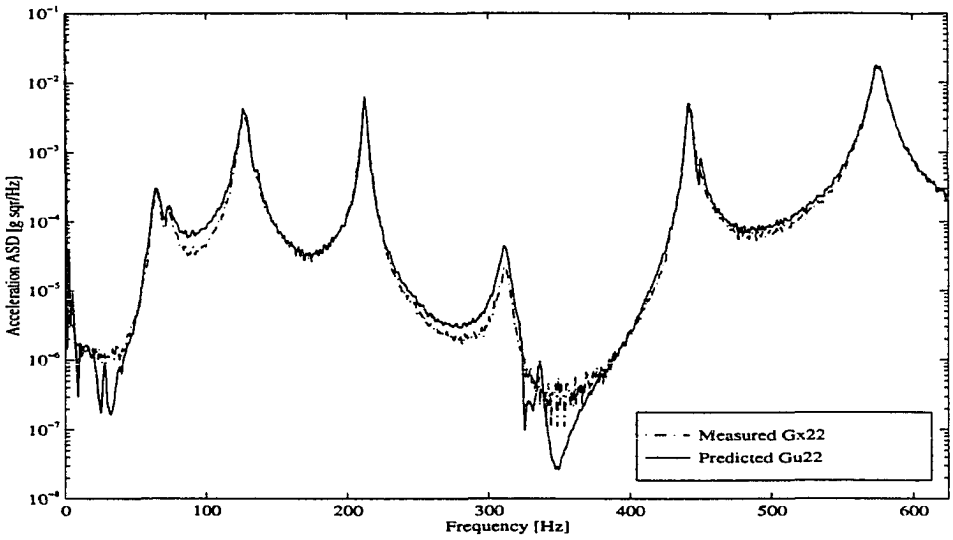

Figure 7.41 Comparison of measured and least squares prediction of external acceleration ASD $\boldsymbol{Gu}_{22}$ when the measured $\boldsymbol{Gx}_{11}$ is used to formulate the over-determined problem. The curve-fitted FRFs are used in this case

to node points of mode shapes that fall within the frequency range of interest, as observed by other researchers as well [10, 11, 13, 30].

Summary of Random Forces Predictions

The results obtained in the experimental analysis using random excitation and response signals can be summarized as follows:

- The pseudo-inverse technique is feasible when working with experimental random signals as long as the experimental acceleration CSDs are accounted for in addition to the acceleration ASDs when solving the inverse problem. *This requirement is independent of forces being correlated or uncorrelated since motions are always correlated.*

- The solution for the unknown input forces were obtained in a least squares sense, since more motions were measured than forces predicted. The location of the

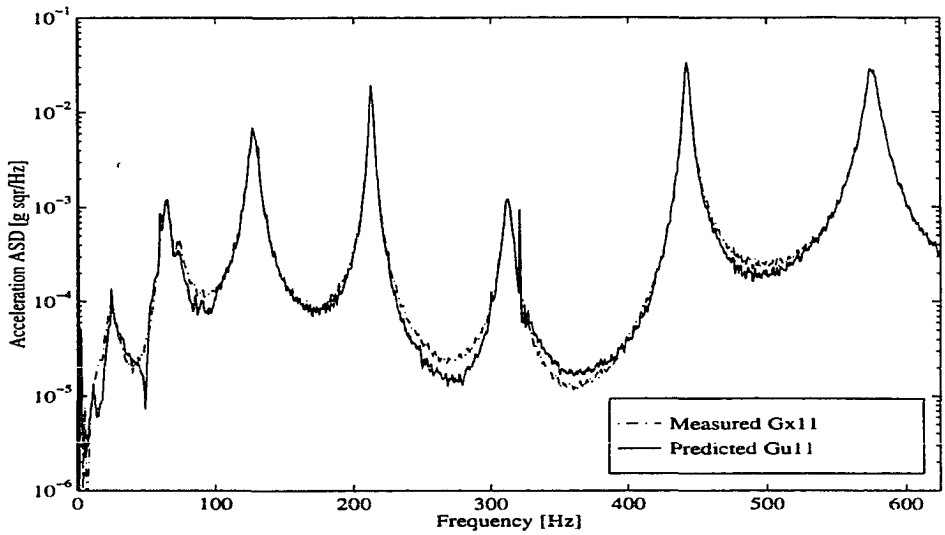

Figure 7.42 Comparison of measured and least squares prediction of external acceleration ASD $G_{u_{11}}$ when the measured $G_{x_{22}}$ is used to formulate the over-determined problem. The experimental FRFs are used in this case

input forces were assumed to be known since the accelerations as well as FRFs for the excitation locations were measured and accounted for in the solution of the inverse problem. This is a requirement imposed by the pseudo-inverse technique that if met along with the motion cross correlation requirement leads to reasonable estimates of the input forces.

Summary of External Acceleration Predictions

The results obtained in the experimental analysis involving the **Q-T** matrix approach can be summarized as follows:

- When only *interface* acceleration ASDs and CSDs are used as test item inputs in the **Q-T** matrix procedure, the inversion of test item interface accelerance FRF tends to be rank deficient even though $[T_{cc}]$ is square and symmetric. This rank deficiency seriously affects the results by causing *false* peaks and valleys to appear

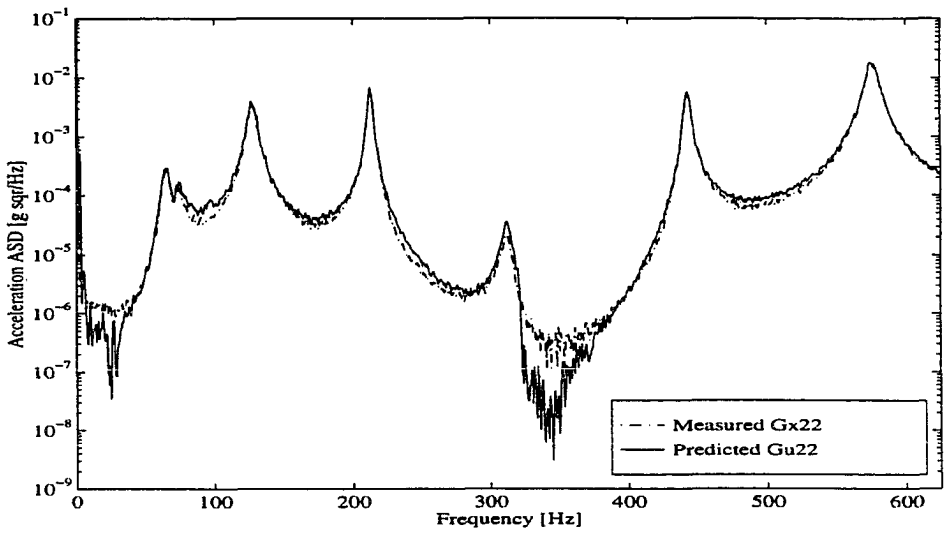

Figure 7.43 Comparison of measured and least squares prediction of external acceleration ASD $G\boldsymbol{u}_{22}$ when the measured $G\boldsymbol{x}_{11}$ is used to formulate the over-determined problem. The experimental FRFs are used in this case

in the predicted external acceleration ASDs between acceleration peaks.

- The rank deficiency problem may be overcome by using *external* accelerations in addition to *interface* accelerations as test item inputs. In this case, the resulting set of equations represents an over-determined problem where the solution for external motions is obtained in a least square sense.

- The results obtained when curve fitted FRFs were used show that the inversion of the accelerance FRF matrix formed from interface and external FRFs is very sensitive to variations in the test item mode shapes since small errors present in the curve fitted FRF around natural frequencies tend to introduce large errors in the predicted external motions. Ewins [9] arrived at a similar conclusion by performing similar experiments on a cantilever beam. Thus, care should be taken when using curve fitted FRFs in the inversion process.

8 CONCLUSIONS

Summary

A theoretical framework (**READI**) is developed to describe the variables and processes that control the vibration data that needs to be measured in defining suitable test item inputs to either a laboratory experiment or a finite element model of a given test item. Frequency domain substructuring concepts are used to investigate the structural interactions that occur in test environments where the test item has several interface connector points. Four laboratory test scenarios are described in defining the test item inputs in terms of deterministic and random excitation and response signals.

Lumped parameter models are used in numerical simulations using deterministic and random signals in order to illustrate the different laboratory test scenarios. In these simulations, the test item is modeled as a free structure in space while the vehicle is modeled in an "as is" condition, i.e., it can be free or grounded. The test scenario using the bare vehicle interface motions is illustrated as well as test scenarios using field interface forces and test item interface and external motions. Field conditions where the test item is subjected to interface and external forces are used to generate field data for laboratory simulations. In the laboratory environment, the field data is used to define test item inputs to be used in each test scenario. Field external forces effects in laboratory simulations are discussed in these numerical simulations.

Simulations are performed in order to investigate the consequences of using a flexible or rigid test fixture and enveloped test item inputs in laboratory testing using a single

vibration exciter. It is found that the fixture's dynamic characteristics dramatically alters the test item dynamic response by changing its natural frequencies, mode shapes, and vibration levels. Laboratory inputs obtained by enveloping the bare vehicle interface accelerations are shown to cause unrealistic over-testing. A simple figure of merit based on the test item laboratory relative displacements is proposed to access the amount of over-testing when these standard recommendations are followed.

The single point acceleration transmissibility concept is extended by defining a transformation called **Q**-Transmissibility matrix approach. This transformation matrix is obtained from the test item accelerance FRFs and its use is restricted to situations where the test item is subjected to interface connector forces only. The **Q-T** matrix is successfully applied to numerically simulated and experimental data to estimate the test item external accelerations from the measured interface accelerations.

The pseudo-inverse technique is used in obtaining the test item laboratory inputs from field motions. The feasibility of this tool in solving the inverse problem is investigated in terms of deterministic and random signals. Numerically simulated as well as experimental results of the force identification problem using the pseudo-inverse technique were presented. In the case of random force identification, it is shown that a commonly employed assumption that forces and motions are uncorrelated is not true. The rank deficiency presented by the FRF matrix in the pseudo-inversion process is analyzed by plotting the singular values of the FRF matrix as a function of the excitation frequency. The effects of using curve-fitted FRFs in the pseudo inversion process of the FRF matrix as opposed to experimental FRFs are shown.

Conclusions

The following conclusions are obtained from this investigation:

- Test item laboratory inputs can be obtained from the bare vehicle interface accelerations as long as the vehicle's interface driving point and transfer FRFs are accounted for. The test condition using the bare vehicle interface motions is valid only in situations where field external forces are negligible.

- Field external force effects must be properly accounted for in laboratory simulations, otherwise incorrect test item motions will be obtained. If this external force is satisfied, then field interface forces and motions constitute appropriate test item inputs.

- In the case of random signals, acceleration cross spectral densities must be accounted for in addition to acceleration auto spectral densities when using the pseudo-inverse technique to predict forces from measured motions. This cross spectral density is automatically satisfied in the case of deterministic signals since the frequency spectra automatically satisfy cross correlation requirements. The solution for the unknown input forces must be obtained in a least squares sense to reduce noise effects as well as singularity problems in the inversion of the test item FRF matrix

- Often unrealistic test results are obtained when using a single vibration exciter with a rigid or flexible test fixture when the inputs are defined from enveloping the bare vehicle interface motions. These unrealistic results are due to changing mode shapes and natural frequencies due to the rigid test fixtures as well as enveloping process.

- The Q-Transmissibility matrix approach is potentially a useful tool in obtaining the test item external motions when interface motions are used as test item inputs

in the absence of external forces. The advantage of this procedure is that the interface forces are not directly solved for.

Further Research

This investigation uncovered several additional issues that need further research. These issues are

- Application of the proposed theoretical framework to real situations in order to access the practical difficulties in obtaining field interface forces and test item interface and external motions in actual test scenarios.

- Development of an effective control system to be used in laboratory simulations with multiple exciters that be able to generate and control independently each input signal with the correct phase compensation between inputs so that time domain cross correlation requirements between excitation channels are satisfied.

- Development of frequency domain coupling techniques to account for nonlinearities that occur at the interface points between test item and vehicle.

- A detailed study of fatigue accumulation for various test fixture arrangements is required in single exciter test configurations to better access the amount of over-testing imposed to the test item when using enveloping techniques to define test item inputs.

- An investigation on the influence of angular measurements (moments and accelerations) on the test item's response so that finite element model updating techniques from experimentally obtained data can be improved.

- Development of new and improvement of existing measurement procedures and instrumentation to make angular measurements feasible.

APPENDIX - THE SINGULAR VALUE DECOMPOSITION (SVD) TECHNIQUE

This appendix outlines the Singular Value Decomposition (SVD) technique [23, 48] and some of its applications to the field of vibration testing. The goal is to provide a simple description of this powerful numerical technique in order to gain additional insights when using it to compute the pseudo-inverse of an FRF matrix.

Basics of the SVD Technique

If $[T]$ is a complex M x N matrix ($M > N$) ($[T] \in C^{MxN}$), the SVD of $[T]$ is expressed as

$$[T] = [U]\,[\Sigma]\,[V]^H \tag{A.1}$$

where "H" denotes the Hermitian operator. The M x M and N x N complex $[U]$ and $[V]$ are *unitary* matrices, i.e.

$$[U]^H[U] = [U][U]^H = [I] \tag{A.2}$$

$$[V]^H[V] = [V][V]^H = [I] \tag{A.3}$$

where $[I]$ denotes the identity matrix. Equations A.2 and A.3 imply that

$$[U]^{-1} = [U]^H \tag{A.4}$$

$$[V]^{-1} = [V]^H \tag{A.5}$$

The columns of $[U]$ are called the *Left Singular Vectors* of $[T]$, and they also represent the orthonormal eigenvectors of $[T][T]^H$ [48]. Similarly, the columns of $[V]$ are the *Right Singular Vectors* of $[T]$, and they represent the orthonormal eigenvectors of $[T]^H[T]$.

The M x N matrix $[\Sigma]$ is given as

$$[\Sigma] = \begin{bmatrix} [S] & [0] \\ [0] & [0] \end{bmatrix} \tag{A.6}$$

where the N x N diagonal matrix $[S]$ contains the *Singular Values* σ_p, $p = 1, \ldots, N$ of the complex matrix $[T]$ in decreasing order ($\sigma_1 > \sigma_2 > \ldots > \sigma_N$).

The singular values represent the non-negative square-roots of the eigenvalues of the matrix $[T]^H[T]$. Since $[T]^H[T]$ is hermitian, their eigenvalues are always real and therefore the singular values σ_p are also real.

The rank of $[T]$ (number of linearly independent column vectors in $[T]$) is the number of non-zero singular values of $[T]$ [48]. In obtaining the rank of the matrix $[T]$, a criterion is needed to either accept a small σ_N or discard it. This criterion depends on the accuracy of expected results. A reasonable criterion is to calculate the consecutive ratios of singular values, σ_1/σ_2, σ_2/σ_3, σ_3/σ_4, $\ldots$, σ_{N-1}/σ_N,. For example, if the rank of $[T]$ is 3 then σ_4 will be very small and the ratio σ_3/σ_4 will be very high compared with σ_2/σ_3.

The ratio of singular values can also be employed in the calculation of the spectral condition number ρ of $[T]$ [48], that is given by the ratio of the largest to the smallest non-zero singular value or

$$\rho = \frac{\sigma_{max}}{\sigma_{min}} \tag{A.7}$$

The condition number is used as an indicator of potential difficulties in obtaining the pseudo-inverse of $[T]$ since a high value of ρ reflects an ill-conditioned matrix.

Obtaining the Pseudo-Inverse Through SVD

The N x M matrix $[T]^+$ is called the Moore-Penrose [48] pseudo-inverse of $[T]$ if the following four conditions are satisfied

$$\begin{aligned} [T][T]^+[T] &= [T] \\ [T]^+[T][T]^+ &= [T]^+ \\ [T][T]^+ &\ \textit{is}\ \textit{symmetric} \\ [T]^+[T] &\ \textit{is}\ \textit{symmetric} \end{aligned} \tag{A.8}$$

Thus, if $[T]$ obeys all conditions expressed in Equations A.8, then there always exist $[T]^+$ and it is *unique*. Calculation of the pseudo-inverse of Equation A.1 leads to

$$[T]^+ = ([V]^H)^+ \, [\Sigma]^+ \, [U]^+ \tag{A.9}$$

Since matrices $[U]$ and $[V]$ are unitary, Equation A.9 can be simplified by using the identities expressed in Equations A.2 and A.3 along with Equations A.4 and A.5. The result is

$$[T]^+ = [V] \, [\Sigma]^+ \, [U]^H \tag{A.10}$$

and $[\Sigma]^+$ is a real N x M matrix that is obtained from Equation A.6 as

$$[\Sigma]^+ = \begin{bmatrix} [S]^+ & [0] \\ [0] & [0] \end{bmatrix} \tag{A.11}$$

Since $[S]$ is a N x N diagonal matrix, its pseudo-inverse coincides with the standard inversion that is given by the inverse of the singular values appearing on the main diagonal entries

$$[S]^{+} = \begin{bmatrix} \frac{1}{\sigma_1} & 0 & \dots & 0 \\ 0 & \frac{1}{\sigma_2} & \dots & 0 \\ \vdots & \ddots & \ddots & \vdots \\ 0 & 0 & \ddots & \frac{1}{\sigma_N} \end{bmatrix} \tag{A.12}$$

Thus, once the SVD of the complex matrix $[T]$ is obtained, the calculation of its pseudo-inverse is easily obtained by using the result expressed in Equation A.12. Equation A.12 also shows that once one or more singular values become very small the inversion of the N x N $[S]$ matrix tends to become ill conditioned, since the reciprocal of these small singular values gives large numbers and this may seriously affect the pseudo-inversion process.

Solution of an Over-Determined System of Linear Equations by SVD

The SVD can be used to solve the over-determined system of equations expressed as

$$[T]\{F\} = \{X\} \tag{A.13}$$

where as before, $[T]$ is a M x N $(M > N)$ complex matrix, the N x 1 vector $\{F\}$ is contains the unknowns and the M x 1 $\{X\}$ is the vector of independent terms. Equation A.13 may resemble, for example, the situation where a set of unknown input forces that are applied to a test item is obtained in terms of a set of measured output accelerations. In this case, matrix $[T]$ is the test item's accelerance matrix.

Application of the definition shown in Equation A.1 to the left hand side of Equation A.13 leads to the following expression

$$[U]\,[\Sigma]\,[V]^H\,\{F\} = \{X\} \tag{A.14}$$

Equation A.14 can be rewritten as

$$[\Sigma]\,\{\hat{F}\} = \{\hat{X}\} \tag{A.15}$$

with

$$\{\hat{F}\} = [V]^H\,\{F\} \tag{A.16}$$

$$\{\hat{X}\} = [U]^H\,\{X\} \tag{A.17}$$

Equation A.15 reflects a system of M uncoupled equations with N unknowns. Solution of this equation for vector $\{\hat{F}\}$ is given as

$$\{\hat{F}\} = [\Sigma]^+\,\{\hat{X}\} \tag{A.18}$$

where $[\Sigma]^+$ is given in Equations A.11 and A.12

Notice that the present discussion reflects the application of the SVD to situations where the matrices and vectors involved in the calculation process are frequency dependent. Thus, the solution process for the singular values as well as the pseudo-inverse must be performed for each frequency component in the desired frequency range.

BIBLIOGRAPHY

[1] Abdelhamid, M. K., 1996, "Judder: Diagnosis and Prevention", *Proceedings of the 14th International Modal Analysis Conference, (IMAC)*, Dearborn, MI, Volume 1, February, pp. 166-171.

[2] Allison, H., 1979, "Inverse Unstable Problems and Some of their Applications", *Mathematical Scientist*, N. 4, pp. 9-30.

[3] Bathe, K, J., 1982, *Finite Element Procedures in Engineering Analysis*, 1st Edition, Prentice Hall, Englewood Cliffs, New Jersey.

[4] Bendat, J. and Piersol, A., 1986, *Random Data, Analysis and Measurement Procedures*, 2nd Edition, John Wiley & Sons, New York, New York.

[5] Clough, R. and Penzien J., 1993, *Dynamics of Structures*, 2nd Edition, McGraw Hill, New York, New York.

[6] Craig Jr., R., 1981, *Structural Dynamics: An Introduction to Computer Methods*, John Wiley & Sons, New York, New York.

[7] Data Physics Corporation, 1989, *Dp420 FFT Analyzer Manual*, Version Dp420, San Jose, California.

[8] United States Department of Defense, 1983, *Environmental Test Methods and Engineering Guidelines, MIL-STD-810D*, Wright-Patterson AFB, OH, july.

[9] Ewins, D., 1984, *Modal Testing: Theory and Practice*, 1st Edition, Research Studies Press, London, United Kingdom.

[10] Fabunmi, J., 1986, "Effects of Structural Modes on Vibratory Force Determination by the Pseudoinverse Technique", *AIAA Journal*, Volume 24, N. 3, March, pp. 504-509.

[11] Fabunmi, J. A, 1987, "Feasibility of Dynamic Load Determination from Measured Mobilities", *Proceedings of the SEM Spring Conference*, Houston, Texas, June, pp. 845-850.

[12] Fletcher, J. N., Vold, H., Hansen, M. D., 1995, "Enhanced Multiaxis Vibration Control Using a Robust Generalized Inverse Matrix", *Journal of the Institute of Environmental Sciences (IES)*, pp. 36-42, March-April.

[13] Fregolent, A. and Sestieri, A., 1990, "Assessment of Procedures for Force Identification From Experimental Response", *Proceedings of the 15th International Seminar on Modal Analysis*, Leuven, Belgium, Part II pp. 825-838.

[14] Gordis, J. H., 1994, "Structural Synthesis in the Frequency Domain: A General Formulation", *Proceedings of the 12th International Modal Analysis Conference (IMAC)*, Honolulu, Hawaii, Volume I, February, pp. 575-581.

[15] Gregory, D. C., Priddy, T. G., Smallwood, D. O., 1987, "Experimental Determination of the Dynamic Forces Acting on Non-rigid Bodies", *Proceedings of the Society of Automotive Engineering (SAE)* Paper N. 861791, pp. 1-11.

[16] Han, M-C and Wicks, A. L., 1990, "Force Determination with Slope and Strain Response Measurement", *Proceedings of the 8th International Modal Analysis Conference (IMAC)*, Kissimmee, Florida, Volume I, February, pp. 365-372.

[17] Hansen, M., Starkey J. M., 1990, "On Predicting and Improving the Condition of Modal-model-based Indirect Force Measurement Algorithms", *Proceedings of the 8th International Modal Analysis Conference (IMAC)*, Orlando, Florida, Volume I, February, pp. 115-120.

[18] Hillary, B., 1983, *Indirect Measurement of Vibration Excitation Forces*, PhD Thesis, Imperial College of Science Technology and Medicine, London, United Kingdom.

[19] Hillary, B. and Ewins, D. J., 1984, "The Use of Strain Gages in Force Determination and Frequency Response Measurements", *Proceedings of the 2nd International Modal Analysis Conference (IMAC)*, Orlando, Florida, Volume I, February, pp. 627-634

[20] Imperial College of Science, Technology and Medicine, 1994, *MODENT, Reference Manual, ICATS, version 2.19, Imperial College Testing and Software*, Mechanical Engineering Department, Exhibition Road, London, SW72BX, United Kingdom.

[21] Lee, J. K., Park, Y., 1994, "Response Selection and Dynamic Damper Application to Improve the Identification of Multiple Input Forces of Narrow Frequency Band", *Mechanical Systems and Signal Processing*, Volume 8, N. 6, pp. 649-664.

[22] Leung, A. Y. T., 1993, *Dynamic Stiffness and Substructures*, 1st Edition, Springer-Verlag, New York, New York.

[23] Maia, N. M. M., 1989, "An Introduction to the Singular Value Decomposition Technique (SVD)", *Proceedings of the 7th International Modal Analysis Conference (IMAC)*, Las Vegas, Nevada, Volume I, February, pp. 335-339.

[24] The MathWorks Inc., 1994, *MATLAB - User's Guide*, Version 4.2c, November, New York, New York.

[25] McConnell, K. G, 1995, *Vibration Testing: Theory and Practice* John Wiley & Sons, New York, New York.

[26] McConnell, K. G, 1994, "From Field Vibration Data to Laboratory Simulation", *Experimental Mechanics*, Volume 34, N. 3, September, pp. 181-193.

[27] Murfin, W. B., 1968, "Dual Specification in Vibration Testing", *Shock and Vibration Bulletin*, N. 38, August, Part I, pp. 109-113

[28] Otts, J. V., 1965, "Force-Controlled Vibration Tests: A Step Toward Practical Application of Mechanical Impedance", *Shock and Vibration Bulletin*, N. 34, Part 5, pp. 45-53.

[29] Otts, J. V., Hunter, N. F., 1968, "Random-Force Vibration Testing",*Shock and Vibration Bulletin*, N. 37, Part 3, pp. 61-73.

[30] Penny, J. E. T., Friswell, M. I., Garvey, S. D, 1994, "Automatic Choice of Measurement Locations for Dynamic Testing", *AIAA Journal*, Volume 32, N. 2, pp. 407-413.

[31] Rogers, J. D., Beightol, D. B, Doggett, J. W., 1990, "Helicopter Flight Vibration of Large Transportation Containers - A Case For Test Tailoring", *Proceedings of the 36th Annual Technical Meeting, Institute of Environmental Sciences (IES)*, New Orleans, Louisiana, April, pp. 515-521.

[32] Rogers, J., Hendrick, D. M, 1990, "Sandia National Laboratories New High Level Acoustic Test Facility", *Proceedings of the 36th Annual Technical Meeting, Institute os Environmental Sciences (IES)*, New Orleans, Louisiana, April, pp. 574-579.

[33] Scharton, T., 1990, "Motion and Force Controlled Vibration Testing", *Proceedings of the 36th Annual Technical Meeting, Institute of Environmental Sciences (IES)*, Volume I, April, New Orleans, Louisiana, pp. 77-85.

[34] Scharton, T., 1995, "Vibration-Test Force Limits Derived from Frequency-Shift Method", *Journal of Spacecrafts and Rockets*, Volume 32, N. 2, pp. 312-316.

[35] Scharton, T. D., 1994, "Force Limited Vibration Testing "Top Ten" Research Problems", *Handouts, Tutorial Session on Vibration Test Tailoring, 13th International Modal Analysis Conference (IMAC)*, February, Nashville, Tennessee.

[36] Scharton, T. D., 1991, "Dual Control Vibration Tests of Flight Hardware", *Proceedings of the 37th Annual Technical Meeting, Institute of Environmental Sciences (IES)*, Volume I, May, San Diego, California, pp. 68-77.

[37] Scharton, T. D., Boatman, D. J., Kern, D. L., 1990, "Motion and Force Controlled Vibration Testing", *Proceedings of the 12th Aerospace Testing Seminar*, Manhattan Beach, California, pp. 77-85.

[38] Scharton, T. D., 1990, "Analysis of Dual Control Vibration Testing", *Proceedings of the 36th Annual Technical Meeting, Institute of Environmental Sciences (IES)*, Volume I, April, New Orleans, Louisiana, pp. 140-146.

[39] Smallwood, D. O., 1982, " A Random Vibration Control System for Testing a Single Test Item with Multiple Inputs", *Proceedings of the Society of Automotive Engineering (SAE)*, paper N. 821482, pp. 4571-4577.

[40] Smallwood, D. O., 1978, "Multiple Shaker Random Vibration Testing with Cross Coupling", *Proceedings of the 24th Annual Technical Meeting, Institute of Environmental Sciences (IES)*, April, Fort Worth, Texas, pp. 341-347.

[41] Smallwood, D. O., 1989, "An Analytical Study of a Vibration Test Method Using Extremal Control of Acceleration and Force", *Proceedings of the 35th Annual Technical Meeting, Institute of Environmental Sciences (IES)*, Volume I, May, pp. 263-271, Anaheim, California, pp. 263-271.

[42] Smallwood, D. O., 1976, "The Applications of Unloaded (Free) Motion Measurements and Mechanical Impedance to Vibration Testing", *Proceedings of the 22nd Annual Technical Meeting, Institute of Environmental Sciences (IES)*, Volume I, May, Philadelphia, Pennsylvania, pp. 71-82.

[43] Starkey J. M., Merrill, G. L., 1989, "On the Ill-conditioning Nature of Indirect Force-measurement Techniques", *International Journal of Analytical and Experimental Modal Analysis*, Volume 4, N. 3, pp. 103-108.

[44] Sweitzer, K. A., 1987, "A Mechanical Impedance Correction Technique for Vibration Tests", *Proceedings of the 33rd Annual Technical Meeting, Institute of Environmental Sciences (IES)*, Volume I, May, San Jose, California, pp. 73-76.

[45] Sweitzer, K. A., 1994, *Vibration Models Developed for Subsystem Test*, M.Sc. Thesis, Syracuse University, Utica, New York, May.

[46] Szymkowiak, E., A., Silver II W., 1990, " A Captive Store Flight Vibration Simulation Project", *Proceedings of the 36th Annual Technical Meeting, IES*, New Orleans, Louisiana, April, pp. 531-538.

[47] To, W. M., Ewins, D. J., 1995, "The Role of the Generalized Inverse in Structural Dynamics", *Journal of Sound and Vibration*, Volume 186, N. 2, pp. 185-195.

[48] Watkins, D. S., 1990, *Fundamentals of Matrix Computations*, 1st Edition, John Wiley & Sons, New York, New York.

[49] Zhang, L., 1985, "An Investigation of Random Force Identification by Parametric Model Method", *Proceedings of the 10th International Seminar on Modal Analysis*, K. U. Leuven, Belgium, pp. 1-10.

BIOGRAPHICAL SKETCH

Paulo Sergio Varoto was born July 17, 1964 in São Carlos, São Paulo, Brazil. He received the Bachelor of Science in Mechanical Engineering from the University of São Paulo in 1987 and the Master of Science in Mechanical Engineering from the University of São Paulo in 1991. He has been working as a lecturer at the University of São Paulo in the field of Dynamics and Vibrations since 1989.